ASTROPHYSICS AND SPACE SCIENCE PROCEEDINGS

R.K. Chaudhuri
M.V. Mekkaden
A.V. Raveendran
A.S. Narayanan
Editors

Recent Advances in Spectroscopy

Theoretical, Astrophysical and Experimental Perspectives

Springer

Astrophysics and Space Science Proceedings

For further volumes:
http://www.springer.com/series/7395

Recent Advances in Spectroscopy

Theoretical, Astrophysical and Experimental Perspectives

Editors

R.K. Chaudhuri
M.V. Mekkaden
A.V. Raveendran
A. Satya Narayanan

Indian Institute of Astrophysics, Bangalore, India

Springer

Editors
R.K. Chaudhuri
Indian Institute of Astrophysics
II Block, Koramangala
Sarjapur Road
Bangalore-560034
India
rkchaudh@iiap.res.in

M.V. Mekkaden
Indian Institute of Astrophysics
II Block, Koramangala
Sarjapur Road
Bangalore-560034
India
mvm@iiap.res.in

A.V. Raveendran
Indian Institute of Astrophysics
II Block, Koramangala
Sarjapur Road
Bangalore-560034
India
avr@iiap.res.in

A. Satya Narayanan
Indian Institute of Astrophysics
II Block, Koramangala
Sarjapur Road
Bangalore-560034
India
satya@iiap.res.in

ISSN 1570-6591 e-ISSN 1570-6605
ISBN 978-3-642-10321-6 e-ISBN 978-3-642-10322-3
DOI 10.1007/978-3-642-10322-3
Springer Heidelberg Dordrecht London New York

Library of Congress Control Number: 2010924625

Cover design: eStudio Calamar S.L.

Printed on acid-free paper

Springer is part of Springer Science+Business Media (www.springer.com)

Preface

Spectroscopy is the basic tool employed in astronomy to derive physical parameters, like temperature, density, chemical composition, velocity and magnetic fields, that give insights into the physical processes that are operative in the celestial objects. Much of our understanding of stellar atmospheres and even low-density collisionally excited plasma, such as supernova remnants, is based on the understanding of plasma processes in the solar atmosphere. Although some of these processes can be studied by high spatial resolution images of the sun, our knowledge of the temperature, densities and dynamics of different regions of the solar atmosphere is based on the high-resolution spectroscopy in the X-ray, UV and optical spectral regions.

The atomic and molecular spectroscopy plays a key role in understanding astrochemistry. For example, the carbon bearing molecules, such as polycyclic aromatic hydrocarbons (PAHs), are now thought to be widespread in the interstellar medium in their neutral and ionized forms. Identifying the carriers responsible for several observed interstellar bands will allow us to derive important information on cosmic elemental abundance as well as on the physical conditions reigning in specific interstellar environments. The identifications of these carriers are the key for a correct understanding of the energetic mechanisms that govern the origin and evolution of the interstellar medium.

Comprehensive and accurate transition probability data are needed to determine the abundances of neutral atom and all of its ions in different astrophysical environments. Determination of radiative lifetimes can provide the absolute scale for converting the branching fractions into atomic transition probabilities and vice versa. Since the derivation of the physical parameters of the prevailing astrophysical conditions is an inverse problem, accurate theories of line formation under widely varying conditions that one encounters in celestial objects have to be developed.

It is imperative that a multi-disciplinary approach, by combining astrophysical observation with laboratory simulations and theoretical modeling, is essential to address the complex issues involved in interpreting the data for a better understanding of the physical conditions prevalent in celestial objects. Also for a proper interpretation of the high-resolution data that we obtain from space missions, it has become necessary to improve the accuracy of the theory of line formation to a great extent. It is with this idea that the *International Conference on Recent Advances in Spectroscopy : Theoretical, Experimental, and Astrophysical Perspectives* was organized at Kodaikanal, India. Peers in the areas of theoretical and experimental atomic physics, and observational astrophysics were brought together during the conference.

The conference began with a welcome note and opening remarks by M. V. Mekkaden. The conference had 12 sessions spread over three and half days. The first two sessions were devoted to the general aspects of Atomic and Molecular Spectroscopy. They were followed by three sessions on theoretical aspects of spectroscopy. One session was devoted to line formation in stellar atmospheres. There were two sessions on observations and analysis on Solar spectroscopy and three sessions on similar topics in Stellar spectroscopy. The conference was summarized by T. P. Prabhu, while the vote of thanks was delivered by R. K. Chaudhuri.

We would like to acknowledge the sponsors, Indian Institute of Astrophysics (IIA), Department of Science and Technology (DST), Council of Scientific and Industrial Research (CSIR), and Board of Research in Nuclear Sciences (BRNS), without whom the conference would not have materialized. We thank Prof. Siraj S Hasan, Director, IIA, for his whole-hearted support, encouragement, and advice, right from the planning of this conference. Dr K. Sundararaman and his colleagues of the Kodaikanal Observatory are thanked for their unstinted support during the conference. Dr C. Kathiravan helped us in designing the cover pages for both the abstract book and the proceedings. The untiring support of the LOC and SOC members is gratefully acknowledged.

Bangalore,
August 2009

R K Chaudhuri
M V Mekkaden
A V Raveendran
A Satya Narayanan

Contents

List of Participants

Adhikari S, Department of Physical Chemistry, Indian Association for the Cultivation of Science
Jadavpur Kolkata 700032, India
`pcsa@iacs.res.in`

Arunan E, Department of Inorganic and Physical Chemistry
Indian Institute of Science
Bangalore 560012, India
`arunan@ipc.iisc.ernet.in`

Ashok N M, Physical Research Labortory
Ahmedabad 380009, India
`ashok@prl.ernet.in`

Bagare S P, Indian Institute of Astrophysics
Bangalore 560034, India
`bagare@iiap.res.in`

Banerjee D, Indian Institute of Astrophysics
Bangalore 560034, India
`dipu@iiap.res.in`

Banerjee D, Department of Physics, Shibpur Dinobundhoo Institution (College), Shibpur
Howrah 711102, India
`banerjee.debi@gmail.com`

Banerjee K, S.N. Bose National Centre for Basic Sciences, Salt Lake
Kolkata, India
`kinshukb@bose.res.in`

Chatterjee S, Department of Chemistry, Bengal Engineering and Science University, Shibpur
Howrah 711103, India
`sudipchattopadhyay@rediffmail.com`

Chatterjee S, Indian Institute of Astrophysics
Bangalore 560034, India
`chat@iiap.res.in`

Chaudhuri R, Indian Institute of Astrophysics
Bangalore 560034, India
`rumpa@iiap.res.in`

Chaudhuri R K, Indian Institute of Astrophysics
Bangalore 560034, India
`rkchaudh@iiap.res.in`

Dasgupta A, Plasma Physics Division, Naval Research Laboratory, 4555 Overlook Avenue
SW Washington, DC 203755346
USA
`dasgupta@ppdmail.nrl.navy.mil`

Goswami A, Indian Institute
of Astrophysics
Bangalore 560034, India
aruna@iiap.res.in

Hirata S, Quantum Theory Project
Department of Chemistry and
Department of Physics University
of Florida, USA
hirata@qtp.ufl.edu

Mallik D C V, Indian
Institute of Astrophysics
Bangalore 560034, India
dcvmlk@iiap.res.in

Mallik S V, Indian
Institute of Astrophysics
Bangalore 560034, India
sgvmlk@iiap.res.in

Mekkaden M V, Indian
Institute of Astrophysics
Bangalore 560034, India
mvm@iiap.res.in

Mukhopadhyay A, Department
of Physical Chemistry, Indian
Association for the Cultivation
of Science, Jadavpur
Kolkata 700032, India
pcam@iacs.res.in

Mukhopadhyay M, Department
of Physical Chemistry, Indian
Association for the Cultivation
of Science, Jadavpur
Kolkata 700032, India
pcmm@iacs.res.in

Muneer S, Indian Institute
of Astrophysics
Bangalore 560034, India
muneers@gmail.com

Nagaraju S, Indian Institute
of Astrophysics
Bangalore 560034, India
nagaraj@iiap.res.in

Nagendra K N, Indian
Institute of Astrophysics
Bangalore 560034, India
knn@iiap.res.in

Nataraj H S, Indian Institute
of Astrophysics
Bangalore 560034, India
nataraj@iiap.res.in

Nayak M, Theoretical Chemistry
Section, Bhabha Atomic
Research Centre, Trombay
Mumbai-400085, India
mknayak@barc.gov.in

Pal S, Physical Chemistry Division,
National Chemical Laboratory
Pune 411008, India
spal@ncl.res.in

Pandey G, Indian Institute
of Astrophysics
Bangalore 560034, India
pandey@iiap.res.in

Parihar P, Indian Institute
of Astrophysics
Bangalore 560034, India
psp@iiap.res.in

Prabhu T P, Indian Institute
of Astrophysics
Bangalore 560034, India
tpp@iiap.res.in

Pradhan A K, Department
of Astronomy, The Ohio State
University, Columbus, Ohio 43210
USA
pradhan@astronomy.ohio-state.edu

Priya S, Department of
Astronomy, Osmania University
Hyderabad, India
`shantipriya@osmania.ac.in`

Ramya S, Indian Institute
of Astrophysics
Bangalore 560034, India
`ramya@iiap.res.in`

Rangarajan K E, Indian Institute
of Astrophysics
Bangalore 560034, India
`rangaraj@iiap.res.in`

Rao J V S V, Indian Institute
of Astrophysics, Kodaikanal, India
`jvsv52@gmail.com`

Rao M S, Indian Institute
of Astrophysics
Bangalore 560034, India
`msrao@iiap.res.in`

Rao N K, Indian Institute
of Astrophysics
Bangalore 560034, India
`nkrao@iiap.res.in`

Raveendran A V, Indian
Institute of Astrophysics
Bangalore 560034, India
`avr@iiap.res.in`

Ray Chaudhuri J P, Department
of Physics, Katwa College, Katwa
Burdwan 713130, India
`jprc_8@yahoo.com`

Rutten R J, Sterrekundig Instituut
Utrecht University, Utrecht
The Netherlands Institutt
for Teoretisk Astrofysikk
Oslo University, Oslo, Norway
`R.J.Rutten@uu.nl`

Samanta A K, Department
of Physical Chemistry, Indian
Association for the Cultivation
of Science, Jadavpur
Kolkata 700032, India
`pcaks@iacs.res.in`

Sarkar B, Department
of Chemistry, North Eastern
Hill University, Shillong 793022 India
`s.biplab@gmail.com`

Satya Narayanan A, Indian
Institute of Astrophysics
Bangalore 560034, India
`satya@iiap.res.in`

Sengupta S, Indian Institute
of Astrophysics
Bangalore 560034, India
`sujan@iiap.res.in`

Silver E, Harvard-Smithsonian
Center for Astrophysics, 60 Garden
Street, Cambridge, MA 02138, USA
`esilver@cfa.harvard.edu`

Sinha Mahapatra U, Department
of Physics, Taki Government College
Taki, North 24 Parganas, India
`uttam_sinhamahapatra@`
`rediffmail.com`

Subramaniam A, Indian
Institute of Astrophysics
Bangalore 560034, India
`purni@iiap.res.in`

Sundararaman K Indian Institute
of Astrophysics, Kodaikanal, India
`sundar@iiap.res.in`

Sutherson D, Indian Institute
of Astrophysics, Kodaikanal, India
`mailsuther@gmail.com`

Vaval N, Physical Chemistry
Division, National Chemical
Laboratory, Pune 411008, India
`np.vaval@ncl.res.in`

Werner K, Institute for Astronomy
and Astrophysics, Kepler Center
for Astro and Particle Physics
University of Tubingen, Sand 1
72076 Tubingen, Germany
`werner@astro.uni-tuebingen.de`

"Recent Advances in Spectroscopy:
Theoretical, Astrophysical, and Experimental Perspectives"
Eds. Chaudhuri R K, Mekkaden M V, Raveendran A V, Satya Narayanan A
Astrophysics and Space Science Proceedings, Springer-Verlag, Berlin, 2010.

X-Ray Spectroscopy of Highly Charged Ions in Laboratory and Astrophysical Plasmas

E. H. Silver[1], N. S. Brickhouse[1], T. Lin[1], G. X. Chen[2], K. Kirby[2],
J. D. Gillaspy[3], J. N. Tan[3], and J. M. Laming[4]

[1] Harvard-Smithsonian Center for Astrophysics, Cambridge, MA, USA
[2] *ITAMP*, Harvard-Smithsonian Center for Astrophysics, Cambridge, MA, USA
[3] National Institute of Standards and Technology, Gaithersburg, MD, USA
[4] Center for Space Science, US Naval Research Laboratory, Washington, DC, USA

Summary. The Universe is rich with X-ray sources which can now be observed with unprecedented resolution using instruments on *Chandra* and *XMM-Newton*. In order to interpret their spectral signatures and derive reliable information regarding the physical characteristics and the dynamics of these objects and their environments, detailed spectral models have been developed which require vast amounts of highly accurate data on atomic collisional and radiative properties for ions in a broad range of ionization states. These data are usually obtained from theoretical calculations through which a large parameter space of physical conditions such as temperature and density can be explored. Critical to the reliability of these models is the careful benchmarking of the theoretically generated data through high-precision laboratory measurements. To provide a picture of the astrophysics, the goal is to develop a set of key spectroscopic diagnostics with an accuracy ($\sim$ 5–10%) that is commensurate with the uncertainties in the highest quality astrophysical spectra. Using a broad band, high resolution X-ray microcalorimeter coupled to an EBIT, we are studying the behavior of highly charged plasma ions. Our goals for accuracy and reliability are now achievable and some of our results are presented here. A new technique for improving the measurement accuracy is also described.

1 Introduction

X-ray spectroscopy measurements are used to determine the temperature distribution, density, ionization state, and elemental composition of hot cosmic plasmas. A knowledge of these basic parameters provides an understanding of physical processes in the hot universe such as atmospheric heating, transport, shock waves and accretion. Plasmas of special interest are found in the magnetically heated coronae of late-type stars, the accretion disks surrounding collapsed stellar objects, the bubbles of gas heated by supernovae and the tunnels throughout interstellar space that they create, the halos of elliptical galaxies, the nuclei of active galaxies and the vast regions in galaxy clusters.

The determination of the physical parameters that define the plasmas relies on complex models of the continuum and line emission and absorption.

X-ray grating spectra from *Chandra* and *XMM-Newton* have provided new insights into the physical processes present in astrophysical sources. However, our understanding of fundamental high energy processes occurring in highly ionized plasmas is not commensurate with the quality of data obtained by the new X-ray telescopes and spectrometers. Spectral modeling in X-ray astronomy relies on atomic theoretical calculations over a broad parameter space to produce line flux predictions for millions of lines. Many of these lines are weak and uninteresting diagnostically, but they may blend with lines of interest and/or with weak neighbors to produce an apparent pseudo-continuum if the resolving power of the spectrometer is not adequate. Current theoretical capabilities can produce large models to generate a complete enough set of lines for most astrophysical purposes [Ferland *et al.* 1998; Bautista & Kallman 2001; Smith *et al.* 2001; Gu 2007]; new theoretical methods are now improving the calculated energy levels such that X-ray wavelengths are accurate to a few mÅ [Kotochigova *et al.* 2005]. Thus, while surveys of individual ion spectra continue to provide useful benchmarks [Brown *et al.* 1998, 2002], the credibility of our models depends on the accuracy of our diagnostics.

2 The electron beam ion trap (EBIT)

In traditional laboratory plasma X-ray sources such as tokamaks, mirror machines and those produced with lasers, the physical processes cannot be easily isolated. The interpretation of the spectra obtained from these sources requires modeling of the charge balance and a mix of line formation physics. The Electron Beam Ion Trap (EBIT) is a source that operates at effective electron densities $\sim 10^{12}\mathrm{cm}^3$. It eliminates the transport issues and line-of-sight integrations that introduce uncertainties into the interpretation of tokamak spectra.

At the NIST EBIT, an energy-tunable, 0-150 mÅ, electron beam can be accelerated to moderate energies (100 eV-30 keV) by a series of cylindrical electrodes (drift tubes). The beam is focused to a small diameter ($\sim$70 μm) by a superconducting, Helmholtz pair magnet that provides a maximum axial field of 3 T. Atoms or low charge ions introduced into the center of the middle drift tube, where the electron beam has its tightest focus, are stripped of their outer electrons by impact ionization and reach successively higher charge states. The limiting charge state is determined by the voltage applied to the center drift tube. It is reached when the ionization potential of the ion is greater than the energy of the colliding electrons. An axial trap for the ions is controlled by applying a small positive bias ($<$500 V) on the end cap drift tubes located on either side of the center drift tube. Radial trapping is provided by the space charge of the electron beam itself, and also by the axial magnetic field. In addition to creating the highly charged ions and trapping them, the electron beam plays a third important role: it excites transitions, which provide photon emission for spectroscopy.

When compared with a conventional plasma that has a broader electron distribution, such as a Maxwell-Boltzman distribution, the electron beam is monoenergetic. It is precisely tunable, and rapidly switchable in energy (at rates of several keV per millisecond). A wide range of species to be studied can be loaded into the trap either as gases or metal ions. A gas at room temperature, or vapor from a volatile liquid or solid, can be introduced as neutral atoms through a series of collimating holes through a side port. Metals can be loaded along the magnetic field axis using a metal vapor vacuum arc (MEVVA) ion source. The MEVVA design used at NIST allows uninterrupted ion injection for long periods of time. It allows eight independent electrodes to be changed in vacuum with the flip of a switch, each one of which significantly outlasts a single electrode in older MEVVA designs [Holland *et al.* 2005]. The NIST EBIT has been described in detail in many journal articles (see http://physics.nist.gov/MajResFac/EBIT).

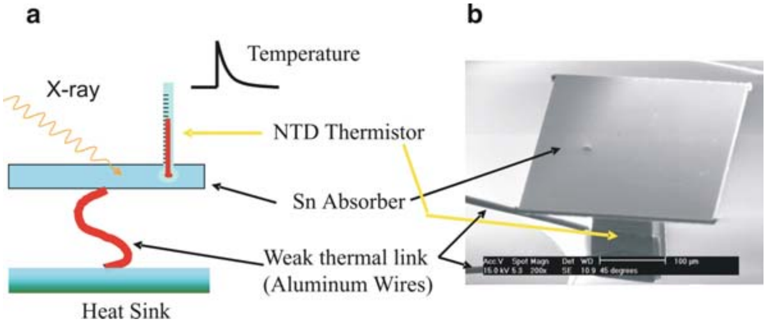

Fig. 1. A) Schematic representation of the microcalorimeter; B) micrograph of a single NTD-Ge microcalorimeter with Sn absorber.

3 The microcalorimeter

Broad-band energy-dispersive devices such as proportional counters, solid state ionization detectors (Si(Li) and HP Ge) and several kinds of scintillating materials obtain spectra over an energy range of many keV. They have quantum efficiencies approaching 100% but their energy resolution is poor to modest ($5 < E/\Delta E < 60$). For certain applications, arrays of these detectors are used for imaging as well (CCDs are one type). Narrow-band, wavelength-dispersive instruments such as diffraction gratings or Bragg crystals study discrete spectral features. These possess high resolving power ($100 < E/\Delta E < 10{,}000$) but only modest efficiencies and are not easily adapted for imaging spectroscopy. Position-sensitive broad-band detectors are used to record the wavelength dispersed spectrum.

Although these instruments have yielded many excellent results, their limitations have made it difficult to address scientific problems that require high spectral resolution, broad energy coverage and high efficiency simultaneously.

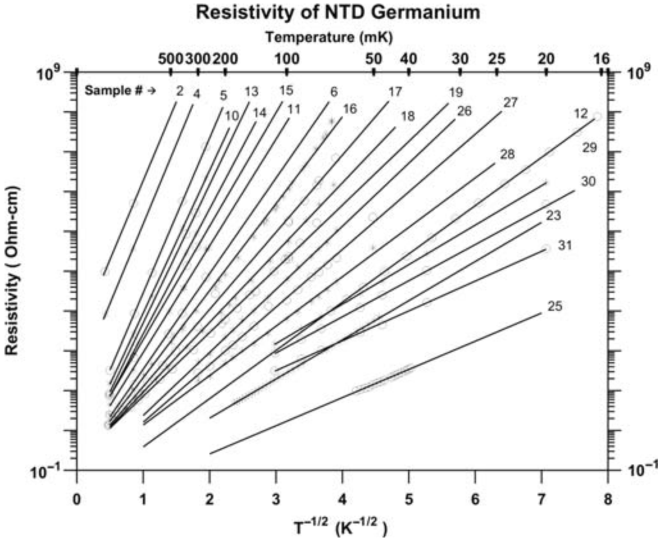

Fig. 2. The resistivity vs the inverse of the square root of the temperature for a variety of dopant concentrations for NTD Ge.

In a microcalorimeter (operating at ~60 mK), X-ray photons are absorbed by a metal foil and converted into heat. The temperature of the foil will increase because the heat capacity of the supercold foil is ~ 10^{-14} J/K. This temperature rise (~10 mK for a 6 keV X-ray) is proportional to the X-ray energy and is transformed by a thermistor into an electronic signal (see Fig. 1A). Microcalorimeters combine the broad-band energy response and high efficiency of the conventional energy-dispersive detector with a resolving power approaching that of a crystal or grating spectrometer.

To date, the microcalorimeter spectrometer in the Atomic Physics Division at NIST incorporates a 1x4 pixel array. Each pixel consists of a germanium thermistor attached to a superconducting tin (Sn) absorber. A SEM micrograph of one of these pixels is shown in Fig. 1B. The Sn is 0.3 mm x 0.3 mm x 7 μm thick. The thermistor, which is doped via neutron transmutation (NTD), is shown below the Sn. The relationship between resistivity and temperature is shown in Fig. 2. Each curve corresponds to a different dopant concentration and this catalog makes it relatively straightforward to fabricate a thermistor to operate at a specific temperature with a resistance that minimizes the electronic noise when read out by the negative voltage feedback preamplifier shown in Fig. 3.

The microcalorimeter on the NIST EBIT uses liquid helium as the only expendable cryogen and it lasts for three days between refills. It includes a 2-stage adiabatic demagnetization refrigerator (ADR) of novel design that can maintain a temperature of 60 mK ± 1.8 μK for up to 52 hours before the magnets are recycled. The detectors routinely achieve an energy resolution of ∼5 eV (in the EBIT laboratory) and under optimal conditions, 3 eV has been achieved at 6 keV [Silver *et al.* 2005] and 2.5 eV at 2 keV. The spectrometer can synchronize photon detection with the temporal behavior of the EBIT.

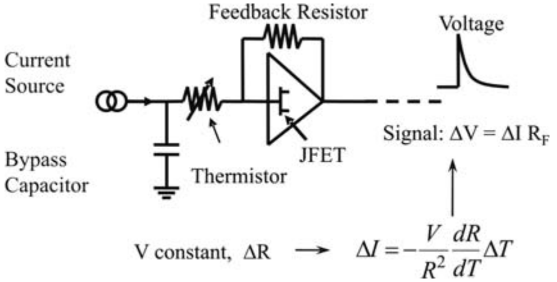

Fig. 3. The negative voltage feedback preamplifier readout is derived from charge sensitive circuitry used by Si(Li) and HP Ge ionization detectors.

4 Measuring the efficiency of the microcalorimeter

The microcalorimeter system now incorporates a unique spectroscopic technique for measuring the transmission efficiency of the cryostat's internal windows while it is attached to the EBIT. This is especially important for measurements of X-rays below 1 keV. Several nested thermal barriers are used to limit the radiation load on the microcalorimeter; without these thermal shields, the detector could not be cooled to 60 mK. The temperatures of these shields are approximately 190 K, 90 K, 4 K, 1.2 K and 60 mK. Each shield has a thin window made of polyimide coated with aluminum to allow low energy X-rays to be transmitted to the detector. The X-ray transmission of these windows is a steeply varying function of energy below 1 keV. Uncertainties in the transmission can affect the measured X-ray line ratios from highly charged ions, especially if the energies of the lines are separated by a few hundred eV. Although the transmission function can be calculated from our knowledge of the nominal thicknesses of the polyimide and aluminum coating on each window, there is the possibility that these windows can become coated with thin layers of water and/or other residual gases in the cryostat, thereby changing slightly the window transmission properties. To account for this, we have developed a technique for calibrating the total window transmission in-situ. This is typically performed before and after each experimental run. Referring to Fig. 4, copper and silver X-rays are produced in an X-ray tube that is attached to the beam line connecting the microcalorimeter to the

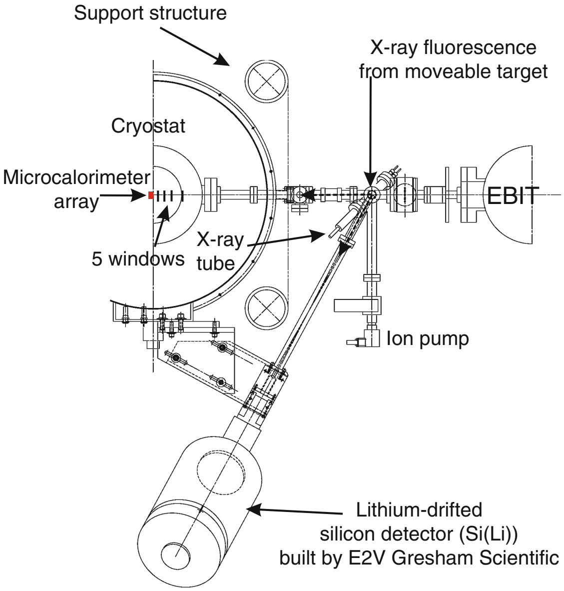

Fig. 4. Top view of the the instrumentation used to measure the microcalorimeter window transmission in-situ (the brand name is given for scientific completeness and should not be interpreted as an endorsement of the product.)

EBIT. These X-rays fluoresce emission lines of C K_α (277 eV), O K_α (525 eV), F K_α (677 eV), Cu L_α (929 eV) and Al K_α (1487 eV) in a target that can be moved in and out of the beam line. The fluorescent X-rays are detected by the microcalorimeter and a Si(Li) detector whose intensity response has been absolutely calibrated [Detector properties determined by E2V and SAO]. To check that each detector views the X-ray targets at an angle that is equal to but opposite in sign from the surface normal, the Si(Li) detector was placed at the end of each arm of the beamline to measure the relative intensities of the X-ray lines emitted by the target. Variations in these line ratios are attributed to slight geometrical differences in the orientation of each beamline arm and are accounted for in the analysis. (In actuality, only a 1-2% variation was observed). In practice, the intensity differences between the Si(Li) and microcalorimetor for each energy are thus due to the respective solid angles subtended by the detectors at the target and the total efficiencies of the two detectors. (The total efficiency includes the transmission of windows and the absorption properties of the detector elements; at these energies the absorption of the detectors is 100%). Since the efficiency of this particular Si(Li) detector is known and the solid angles are measured, the microcalorimeter window transmission can be obtained routinely. Fig. 5 (left) shows sample spectra from the fluorescing target as measured by the Si(Li) detector (top) and microcalorimeter (bottom). From this data the transmission of the windows is modeled by including the nominal thicknesses of the polyimide, aluminum coatings and additional residual gases, if necessary. The solid curve in Fig. 5 (right) is the expected transmission for all of the windows (6770 Å polyimide and 2664 Å of aluminum). The dashed curve is the best fit to the measured data points. To fit the data, 2300 Å of water vapor and 1000 Å of nitrogen were added to the nominal thicknesses of the windows, which represents a small amount of gas adsorbed on the windows. Such a correction to the transmission would change the measured intensity ratio of emission lines at 730 eV and 830 eV by 7% of its magnitude. This new system allows us to test the estimates made in Laming et al. [Laming *et al.* 2000] and confirms that the corrections to the expected window transmission are small.

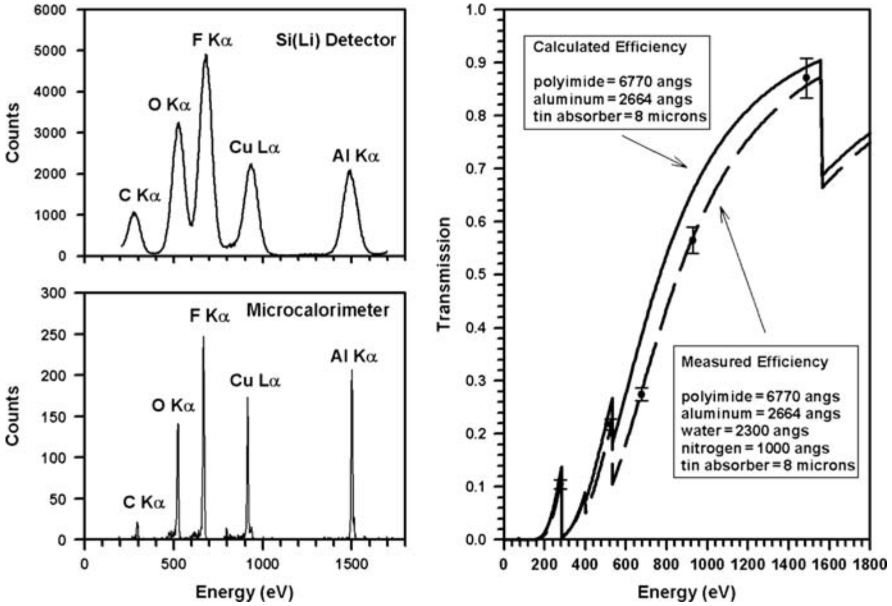

Fig. 5. Left top: The spectrum of the calibration lines measured by the Si(Li) detector; Left bottom: The spectrum of the calibration lines measured by the microcalorimeter. Right: The window transmission obtained from the data.

5 Astrophysical and laboratory plasma diagnostics

The grating spectrometers on *XMM-Newton* and *Chandra* have maximum sensitivity for the wavelength range of 35-5 Å (0.3-2.5 keV), the region where most cosmic X-ray sources emit copiously from L-shell transitions in Fe and Ni. This energy band also includes numerous K-shell transitions from H- and He-like ions of N, O, Ne, Mg, and Si. At energies between 2 and 7 keV, the H- and He-like ions of heavier elements such as S, Ar, Ca, Fe, Ni are prominent in relatively low resolution spectra taken with CCDs of *Chandra* and *XMM-Newton*. For the highest quality astrophysical spectra, the line ratios used to determine temperatures, densities, elemental abundances, ionization states, and opacities can be very accurately measured to 10% or even better for closely spaced lines. On the other hand, we are still using predicted line fluxes with typical uncertainties of 20 to 30% or worse, even for the strongest and most common lines, namely those of the abundant H-like and He-like ions and Fe and Ni L-shell ions. Interpreting the exquisite astrophysical spectra requires improvement in the accuracy of the atomic data. Fortunately, these improvements are now achievable given modern calculation and laboratory measurements. Fully relativistic R-matrix theory using large atomic structure models and modern computational approaches is, in principle, capable of achieving an accuracy of 5 to 10% [Chen *et al.* 2006]. While the parameter space available from models far exceeds the capacity of existing laboratories, targeted experimental measurements of comparable accuracy are now guiding and testing theory.

The importance of He-like diagnostics obtained from ions of C through Fe cannot be overstated. The intercombination, forbidden, and resonance lines provide density and temperature diagnostics over a wide range of parameters in both photoionized and collisionally ionized plasmas. The He-like ions N VI, O VII, Ne IX and Mg XI are especially important diagnostic line ratios for the electron density and are widely used in X-ray astronomy. These lines are easily identified in spectra and are unblended. N VI and O VII lines are density sensitive above 10^{10}cm^3 while Ne IX and Mg XI are useful from 10^{11}-10^{12}cm^3. O VII densities in this range have been observed only in solar flares [Doschek *et al.* 1981] These density ranges are well matched to the electron density that can be obtained in the EBIT electron beam (up to $\sim 5 \times 10^{12}$cm^3).

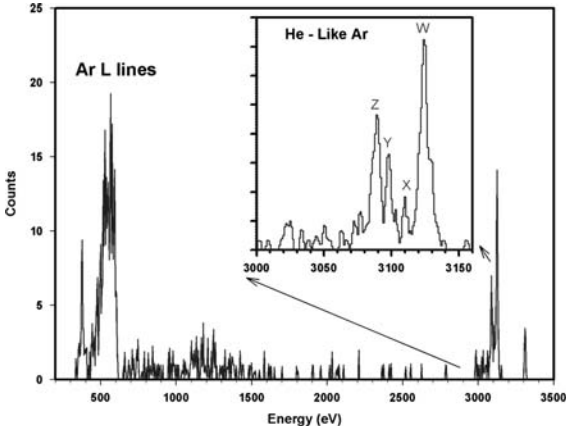

Fig. 6. Simultaneously observed K and L spectra from Argon. The inset is an expanded view of the He-like complex of Ar XVII (not corrected for window transmission).

Laboratory measurements made with the microcalorimeter under controlled conditions in the NIST EBIT have been published for the He-like and H-like (Lyman α) transitions of nitrogen (N VI and N VII) and oxygen (O VII and O VIII) along with some higher transitions ($1s^2$-1snp; n>2) [Silver *et al.* 2000]. Here we show a more recent broadband spectrum of argon that includes the L-emission lines between 400 and 700 eV and the K emission lines at approximately 3100 eV (see Fig. 6). Simultaneous high-resolution measurements of the L- and K-emission from the same portion of the plasma are not possible with any X-ray spectrometer other than a microcalorimeter. The contributions from the Ar XVII He-like lines are clearly resolved.

Fe XVII produces strongest lines in the X-ray spectra of solar active regions and is routinely observed in most collisionally ionized sources in astrophysics. Until the recent breakthroughs, this system had also become one of the longest standing problems in atomic data for X-ray spectroscopy, namely the failure of the dozens of calculations of the ratio 3C/3D (the ratio of the 15.014 Å line to the 15.265 Å line) to agree with each other to better than about 50%. Since both of these lines are strong resonance lines, many of the notoriously complicated atomic processes (such as resonances near threshold in the excitation cross section or cascades from dielectronic recombination) are of minor significance. Of particular concern, the solar observations themselves ranged over more than 60% but never reached a value as high as the lowest of the theories (including recent calculations of Gu [Brown *et al.* 2006] and Loch et al. [Loch *et al.* 2006]). While the range in solar values was potentially interesting as a diagnostic of resonant scattering, the diagnostic could not be used without an accurate fiducial in the optically thin limit.

Early *Chandra* observations of stellar coronae, such as those of Capella [Canizares *et al.* 2000], agreed with the uppermost solar values. Measurements from the two U.S. EBIT groups have shown good agreement with each other [Brown *et al.* 1998; Laming *et al.* 2000] and with the highest of the solar line ratio values, convincingly demonstrating that the theoretical ratios were 15 to 20% high. These experiments inspired further theoretical work, including larger number of energy grid points, additional convergence tests and careful attention to the electron energy distribution functions for both the narrow Gaussian beam characteristic of EBIT plasmas and the Maxwellian assumed in astrophysics [Chen *et al.* 2008]. With these theoretical values benchmarked by the EBIT experiments, the solar problem has finally been resolved, indicating that there is no resonance scattering in solar flares [Brickhouse *et al.* 2006]. We have done additional laboratory work to understand the intensity ratios of lines more widely spaced in energy in the Fe XVII system and a new manuscript is forthcoming.

Lines of the analogous Ne-like system Ni XIX have recently been observed with *Chandra* in nonstellar sources such as galactic black holes and AGN [Miller *et al.* 2005; Krongold *et al.* 2003], as well as in solar and stellar coronae. Ni abundances are of great interest for understanding heavy element formation and the role of supernova explosions in populating the interstellar medium.

Furthermore, Ni can be more abundant than Fe in the first few days after a supernova explosion and may dominate the early-time spectra from gamma ray bursts (GRBs). Recent work suggests that earlier reported observations of Fe in GRBs were actually those of Ni [Reeves *et al.* 2002]. Laboratory work by the U.S. EBIT groups provides benchmarks for Chen's new theory, giving agreement to better than 10% [Chen *et al.* 2006; Gu *et al.* 2004]. For Ni XIX, Chen's calculations show temperature sensitivity due to resonances in the excitation cross sections near threshold, now confirmed by our group's EBIT measurements [Chen *et al.* 2006]. Chen et al. showed the results of a fully relativistic close-coupling calculation of the Ni XIX 3C/3D line intensity ratio, with an uncertainty of 5%, together with independent measurements from the NIST EBIT that agree with calculations. To the best of our knowledge there is no other accurate ab initio calculation in the literature which reliably predicts the astrophysically important 3C/3D line ratio in Ni XIX.

Acknowledgement. E. Silver acknowledges support in part from NASA Grant NNX-08-AK33G. We thank J. Pomeroy for assistance in some of the experiments.

References

Bautista, M. A. and Kallman, T. R. 2001, ApJS, 134, 139
Brickhouse, N. S. and Schmelz, J. T. 2006, ApJ, 636, L53
Brown, G. V. et al. 1998, ApJ, 502, 1015
Brown, G. V. et al. 2002, ApJS, 140, 589
Reported in Brown, G. V. et al. 2006, Phy. Rev. Lett., 96, 253201
Canizares, C. R. et al. 2000, ApJ, 539, L41
Chen, G. X. 2008, MNRAS, 386, L62
Chen, G. X. et al. 2006, Phys, Rev, Lett., 97, 143201
Doschek, G. A. et al. 1981, ApJ, 249, 372
Ferland, G. J., et al. 1998, PASP, 110, 761
Gu, M. F. et al. 2004, ApJ, 607, L143
Gu, M. F. 2007, ApJS, 169, 154
Holland, G. E. et al. 2005, Review of Scientific Instruments, 76, 073304
Kotochigova, S. A. et al. 2005, AIP 774, 161
Krongold, Y. et al. 2003, ApJ, 597, 832
Laming, J. M. et al. 2000, ApJ, 545, L161
Loch, S. D. et al. 2006, J. Phys. B , 39, 85
Miller, J. M. et al. 2005, ApJ, 620, 398
Reeves, J. N. et al. 2002, Nat, 416, 512
Silver, E. et al. 2000, ApJ, 541, 495
Silver, E. et al. 2005, Nucl. Inst. & Meth. in Phys. Res. A 545, 683
Smith, R. K. et al. 2001, ApJ, 556, L91

"Recent Advances in Spectroscopy:
Theoretical, Astrophysical, and Experimental Perspectives"
Eds. Chaudhuri R K, Mekkaden M V, Raveendran A V, Satya Narayanan A
Astrophysics and Space Science Proceedings, Springer-Verlag, Berlin, 2010.

X-ray Spectroscopy of Astrophysical and Laboratory Z-pinch Plasmas

A. Dasgupta[1], R. W. Clark[2], J. Davis[1], and J. G. Giuliani[1]

[1] Naval Research Laboratory, Washington, DC, USA
[2] Berkeley Research Associates, Beltsville, MD, USA

Summary. In recent years, there have been significant advances in instrumental capabilities for making X-ray spectroscopic measurements of astrophysical plasmas. There have been corresponding improvements in X-ray diagnostics for advanced multi-mega-ampere pulse power machines which produce increasingly large radiative yields from gas-puff and wire array Z pinch plasmas. Analysis used for Z pinches can be used to study ICF and also astrophysical plasmas where laboratory measurements and simulations are the only means to interpret observed data. The astrophysical data for Fe, the most cosmically abundant high Z element, can provide a wealth of information about cosmic plasmas. Fe is also the key element in stainless steel (SS) wire arrays that are investigated as an intensive X-ray radiation source at the Z machine in the US Sandia National Laboratories. The implosion dynamics of an array of SS wires on the Z and/or refurbished Z (ZR) accelerator produces an abundance of radiation from the K- and L-shell ionization stages. These dynamic plasmas are inherently non-LTE, with opacity and other factors influencing the X-ray output. As the plasma assembles on axis, a number of time resolved snapshots provide temperature and density profiles and map the emitting region. We will analyze the ionization dynamics and generate K- and L-shell spectra using the conditions generated in the Z and/or ZR, described by a 1-D non-LTE radiation hydrodynamics model. Diagnostics based on spectral shape of L-shell emissions are inherently more difficult than those based on K-shell emissions because of more complex multiplet structures and line overlaps. The non-LTE populations are obtained using detailed atomic models that include all important excitation, ionization, and recombination processes. We will highlight the connection between laboratory Z-pinch plasma simulations and astrophysical plasmas.

1 Introduction

X-ray emission spectra from the K-and particularly complex L-shell of high Z ions provide valuable information with which to assess plasma conditions and X-ray performance in a variety of laboratory plasmas such as Z-pinch plasmas. Recent years have witnessed increased activities due to the advancements in multi-mega-ampere pulsed power driven machines and improvements in load designs. Experiments on the Z facility at Sandia National Laboratories (SNL) provide a unique opportunity to obtain high-quality data and to test complex theories and models of X-ray production. The Z machine produces up to 250 TW and 1.8 MJ of radiation (Deeney 1998) by driving 20 MA with a 100 ns rise time through a cylindrical array or nested array of several hundred fine wires. The self-generated jXB force implodes the array, creating a high-energy-density, radiating plasma column on the axis of symmetry. Fig. 1 shows a cross section of the Z machine (left) and the pinch (right).

Typically there are two main classes of radiation sources that are studied on the Z machine. Low-to-mid atomic number loads with large diameter (40-80 mm) are employed to generate K- and L –shell emission in the 1-10 keV photon energy range and also compact high-atomic number material such as tungsten wire arrays provide powerful < 1 keV soft x-ray sources for driving inertial confinement fusion (ICF) (Jones 2008). Our work is motivated by the need to analyze and interpret the experiments on the Z and the refurbished Z facilities at SNL using various wire arrays. Space and time resolved spectroscopy is the most important diagnostic tool and comparison of these with synthetic spectra, produced from detailed atomic models, can produce a wealth of information about the plasma state. A test of the accuracy and reliability of our atomic model and simulation comes from the results of this comparison. The analysis used for Z pinch plasmas can be used to study ICF and also astrophysical plasmas where laboratory measurements and simulations are the only means to interpret observed data.

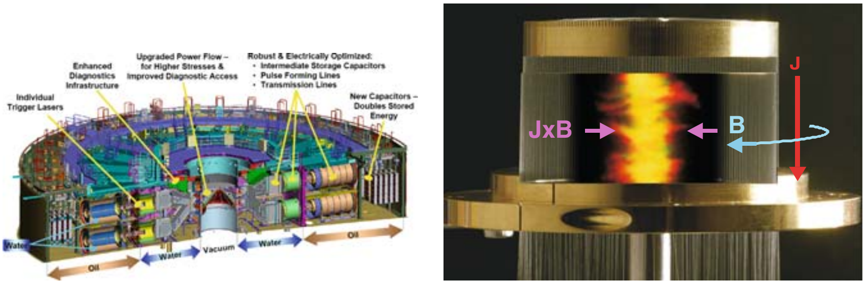

Fig. 1. (left) Refurbished Z machine ; (right) **JxB** force pinches wire array into a dense radiating plasma column.

The production and transport of laboratory plasmas are often modeled using average and approximated atomic models and assuming Local Thermodynamic Equilibrium (LTE) conditions. But the plasmas produced in the laboratory experiments are neither in LTE nor in Coronal Equilibrium (CE). Therefore to predict the emitted radiation and yield, a detailed Collisional Radiative Model (CRM) must be used. Since the radiation field can affect the populations through photoionization and photoexcitaion and at the same time populations determine emissivities and opacities, the full CRM model must include non-local radiation transport. In this model, the level populations are determined by solving rate equations that include all important collisional and radiative processes. The detailed CRM also has the advantage of reducing to the CE model in the high temperature, low density limit and to LTE in the opposite limit (Davis 2001). Since calculating the X-ray spectra of hot plasmas requires knowledge of atomic data and structure to evaluate the precise ionization dynamics, it is imperative that the data needed for CRM be generated using state-of-the art computer codes. Due to the enormity of the data involved for many atomic levels, especially for complex ions, simple approximations and crude atomic models are often employed for analysis that can lead to erroneous interpretation of plasma conditions and emission spectra. A major issue of this investigation becomes how to construct an atomic model containing a detailed yet manageable number of levels that will adequately describe the plasma. The challenges arise from the complicated and computer intensive task of solving the coupled set of equations describing the ionization dynamics and radiation transport. Often, a compromise is reached by treating the radiation physics in an approximate way, but for high to moderate Z plasmas both ionization physics and radiation transport issues are equally important and should be treated in an equitable manner.

Kinetic Model and Radiation Transport

The non-equilibrium ionic populations in optically thin plasmas are determined by solving a set of atomic rate equations given by:

$$\frac{dN_Z^k}{dt} = \sum_{Z'}\sum_{k'}(R_{Z'Z}^{kk'}N_{Z'}^{k'} - R_{ZZ'}^{k'k}N_Z^k), \tag{1}$$

where N_Z^k is the population density of excited level k with ionization stage Z and $R_{Z'Z}^{kk'}(R_{Z'Z}^{k'k})$ are creation(destruction) rates. Steady-state population densities are obtained by solving the equilibrium equations, $dN^{k}{}_{Z}/dt=$ 0. However, for situations when the plasma conditions are changing faster than the atomic rates populating the excited levels, one needs to solve the non-equilibrium rate equations. In the ion density region of interest, 10^{18} $\leq n_i$ $\leq 10^{22}$ cm-^{3}, the plasma ionization condition cannot be described by *corona equilibrium*, in which radiative decay rates are much larger than collisional excitations, and essentially all ions exist in the ground and Δn=0 levels. Neither can the plasma be described as being in LTE, where all states of a given configuration are statistically populated. For K- and L-shell ions of moderate Z ions, only at densities above this range do the excited levels come into statistical equilibrium. Thus a full non-LTE kinetics model is needed to investigate the higher electron density regimes found in laboratory plasmas. Our atomic model has been constructed using a very detailed yet computationally efficient level structure for a large number of excited states and the processes coupling these levels. Although collisional excitation has the most significant contribution in populating the excited levels, dielectronic recombination (DR) is the dominant recombination and often the most important process in many laboratory and astrophysical plasmas(Dasgupta 1992, 1997, 2009). When radiation trapping becomes important, non-local coupling of photo-pumping and photoionization needs to be included to the equation and this describes the full CRM. All the atomic structure data were self-consistently generated using the Flexible Atomic Code (FAC) suite of codes (Gu 2003). Our structure data and rates for collisional and radiative processes compare very well in most cases with other available published data. All ground levels and excited levels with $n \leq 4$ are kept at the fine-structure levels, while for $5 \leq n \leq 7$, the configuration-averaged level structures are used. A more limited level structure is embedded in a configuration state model for the remainder of the ionization stages. Data for the atomic processes involved in level populations included in this calculation include:

(i) Spontaneous radiative decay- Atomic structure data including energy levels and radiative transition rates are obtained using the FAC code where the bound states of the atomic system are calculated in the configuration mixing approximation with convenient specification of mixing schemes. The radial orbitals for the construction of basis states are derived from a modified self-consistent Dirac-Fock-Slater iteration on a fictitious mean configuration with fractional occupation numbers, representing the average electron cloud of the configurations included in the calculation. The radiative transition rates are calculated in the single multipole approximation with arbitrary ranks (Gu 2008).

(ii) Collisional excitation- Electron impact excitation cross sections from ground to the excited states and collisional coupling among all the excited states are calculated using FAC. Excitation cross sections for the most important n=2-3 excitation are in good agreement when compared with other published work. Extrapolations to high energies are obtained by using appropriate polynomial fitting formulas as FAC suggested formulas were not adequate for non-allowed transitions.

(iii) Collisional Ionization- The detailed level-to-level electron impact ionization cross sections for ground as well as all the excited levels in our model are obtained using FAC, incorporating the relativistic distorted-wave (DW) approximation, extending the factorization-interpolation method developed for the calculation of electron impact excitation cross sections. As noted in (Gu 2008), the implementation allows for the most general configuration mixing to be included and much more efficient methods based on the Coulomb-Born-Exchange (CBE) approximation or the Binary-Encounter-Dipole (BED) theory are also implemented.

(iv) Photoionization- The non-resonant photoionization cross sections are calculated using FAC where the continuum wavefunctions are obtained in the relativistic distorted-wave approximation. The non-relativistic multipole operators, rather than electric dipole (E1), are used for the calculation of bound-free differential oscillator strengths, although no interference between different multipoles are taken into account. In FAC, an efficient factorization-interpolation procedure is implemented by separating the coupling of the continuum electron from the bound states. FAC generated near threshold cross sections for both collisional and photoionization cross sections were not very accurate in many cases and therefore extrapolated values from higher energies were used to replace those cross sections.

(iv) Dielectronic recombination (DR)- Calculations of DR rates pose major challenges due to complexities involved in handling the complex atomic structures of large number of singly and doubly excited levels. DR involves competing processes of autoionization and radiative transition. DR is a dominant recombination process for ions in laboratory and astrophysical plasmas and is a significant contributor in kinetics calculations for level populations (Dasgupta 1992). In Fig. 2, we show the DR rate coefficient for Fe XVI for a wide range of temperatures obtained using FAC and compare them with those obtained by Altun *et al.* (Altun 2006) using the AUTOSTRUCTURE code. In FAC, DR data are calculated in the independent-process, isolated resonance approximation. In this calculation, Δn=0 channels that contribute mainly and significantly to the low-temperature DR rates are included along with the Δn =1 excitations.

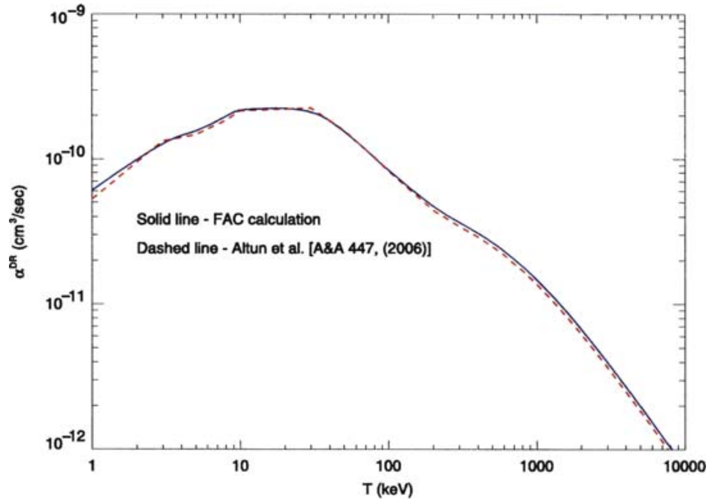

Fig. 2. Total dielectronic rates from ground state of Fe XVI. Solid line is FAC calculations and dashed line is calculations of Altun *et al., Altun 2006.*

(v) Photoexcitaion- The photoexcitation rate can be calculated from the radiative couplings $C_{kk'}$ which is defined as the probability that a photon emitted in zone k is absorbed in zone. If $k_{\nu k}$ is the total opacity in zone k for frequency ν, and ${k_{\nu k}}^{ii'm}$ is the partial opacity for transition i-i' of material m, the photoexcitation rate for transition i-i' can be written as:

$$w_{ii'mk} = 4\pi \sum\nolimits_{\nu} [k_{\nu k}^{ii'm}/k_{\nu k}] \sum\nolimits_{k' \neq k} [C_{\nu k' k} J_{\nu k'} V_{k'} d\nu]/[n_{km} f_{ikm} E_{ii'm} V_k], \quad (2)$$

where $\mathbf{J}_{\nu k'}$ is the total emissivity for frequency ν in zone k', n_{km} is the ion density of species m in zone k, f_{ikm} is the atomic population of the lower level in zone k, $E_{ii'm}$ is the transition energy, and V_k is the volume of zone k.

The rate coefficients for all the processes are thus obtained by integrating the cross sections over a Maxwellian electron distribution. The reverse processes such as collisional deexcitation, collisional recombination or 3-body recombination, radiative recombination and autoionization rates are obtained by detailed balancing.

Calculating X-ray and UV spectra of a hot plasma requires a knowledge of atomic data and codes to evaluate the precise model, and atomic processes which determine the populations of the atomic levels are functions of the local electron temperature and density. The radiation field arising from line transitions and radiative recombination processes can affect the populations through photoionization and photoexcitation. This couples all the spatial zones in the plasma. For non-LTE dense plasmas atomic kinetics must be coupled with radiation transport to include opacity effects. Because the populations determine the local radiation emissivities and opacities, and the radiation modifies the populations by significant redistribution, an iterative process must be employed. In our model, an iterative procedure is used where level populations are calculated using radiation field from the previous iteration and these populations are used to calculate a new radiation field until convergence is reached.

We have used the probability-of-escape method (Apruzese 1980,1985) where an escape probability is derived, integrated over the line profile, as a function of line-center optical depth based on a frequency of maximum escape. For bound-free continuum radiation arising from radiative recombination, an escape probability is derived, integrated over the bound-free profile, as a function of optical depth at the edge. The probabilistic method of transport of both line and continuum radiation is an economic and efficient way for simulation of most laboratory and astrophysical plasmas. Because the free-free emission and opacity have a gentle dependence on photon energy, a coarse multi-frequency treatment gives adequate accuracy for free-free escape probability.

Often, for very dense and optically thick plasmas, the probability-of-escape method may not be adequate to resolve spectral lines and a multi-frequency method may be necessary. In the multi-frequency case, each line is resolved using multiple frequencies which resolve the line profile.

Application to Z-Pinches

The atomic, kinetic and radiation transport models described above were used in this investigation to analyze Z-pinch stainless steel (SS) data obtained from experiments on the Z machine at SNL. Recent experiments on the Z accelerator employing nested stainless steel wire arrays have produced K-shell x-ray yields in excess of 50 kJ in the range 5.5 to 8.0 keV. Stainless steel spectra are sensitive to the implosion history and to the accuracy of the atomic modeling. In Fig. 3 (left) we show a time-integrated experimental Z-pinch spectrum for SNL shot Z-581 (SS data; courtesy of Christine Coverdale) and compare it with a portion of a Li-like L-shell spectrum in the energy range between 1.05 and 1.2 keV. The time integrated synthetic spectrum utilized a full detailed-configuration FAC model for iron with full simulations (time-dependent implosion) of Z 581.

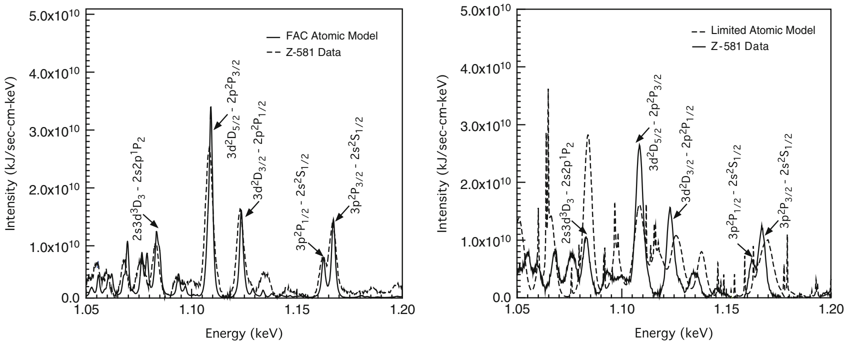

Fig. 3. (left) Li-like Fe-spectra at fixed Ti=75 keV compared with shot Z 581; (right) Same simulated Li-like spectra as shown in left but with a limited atomic model.

In order to show the significance of detailed and accurate atomic modeling, we also compare the data in Fig. 3 (right) with an older but much used atomic model with limited number of excited levels and atomic data which are less accurately obtained. This comparison clearly shows the importance of proper atomic modeling.

Application to X-ray Astronomy

Astrophysically abundant heavy elements ("metals") such as C, N, O, Ne, Mg, Si, S, Ar, Ca, Fe, Ni are all produced by steady nuclear burning inside massive stars, or by explosive nuclear burning in the supernova that terminate stellar evolution. Emitted X-rays can be used to measure electron densities, temperatures, and ion charge state distributions for information on plasma heating and cooling in various sources. In X-ray astronomy we generally are faced with more unknowns than in the laboratory, so beyond diagnostics of e.g. temperature, density, Doppler shifts etc, we are also interested in element abundances. Absolute abundances are usually measured from line-to-continuum ratios, at least in relatively quiescent objects such as supernova remnants (SNR) or clusters of galaxies that only evolve on timescales of many years. Relative abundances involve line-to-line comparisons. Fig. 4 (left) shows the Cassiopeia A SNR with explosion date around 1680 AD and at a distance of 3.4 kpc (1.e22 cm, 11,000 light years). This was the target of a 1 million second observation with Chandra, performed over 3 weeks in April and May of 2004 with $\sim 3e8$ photons collected. This long exposure allowed good signal to noise in spectra extracted from small regions, using the arc-second spatial resolution of *Chandra* mirrors to the fullest extent.

The CCD spectra shown in Fig. 4 (right) appear to be almost pure Fe with no Si, S, Ar, Ca emission lines that usually accompany Fe lines. This implies that this plasma must have originated in the very center of the explosion and has been thrown to the outer layers of the explosion by instabilities in the core. We can quantify this by measuring the departure from collisional ionization equilibrium (CIE) by measuring ratios of Fe XXV to lower charge states, Fe XXIV, Fe XXII, etc. at the temperature given by the continuum. This represents heating by the shock followed by partial relaxation to CIE. By estimating the time since shock passage using the observed spectral signature and modeled evolution for the SNR, we can build up a precise picture of the element abundance distribution produced by the explosion. Currently analysis of around 6000 spectra from different regions of the SNR is under way. Thus X-ray spectroscopy can be used to determine absolute elemental abundance in astrophysical objects.

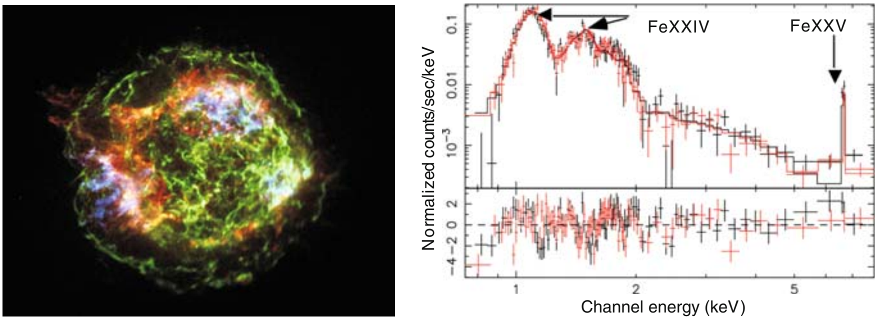

Fig. 4. (left) Cassiopeia A SNR 1 million second observation with Chandra.; (right) The 2000 and 2002 fitted epoch ACIS spectra of the diffuse Fe cloud with a single-temperature model.

X-ray spectroscopy can also be used to determine relative abundances in astronomical objects such as stellar coronae. The High Energy Transmission Gratings Spectrometer (HETGS) on Chandra provides a powerful tool for the study of X-ray emission from stars. Fig. 5 shows spectra of 13-16 angstrom region in various stellar coronae(Kastner 2002). The region encompasses Ne IX (highlighted by three lines on the left), Fe XVII, XVIII, XIX, and O VIII (highlighted by the line on the right), all formed at similar temperatures and allowing relative abundances to be determined. Abundances in stellar coronae are in general different due to the underlying stellar photosphere. A fractionation occurs, separating elements which are ionized in the chromosphere from those that are neutral. This has recently been explained by (Laming 2004, Laming 2009) as being due to the ponderomotive force associated with Alfven turbulence. The varying Ne/Fe abundance ratio,

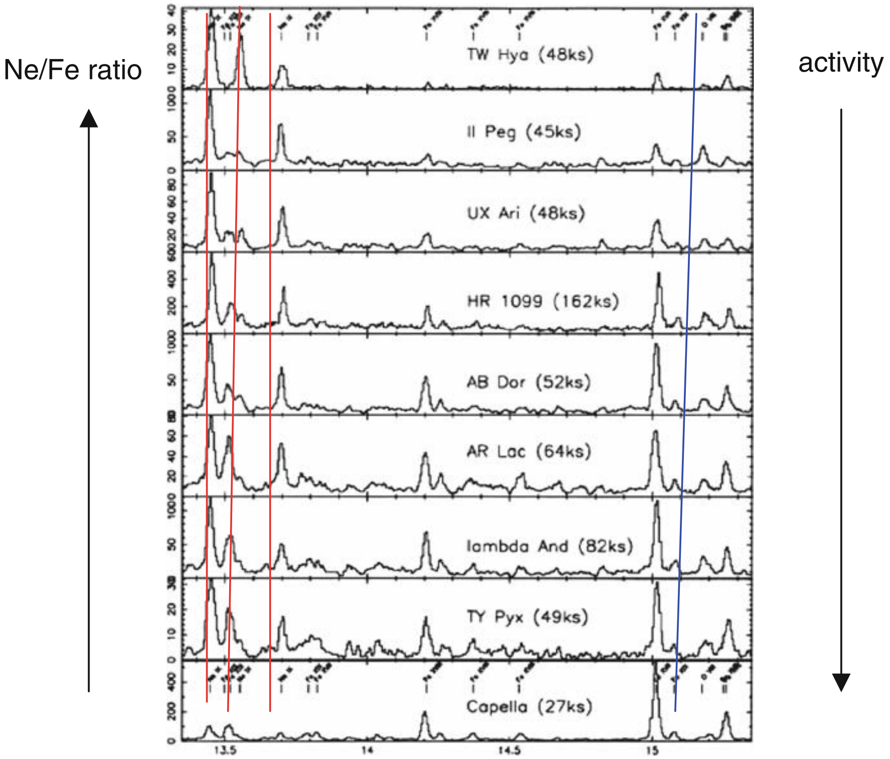

Fig. 5. Chandra/HETGS spectra of stellar coronae, showing abundance ratio Ne/Fe varying inversely with activity level. Such fractionation offers novel insight into the properties of turbulence in stellar atmospheres.

decreasing with increasing stellar activity, is probably a related phenomenon. In this unexpected way, careful spectroscopy of coronal ions may be telling us something about turbulence in stellar atmospheres.

Summary

The reliability and scalability of atomic data used in the ionization calculations of K- and L-shell moderate-Z elements are of great concern. It is critical to include an adequate number of excited levels per ion and all dominant processes and opacity effects by coupling radiation transport for non-LTE plasmas to generate synthetic spectra with which to diagnose plasma conditions. Dielectronic recombination has been shown to have a dominant effect on the populations in CRE simulations and therefore exclusion of DR rates or inclusion of crude and inaccurate semi-empirical DR rates must be replaced by detailed and accurate DR calculations. Experimental data for complex L-shell ions provide a wealth of information about plasma conditions. Analysis of our spectra using self consistently generated data from state-of-the-art codes such as FAC show excellent agreement with experiments on the Z machine at Sandia National Laboratories. This gives us confidence in our model and for benchmarking atomic and hydrodynamics calculations. Although the same analysis used for Z-pinches can be used to study ICF and astrophysical plasmas, spectroscopic simulations provide different kinds of knowledge that are relevant for laboratory and astrophysical plasmas.

Acknowledgement. This work was supported by the US Department of Energy/ NNSA.

References

Altun, Z. et al. 2006, Astron. Astrophys., 447, 1165
Apruzese, J. P. et al. 1980, JSQRT, 23, 479; 1985, JSQRT, 34, 447
Clark, R. W. et al. 1995, JSQRT, 53, 307
Dasgupta, & Whitney K. G. 1992, Phys. Rev. A., 46, 5973
Dasgupta, A. et al. 1997, Phys. Rev. A., 55, 3460
Dasgupta, A. et al. 2009, AIP conference Proceedings, 1088 37
Davis, J. et al. 2001, Laser and Particle Beams, 19, 557
Deeney, C. et al. 1998, Phys. Rev. Lett., 81, 4883
Gu, M. F. 2003, Astrophys. J., 590, 1131
Gu, M. F. 2008, Can. J. Phys., 86, 675
Jones, B. et al. 2008, Phys. Plasmas, 15, 122703-1
Kastner, J. L. & Weintraub D. A. 2002, Astrophys. J., 567, 434
Laming, J. M. & Hwang U. 2004, Astrophys. J., 597, 347
Laming, J. M. & Hwang U. 2009, Astrophys. J.,(in press)

"Recent Advances in Spectroscopy:
Theoretical, Astrophysical, and Experimental Perspectives"
Eds. Chaudhuri R K, Mekkaden M V, Raveendran A V, Satya Narayanan A
Astrophysics and Space Science Proceedings, Springer-Verlag, Berlin, 2010.

Computational Interstellar Chemistry

So Hirata[1,2], Peng-Dong Fan[1,3], Martin Head-Gordon[4], Muneaki Kamiya[1,5],
Murat Keçeli[2], Timothy J. Lee[6], Toru Shiozaki[1,7], Jan Szczepanski[1],
Martin Vala[1], Edward F. Valeev[8], and Kiyoshi Yagi[7,9]

[1] Department of Chemistry, University of Florida, U.S.A.
[2] Department of Physics, University of Florida, U.S.A.
[3] Pacific Northwest National Laboratory, U.S.A.
[4] Department of Chemistry, University of California, Berkeley, U.S.A.
[5] Faculty of Regional Studies, Gifu University, Japan
[6] NASA Ames Research Center, U.S.A.
[7] Department of Applied Chemistry, The University of Tokyo, Japan
[8] Department of Chemistry, Virginia Tech, U.S.A.
[9] Nanomaterials Research Center for High Performance Fuel Cells, University of Yamanashi, Japan

Summary. Computational applications of electronic and vibrational many-body theories are increasingly indispensable in interpreting and, in some instances, predicting the spectra of gas-phase molecular species of importance in interstellar chemistry as well as in atmospheric and combustion chemistry. This chapter briefly reviews our methodological developments of electronic and vibrational many-body theories that are particularly useful for these gas-phase molecular problems. Their applications to anharmonic vibrational frequencies of triatomic and tetratomic interstellar molecules and to electronic absorption spectra of the radical ions of polycyclic aromatic hydrocarbons, which are ubiquitous in the interstellar medium, are also discussed.

1 Introduction

The molecules in neutral and ionic forms that exist uniquely in the radiation-rich and dilute interstellar medium are hard to synthesize in the terrestrial environment and the interpretations of astrophysical observations of these molecules must often rely on quantitative chemical simulations. Furthermore, many of the most sophisticated methods of computational chemistry work well for relatively small gas-phase molecules that consist of main-group elements—the characteristics shared by many of the confirmed interstellar molecules. For these reasons, computational chemistry is particularly useful in interstellar chemistry as well as in related areas of atmospheric and hydrocarbon combustion chemistry.

The methods in computational chemistry are grouped in electronic or vibrational many-body methods, depending on whether they attempt to solve the electronic or nuclear Schrödinger equation within the Born–Oppenheimer approximation. Both classes of methods are indispensable in computational interstellar chemistry as UV/vis and infrared absorptions (and emissions) due to electronic and vibrational transitions are the principal observables in interstellar chemistry. The electronic many-body methods are further divided into *ab initio* molecular orbital (MO) theory or density-functional theory (DFT).

MO theory approximates an electronic wave function as a linear or nonlinear combination of Slater determinants, namely, antisymmetrized products of spinorbitals:

$$\Psi = \Big(1 + \sum_{i}\sum_{a} C_i^a \hat{E}_i^a + \sum_{i<j}\sum_{a<b} C_{ij}^{ab}\hat{E}_{ij}^{ab} + \dots\Big)\Phi_0 \tag{1}$$

or

$$\Psi = \exp\Big(\sum_{i}\sum_{a} C_i^a \hat{E}_i^a + \sum_{i<j}\sum_{a<b} C_{ij}^{ab}\hat{E}_{ij}^{ab} + \dots\Big)\Phi_0, \tag{2}$$

where Φ_0 is the Hartree–Fock (HF) determinant, $\hat{E}_{ij\dots}^{ab\cdots}$ is an operator that promotes electrons in the occupied spinorbitals $(i, j, \dots)$ in Φ_0 to the unoccupied (virtual) spinorbitals $(a, b, \dots)$, and $C_{ij\dots}^{ab\cdots}$ is the corresponding expansion coefficient. A spinorbital is the product of an MO and a spin function and the MOs $\{\psi_p\}$ are expanded by a set of basis functions $\{\chi_\mu\}$, which are typically atom-centered Gaussian functions:

$$\psi_p(\mathbf{r}) = \sum_{\mu} c_p^\mu \chi_\mu(\mathbf{r}). \tag{3}$$

Various approximations of MO theory are characterized by the truncation lengths of Eq. (1) or (2) and of Eq. (3) as well as how the coefficients $\{C\}$ and $\{c\}$ are determined. While $\{c\}$ are usually evaluated variationally (defining the HF method), the coefficients $\{C\}$ are determined by various methods such as those based on configuration-interaction (CI), coupled-cluster (CC), and many-body perturbation theories (MBPT).

The rank-n CI methods are defined by Eq. (1) truncated after the nth term with $\{C\}$ determined variationally. The CC and MBPT methods approximate a wave function by Eq. (2) truncated after a certain term and determine the coefficients $\{C\}$ either by solving a set of nonlinear equations in an iterative algorithm (CC) or by evaluating perturbation theory formulas in a noniterative algorithm (MBPT). The approximations of CI, CC, and MBPT are increasingly more accurate (and more expensive computationally) as the highest rank of excitation operator included in the expansion is raised and as the basis set is extended. Executing the series of MO calculations with different basis sets, therefore, one can systematically reduce the errors in the calculations and make reliable predictions of molecular properties in the absence of experimental data.

DFT approximates a portion (the exchange and correlation energy) of the total electronic energy by a functional (E_{xc}) of electron density. Unlike MO theory, DFT does not have systematic, converging approximations for wave functions and energies. It is, therefore, not possible to estimate the errors in DFT results or to improve the accuracy when a particular approximation of E_{xc} fails in an application. Nonetheless, it is widely agreed that various existing approximations of E_{xc} are superior in terms of cost-accuracy balance to low-rank members of MO theory for a certain class of molecules and molecular properties. Hence, DFT is still widely used in applications that are unfeasible by MO theory.

The mathematical techniques that are established in MO theory are also useful in solving the Schrödinger equation for bound nuclear motion, namely, anharmonic molecular vibrations and vibrationally averaged molecular properties. The vibrational methods based on these techniques approximate a vibrational wave function by Eq. (1) or (2), where Φ_0 is now a Hartree product of one-mode functions or "modals." Each modal can be expanded by a set of harmonic oscillator wave functions in a normal coordinate. The truncation of Eq. (1) after the first term and variationally optimizing the modals defines the vibrational analogue of the HF method called the vibrational self-consistent field (VSCF) method (Bowman 1986). Vibrational counterparts of CI, CC, and MBPT have also been proposed and implemented (Christiansen 2007). A unique issue in vibrational problems is the high and variable dimensionality of the Hamiltonian or its potential energy surface term. A practical vibrational method must, therefore, address questions such as which portion or dimensions of a potential energy surface should be explored and how the surface will be mathematically expressed and stored.

We have made methodological advances in each of these fields that are of general utility and also performed applications of these methods to molecules that are directly relevant to interstellar chemistry. Section 2 (with original contributions from Hirata, Fan, Kamiya, Shiozaki, and Valeev) will summarize our general methodological developments in MO theory. Section 3 (Keçeli, Hirata, Shiozaki, and Yagi) will review our methodological developments in vibrational many-body theory and their applications to triatomic and tetratomic interstellar molecules. Section 4 (Hirata, Head-Gordon, Lee, Szczepanski, and Vala) is concerned with our DFT calculations of excited states of the radical ions of polycyclic aromatic hydrocarbons (PAHs), which are ubiquitous in the interstellar medium but may be too large for MO theory. These three topics are hoped to impress the reader with the increasingly important role played by computing in interstellar chemistry.

2 Advances in electronic many-body methods

MO theory has the advantage of having the series of systematic approximations of increasing accuracy such as CI, CC, and MBPT and of being able to increase the fidelity of computer simulations (Hirata & Yagi 2008). Their wide use is, however, hindered by (1) the immense complexity and cost of *implementing* some of the high-rank members of these series and the difficulty of code verification and optimization (including parallelization) and by (2) the immense cost of *executing* the calculations using these methods.

The first of the two problems has been solved by a computerized symbolic algebra system (Hirata 2003, 2006) that largely automates the mathematical derivations of formulas defining these exceedingly complex electronic many-body methods and their implementation into massively-parallel execution programs. The symbolic algebra system, an object-oriented program written in PYTHON, takes expectation values of normal-ordered second-quantized operator sequences in Φ_0 as an input, performs contractions of the operators using Wick's theorem, and arrives at sum-of-product matrix expressions of molecular integrals and excitation amplitudes. It then suggests computational sequences to evaluate these expressions efficiently, by finding the optimal orders of multiplying the matrices, identifying common matrix multipliers and factoring them, and also determining which common multipliers need to be stored for reuse. These computational sequences are automatically translated into FORTRAN codes.

With the computer algebra, we have developed parallel execution programs (many for the first time) of a variety of existing and new methods listed in Table 1. They include CI, CC, and MBPT methods up to high ranks (Hirata 2003), combined CC and CI methods for excitation (Hirata 2004), ionization (Kamiya & Hirata 2006), and electron-attachment energies (Kamiya & Hirata 2007), combined CC and MBPT methods (Hirata et al. 2004a), combined CI and MBPT methods (Hirata 2005), active-space methods (Fan & Hirata 2006; Fan et al. 2007), relativistic methods (Hirata et al. 2007), and combined CC, CI, and MBPT methods (Shiozaki et al. 2007). The synthesized programs make use of sparsity and data dependency caused by spin symmetry, spatial symmetry, and index-permutation symmetry and are scalable to hundreds of processors. They have enabled highly accurate predictions of spectroscopic properties of small molecules, some containing heavy elements (Hirata et al. 2004b, 2007). The CCSDTQ code alone is over two million lines of FORTRAN and its manual development will take at least several months for an expert. Our computer algebra reduces it to just hours of work for a nonexpert.

The second issue relates to the convergence rate of energies and wave functions with respect to the excitation rank [Eq. (1) or (2)] and the size of basis set [Eq. (3)]. The convergence with respect to the former is extremely rapid with the combined CC and MBPT methods for ground-state properties and with the combined CC and CI methods for excited, ionized, and electron-attached states. The convergence with respect to the latter is notoriously slow, necessitating the use of large basis sets and an extrapolation of complete-basis-set limits based on some empirical formulas. The slow convergence is caused at least partly by the r_{12}^{-1} singularities in the operators of interelectronic interactions (r_{12} is an interelectronic distance) and the inability of one-electron basis

Table 1. Electronic methods developed by computer algebra (Hirata & Yagi 2008).

Acronym	Definition
CCD	Coupled-cluster doubles
LCCD	Linearized CCD
CCSD	Coupled-cluster singles and doubles
LCCSD	Linearized CCSD
QCISD	Quadratic configuration-interaction singles and doubles
CCSDT	Coupled-cluster singles, doubles, and triples
CCSDTQ	Coupled-cluster singles, doubles, triples, and quadruples
MBPT(2)	Second-order many-body perturbation theory
MBPT(3)	Third-order many-body perturbation theory
MBPT(4)	Fourth-order many-body perturbation theory
CISD	Configuration-interaction singles and doubles
CISDT	Configuration-interaction singles, doubles, and triples
CISDTQ	Configuration-interaction singles, doubles, triples, and quadruples
EOM-CCSD	Equation-of-motion CCSD
EOM-CCSDT	Equation-of-motion CCSDT
EOM-CCSDTQ	Equation-of-motion CCSDTQ
IP-EOM-CCSD	Ionization-potential EOM-CCSD
IP-EOM-CCSDT	Ionization-potential EOM-CCSDT
IP-EOM-CCSDTQ	Ionization-potential EOM-CCSDTQ
EA-EOM-CCSD	Electron-attachment EOM-CCSD
EA-EOM-CCSDT	Electron-attachment EOM-CCSDT
EA-EOM-CCSDTQ	Electron-attachment EOM-CCSDTQ
CCSD[T]	CCSD with a triples correction
CCSD(T)	CCSD with a triples correction
CR-CCSD(T)	Completely-renormalized CCSD(T)
CCSD$(2)_T$	CCSD with a second-order triples correction
CCSD$(2)_{TQ}$	CCSD with a second-order triples and quadruples correction
CCSD$(3)_T$	CCSD with a third-order triples correction
CCSD$(3)_{TQ}$	CCSD with a third-order triples and quadruples correction
CCSDT$(2)_Q$	CCSDT with a second-order quadruples correction
EOM-CCSD$(2)_T$	EOM-CCSD with a second-order triples correction
EOM-CCSD$(2)_{TQ}$	EOM-CCSD with a second-order triples and quadruples correction
EOM-CCSD$(3)_T$	EOM-CCSD with a third-order triples correction
CIS	Configuration-interaction singles
CIS(D)	CIS with a doubles correction
CIS(3)	CIS with a third-order correction
CIS$(4)_P$	CIS with a partial fourth-order correction
CCSDt	CCSD with active-space triples
CCSDTq	CCSDT with active-space quadruples
CCSDtq	CCSD with active-space triples and quadruples
EOM-CCSDt	EOM-CCSD with active-space triples
EOM-CCSDTq	EOM-CCSDT with active-space quadruples
EOM-CCSDtq	EOM-CCSD with active-space triples and quadruples
IP/EA-EOM-CCSDt	IP/EA-EOM-CCSD with active-space triples
IP/EA-EOM-CCSDTq	IP/EA-EOM-CCSDT with active-space quadruples
IP/EA-EOM-CCSDtq	IP/EA-EOM-CCSD with active-space triples and quadruples

functions of Eq. (3) to describe the wave functions at $r_{12} \approx 0$ qualitatively correctly.

This issue is addressed by introducing a new basis functions that explicitly depend on r_{12} and can describe the wave functions at $r_{12} \approx 0$ quantitatively correctly (Klopper et al. 2006). The sum-of-product matrix equations defining a variety of high-rank CC methods and combined CC and MBPT methods as well as MBPT(2) that include basis functions of r_{12} (the so-called explicitly correlated or "R12" methods) have been derived and implemented into efficient programs by the computerized symbolic algebra system (Shiozaki et al. 2008a,b, 2009). Additional algebraic transformation steps specific to the R12 methods have also been computerized, namely, the identification and isolation of the molecular integrals that arise uniquely in this class of methods and the resolution-of-the-identity insertion to facilitate the evaluation of some of these molecular integrals that are high dimensional.

These R12 methods form a hierarchy of systematic approximations that converge very rapidly toward the exact solutions of the Schrödinger equations with respect to both the highest excitation rank and basis-set size. Combining these CC-R12 methods with the grid-based, numerical HF equation solver (Shiozaki & Hirata 2007), the solutions (eigenvalues) of the Schrödinger equations of neon, boron hydride, hydrogen fluoride, and water at their equilibrium geometries have been obtained within 2 kcal/mol of the exact, nonrelativistic, Born–Oppenheimer values derived experimentally (Shiozaki et al. 2009) (Table 2). Although the absolute values of total molecular energies are rarely of interest to chemists, our computational ability to solve the Schrödinger equation of water, which is a 30-dimensional partial differential equation with 75 singularities, with the 99.998% accuracy has the strong implication of a greater impact of computing on chemistry research.

Table 2. The HF, correlation, and total energies (in E_h) of Ne, BH, FH, and H_2O computed by the CC-R12 methods (Shiozaki et al. 2009). The values in parentheses are the estimated errors in the last digits. See Shiozaki et al. 2009 for the sources of the experimental values which are also adjusted by computed results. The experimental value of BH is likely to be in a greater error than the computed value.

	Ne	BH	FH	H_2O
HF energy	−128.54710	−25.13164	−100.07080	−76.06559
Correlation energy	−0.3906(4)	−0.1575(2)	−0.388(1)	−0.371(3)
Total energy	−128.9377(4)	−25.2892(2)	−100.459(1)	−76.437(3)
Experiment	−128.9376	−25.2879	−100.460	−76.4389

3 Anharmonic vibrational frequencies of interstellar molecular species

A general scheme to predict anharmonic vibrational frequencies and vibrationally averaged structures and rotational constants of gas-phase molecules has been developed (Yagi et al. 2000, 2002, 2003, 2004, 2007a,b, 2008) with applications to seven triatomic and tetratomic molecules (Keçeli et al. 2009). HCO^+, HCO, HNO, CH_3^+, and CH_3 are among the identified interstellar molecules, while HOO and HOO^- have not so far been detected in the interstellar medium. The spectroscopic data of HOO^- are scarce.

Table 3. Fundamental vibrational transition energies (in cm^{-1}) (Keçeli et al. 2009).

Molecule	Method	$\tilde{\nu}_1$	$\tilde{\nu}_2$	$\tilde{\nu}_3$	$\tilde{\nu}_4$
HCO^+	Theory	3083	823	2175	—
	Experiment	3089	830	2184	—
HCO	Theory	2432	1079	1874	—
	Experiment	2434	1081	1868	—
HNO	Theory	2683	1503	1572	—
	Experiment	2684	1501	1565	—
HOO	Theory	3447	1399	1121	—
	Experiment	3436	1392	1098	—
HOO^-	Theory	3587	1088	739	—
	Experiment	...	...	775 ± 250	—
CH_3^+	Theory	2940	1383	3096	1384
	Experiment	...	1359 ± 7	3108	1370 ± 7
CH_3	Theory	3002	565	3139	1377
	Experiment	3004	606	3161	1400 ± 4

A combination of the CCSD, $CCSD(2)_T$, and $CCSD(2)_{TQ}$ methods (Table 1) and a correlation-consistent basis set series has been employed to achieve the near-exact, nonrelativistic, Born–Oppenheimer limits of the potential energy surfaces of these molecules in the vicinity of their equilibrium geometries. A new representation of potential energy surfaces that combines two widely-used representations, namely, a fourth-order Taylor expansion (Yagi et al. 2004) and numerical values on a rectilinear grid, has been proposed and shown to yield accurate frequencies, when combined with the vibrational CI method. The anharmonic frequencies and vibrationally averaged rotational constants calculated with the program SINDO (Yagi 2006) can be directly and unambiguously compared with experimental results of these seven molecules. For the molecules of which reliable values of fundamental transition frequencies are observed, the theory reproduces them within 11 cm^{-1} on average (Table 3). For some molecules and some modes of which the experimental frequencies are either unknown or uncertain, our predicted frequencies should be correct within ≈ 20 cm^{-1} and helpful for future spectroscopic identifications.

4 Electronic excited states of the radical ions of polycyclic aromatic hydrocarbons

PAHs are a class of conjugated π-electron systems that are responsible for the interstellar infrared emission features and are also speculated to be the carriers of the diffuse interstellar visible absorption bands. They have been detected in meteorites and believed to be a major carbon reservoir in the interstellar medium. A large fraction of PAHs are expected to be in ionic states because of the intense UV radiation field present in the interstellar environment. Ionized PAHs absorb in longer wave lengths with large absorption cross-sections and are more consistent with astrophysical observations than neutral PAHs.

MO calculations of UV/vis absorption energies and oscillator strengths for PAHs would require combined CI and MBPT methods that are unfeasible for all but the smallest PAHs. We have found that the excited-state extensions of DFT called time-dependent DFT (TDDFT) are particularly effective for such applications because of their uniform accuracy and low computational cost (Hirata et al. 1999). The TDDFT application (Hirata et al. 2003) to 51 radical cations and 7 radical anions of PAHs has shown that the computed vertical excitation energies to the several lowest states are invariably within ≈ 0.3 eV of the observed (Table 4). The intensity patterns predicted by the oscillator strengths are also qualitatively correct. This work has established the assignments of many of the UV/vis absorption bands in PAHs.

Our combined experimental and theoretical studies (Szczepanski et al. 2002a,b; Banisaukas et al. 2003, 2004) have also revealed not just the spectroscopic characteristics of individual PAHs but also their rich photochemistry. Take the radical cation of fluorene (Fig. 1) as an example. The CIS method, an MO excited-state method with comparable computational complexity as TDDFT, is utterly incapable of reproducing quantitatively the observed vertical excitation energies of the radical cation of fluorene or most any radical in general (Hirata & Head-Gordon 1999). It also fails in placing the $\pi^* \leftarrow \sigma$ transition in the correct order among the $\pi^* \leftarrow \pi$ transitions. In contrast, the excitation energies computed by TDDFT are within 0.3 eV of the observed and the order in which the $\pi^* \leftarrow \sigma$ transition appears is consistent with the measured onset of σ-ionization manifold in the photoelectron spectrum of neutral fluorene.

Table 4. The mean square deviations of the calculated (TDDFT) electronic transition energies (in eV) from the observed for 25 catacondensed cations, 15 pericondensed cations, 8 noncondensed cations, 3 heterocyclic cations, and 7 anions of PAHs (Hirata et al. 2003).

	Catacondensed	Pericondensed	Nonbenzenoid	Heterocyclic	Anions
Error	0.26	0.24	0.19	0.31	0.17

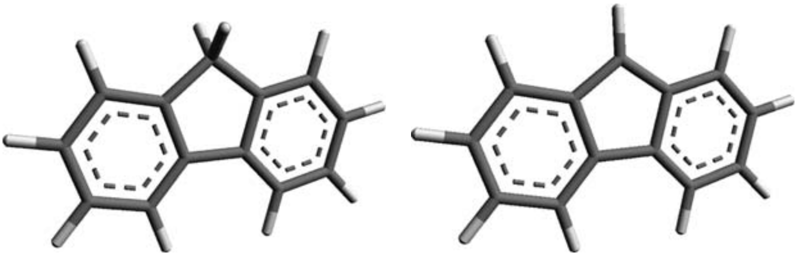

Fig. 1. The structures of fluorene radical cation (left) and sp^3-deprotonated fluorene radical (right).

The experimental studies (Szczepanski et al. 2002b) have suggested that the radical cations of PAHs can readily lose the hydrogen atoms or protons upon visible light irradiation and eventually become pure carbon species, which are also detected in the interstellar medium. Spectroscopically characterizing this dynamic process requires a computational ability to predict the spectra of dehydrogenated or deprotonated PAHs. It has been shown (Szczepanski et al. 2002b) that TDDFT maintains the same accuracy in the vertical excitation energies of the fluorene radical cation before and after the deprotonation and hence is suitable for the studies of photoinduced deprotonation mechanisms.

Table 5. The calculated and observed vertical excitation energies (in eV) of the fluorene radical cation (Szczepanski et al. 2002b).

Excitation	CIS	TDDFT	Obs.
$\pi^* \leftarrow \pi$	3.0	0.9	0.9
$\pi^* \leftarrow \pi$	3.3	1.1	1.2
$\pi^* \leftarrow \pi$	3.5	2.2	2.0
$\pi^* \leftarrow \sigma$	5.8	2.8	3.1
$\pi^* \leftarrow \pi$	4.5	3.7	3.6
$\pi^* \leftarrow \pi$	7.3	3.9	4.1

Acknowledgements. This work was supported by the U.S. Department of Energy (DE-FG02-04ER 15621), the U.S. National Science Foundation (CHE-0844448), and the Donors of the American Chemical Society Petroleum Research Fund (48440-AC6). S.H. is a Camille Dreyfus Teacher-Scholar.

References

Banisaukas, J., Szczepanski, J., Eyler, J., Vala, M., Hirata, S. 2004, J. Phys. Chem. A, 108, 3713

Banisaukas, J., Szczepanski, J., Eyler, J., et al. 2003, J. Phys. Chem. A, 107, 782

Bowman, J. M. 1986, Acc. Chem. Res., 19, 202

Christiansen, O. 2007, Phys. Chem. Chem. Phys., 9, 2942

Fan, P.-D., Hirata, S. 2006, J. Chem. Phys., 124, 104108

Fan, P.-D., Kamiya, M., Hirata, S. 2007, J. Chem. Theo. Comp., 3, 1036

Hirata, S. 2003, J. Phys. Chem. A, 107, 9887

Hirata, S. 2004, J. Chem. Phys., 121, 51

Hirata, S. 2005, J. Chem. Phys., 122, 094105

Hirata, S. 2006, Theor. Chem. Acc., 116, 2

Hirata, S., Fan, P.-D., Auer, A. A., Nooijen, M., Piecuch, P. 2004a, J. Chem. Phys., 121, 12197

Hirata, S., Head-Gordon, M. 1999, Chem. Phys. Lett., 302, 375

Hirata, S., Head-Gordon, M., Szczepanski, J., Vala, M. 2003, J. Phys. Chem. A, 107, 4940

Hirata, S., Lee, T. J., Head-Gordon, M. 1999, J. Chem. Phys., 111, 8904

Hirata, S., Yagi, K. 2008, Chem. Phys. Lett., 464, 123

Hirata, S., Yanai, T., de Jong, W. A., Nakajima, T., Hirao, K. 2004b, J. Chem. Phys., 120, 3297

Hirata, S., Yanai, T., Harrison, R. J., Kamiya, M., Fan, P.-D. 2007, J. Chem. Phys., 126, 024104

Kamiya, M., Hirata, S. 2006, J. Chem. Phys., 125, 074111

Kamiya, M., Hirata, S. 2007, J. Chem. Phys., 126, 134112

Keçeli, M., Shiozaki, T., Yagi, K., Hirata, S. 2009, Mol. Phys., 107, 1283

Klopper, W., Manby, F. R., Tenno, S., Valeev, E. F. 2006, Int. Rev. Phys. Chem., 25, 427

Shiozaki, T., Hirao, K., Hirata, S. 2007, J. Chem. Phys., 126, 244106

Shiozaki, T., Hirata, S. 2007, Phys. Rev. A, 76, 040503(R)

Shiozaki, T., Kamiya, M., Hirata, S., Valeev, E. F. 2008a, Phys. Chem. Chem. Phys., 10, 3358

Shiozaki, T., Kamiya, M., Hirata, S., Valeev, E. F. 2008b, J. Chem. Phys., 129, 071101

Shiozaki, T., Kamiya, M., Hirata, S., Valeev, E. F. 2009, J. Chem. Phys., 130, 054101

Szczepanski, J., Banisaukas, J., Vala, M., Hirata, S. 2002a, J. Phys. Chem. A, 106, 6935

Szczepanski, J., Banisaukas, J., Vala, M., et al. 2002b, J. Phys. Chem. A, 106, 63

Yagi, K., Hirao, K., Taketsugu, T., Schmidt, M. W., Gordon, M. S. 2004, J. Chem. Phys., 121, 1383

Yagi, K. 2006, SINDO (The University of Tokyo, Tokyo, Japan).

Yagi, K., Hirata, S., Hirao, K. 2007a, J. Chem. Phys., 127, 034111

Yagi, K., Hirata, S., Hirao, K. 2007b, Theor. Chem. Acc., 118, 681

Yagi, K., Hirata, S., Hirao, K. 2008, Phys. Chem. Chem. Phys., 10, 1781

Yagi, K., Oyanagi, C., Taketsugu, T., Hirao, K. 2003, J. Chem. Phys., 118, 1653

Yagi, K., Taketsugu, T., Hirao, K. 2002, J. Chem. Phys., 116, 3963

Yagi, K., Taketsugu, T., Hirao, K., Gordon, M. S. 2000, J. Chem. Phys., 113, 1005

"Recent Advances in Spectroscopy:
Theoretical, Astrophysical, and Experimental Perspectives"
Eds. Chaudhuri R K, Mekkaden M V, Raveendran A V, Satya Narayanan A
Astrophysics and Space Science Proceedings, Springer-Verlag, Berlin, 2010.

State specific calculation of dissociation potential energy curve using multireference perturbation theory

Uttam Sinha Mahapatra[1] and Sudip Chattopadhyay[2]

[1] Department of Physics, Taki Government College Taki, North 24 Parganas, India `uttam.mahapatra@linuxmail.org`
[2] Department of Chemistry, Bengal Engineering and Science University, Shibpur, Howrah - 711 103, India `sudip_chattopadhyay@rediffmail.com`

Summary. We have applied multireference (MR) perturbation theory to a degenerate case using the state-specific or single root MR approach (SS-MRPT). The objective of this paper is to provide an account of the applications of both Brillouin-Wigner and Rayleigh-Schrödinger versions of the SS-MRPT with Möller-Plesset partitioning of the hamiltonian. The method is very effective to provide an accurate and balanced treatment of dynamical and non-dynamical correlations over a wide range of geometrical parameters of the molecule under study, and hence, seeks to address bond breaking process in an accurate manner. Studies on dissociation potential energy curve and spectroscopic constants of the ground state of F_2 are carried out to gauge its accuracy. F_2 is a particularly challenging system for electronic structure theory due to strong dynamical and non-dynamical correlation effects. The calculations are compared with other available theoretical results and experimental spectroscopic data. The accuracy of the results appears to be encouraging, taking into account the low computational cost which supports the effectiveness of the method.

1 Introduction

To obtain a smooth dissociation potential energy curve (PEC) treatment of dynamical and non-dynamical correlation effects [a multireference (MR) situation] in an accurate and a balanced manner is mandatory over the wide range of geometries. To treat MR situation in a balanced way, it is conceptually attractive to include the dominant determinants in the reference function, which takes care of nondynamical correlation effects, and then build up dynamical correlation effects for each determinant, as was done in Jeziorski-Monkhorst (JM) ansatz (Jeziorski & Monhorst 1981) based methods (Hilbert space or state universal approach). The effective hamiltonian-based Hilbert space MR method is suitable for computing energies over the various geometries but it is not a practical tool, since it necessarily faces intruder state problems (occurring when a function outside the model space closely approaches the energy of a state inside the space at some point on a PEC) leading to a divergence in the iterative numerical procedure used to determine the wave function amplitudes and thus may lead to unphysical features on computed PEC(s). Truly, any kind of effective Hamiltonian-based theory can encounter intruders. This, however, has not stopped the development effort of the multiroot MR methodology (Jeziorski & Monhorst 1981; Mukherjee & Pal 1989; Paldus & Li 1999). To obviate the intruder problem and in order to ensure continuous PECs, one should ideally use a single parametrization for the wave function across the complete region of interest- such type of method is termed as state specific approach. Such difficulties, coupled with the need for MR, state-specific multireference theories (SSMR) for treating one electronic state at a time, have spawned new formal developments. To compute smooth and chemically accurate PEC(s) avoiding the intruder states problem efficiently, the JM ansatz should be employed in a state specific fashion (Malrieu et al 1994; Meller et al 1996; Mášik & Hubač 1999; Mahapatra et al 1999a; Pahari et al 2005; Evangelista et al 2007, 2008; Bhaskaran et al 2008).

One of the most popular strategies for solving the MR situations in quantum chemistry is multireference perturbation theory (MRPT) (Andersson et al 1990; Hirao 1992; Nakano 1992; Finley et al 1996; Zaitevski et al 1996; Mahapatra et al 1999b; Ghosh et al 2002). MRPT is applied to a great variety of problems and the number of reference states can be very large. Seeking of an efficient and formally corrected state specific MRPT method remains a valuable task in spite of the various developments in this direction in the last few decades. Among the different SS-based MRPT methods using a Möller-Plesset (MP) zero-order Hamiltonian, CASPT of Roos and co-workers (Andersson et al 1990) and MRMPPT of Hirao and co-workers (Hirao 1992) are quite suitable to provide accurate values of the ground state and excitation energies with a reasonable cost. However, the methods are not always strictly size-consistent.

Perturbation theory formulated using Brillouin and Wigner (Wenzel & Steiner 1998; Hubač & Wilson 2000) scheme is very effective due to the rapid convergence behavior with respect to the other version of perturbation theory along with intruder free nature. Although the BWPT is formally very simple, the operator depends on the exact energy of the target state, and hence, does not lead to expressions which have correct (linear) scaling with the number of electrons in the system being studied i.e. a more rigorous objection against BWPT is its lack of size-extensivity, even for a CAS. Lack of size-extensivity implies that errors from the exact energy increase as more electrons enter the calculation. The more sophisticated BWPT version developed by Bloch and Horowitz (Bloch & Horowith 1958) scales somewhat better in the sense that it generates the shift of energy relative to the closed shell core, so that the error scales as the number of valence occupancies. It is nevertheless still not fully extensive. The need to formulate BWPT formalisms which can generate a size-consistent and size-extensive expansion of energy yet avoiding intruders is thus very much warranted.

The success of SS-MRCC (Mahapatra et al 1999a) using CAS has inspired Mukherjee and his group to extend the full-blow SS-MRCC to PT scheme. By invoking suitable partitioning of the hamiltonian, very convenient perturbative versions of the parent SS-MRCC formalism in the Rayleigh-Schrödinger (RS) and Brillouin - Wigner (BW) form have been developed for the second order energy. The unperturbed Hamiltonians for the theory can be chosen to be of both Möller - Plesset and Epstein - Nesbet (EN) type. In SS-MRPT approach, the Fock operator is defined for each model function rather than the entire reference function, and thus it is a multi-partitioning strategy. Among the various single root MRPT methods, SS-MRPT of Mukherjee and co-workers (Pahari et al 2005; Mahapatra et al 1999b) are very promising. Viability of both the RS-based SS-MRPT [SS-MRPT(RS)] and BW-based SS-MRPT [SS-MRPT(BW)] have already been demonstrated in some applications (Pahari et al 2005; Mahapatra et al 1999b, 2008, 2009). The main features of the SS-MRPT method are: (i) it is a wave operator based formalism and the energy is obtained as an eigenvalue of an effective Hamiltonian; (ii) it is a state-specific Hilbert space method retaining all of the flexibility of the wave function for optimizing the description of the target single state; (iii) it avoids instabilities in converging the cluster amplitudes finding equations due to intruder states in a natural manner; (iv) it is rigorously size extensive and size consistent with localized molecular orbitals; and (v) it is a computationally cost effective theory to apply to large chemical systems of arbitrary generality. From these features it is now evident that the SS-MRPT approach is very effective to study the PECs over the wide range of geometrical distortions (throughout the single and multireference regions of geometric configuration space).

In this paper we want to present the numerical implementations of both BW and RS versions of the SS-MRPT with MP partitioning of the hamiltonian using different orbitals (RHF an CASSCF) and basis sets (DZP+ and cc-pVXZ with X=T,Q and 5Z) (http://www.emsl.pnl.gov/forms/basisform.html). We aim to show how the BW-based SS-MRPT approach can modify the results towards the accuracy with respect to experiment and with other sophisticated *ab initio* results in comparison to its RS counter part. This paper is not to advocate replacement of the SS-MRPT(RS) approach with the SS-MRPT(BW) one, rather, it is to throw light on the role of the scheme of perturbative expansion in the treatment of the coupling term maintaining size-extensivity. It is pertinent to note that the computational cost of BW-based scheme is slightly higher than the corresponding RS-based scheme. We expect that many new and longstanding chemical problems will be solved by SS-MRPT(BW) method and its various variants as that of the SS-MRPT(RS) one. Test calculations on the dissociation of F_2 molecule reveal some interesting features of the SS-MRPT approach. The dissociation of F_2 is a very complicated MR problem characterized by a rapid increase of the non-dynamical correlation effects as the $F - F$ bond stretches, which is difficult to capture with single-reference methods. An accurate description of the F_2 dissociation with the single-reference CC methods may require an explicit incorporation of quadruply excited clusters (Kowalski et al 2001; Musial et al 2005).

2 Theory: A brief resume

In this section, without going into the details of derivation (see Mahapatra et al 1999a,b), we present below the working equations of the SS-MRPT formalism. The form of the working equations for the first-order perturbation equations for the cluster amplitudes can be written as follows:

$$t_\mu^{l(1)} = \frac{H_{l\mu}}{[E_0 - H_{ll}]} + \frac{\sum_\nu^{\nu\neq\mu} \langle \chi_l^\mu | T^{\nu(1)} | \phi_\mu \rangle H_{\mu\nu} (c_\nu^0 / c_\mu^0)}{[E_0 - H_{ll}]} \tag{1}$$

for RS and

$$t_\mu^{l(1)} = \frac{H_{l\mu}}{[E - H_{ll}]} + \frac{\sum_\nu^{\nu\neq\mu} \langle \chi_l^\mu | T^{\nu(1)} | \phi_\mu \rangle \widetilde{H}_{\mu\nu} (c_\nu / c_\mu)}{[E - H_{ll}]} \tag{2}$$

for BW.

In SS-MRPT theory, the energy is obtained as an eigenvalue of the effective Hamiltonian matrix. The coefficients and the energy of the target state are generated by diagonalizing an effective operator (non-Hermitian) $\widetilde{H}_{\mu\nu}^{(2)}$ defined in CMS (or CAS):

$$\sum_\nu \widetilde{H}_{\mu\nu}^{(2)} c_\nu = E^{(2)} c_\mu, \tag{3}$$

where $\widetilde{H}_{\mu\nu}^{(2)} = H_{\mu\nu} + \sum_l H_{\mu l} t_\nu^{l(1)}$ and $\{\chi_l^\mu\}$ (for all μ) are the set of virtual functions spanning the space complementary to the CAS (or CMS). Here, $H_{l\mu} = \langle \chi_l | H | \phi_\mu \rangle$, and $H_{ll} = \langle \chi_l | H_0 | \chi_l \rangle$. χ_μ^l stands for a general (mono/bi)-excitation from ϕ_μ, and H_0 is the zeroth-order Hamiltonian. Equations (1)/(2) and (3) are the working expressions used in this work for the evaluation of cluster operators and energy in the perturbative framework. The sets $\{T^\mu\}$ and $\{c_\mu\}$ are coupled through Eqs. (2) and (3) in the case of BW. In the RS theory E_0 corresponds to the CAS energy. In general, the forms of working equation ensure the removal of all the inextensive terms and thereby maintain extensivity. Solving these coupled set of equations gives us the cluster amplitudes and the converged coefficients from the diagonalization. Since the theory is state specific, only one eigenvalue represents the exact energy, while the remaining eigenvalues have no physical meaning. The crucial feature of the formalism in the RS formulation is the use of the zeroth-order coefficients c_μ^0 to compute the cluster operators and $\widetilde{H}$, however, allowing the coefficients to relax while computing energy, since this is obtained by diagonalization. In the BW case, on the other hand, the coefficients also get updated iteratively.

From the working equations of the cluster amplitudes, it is evident that as long as the target state energy E_0 or E remains well-separated from the virtual functions, the denominators in Eq. (1) remain reasonable (in contrast to the effective Hamiltonian based theories) and this poses no difficulties in converging the amplitude equations which are mainly responsible for circumventing intruder states problem. We should emphasize here, since the reference determinants span a CAS, it also follows that the energy obtained (up to second order of energy) as the eigenvalue of Eq. (3) is size-extensive. The extensivity of the energy also implies correct separation into fragments generated from the active orbitals and, hence, size-consistency when we use orbitals localized on the separated fragments. One might be taken by surprise at the emergence of a size-extensive BW-type of perturbation theory from the SSMRCC formalism and might wonder whether a BW perturbation theory can be at all size-extensive. We should, however, note carefully that the BW-type structure emerging from our SS-MRCC theory is not of the orthodox type.

3 Results: Numerical applications on F_2 molecule

The deceptively simple F_2 molecule has been a critical test for many sophisticated methods as most of the theoretical methods fail to compute potential energy curve for $F-F$ dissociation: a very weak single-bond breaking process with strong correlation effects which are probably due to very high electronegativity of fluorine. The latter causes the electron density to be very compact. This tight electron distribution may result in the a local, i.e., dynamical, correlation. All the studies in this article use delocalized RHF and CASSCF orbitals and D_{2h} point group. The choice of orbitals in the results obtained via SS-MRPT procedure is very crucial (for that matter for any MRPT) for smooth convergence of the amplitude equations and the diagonalization step. In this paper, calculations are performed using GAMESS(US) package to which the program of the SS-MRPT method is interfaced (using an Intel core 2 duo 2.0 GHz system). The 1s core orbitals of F were kept frozen in all calculations.

The ground state of F_2 molecule is a MR system for very strong non-dynamical and dynamical correlation effects in varying degrees along its PEC in the ground state and the study of the ground state PEC of F_2 is thus a good testing ground for any MR-based theory (Mahapatra et al 1999b; Kowalski et al 2001; Laidig et al 1987; Li & Paldus 1998;2006; Mášik et al 1995;1998; Krylov 2001; Sears et al 2003). Although the PECs via SS-MRPT(RS) using DZP+ basis (Laidig et al (1987)) have already been published by Mahapatra et al (1999b) with EN-type partitioning scheme (using RHF orbitals), we present here the calculation of the PECs to show the basis set size effect on the relative performance of SS-MRPT(RS) and SS-MRPT(BW). With the increase of basis size, relatively large correction occurs around the equilibrium geometry as dynamical correlation is largely influenced by basis size, while the non-dynamical correlation is seldom influenced by it. For a qualitatively correct description of the ground state PEC of F_2 molecule, at least two degenerate or nearly degenerate configurations: (i) $\phi_1 = 1\sigma_g^2 1\sigma_u^2 2\sigma_g^2 2\sigma_u^2 1\pi_g^4 1\pi_u^4 3\sigma_g^2$, and (ii) $\phi_2 = 1\sigma_g^2 1\sigma_u^2 2\sigma_g^2 2\sigma_u^2 1\pi_g^4 1\pi_u^4 3\sigma_u^2$, must be taken into account even at its equilibrium geometry. The functions ϕ_1 and ϕ_2 constitute the CAS as the $3\sigma_g$ and $3\sigma_u$ belong to different symmetries. However, to achieve quantitative accuracy, the CAS wave function must be augmented by dynamic correlation (via SS-MRPT, say). At this point, it is important to note that near the equilibrium domain, the $1\pi_g$ orbital plays the role of the HOMO whereas this role is played by the $3\sigma_g$ orbital in the bond-breaking regions of molecular PEC. Then the computation for dissociation PEC encounters the perennial "intruder state problem" due to the $1\pi_g \rightarrow 3\sigma_u$ excitations (leading to convergence difficulties for determining the cluster amplitudes). The pronounced non-dynamical character along with the intruder states problem (which warrants a SSMR description of the system) has been the motivation behind the recent study of complete PEC of the ground state of F_2 molecule using SS-MRPT method.

In our first set of calculation, we have used DZP+ basis [Laidig et al 1987] which enables a comparison with the results predicted by several theoretical methods available in the literature as various systems have been studied by several researchers using this basis [Laidig et al 1987; Mášik et al 1995;1998; Krylov 2001]. PECs for SS-MRPT are plotted in Fig. 1(a) along with other theoretical results (such as (i) MRCISD and MRLCCM [Laidig et al 1987] (ii) MRMBPT(2) and CASPT2 [Mášik et al 1995;1998] and (iv) VOO-CCD(2) and SF-OD Krylov (2001)). The reference space in the MRCISD calculations is spanned by 10 configurations, and the size of the reference space appears as a suffix to the MRCISD. It is pertinent to mention in this context that the MRCISD10 energies of Laidig et al. [Laidig et al 1987] are not size-extensive. To alleviate the problem of intruder states, Hubač and co-workers [Mášik et al 1995;1998] have implemented several ad-hoc shifting techniques and applied then to compute the PEC of F_2 molecule via the MRMBPT(2) method within a full-valence space. This becomes mandatory in the said case, since the method is an effective Hamiltonian based strategy. The CASPT2 results [Andersson et al 1990] have been obtained using active space of full valence. It should be emphasized here that the MRMBPT(2) and CASPT2 PECs are not smooth over the entire nuclear geometries. Actually, these two methods display a very narrow hump around the nuclear distance of 6.0 a.u [Mášik et al 1995;1998]. A computationally economic alternative in this regard is the valence orbital optimized coupled cluster doubles (VOO-CCD) [Krylov 2001] which adapts the full valence CASSCF model and is naturally a good candidate for studying single bond dissociation phenomena and processes involving the diradicals. The dynamical correlation is included in the VOO-CCD method through the traditional second-order perturbation theory which leads to the VOO-CCD(2) model, and it embeds size-consistency. The last two methods, the VOO-CCD and the SF-OD - offer promise in describing single bond breaking situations within the SR framework. The energies computed via the MBPT3 (within the realm of SR model) method go down dramatically in the region of dissociation which explains the singular behavior of the method in the case of the HOMO-LUMO degeneracy. Actually, we observed that the larger the internuclear separation, the worse the results of the SR-based methods. This is precisely the desired effect. Fig.1(a) displays that the SS-MRPT(RS) potential lies considerably above the SS-MRPT(BW) potential for DZP+ basis (also true for other basis sets). We also envisage that the SS-MRPT(RS) is energetically quite proximate to the CASPT2 and MR-CISD10. The figure clearly reflects that the SS-MRPT methods are capable of reproducing the pattern of the ground-state PEC of the F_2 molecule in a well-behaved and balanced manner over the wide range of internuclear distances as that of other MR methods.

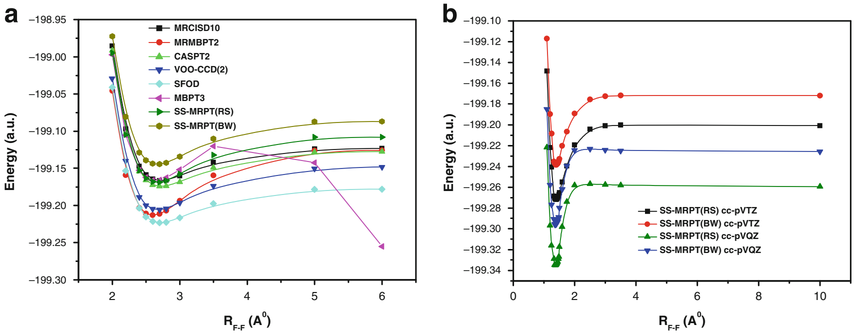

Fig. 1. (a) Ground state PEC of the F_2 molecule with various methods using DZP+ basis set and RHF orbitals and (b) Ground state SS-MRPT PEC of the F_2 molecule using various basis sets and RHF orbitals.

As the full CI results are also not available in this basis, it is natural to test the efficacy of the various methods to generate the correct PEC in a very accurate manner via the computation of various spectroscopic constants, such as equilibrium geometries(R_e), dissociation energies(D_e), and harmonic vibrational frequencies(ω_e) using our calculated dissociation curve and compare these spectroscopic properties with other theoretical and experimental results. We have extracted spectroscopic parameters via polynomial fits to the computed PECs. We have observed that the computed spectroscopic constants remained almost unaltered due to the variations in the degree or the number of points. The spectroscopic properties derived from our potential energy curves are reported in Table 1 along with the data calculated by the various methods. The table also depicts that the spectroscopic constants of the MRCISD and MRLCCM methods do not improve much on going from the reference space consisting of 10 configurations to the reference space consisting of 32 configurations, although the calculations involved in MRCISD32 and MRLCCM32 are much more computationally demanding than those of

MRCISD10 and MRLCCM10. The very large error in the CCSD frequency and dissociation energy is due to the fact that the CCSD method is incapable to describe the PEC of F_2 molecule (even around the equilibrium geometry) due to the convergence difficulties of the cluster amplitudes. Actually CASCI, SF-CIS and UHF-CCSD methods grossly underestimate the dissociation energy, whereas both $(SC)^2$-SDCI and MRMBPT2 methods overestimate the dissociation energy. The MRMBPT2 method gives worse results for ω_e. Here, we must emphasize that the quality of ω_e depends solely on the shape of the PEC. An inspection of the comparison presented in Table 1 clearly shows that the SS-MRPT approach for DZP+ basis is capable of computing spectroscopic constants of F_2 molecule in a accurate manner. The spectroscopic constants generated via SS-MRPT method agree better with experimental findings in comparison to the MR-CISD ones. For this basis set the performance of the SS-MRPT to compute ω_e and D_e is closer to experimental values than that of the VOO-CCD(2).

In our next set of calculations, we have used various basis sets: cc-pVTZ, cc-pVQZ and cc-pV5Z. The plot of total energies (computed by the SS-MRPT method using various basis sets) as a function of $F - F$ bond length is visualized in Fig. 1(b). From Fig. 1(b), we have observed that the computed PEC using different basis sets are smooth in nature and provide the corrected dissociation limit. Fig. 1(b) demonstrates the effect of basis sets size on the shape and accuracy of the ground state PEC of the F_2 system. This is often the dominant factor away from the equilibrium geometry. Since the PEC obtained using our SS-MRPT approach is seen to be very well behaved as well as smooth throughout the entire region and FCI calculations are also not possible for these basis sets, we have calculated the spectroscopic constants also. The spectroscopic results obtained with various cc-pV basis sets are summarized in Table 1. Table 1 compares results calculated by BW-MRCCSD and Mk-MRCCSD (reported in Evangelista et al 2007, 2008; Bhaskaran et al 2008) for the sake of comparison of the potentiality of the SS-MRPT method to the others. Note that the BW-MRCCSD theory in its original formulation is not size-extensive. In Ref. (Li & Paldus 1998;2006), Li and Paldus reported that with the cc-pVQZ basis, the computed CCSD(T), CR-CCSD(T), and CR-CC(2,3) harmonic vibrational frequencies are 921.1, 951.9, and 937.0 cm^{-1}, respectively.

Table 1 displays that the equilibrium bond distance and harmonic frequency computed by SS-MRPT and Mk-MR methods for correlation consistent basis are close to the corresponding experimental values. The SS-MRPT in both forms is able to yield R_e and ω_e results in close agreement with those obtained from the parent Mk-MRCCSD method. It should be mentioned that in Mk-MRCCSD approaches, Evangelista et al (2007, 2008), and Bhaskaran et al (2008) have employed a spin non-adapted, four-reference model space based on (2×2) active space. On the other hand, the SS-MRPT approach applied in this paper is spin-adapted in nature. A potentially problematic feature of the spin non-adapted methods is their spin incompleteness, which

Table 1. Spectroscopic constants for the electronic ground state of F_2 molecule using RHF orbitals and different basis sets with the (σ,σ^*) active space. The values in parentheses indicate the SS-MRPT values for CASSCF (Canonical) orbitals.

Basis	Method	$R_e(\AA)$	$\omega_e(\mathrm{cm}^{-1})$	D_e(ev)
DZP+	CASCI	1.5107	619	0.63
	SS-MRPT(RS)	1.4225 (1.4330)	886 (859)	1.65(1.42)
	SS-MRPT(BW)	1.4261 (1.4321)	873(844)	1.56 (1.35)
	SS-MRCCSD	1.428	800	1.397
	SF-CIS(singlet Orbs)^a	1.469	826.44	1.29
	SF-CIS(triplet Orbs)^a	1.448	855.94	1.37
	SF-CIS ^{a}	1.567	468	0.28
	SF-CISD^a	1.429	824	1.14
	SF-OD^a	1.437	831	1.24
	VOO-CCD(2)^a	1.417	899	1.51
	UHF-CCSD^b	1.410	1006	0.95
	MRCISD10^b	1.435	821	1.222
	MRLCCM10^b	1.439	842	1.221
	MRCISD32^b	1.436		1.275
	MRLCCM32^b	1.439		1.257
	$(SC)^2$-SDCI^c	1.407	947	2.306
	CASPT2^c	1.442	819	1.275
	sr-MRBWCCSD^c	1.421	888	1.703
	MRMBPT(2)^c			
	simple averaging	1.374	1054	2.348
	double averaging	1.377	1040	2.196
cc-pVTZ	CASCI	1.4828	705	0.78
	SS-MRPT(RS)	1.3893(1.408)	1016(966)	1.93(1.97)
	SS-MRPT(BW)	1.3923 (1.407)	999 (948)	1.81 (1.85)
	CCSD^d	1.3946	1012	1.22
	CCSDT^d	1.4154	923	1.50
	BW-MRCCSD^d	1.4060	953	2.03
	Mk-MRCCSD^d	1.4127	925	1.71
cc-pVQZ	CASCI	1.5034	665	0.75
	SS-MRPT(RS)	1.3897(1.412)	1002(936)	2.06 (1.80)
	SS-MRPT(BW)	1.3938 (1.410)	987 (915)	1.91(1.69)
	CCSD^d	1.3906	1016	1.29
	CCSDT^d	1.4124	925	1.58
	BW-MRCCSD^d	1.4024	955	2.12
	Mk-MRCCSD^d	1.4093	926	1.79
cc-pV5Z	SS-MRPT(RS)	1.3852 (1.4119)	998 (939)	2.13(1.81)
	SS-MRPT(BW)	1.3938 (1.4091)	986 (917)	1.94(1.75))
CBS	BW-MRCCSD^d	1.3988	963	2.20
	Mk-MRCCSD^d	1.4057	934	1.85
	Experiment	1.412	916.64	1.66

CBS: Complete Basis Set limit.

a:Krylov (2001); b:Laidig et al (1987); c:Mášik et al (1995;1998); d:Evangelista et al (2007, 2008); Bhaskaran et al (2008); Experiment: Ref. Huber & Herzberg (1979).

may lead to spin contamination of the target wave functions, particularly in the bond-breaking process involving open shell species. In fact, all methods with basis sets of the cc-pV quality (reported in Table 1) overshoot the dissociation energy, except CASCI. The performance of the SS-MRPT(RS) in this context is slightly unsatisfactory. The dispersion of D_e from the experimental value increases for SS-MRPT as one moves from cc-pVTZ to cc-pV5Z basis sets. Note that an extrapolation to the complete basis set (CBS) limit slightly increase the value of D_e in the case of Mk-MRCCSD approach. The basis set dependence of the calculated values of spectroscopic constants show a small difference between the various basis sets considered. That means that adding extra diffuse functions to the basis set does not have a large effect on the ground state wave function in the equilibrium interatomic distance range. However, the D_e value, is slightly more sensitive.

As CASSCF is theoretically a very effective choice to construct reference function for MR situation, in Table 1, we have also presented the results (values in parentheses) generated via SS-MRPT method using canonical CASSCF orbitals along with RHF ones. In general, it is found that the accuracy increases upon using CASSCF orbitals instead of RHF ones for the system studied by us in this article. With CASSCF orbitals SS-MRPT approach provides very good results for R_e, ω_e and D_e of F_2 with respect to the experiment. From Table 1 it is quite evident that on improving the basis from cc-pVQZ to cc-pV5Z, the changes in the values of the spectroscopic constants are negligibly small (at least for the system concerned). This clearly brings out the fact that the effect of dynamical correlation is being incorporated within the SS-MRPT quite effectively. Additionally, it is to be pointed out that for both the basis sets, the spectroscopic constants are quite close to the experimental results.

The spectroscopic data of SS-MRPT method demonstrates that the curvature of the PEC produced by the SS-MRPT method is reasonably well which indicates that the performance and capabilities of SS-MRPT method are quite reliable for the computation of the ground state PEC of the F_2 molecule. As far as the quality of spectroscopic constants is concerned, the SS-MRPT results are competitive with the full-blown SS-MRCC (/Mk-MRCCSD) ones which involves a huge number of CSFs (limits its application to very small systems) in comparison to the SS-MRPT approach. It is noticeable that SS-MRPT approach essentially reproduces the Mk-MRCCSD (or BW-MRCCSD) result while requiring much less numerical effort. Thus our work shows that the SS-MRPT approach is a widely applicable tool for the study of real chemical problems where the static correlation plays an important role.

4 Conclusion

In this paper, we have applied the size-extensive SS-MRPT(RS) and (BW) methods to study the complete PEC of the ground state of F_2 molecule using various basis sets with the CAS(2×2). The potential curve calculated via SS-MRPT method has the correct dissociation limit. To compare with the experimental spectroscopic data and other theoretical results, we have also computed various spectroscopic constants from the computed PEC. Very good agreement with experimental spectroscopic results have been observed. The overall performance of the SS-MRPT is also very encouraging when compared with its parent SS-MRCC (Mk-MRCC) method, considering the rather low numerical demands. Thus, the SS-MRPT approach can be viewed as a useful, robust and effective, yet economical approximation to the full-blown SS-MRCC theory to treat the dissociation process of a molecule (like F_2) in the presence of intruder effects.

Acknowledgement. The Financial support from the Department of Science and Technology, India (Grant No.SR/S1/PC-32/2005) is thankfully acknowledged.

References

Andersson, K., Malmqvist, P. A., Roos, B. O., Sadlej A. J. and Wolinski, K., J. Chem. Phys. **94**, 5483 (1990).

Bhaskaran-Nair, K., Demel, O. and Pittner, J., J. Chem. Phys. **129**, 184105 (2008).

Bloch, C. and Horowitz, J., Nucl Phys, **8**, 91 (1958).

Evangelista, F. A., Simmonett, A. C., Allen, W. D., Schaefer, III H. F. and Gauss, J, J. Chem. Phys. **128**, 124104 (2008).

Evangelista, F. A., Allen, W. D. and Schaefer, III H. F., J. Chem. Phys. **127**, 024102 (2007).

Finley, J. P., Chaudhuri, R. K. and Freed, K. F., Phys. Rev. A **54**, 343 (1996).

Ghosh, P., Chattopadhyay, S., Jana, D. and Mukherjee, D.. Int. J. Mol. Sci. **3**, 733 (2002).

Hirao, K., Chem. Phys. Lett. **190**, 374 (1992), Int. J. Quantum Chem. **S26**, 517 (1992).

Hubač, I. and Wilson, S., J. Phys. B 365 (2000).

Huber, K. P, and Herzberg, G., Molecular Structure and Molecular Spectra. IV. Constants of Diatomic Molecules (Van Nostrand-Reinhold, New York, 1979).

Jeziorski, B. and Monkhorst, H. J., Phys. Rev. **24**,1668 (1981);

Kowalski, K. and Piecuch, P., Chem. Phys. Lett. **344**, 165 (2001);

Krylov, A. I., Chem. Phys. Let. **350**, 522 (2001).

Laidig, W. D. and Bartlett, R. J., J. Chem. Phys. **86**, 887 (1987).

Li, X. and Paldus, J., J. Chem. Phys. **108**, 637 (1998); *ibid.* **125**, 164107 (2006).

Mášik, J., Hubač, I., and Mach, P., Int. J. Quantum Chem. **53**, 297 (1995); J. Chem. Phys. **108**, 6571 (1998).

Mášik, J. and Hubač, I., Adv. Quantum Chem. **31**, 75 (1999).

Mahapatra, U. S., Chattopadhyay, S. and Chaudhuri, R. K., J. Chem. Phys. **130**, 014101 (2009).

Mahapatra, U. S., Chattopadhyay, S. and Chaudhuri, R. K., J. Chem. Phys. **129**, 024108 (2008).

Mahapatra, U. S., Datta, B. and Mukherjee, D., J. Phys. Chem. **103**, 1822 (1999b).

Mahapatra, U. S., Datta, B., and Mukherjee, D., J. Chem. Phys. **110**, 6171 (1999a).
Malrieu, J. P., Daudey, J. P. and Caballol, R., J. Chem. Phys. **101**, 8908 (1994);
Meller, J., Malrieu, J. P. and Caballol, R., J. Chem. Phys. **104**, 4068 (1996).
Mukherjee, D. and Pal, S., Adv. Quantum Chem. **20**, 561 (1989).
Musial, M. and Bartlett, R. J., J. Chem. Phys. **122**, 224102 (2005).
Nakano, H., J. Chem. Phys. **99**, 7983 (1993).
Pahari, D., Chattopadhyay, S., Das, S., Mukherjee, D. and Mahapatra, U. S. in Theory and Applications of Computational Chemistry: The First 40 Years, Eds. Dytkstra C E, Frenking G Kim, K S and Scuseria G E 581, (Elsevier, Amsterdam, 2005).
Paldus, J. and Li, X., Adv. Chem. Phys. **110**, 1 (1999).
Sears, J. S., Sherrill, C. D. and Krylov, A. I., J. Chem. Phys. **118**, 9084 (2003).
Wenzel, W. and Steiner, M. M., J. Chem. Phys. **108**, 4714 (1998).
Zaitevskii, A. and Malrieu, J. P., Theor. Chim. Acta. **96**, 269 (1997).

"Recent Advances in Spectroscopy:
Theoretical, Astrophysical, and Experimental Perspectives"
Eds. Chaudhuri R K, Mekkaden M V, Raveendran A V, Satya Narayanan A
Astrophysics and Space Science Proceedings, Springer-Verlag, Berlin, 2010.

C–H···O Hydrogen Bonded Complexes Between Chloroform and Cyclic Ketones: Correlation of Spectral Shifts and Complex Stability with Ring Size

Anamika Mukhopadhyay and Tapas Chakraborty

Department of Physical Chemistry, Indian Association for the Cultivation of Science, Jadavpur, Kolkata 700032, India. `pcam@iacs.res.in`, `pctc@iacs.res.in`

Summary. Stable C–H···O hydrogen bonded complexes between choloroform and three small cyclic ketones (cyclohexanone, cyclopentanone, cyclobutanone) are identified by use of FTIR spectroscopy in CCl_4 solution at room temperature. The C–H stretching fundamental of chloroform ($\nu_{\text{C-H}}$) in the said three complexes exhibits blue shifting with enhancement in $\nu_{\text{C-H}}$ transition intensity. However, the red shifts of the $\nu_{\text{C=O}}$ bands of the cyclic ketones in the complexes show no apparent correlation with the corresponding blue shifts of $\nu_{\text{C-H}}$. The spectral analysis reveals that the stability of the complexes decreases with the ring size of the cyclic ketones. Electronic structure calculation at DFT/B3LYP/6-311++G(d,p) and MP2/6-31+G(d) levels predict that the complex binding energies are correlated with the dipole moment, proton affinity, and n(O)$\rightarrow \sigma^*$(C–H) hyperconjugative charge transfer ability of the cyclic ketones.

1 Introduction

A hydrogen bond (HB) is a weak attractive interaction between a covalently bound hydrogen atom (H–X) and an electronegative atom (Y), where the latter (Y) could be a part of the same or different molecule (X–H)···Y (Desiraju et al 1999; Buckingham et al. 2008). If both X and Y are strongly electronegative, the X–H···Y HB is categorized as classical HB. The spectroscopic manifestation of such bond is red-shifting of X–H stretching frequency with concomitant enhancement in infrared transition intensity (Desiraju et al 1999; Buckingham et al. 2008). On the other hand if X is weakly electronegative, the X–H stretching frequency might exibit blue-shifting with either enhancement or diminution in infrared transition intensity. The second category of HBs is known as improper or blue-shifting HBs (Hozba & Havlas 2000; McDowell & Buckingham 2005). A scrutiny of the spectroscopic data reported till the date reveals that HBs having C–H$\cdots$O type linkages usually display blue-shifting of the $\nu_{\text{C-H}}$ frequency. However, most of such studies with model systems were performed only in low temperature environments like in inert gas liquids (Delanoye et al 2002) supersonic jet expansion (Venkatesan et al 2004) and solid inert gas matrices (Dozova et al 2005). On the other hand, the experimental results presented here show that stable blue-shifting C–H$\cdots$O H-bonded complexes between cyclic ketones and chloroform can be produced in CCl_4 solutions at room temperature.

The cyclic ketones used here as model systems are interesting molecules, because their C=O strechig frequencies are ring size dependent (Silverstein et al 2005), for example the measured values of $\nu_{\text{C=O}}$ of cyclobutanone (CBN), cyclopentanone (CPN) and cyclohexanone (CHN) are 1788, 1748 and 1717 cm^{-1}, respectively. The differences imply that the C=O bonding parameters of the three ketones are different owing to different ring strains. We show that the ring strains also affect the HB acceptor ability of these ketones. The

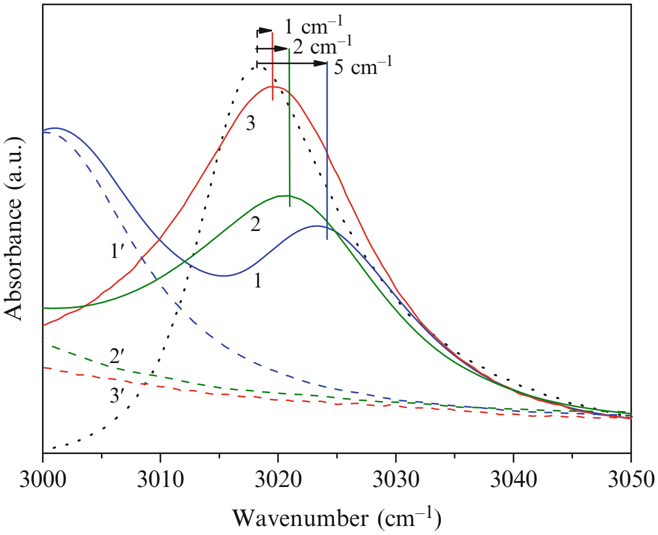

Fig. 1. $\nu_{\text{C-H}}$ of (black dotted curve) free chloroform and its 1:1 complexes with (red, 1) CHN, (green, 2) CPN and CBN (blue, 3). The vertical lines denote the peak positions of the curves. In the same spectral range, the higher frequency regions of the ring CH bands of the three cyclic ketones (0.025M) are also presented here (dashed curve, marked with X') with the respective color codes for comparison

cyclic ketones and chloroform were procured from sigma Aldrich, and used as supplied. The FTIR spectra of the solutions were recorded using a Bruker

IFS 66/S infrared spectrometer equipped with a deutarated triglycine sulfate (DTGS) detector and a KBr beam splitter. The instrument resolution was 0.5 cm^{-1}, and the path length of the KBr liquid cell used was 0.5 mm.

Geometries of the cyclic ketones, chloroform and their 1:1 complexes were optimized at DFT/B3LYP/6-311++G(d,p) and MP2/6-31+G(d) levels of theory. BSSE corrected stabilization energies were calculated by counterpoise method. The normal mode vibrational frequencies were calculated by MP2/6-31+G(d) method. Evolutions of different electronic structure parameters and spectral shifts as a function of HB distance ($R_{H\cdots O}$) were calculated by varying the latter in a relaxed scan mode. For predictions of natural charges on binding sites (donor-acceptor) and the contribution of n(O)→ σ^*(C–H) hyperconjugation interaction energies we performed NBO analysis. G03 program package was used to perform all the calculations presented here (Frisch et al 2004).

2 Results and Discussion

2.1 FTIR Spectra of the Complexes:

Formation of stable H-Bonded complexes in CCl_4 solutions between chloroform and the cyclic ketones were probed by monitoring the evolution of ν_{C-H} band of chloroform and $\nu_{C=O}$ band of the ketones. Throughout the measurements, the ketone concentration in all solutions was 0.025M, and chloroform concentration was varied so that the ketone to chloroform concentration ratios in four solutions were 1:1, 1:5, 1:10 and 1:15.

Figure 1 shows the changes of ν_{C-H} of chloroform on complexation. The ketone:chloroform mole ratio in each solution was 1:10. A $CHCl_3$ solution of same concentration was used to record the background and the dotted curve represents the corresponding ν_{C-H} of the uncomplexed chloroform. The positive sign of other curves indicates that the ν_{C-H} transition intensity is enhanced upon complexation in each case, and the shifts of the band center are 1, 2 and 5 cm−1 for CHN, CPN and CBN, respectively. The estimated values of complexation are, -0.60, 0.09, and 0.47 kcal/mol, respectively, for the three ketones. Thus, the blue shiftings of donor C–H group are correlated with the ring size of the acceptor molecules and relative stability of the complexes. Figure 2 shows the change of $\nu_{C=O}$ band of the three ketones upon formation of the complexes. A commercial curve fitting programme (OriginPro7.5) was used to deconvolute the spectra and those are shown in the right hand side of the panels. Thus, for CHN, CPN and CBN the bands are red-shifted by 8, 19 and 6 cm−1, respectively. Distinct isosbestic points appear in all three cases, and these indicate that the stoichiometry of each complexe is 1:1.

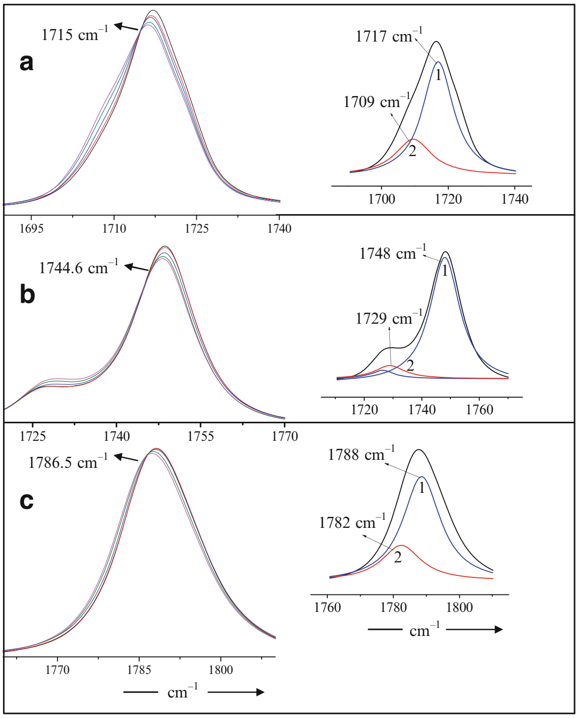

Fig. 2. $\nu_{C=O}$ region of the FTIR spectra of the three cyclic ketones, (a) CHN, (b) CPN and (c) CBN in CCl_4 solution with a concentration of 0.025M and varying $CHCl_3$ concentration. In all three cases, appearances of distinct isosbestic points (denoted by arrows) indicate the 1:1 stoichiometry of the complexes. Red, blue, green and magenta curves represent 1:1, 1:5, 1:10 and 1:15 ketone to chloroform mole ratios in CCl_4, respectively. On the right hand side of each ketone spectra, the deconvoluted spectrum for a solution of 1:10 ketone to chloroform mole ratio is depicted. The blue curve (1) denotes the C=O band of monomer and red dotted curve (2) denotes the corresponding complex in the envelope. In case of CPN, the complex at 1729 cm-1 overlaps nearly with a monomer band at 1727 cm^{-1}.

2.2 Correlation of Spectra with stability of the Complexes:

The primary factors responsible for stability of the complexes are (i) long range electrostatic interaction between the weakly polar C–H bond of chloroform and polar carbonyl groups of the cyclic ketones, via dipole-dipole and dipole induced dipole type interactions (Desiraju et al 1999; Buckingham et al. 2008) and (ii) hyperconjugation charge transfer from the non-bonding orbitals of oxygen n(O) to the vacant anti bonding orbital of C–H bond σ^*(C–H) of

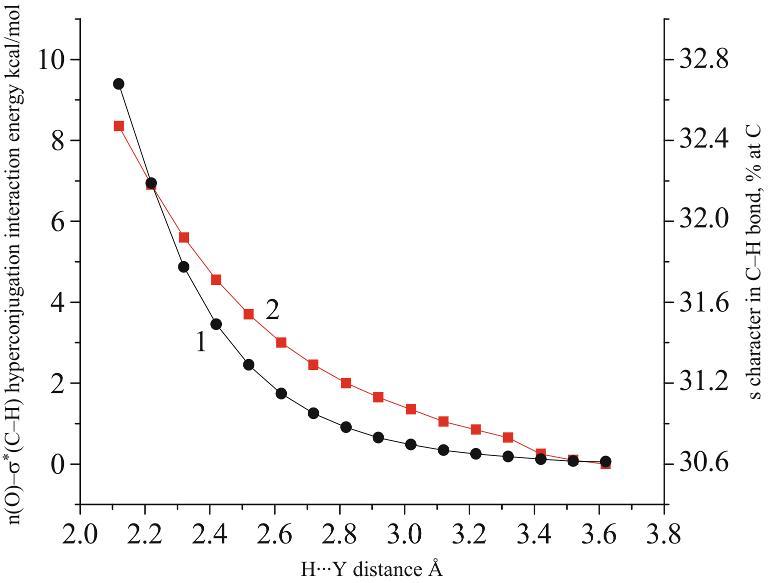

Fig. 3. Change in n(O)→ σ^*(C–H) hyperconjugation interaction energy (1) and s character (%) in the carbon hybrid orbital (2) of the C–H bond of chloroform as a function of $R_{H\cdots O}$ of CBN· · · $CHCl_3$ complex obtained from NBO analysis in a scan performed at MP2/6-31+G(d) level of calculation.

chloroform (Alabugin et al 2003). The latter is a short range interaction, and manifests only when the donor-acceptor moieties are spatially closer and they are oriented favourably for sufficient orbital overlap. We argue below that the contribution of these interactions in the three complexes are different; and correlate them with the ring size of the cyclic ketones.

A few relevant structural parameters of the optimized structures of the molecules are shown in Table 1. The ∠ C–CO–C bond angle of CBN being smallest, the s character (%) of the σ bonding orbital of its carbonyl carbon atom is largest. For the same reason, the s character of the same orbital is smallest in case of CHN. The differences imply that the σ bonding electrons of the C=O group of CBN are more tightly bound toward carbonyl carbon compared to that in the cases of CHN. Consistent with such expectations, the NBO analysis reveals that the C=O bond of CHN is more polar than that of

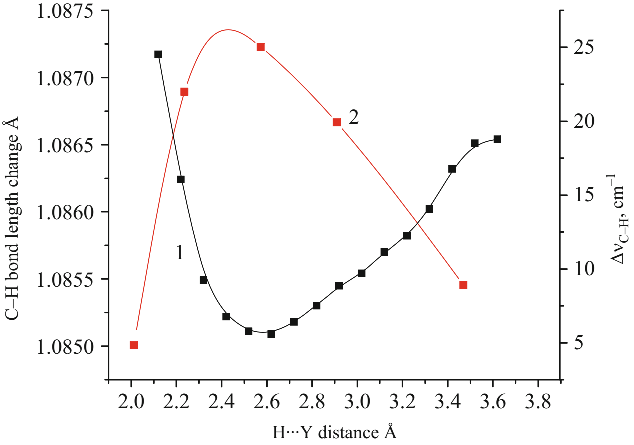

Fig. 4. Change in C–H bond length (1) and predicted ν_{C-H} of chloroform (2) with $R_{\mathrm{H\cdots O}}$ of CBN$\cdots$CHCl$_3$ complex in a scan at MP2/6-31+G(d) level.

CBN. In consequence, the dipole moment of the three ketones follows the order CHN > CPN > CBN, and the same sequence is also predicted for their proton affinity values. The natural negative charge on carbonyl oxygen of CHN being maximum, the hyperconjugative n(O)$\rightarrow \sigma^*$ (C–H) charge transfer interaction with chloroform is also expected to be maximum for CHN. Thus, the overall stability of 1:1 H-bonded complexes of the three ketones should follow the sequence CHN > CPN > CBN. This expectation agrees with the calculated (at DFT/B3LYP/6-311++G(d,p) level) binding energies of the three complexes, 4.39, 3.95, and 3.64 kcal/mol, respectively and the sequence of experimentally estimated ΔG_f^o values. The hyperconjugation interaction energies of the said three ketones calculated by the same level of theory are, 5.06, 4.98, and 4.50 kcal/mol, respectively.

Figure 3 shows, the variation of hyperconjugation interaction energy with $R_{\mathrm{H\cdots O}}$ of the prototype CBN$\cdots$CHCl$_3$ complex. For an increase of 0.3$\mathring{A}$ of $R_{\mathrm{H\cdots O}}$ from the optimized value, the hyperconjugation interaction energy is decreased by 50%. This information is important because in the liquid phase the nearest separations between the H-bonded partners are limited by the solvent shells around the molecules, and it is likely that the intermolecular separations are larger compared to the predictions of gas-phase calculations. Furthurmore,the variation of C–H bond length and $\Delta\nu_{\mathrm{C--H}}$ with $R_{\mathrm{H\cdots O}}$ of the complex are shown in Figures 4 and 5, respectively. For smaller values of $R_{H\cdots O}$, the C–H bond length displays a sharp change, and this happens because of dominant contribution of hyperconjugation interaction. At larger intermolecular separation, the C–H bond length exhibits a gradual shortening with decrease in $R_{H\cdots O}$, and passes through a minimum. The predicted variation of ν_{C--H} with $R_{H\cdots O}$ is correlated with C–H bond length change, i.e., as the latter passes through the minimum, the former passes through a maximum.

The blue shifting of chloroform ν_{C--H} transition due to complexation with the three cyclic ketones observed in this study could be explained considering rehybridyzation/repolarization mechanism in addition to hyperconjugation and electrostatics interactions (Alabugin et al 2003). The NBO analysis of the electronic structure parameters of the complexes indicates that there is enhancements of the natural charges at both the binding sites due to complexation (Table-1). The increased positive charge on the H atom of C–H bond chloroform implies decrease of its effective electronegativity, and it causes repolarization of this bond. According to Bent's rule, the s character in a hybrid orbital of an atom is increased when attached with an electropositive substituent. Conversely, the p character in the hybrid orbital is increased when the atom is attached with an electronegative substituent (Bent 1961). Applying this rule to the systems studied here one can conclude that the s character of the carbon hybrid orbital of the C–H bond of $CHCl_3$ is increased upon complex formation, and it makes the bond stronger and results blue shifting of the ν_{C-H} frequency. The variation of hybridization of carbon bonding orbital of C–H bond with $R_{H\cdots O}$ of this complex as predicted by NBO calculation is presented in Figure 3.

Thus, the red or blue shifting of the stretching frequencies of the donor-acceptor groups are the outcome of subtle balance between hyperconjugation and rehybridization effects. The former interaction is least for CBN$\cdots CHCl_3$ complex and largest for CHN$\cdots CHCl_3$, and the net blue shifting effect by the ketones are rationalized to follow the sequence CBN > CPN > CHN.

As depicted in Figure 2, the complexation induced shifts at the acceptor sites, i.e., $\Delta\nu_{C=O}$ of the three cyclic ketones show no correlation with the ring size and the binding energies of the complexes. The observation is contrary to the common perception that red shifting is proportional to the complex binding energy. A possible reason for this apparent contradiction is due to change in potential energy distribution (PEDs) of the $\nu_{C=O}$ normal mode. Calculation at MP2/6-31+G(d) level predicts that $\Delta\nu_{C=O}$ normal mode is not localized only on C=O bond, but has contribution from displacements of other internal coordinates as well. It was shown earlier that the contribution of the former is $\sim 78\%$ in case of CPN and $\sim 75\%$ in case of CHN (Kartha et al 1973; Fuhrer et al 1972). Our calculation predicts that in the case of CPN$\cdots CHCl_3$ complex, the mode has contribution from C–H bending coordinate, and this could be a reason for larger spectral shift for this molecule.

Table 1. Some important geometric parameters, dipole moment, PA, and results of NBO analysis of the three cyclic ketones predicted by MP2/6-31+G(d) and DFT/B3LYP/6-311++G(d,p) theoretical methods.

Parameters	MP2/6-31+g(d)			DFT/6-311++g(d,p)		
	CHN	CPN	CBN	CHN	CPN	CBN
∠C-CO-C (deg)	115.21	108.75	92.94	115.28	108.43	92.59
μ (Debye)	3.93	3.83	3.68	3.47	3.28	3.11
PA (kcal/mol)	199	195	165	208	204	194
q(O)	-0.652	-0.6483	-0.6337	-0.559	-0.556	-0.5351
Δq(O)	0.0395	0.0364	0.0297	0.032	0.0316	0.0256
Hybridization[1]	$sp^{2.19}$	$sp^{2.09}$	$sp^{1.99}$	$sp^{2.18}$	$sp^{2.09}$	$sp^{1.99}$
% s[2]	31.26	32.32	33.35	31.40	32.30	33.36
		$CHCl_3$			$CHCl_3$	
q(H)	0.2898			0.2069		
Δq(H)	0.0355	0.038	0.035	0.0429	0.0436	0.0376

[1] Hybridization of C_C in C=O bond. [2] % of s on C_C(C=O).

3 Conclusion:

Stable 1:1 H-bonded complexes between chloroform and three cyclic ketones are indentified in CCl_4 solution at room temperature. The $\nu_{C\text{-}H}$ of chloroform exihibits blue shifting with enhancement in infrared transition intensity, and the extent of shifts are +1, +2, and +5 cm^{-1} for CHN, CPN and CBN, respectively. The experimentally estimated values of ΔG_f^0 of the complexes with the three ketones are, -0.60, 0.09, and 0.47 kcal/mol, respectively. Thus the stability of the complexes and spectral blue shifts of ν_{C--H} transition follow somewhat reciprocal behaviour. On the other hand, red shifts of $\nu_{C=O}$ of the acceptor molecules do not show any correlation with the corresponding blue shifts. $\Delta\nu_{C=O}$ of CPN is largest inspite of having a relatively smaller binding energy of this complex. We speculated that such apparent anomaly develops as a result of changes in potential energy distribution of the $\Delta\nu_{C=O}$ normal modes of the ketones on complex formation. The origin of blue shifting of chloroform ν_{C--H} transition in the complexes has been explained considering a subtle balance between rehybridyzation/repolarization and hyperconjugation interactions.

Acknowledgement. TC thanks Department of Science andTechnology, Govt. of India for Research grants under the Ramanna Fellowship Scheme.

References

Alabugin, I.V.; Manoharan, M.; Peabody, S.; Weinhold, F. *J. Am. Chem .Soc.* 125, 5973 (2003).

Bent, H. A. *Chem. Rev.*, 61, 275 (1961).

Buckingham, A. D.; Del Bene, J.E.; McDowell, S.A.C. *Chem. Phys. Lett.* 463, 1 (2008) and references therein.

Delanoye, S. N.; Herrebout, W. A.; van der Veken, B. J. *J. Am. Chem .Soc.*, 124, 7490 (2002).

Desiraju, G.R.; Steiner, T. *The Weak Hydrogen Bond:* Oxford University Press: Oxford, 1999.

Dozova, N.; Krim, L.; Alikhani, M. E.; Lacome, N. *J. Phys. Chem. A* 109, 10273 (2005).

Frisch, M. J.; et al. *Gaussian03 revision E.01; Gaussian, Inc.*: Wallingford, CT, 2004.

Fuhrer, H.; Kartha, V. B.; Krueger, P. J.; Mantsch, H. H.; Jones, R. N. *Chem. Rev.*, 72, 439 (1972).

Hobza, P.; Havlas, Z. *Chem. Rev.*, 100, 4253 (2000) and references therein.

Kartha, V. B.; Mantsch, H. H.; Jones, R. N. *Can. J. Chem*, 51, 1749 (1973).

McDowell, S.A.C.; Buckingham, A.D. *J. Am. Chem .Soc.*, 127, 15515 (2005).

Silverstein, R. M.; Webster, F. X.; Kiemle, D. *Sectrometric Identification of Organic Compounds*; Wiley: 2005

Venkatesan, V.; Fujii, A.; Ebata, T.; Mikami, N. *Chem. Phys. Lett.*, 394, 45 (204).

"Recent Advances in Spectroscopy:
Theoretical, Astrophysical, and Experimental Perspectives"
Eds. Chaudhuri R K, Mekkaden M V, Raveendran A V, Satya Narayanan A
Astrophysics and Space Science Proceedings, Springer-Verlag, Berlin, 2010.

Infrared spectroscopic demonstration of cooperative and anti-cooperative effects in C-H--O hydrogen bonds

Amit K. Samanta and Tapas Chakraborty

Department of Physical Chemistry and Raman Centre for Atomic Molecular and Optical Sciences, Indian Association for the Cultivation of Science, Jadavpur, Kolkata 700032, India. `pcaks@iacs.res.in, pctc@iacs.res.in`

Summary. Matrix isolation infrared spectra of 1,2-cyclohexanedione (1,2-CHD) and 3-methyl-1,2-cyclohexanedione are measured in a nitrogen matrix at 8K temperature. The spectra reveal that in the matrix environment both the molecules exist exclusively in monohydroxy tautomeric forms with an intramolecular O–H$\cdots$O=C hydrogen bonding. In the case of 3-MeCD, the fundamental of OH stretching ν_{O--H} band appears more red-shifted with larger bandwidth indicating that the intramolecular O–H$\cdots$O hydrogen bond of this molecule is somewhat stronger compared to that of 1,2-CD. Electronic structure calculations at B3LYP/6-311++G** and MP2/cc-pVTZ levels predict that the monohydroxy tautomer of 1,2-CD is nearly 4.5 kcal/mol more stable than the corresponding diketo tautomer, but in the case of 3-MeCD, the stability difference between the diketo and preferred enol tautomer is more than 7.5 kcal/mol. Analysis of the geometric parameters reveals that the excess stabilization of the latter originates as a result of formation of an intramolecular O$\cdots$H–O$\cdots$H–C type interconnected hydrogen bonding network involving a methyl C-H bond, which interact in a cooperative fashion. The predicted infrared spectrum shows that the formation of such hydrogen bonding network causes large blue-shifting of the H-bonded methyl ν_{C--H} transition, and this spectral prediction matches well with the features displayed in the measured spectrum.

For intermolecular case, 1:1 complex between 1,2-cyclohexanedione and chloroform have been studied. Here two types of complex is possible, interconnected and bifurcated. In the interconnected complex a cooperative stabilizing effect and in the bifurcated complex an anti-cooperative destabilizing effect of the C–H$\cdots$O hydrogen bond on the intramolecular O–H$\cdots$O bond is observable. In the room temperature solution phase of FTIR spectra, the anti-cooperative complex is observable.

1 Introduction:

Cooperativity and anticooperativity are the property of interconnected hydrogen bonds (HBs)(Desiraju et al 1999; Scheiner 1997; Karpen 2002; Parra

2008). The effect refers to enhanced stabilization or destabilization of a system with two interconnected HBs compared to the sum of the energies of the systems with equivalent but isolated HBs. The excess stabilization in the first case originates as a result of mutual polarization of several covalent bonds, and classic examples are the HBs in water clusters (O–H$\cdots$O–H$\cdots$, types), where the stability as well as O–H stretching frequencies depend on cluster size $(H_2O)_n$ (Buck & Huisken 2000; Ohno et al 2005). In recent years, attention has been focused to investigating the cooperative effects in systems involving C–H groups as the HB donors (Wieczorek & Dannenberg 2003; Chen & Dannenberg 2006). Performing crystallographic analysis and electronic structure calculation, existence of cooperative stabilization in hydrogen bonds involving C-H groups have been inferred in such systems (Steiner et al 1997; Steiner 1996; Gatti et al 2002). However, the direct spectroscopic evidence of cooperativity, in terms of shifts of the donor C–H stretching vibrations is rather scarce (Blatchford et al 2002). In the present article we report the infrared spectroscopic signatures of cooperative and anti-cooperative interactions between a classical OH$\cdots$O and weak CH$\cdots$O HBs. In both cases, hydrogen bonds are interconnected intramolecularly or intermolecularly. The systems selected to demonstrate the effects are the monohydroxy tautomers of 3-MeCD and its parent molecule 1,2-CD and also with a 1:1 complex between 1,2-CD and chloroform.

2 Materials and Methods:

1,2-CD and 3-MeCD were procured from Aldrich and used as supplied. The sample vapor mixed with ultrahigh pure nitrogen was deposited on a cold KBr window in a vacuum chamber with a base pressure of 10^{-6} mbar. The KBr window was cooled to a temperature of 8K by a closed cycle helium refrigerator (ARS product, Displex). Care was taken to keep the guest-to-host ratio in the matrix low enough to avoid association. The FTIR spectra was recorded using a Bruker IFS66S Fourier transformed infrared spectrometer equipped with a deuterated triglycine sulphate (DTGS) detector and a KBr beam splitter with 1 cm^{-1} spectral resolution. The spectrometer compartment was constantly purged with dry N_2 to remove water vapor and CO_2.

For measurement in the solution phase, a home-made solution cell consisting of a pair of KBr windows and teflon spacers of varying (0.1-1 mm) thickness was used. The FTIR spectra were recorded in the mid-IR (400 – 4000 cm^{-1}) region at a resolution of 1 cm^{-1}.

The ground state geometries, normal mode vibrational frequencies and infrared intensities of the two molecules were calculated by B3LYP/6-311++G(d,p) and MP2/6-311++G(d,p) theoretical methods using Gaussian 03 program package (Frisch et al 2003). For MP2 calculation cc-pVTZ basis set was also used.

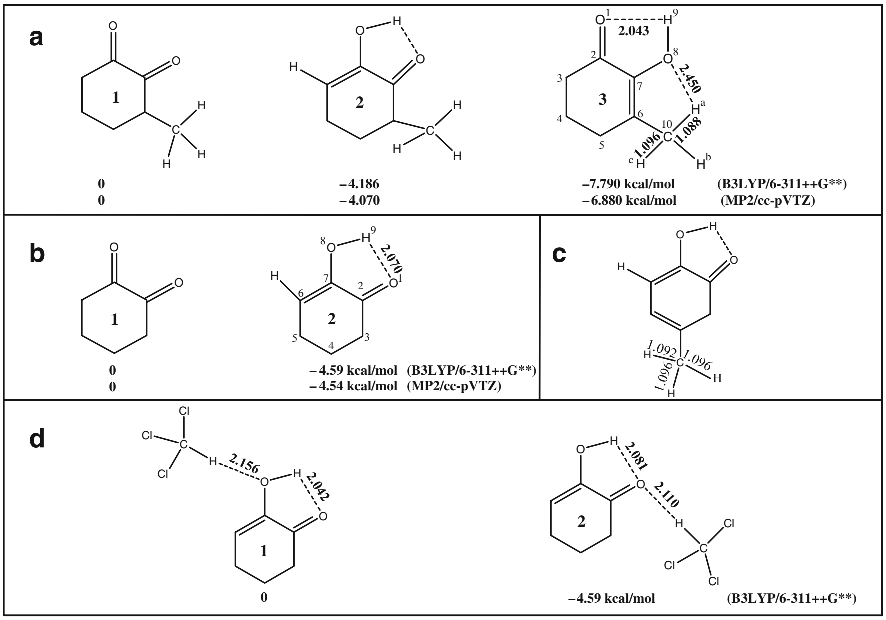

Fig. 1. Optimized structures of the (A) three tautomers of 3-MeCD, (B) two tautomers of 1,2-CD, (C) monohydroxy tautomer of 4-methylcyclohex-4-ene-1,2-dione (4-MeCED). (D) interconnected (1) and bifurcated (2) complexes between 1,2-CD and $CHCl_3$.

3 Results and discussion:

The optimized structures of the tautomers of 3-MeCD along with their relative energies and some important geometric parameters are shown in Figure 1. A doubly hydrogen bonded species A3, where the hydroxy group simultaneously acts as donor for the OH$\cdots$O HB and acceptor for CH$\cdots$O HB is predicted to be the most stable tautomer, and energetically it is favored over the diketo species (A1) by 7.8 kcal/mol. However, the other monohydroxy isomer (A2),

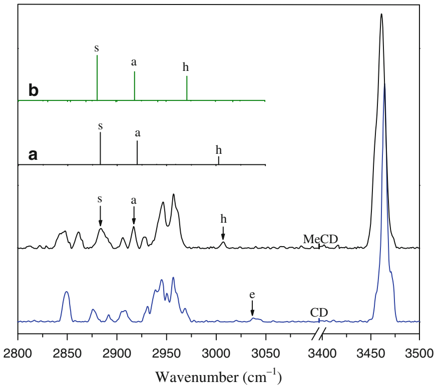

Fig. 2. The FTIR spectra in the C–H and O–H stretching fundamental regions (2800-3500) cm^{-1} of 3-MeCD and CD isolated in the N_2 matrix at 8 K. The bands denoted by inverted arrows correspond to the three ν_{C--H} transitions of the methyl group of 3-MeCD. The corresponding transitions of the calculated IR spectra of 3-MeCD and 4-MeCED are shown in the stick spectra a and b, respectively.

where the hydroxy group is only a donor to the carbonyl oxygen, is much less favoured, and energetically it is similar to the hydroxy tautomer of 1,2-CD (part B of Figure 1). In fact, from the energetic view point, the species A2 apparently displays a kind of anti-cooperative behavior.

The FTIR spectra of the two molecules in the spectral regions of C–H and O–H stretching fundamentals (ν_{C--H} and ν_{O--H}), measured in a N_2 matrix at 8 K temperature, are displayed in Figure 2. Although the overall appearance of the two spectra is similar, but the transitions arising due to specific structural features of the two molecules are vividly displayed. Thus, the most intense bands in the two spectra near 3460 cm^{-1} can be corresponded with the ν_{O--H} transitions of the hydroxy tautomers of the two molecules. These transitions are red-shifted due to intramolecular O–H$\cdots$O=C H-bonding with the α-keto groups (Figure 1). However, the red shift of the band of 3-MeCD is 6 cm^{-1} larger than that of CD, and more importantly the spectral bandwidth of the former is more than twice larger compared to the latter. These spectral features are indications that the OH$\cdots$O HB in the former molecule is relatively stronger. Consistent with these observations, the calculation at B3LYP/6-311++G** level predicts that the $O^1\cdots H^9$ HB distance of A3 tautomer (2.043 $\mathring{A}$)

is optimized significantly shorter compared to that of the hydroxy tautomer of 1,2-CD (2.07 $\AA$), and the ν_{O--H} transition of the former is 8 cm^{-1} more red-shifted than that of latter. The spectral manifestations of the said CH$\cdots$O hydrogen bonding involving one of the three C-H bonds of the methyl group of A3 tautomer, and the resulting cooperative interactions between the two HBs are described in the following paragraphs.

The three bands labeled a, s and h in the spectrum of 3-MeCD, which are absent in the lower panel (1,2-CD), are assigned to the three C–H stretching fundamentals of the methyl group, and the corresponding transitions in the calculated IR spectrum (by B3LYP/6-311++G** method) of A3 tautomer are displayed in Figure 2 as stick plot (A). It is apparent that the agreement between the prediction and suggested assignments of the bands in the measured spectrum is excellent. The bands labeled h (3007 cm^{-1} in the measured spectrum and 3002 cm^{-1} in the calculated spectrum) represent the ν_{C--H} transition of the H-bonded C^{10}–H^{a} bond) methyl group. The bands denoted by s (2884 cm^{-1}) and a (2917 cm^{-1}) correspond to the symmetric and antisymmetric stretching combinations of the two free C–H bonds (C^{10}–H^{b} and C^{10}–H^{c}) of the methyl group, respectively. Below, we provide justifications in support of these assignments.

In the absence of any perturbation, the two antisymmetric stretching modes of the $-CH_3$ group are degenerate (Bernath 1995). However, in the case of A3 tautomer, the said degeneracy is lifted because of the following two reasons: First, because of the C–H$\cdots$O intramolecular H-bonding between a methyl hydrogen (H^{a}) and hydroxy group, and secondly, as a result of electronic conjugation of the C^{10}–H^{b} and C^{10}–H^{c} bonds with the pi-bond network (Creamer et al 1974). The latter factor should cause reduction of ν_{C--H} frequency and increase in the C–H bond length. To assess the effect of this factor, we optimized the geometry and calculated the infrared spectrum of the monohydroxy tautomer of 4-MeCED (Figure 1C). In this system, the C–H$\cdots$O intramolecular H-bonding is not possible but the pi-conjugation remains intact. Because of the latter factor, the C^{10}–H^{b} and C^{10}–H^{c} bond lengths of the methyl group in the optimized geometry are predicted (1.096 $\AA$) longer than the C^{10}–H^{a} bond (1.0915 $\AA$). The IR active methyl ν_{C--H} transitions of this molecule are depicted in stick plot B (Figure 2), and it is seen that the frequencies for s and a transitions are practically same as those of A3 tautomer (Figure 2 plot A), but the frequency of the h band is 31 cm^{-1} smaller. We propose that the major contribution to this vital difference is due to C–H$\cdots$O hydrogen bonding in the A3 tautomer, that causes blue shifting of the ν_{C--H} transition. This spectral blue-shifting is consistent with further shortening of the length of C^{10}–H^{a} bond (1.088 $\AA$) compared to that in case of 4-MeCED (1.092 $\AA$) (Hozba & Havlas 2000; Kar & Scheiner 2004). The lengths of the two free C–H bonds C^{10}–H^{b} and C^{10}–H^{c} of the two molecules are same (1.096 $\AA$), which indicate similar contribution of the hyperconjugation interaction of the methyl group of the two molecules.

Figure 3 shows the variation of the energy of A3 tautomer and the $O^1 \cdots H^9$ HB distance as a function of internal rotation of the methyl group. As the $\angle C^7–C^6–C^{10}–H^a$ dihedral angle deviates from planarity, the $C^{10}H^a \cdots O^8$ HB, is weakened and the response is reflected at the $O^1 \cdots H^9–O^8$ HB, the overall stability of the system is decreased with concomitant lengthening of this HB. These changes clearly display the correlation between the two HBs, and in the measured spectra, the correlation is displayed as larger spectral shift and broader bandwidth of the ν_{O--H} band of 3-MeCD compared to that of CD. Further theoretical studies are highly desirable for detailed electronic structures and in understanding the origin of the cooperative stabilization of the A3 tautomer.

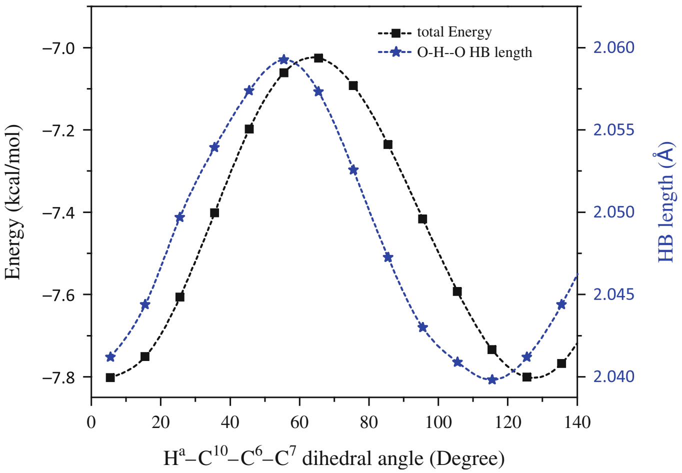

Fig. 3. Variation of the energy of the A3 tautomer of 3-MeCD and its $O^1 \cdots H^9$ HB distance as a function of internal rotation of the methyl group

4 Intermolecular complex with chloroform:

Two types of intermolecular complex are possible between 1,2-CD and chloroform. Interconnected, where the chloroform C-H is hydrogen bonded with enolic oxygen of 1,2-CD (C–H···O type), and bifurcated, when C-H of chloroform forms the hydrogen bond with the keto oxygen. Theoretical calculation predicts that the bifurcated complex is 0.66 kcal/mol more stable than the interconnected one. The optimized geometries along with some important geometrical parameters of both complexes are shown in Figure 1. For interconnected complex the O–H···O hydrogen bond length is shortened further by $\sim 0.03\AA$ upon complexation with chloroform, while for the bifurcated one a reverse effect is predicted, the H-bond length increased by $\sim 0.01\AA$ on complexation. These structural data indicate that there is a cooperative effect of the C–H···O H bond on the O–H···O H bond in case of the interconnected complex, but the bifurcated one acts anti-cooperatively.

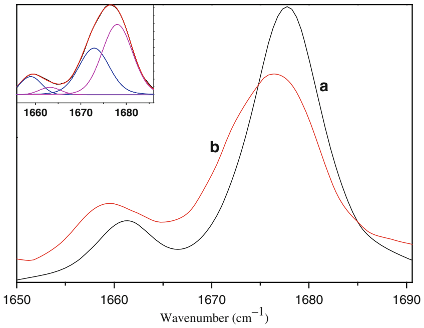

Fig. 4. The FTIR spectra in the C=O stretching fundamental regions of 1,2-CD (a) and 1,2-CD-CHCl$_3$ complex (b) in CCl$_4$ solution. The inset displays the fitted curve for the complex.

The FTIR spectra of 1:1 complex between 1,2-CD and chloroform in CCl$_4$ solution is displayed in Figure 4. It clearly shows that on addition of chloroform to the sample solution, the $\nu_{C=O}$ peak is broadened and is also to some extent redshifted. A spectral fitting operation by OPUS 6.5 program package reveals that there are four bands in the $\nu_{C=O}$ region at 1678, 1673, 1661, 1652 cm^{-1}. The monomer of 1,2-CD shows two bands at 1678 and 1661 cm^{-1}, and two new bands develop at 1673 and 1652 cm^{-1} on addition of chloroform solution. With the aid of calculated frequencies (by B3LYP/6-311++G(d,p) method), we assign the 1673 and 1652 cm^{-1} bands to $\nu_{C=O}$ of the bifurcated complex. The assignment implies that at room temperature the bifurcated complex is stable in CCl_4 solution. Further evidence in support of the assignment is displayed in ν_{O--O} region of the spectrum. The calculation predicts a blue shift of 16 cm^{-1} and red shift od 28 cm^{-1} of ν_{O--O} transition for the bifurcated and interconnected complexes respectively.

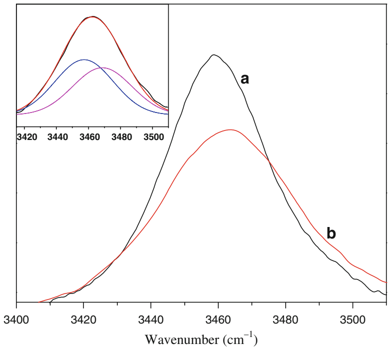

Fig. 5. FTIR spectra in the O—H stretching fundamental regions of 1,2-CD (a) and 1,2-CD-$CHCl_3$ complex (b) in CCl_4 solution. The inset displays the fitted curve for the complex.

In the presence of $CHCl_3$, the measured spectrum (Figure 5) shows two bands at 3453 cm^{-1} and 3471 cm^{-1}. The former is assigned to ν_{O--O} of CD monomer and the latter which is 18 cm^{-1} blue shifted, to the bifurcated complex. Further experiment in the low temperature matrix environment is in progress to verify the suggested assignment.

5 Conclusion:

The spectra and structures of the intramolecular hydrogen bonded tautomers of 1,2-CD and 3-MeCD are investigated by matrix isolation infrared spectroscopy and quantum chemical calculations. From the measured spectral data and predictions of theoretical calculation, we conclude that the intramolecular O–H···O hydrogen bond of the methyl substituted molecule is stabilized further by cooperative interaction of an interconnected C–H···O hydrogen bond involving the methyl group. However, in the case of 1:1 complex of CD with $CHCl_3$ in a CCl_4 solution, the bifurcated hydrogen bonded complex appears more stable.

Acknowledgement. TC thanks Department of Science and Technology, Govt. of India for research grants under Ramanna Fellowship Scheme.

References

Bernath P. F. *Spectra of Atoms and Molecules*; Oxford University Press: New York, 1995.

Blatchford, M. A.; Raveendran, P.; Wallen S. L., J. Am. Chem. Soc., **124**, 14818 (2002).

Buck, U.; Huisken, F., Chem. Rev. **100**, 3863 (2000).

Chen, Y.; Dannenberg, J. J., J. Am. Chem. Soc., **128**, 8100 (2006).

Creamer, D.; Binkley. J. S.; Pople, J. A.; Hehre, W. J., J. Am. Chem. Soc. **96**, 6900 (1974)

Desiraju, G.R.; Steiner, T. *The Weak Hydrogen Bond:* Oxford University Press: Oxford, 1999.

Frisch, M. J.; et al. GAUSSIAN 03, Gaussian, Inc., Pittsburgh, PA, 2003.

Gatti, C.; May, E.; Destro, R.; Cargnoni, F., J. Phys. Chem. A, **106**, 2707 (2002).

Hobza, P.; Havlas, Z., Chem. Rev., **100**, 4253 (2000).

Kar, T.; Scheiner, S., J. Phys. Chem. A, **108**, 9161 (2004).

Karpfen, A., Adv. Chem. Phys., **123**, 469 (2002).

Ohno, K., Okimura, M., Akai, N.m Katsumoto, Y., Phys. Chem. Chem. Phys., 7, 3005 (2005).

Parra, R. D.; Ohlssen, J., J. Phys. Chem. A, **112**, 3492 (2008).

Scheiner, S. *Hydrogen Bonding: A Theoretical Perspective*; Oxford University Press: New York, 1997.

Steiner, T., Cryst. Rev. **6**, 1 (1996).

Steiner, T.; Lutz, B.; van der Mass, J.; Veldman, N.; Schreurs, A. M. M.; Kroon, J.; Kanters, J. A. Chem. Commun., 191 (1997).

Wieczorek, R.; Dannenberg, J. J., J. Am. Chem. Soc., **125**, 8124 (2003).

"Recent Advances in Spectroscopy:
Theoretical, Astrophysical, and Experimental Perspectives"
Eds. Chaudhuri R K, Mekkaden M V, Raveendran A V, Satya Narayanan A
Astrophysics and Space Science Proceedings, Springer-Verlag, Berlin, 2010.

The Single Surface Beyond Born-Oppenheimer Equation for the Excited States of Sodium Trimer

Amit Kumar Paul[1], Biplab Sarkar[2], and Satrajit Adhikari[1]

[1] Department of Physical Chemistry and Raman Center for Atom, Molecule and Optical Sciences, Indian Association for the Cultivation of Science, Jadavpur, Kolkata - 700032, INDIA `pcsa@iacs.res.in`

[2] Department of Chemistry, North-Eastern Hill University, Shillong - 793 022, INDIA `s.biplab@gmail.com`

Summary. We consider a three state diabatic potential matrix to represent the excited states of Na_3 cluster [J. Chem. Phys, **88**, 6068 (1988)] at the pseudo - Jahn - Teller model situation, and analytically calculate the non - adiabatic coupling (NAC) elements and their Curls to explore the nature of the beyond Born - Oppenheimer effect on the adiabatic single surface equation. When the energy gap between the third state ($1^2A_1'/2^2A_1'$) and the doubly degenerate states ($2^2E'/3^2E'$) of the model Hamiltonian for Na_3 cluster is considered to be identically zero, i.e., accidental degeneracy, the Curl for each NAC element clearly vanishes leading to a theoretically valid Extended Born - Oppenheimer (EBO) equation. We calculate the non - adiabatic effects on the photoabsorption spectrum for the ground electronic state by using EBO equation and demonstrate it's validity by comparing with the corresponding diabatic spectrum (locating the initial wavefunction on the same state), when the three states are degenerate at a point. Finally, we calculate the vibrational eigenspectrum of the ground adiabatic state by employing theoretically and numerically valid EBO equation and demonstrate substantial difference from those eigenspectrum obtained within BO approximation.

1 Introduction

For a quite longer period, the presence of singularity in non-adiabatic coupling (NAC) terms had been overlooked until Longuet-Higgins (Longuet - Higgins 1961, 1975) demonstrated that such singularity destroys the single-valuedness of electronic wavefunction in many molecular systems and therefore, it is not worth to pursue dynamical calculations for the nuclei on the multi - valued diabatic potential energy surfaces (PES). Herzberg & Longuet - Higgins (1963) (HLH) corrected this deficiency by multiplying a complex phase factor, known as Longuet - Higgins' phase, leading to a single valued wavefunction.

This ‘modification’ of the electronic eigenfunctions is not an outcome of any first principle based theory but imposed in an *ad hoc* manner. In an alternative way, Mead & Truhlar (1979) introduced a vector potential in the nuclear Hamiltonian to generalize the Born - Oppenheimer (BO) (Born & Oppenheimer 1927) equation, which is a reminiscent of the complex phase factor treatment of Herzberg and Longuet - Higgins. With these theoretical predictions, Mead (1980), Lepetit & Kuppermann (1993); Kuppermann & Wu (1993), Kendrick (2000, 2003), and Juanes-Marcos & Althorpe (2003) calculated the integral and differential scattering cross sections of H_3 isotopic system. The calculations by Kendrick with vector potential approach and by the phase factor treatment of Althorpe *et al.* demonstrated the effect of geometric phase (GP) on the differential cross section (DCS) of the same reaction only at high total energies (>1.8 eV). Adhikari & Billing (1999) evaluated the transition probabilities of a two arrangement channel Jahn - Teller model (Baer et. al. 1996) both by employing vector potential approach and phase factor treatment. All these calculations demand to explore the origin of GP from first principle.

Baer et. al. (1996); Baer (1985); Baer & Englman (1996); Baer (1997) carried out the first principle based BO treatment of two coupled electronic states as sub - Hilbert space and derived a set of two coupled equations by taking into account the effects of NAC terms into the diagonal to formulate the single surface Extended Born - Oppenheimer (EBO) equations. In an alternative approach, Varandas & Xu (2000) performed the first principle based BO treatment of two state adiabatic nuclear Schrödinger equation (SE) by recasting the NAC elements in terms of electronic basis functions angle (ADT angle) (Baer 1975) and formulated the single surface EBO equation. On the other hand, Baer et. al. (2000) and Adhikari et. al. (2000) had persuaded the BO treatment for any N ($\geq$ 3) state coupled BO system in the adiabatic representation of nuclear SE to formulate EBO equation, which has some limitations on the adiabatic Hamiltonian and does not have the scope to demonstrate these aspects: (a) how the Curl conditions are being satisfied - a necessity to pursue adiabatic - diabatic transformation; (b) how the Curls could be, if at all, zeros at and around CI(s) - a necessary condition to formulate EBO equation. Indeed, Sarkar & Adhikari (2006, 2007, 2008, 2009) generalized the BO treatment of any three/four coupled electronic states with a detailed analysis of Curl conditions before the formulation of EBO equations in terms of electronic basis functions/ADT angles.

When a set of three states are strongly coupled with each other and show negligibly weak interaction with other states of the Hilbert space, these states form a sub - Hilbert space leading to the existence of quasi diabatic Hamiltonian. Since the diabatic to adiabatic representation of the Hamiltonian are related through an unitary transformation condition ($\nabla \mathbf{A} + \tau \mathbf{A} = 0$), it could be quite interesting to explore the nature of the non - adiabatic coupling terms starting from a well accepted diabatic Hamiltonian to describe the non - Born - Oppenheimer effects. Since our theoretical development is based on the consideration of a sub - Hilbert space and the diabatic Hamiltonian represents a sub - space by it's very nature, we analytically calculate the NAC terms and their Curls, and find the condition for the existense of an EBO equation. In this article, we present the details of the formulation of EBO equation and it workability, when the three states are accidentally degenerate at a point.

2 Jahn - Teller distortions in presence of accidental degeneracy: The Hamiltonian for the excited states of Na_3 cluster

Jahn - Teller (JT) theorem tells that a doubly degenerate electronic state ($\phi^{\pm}$), in some highly symmetric geometry, can split and lower it's energy by distorting the geometry to lower symmetry. The JT theory is usually applied to the distortions in symmetry degenerate states (E' and E''), but the same treatment can be extended to include the presence of a third non - degenerate state (ϕ^0), which is nearby in energy. Cocchini et. al. (1988) have shown that some of the excited states of Na_3 exhibit three states ($\phi^{\pm}$ and ϕ^0) interactions, namely, between $1^2A_1'$ and $2^2E'$ as well as $2^2A_1'$ and $3^2E'$ states. For an equilateral triangular geometry, the normal modes are defined as bending Q_x, antisymmetric stretching Q_y and symmetric stretching Q_s. When the coupling to the symmetric coordinate Q_s is ignored and the electronic Hamiltonian is expanded in terms of the active modes (complex linear combination of Q_x and Q_y, where $Q^+ = Q_x + iQ_y = \rho e^{i\phi}$ and $Q^- = Q_x - iQ_y = \rho e^{-i\phi}$) considering small distortion from the equilateral triangular geometry (D_{3h}), the system presumably includes *all the nuclear configurations* leading to the following general form of the diabatic Hamiltonian matrix (3×3) for the electron - nuclear BO system:

$$\hat{\mathbf{H}}(\rho,\phi) = \hat{\mathbf{T}}_{\mathbf{N}} \cdot \mathbf{1} + \hat{\mathbf{H}}_{\mathbf{e}}(\rho,\phi), \qquad \hat{\mathbf{T}}_{\mathbf{N}} = -\frac{\hbar^2}{2\mu}\Big(\frac{1}{\rho}\frac{\partial}{\partial\rho}\rho\frac{\partial}{\partial\rho} + \frac{1}{\rho^2}\frac{\partial^2}{\partial\phi^2}\Big),$$

$$\hat{\mathbf{H}}_{\mathbf{e}}(\rho,\phi) = \begin{pmatrix} \frac{\rho^2}{2} + U_2 & U_1 & W_1 - W_2 \\ U_1 & \frac{\rho^2}{2} - U_2 & W_1 + W_2 \\ W_1 - W_2 & W_1 + W_2 & \epsilon_0 + \frac{d\rho^2}{2} \end{pmatrix}, \tag{1}$$

with

$$\begin{aligned} U_1 &= K\rho\cos\phi + \frac{1}{2}g\rho^2\cos(2\phi), \\ U_2 &= K\rho\sin\phi - \frac{1}{2}g\rho^2\sin(2\phi), \end{aligned}$$

where K and g are taken as the characteristic coupling parameters. $\frac{1}{2}\rho^2$ and $\epsilon_0 + \dfrac{1}{2}d\rho^2$ are the energies for the E - and A - type states, respectively, while U_i and W_i $(i = 1, 2)$ are the interaction potentials among those states. The potentials, W_i's, are of the same form as the U_i's but defined in terms of a different set of coupling parameters P and f, which replace K and g, respectively. If K and g are zero, the model mimics the pseudo - Jahn -Teller situation, where the eigenvalues of the matrix appear as:

$$u_1(\rho,\phi) = \frac{1}{2}\Big(\epsilon_0 + \frac{d\rho^2}{2} + \frac{\rho^2}{2}\Big) - \sqrt{\Delta^2 + 2w}, \tag{2}$$

$$u_2(\rho,\phi) = \frac{\rho^2}{2}, \tag{3}$$

$$u_3(\rho,\phi) = \frac{1}{2}\Big(\epsilon_0 + \frac{d\rho^2}{2} + \frac{\rho^2}{2}\Big) + \sqrt{\Delta^2 + 2w}, \tag{4}$$

with $\Delta = \frac{1}{2}\Big(\epsilon_0 + \frac{d\rho^2}{2} - \frac{\rho^2}{2}\Big)$, $w = W_1^2 + W_2^2 = P^2\rho^2 + \frac{1}{4}f^2\rho^4 + Pf\rho^3\cos(3\phi)$ and the columns of the following matrix are the three electronic basis functions:

$$\mathbf{A} = \begin{pmatrix} -\dfrac{(W_1+W_2)}{\sqrt{2w}} & \dfrac{(W_1-W_2)}{\sqrt{2w + \{\Delta - \sqrt{\Delta^2+2w}\}^2}} & \dfrac{(W_1-W_2)}{\sqrt{2w + \{\Delta + \sqrt{\Delta^2+2w}\}^2}} \\ \dfrac{(W_1-W_2)}{\sqrt{2w}} & \dfrac{(W_1+W_2)}{\sqrt{2w + \{\Delta - \sqrt{\Delta^2+2w}\}^2}} & \dfrac{(W_1+W_2)}{\sqrt{2w + \{\Delta + \sqrt{\Delta^2+2w}\}^2}} \\ 0 & \dfrac{\Delta - \sqrt{\Delta^2+2w}}{\sqrt{2w + \{\Delta - \sqrt{\Delta^2+2w}\}^2}} & \dfrac{\Delta + \sqrt{\Delta^2+2w}}{\sqrt{2w + \{\Delta + \sqrt{\Delta^2+2w}\}^2}} \end{pmatrix} \tag{5}$$

The relations, $K = \sqrt{2}P$ and $g = \sqrt{2}f$, have been introduced (Cocchini et. al. 1988) to define the values of P and f, respectively. In the following sections, all analytical derivations and numerical calculations have been carried out with the assumption, $d = 1$, i.e., $\Delta = \epsilon_0/2$.

3 The derivation of the EBO equation from a three state diabatic SE constituted with the excited states of Na$_3$ cluster

When the parameters K and g are zero, the model Hamiltonian (Eq. (1)) mimics the pseudo - Jahn - Teller situation and the diabatic SE in terms of polar coordinates is given by:

$$
\begin{aligned}
&- \frac{\hbar^2}{2m} \begin{pmatrix} \frac{1}{\rho}\frac{\partial}{\partial\rho}\left(\rho\frac{\partial}{\partial\rho}\right) & 0 & 0 \\ 0 & \frac{1}{\rho}\frac{\partial}{\partial\rho}\left(\rho\frac{\partial}{\partial\rho}\right) & 0 \\ 0 & 0 & \frac{1}{\rho}\frac{\partial}{\partial\rho}\left(\rho\frac{\partial}{\partial\rho}\right) \end{pmatrix} \begin{pmatrix} \chi_1 \\ \chi_2 \\ \chi_3 \end{pmatrix} \\
&- \frac{\hbar^2}{2m}\frac{1}{\rho^2} \begin{pmatrix} \frac{\partial}{\partial\phi} & 0 & 0 \\ 0 & \frac{\partial}{\partial\phi} & 0 \\ 0 & 0 & \frac{\partial}{\partial\phi} \end{pmatrix}^2 \begin{pmatrix} \chi_1 \\ \chi_2 \\ \chi_3 \end{pmatrix} \\
&+ \begin{pmatrix} \frac{\rho^2}{2} - E & 0 & W_1 - W_2 \\ 0 & \frac{\rho^2}{2} - E & W_1 + W_2 \\ W_1 - W_2 & W_1 + W_2 & \epsilon_0 + \frac{d\rho^2}{2} - E \end{pmatrix} \begin{pmatrix} \chi_1 \\ \chi_2 \\ \chi_3 \end{pmatrix} = 0, \qquad (6)
\end{aligned}
$$

where

$$
\begin{aligned}
W_1 &= P\rho\cos\phi + \frac{1}{2}f\rho^2\cos(2\phi), \\
W_2 &= P\rho\sin\phi - \frac{1}{2}f\rho^2\sin(2\phi).
\end{aligned}
$$

This equation can be transformed ($\chi = \mathbf{A}\psi$) to the following form of adiabatic representation:

$$
\begin{aligned}
&- \frac{\hbar^2}{2m} \begin{pmatrix} \frac{\partial}{\partial\rho} & \tau_{12}^{\rho} & \tau_{13}^{\rho} \\ \tau_{21}^{\rho} & \frac{\partial}{\partial\rho} & \tau_{23}^{\rho} \\ \tau_{31}^{\rho} & \tau_{32}^{\rho} & \frac{\partial}{\partial\rho} \end{pmatrix}^2 \begin{pmatrix} \psi_1 \\ \psi_2 \\ \psi_3 \end{pmatrix} \\
&- \frac{\hbar^2}{2m}\frac{1}{\rho} \begin{pmatrix} \frac{\partial}{\partial\rho} & \tau_{12}^{\rho} & \tau_{13}^{\rho} \\ \tau_{21}^{\rho} & \frac{\partial}{\partial\rho} & \tau_{23}^{\rho} \\ \tau_{31}^{\rho} & \tau_{32}^{\rho} & \frac{\partial}{\partial\rho} \end{pmatrix} \begin{pmatrix} \psi_1 \\ \psi_2 \\ \psi_3 \end{pmatrix} - \frac{\hbar^2}{2m}\frac{1}{\rho^2} \begin{pmatrix} \frac{\partial}{\partial\phi} & \tau_{12}^{\phi} & \tau_{13}^{\phi} \\ \tau_{21}^{\phi} & \frac{\partial}{\partial\phi} & \tau_{23}^{\phi} \\ \tau_{31}^{\phi} & \tau_{32}^{\phi} & \frac{\partial}{\partial\phi} \end{pmatrix}^2 \begin{pmatrix} \psi_1 \\ \psi_2 \\ \psi_3 \end{pmatrix} \\
&+ \begin{pmatrix} u_1(\rho,\phi) - E & 0 & 0 \\ 0 & u_2(\rho,\phi) - E & 0 \\ 0 & 0 & u_3(\rho,\phi) - E \end{pmatrix} \begin{pmatrix} \psi_1 \\ \psi_2 \\ \psi_3 \end{pmatrix} = 0, \qquad (7)
\end{aligned}
$$

where the forms of $u_1(\rho,\phi)$, $u_2(\rho,\phi)$ and $u_3(\rho,\phi)$ are defined in Eq. (2), (3) and (4).

If we assume the gap between E - and A - type states is zero (ϵ_0=0), the ρ and ϕ components of NAC matrix elements appear as:

$$\tau_{12}^{\rho} = \tau_{13}^{\rho} = -\frac{Pf\rho^2 \sin(3\phi)}{2\sqrt{2}w}, \tag{8}$$

$$\tau_{12}^{\rho} = \tau_{13}^{\phi} = \frac{[2P^2\rho^2 - f^2\rho^4 - Pf\rho^3\cos(3\phi)]}{2\sqrt{2}w}, \tag{9}$$

$$\tau_{23}^{\rho} = \tau_{23}^{\phi} = 0, \tag{10}$$

where the component (ρ and ϕ) matrices commute with each other, i.e., both the matrices can be diagonalized by a matrix ($\mathbf{G}$) as given below:

$$\mathbf{G} = \begin{pmatrix} 0 & \frac{-i}{\sqrt{2}} & \frac{i}{\sqrt{2}} \\ -\frac{1}{\sqrt{2}} & \frac{1}{2} & \frac{1}{2} \\ \frac{1}{\sqrt{2}} & \frac{1}{2} & \frac{1}{2} \end{pmatrix}. \tag{11}$$

Therefore, the Eq. (7) can be transformed ($\psi = \mathbf{G}\phi$) as:

$$\begin{aligned}
&-\frac{\hbar^2}{2m}\begin{pmatrix} \left(\frac{\partial}{\partial\rho} + i\omega_\rho\right)^2 & 0 & 0 \\ 0 & \frac{\partial^2}{\partial\rho^2} & 0 \\ 0 & 0 & \left(\frac{\partial}{\partial\rho} - i\omega_\rho\right)^2 \end{pmatrix}\begin{pmatrix}\phi_1\\ \phi_2\\ \phi_3\end{pmatrix} \\
&-\frac{\hbar^2}{2m}\frac{1}{\rho}\begin{pmatrix} \frac{\partial}{\partial\rho} + i\omega_\rho & 0 & 0 \\ 0 & \frac{\partial}{\partial\rho} & 0 \\ 0 & 0 & \frac{\partial}{\partial\rho} - i\omega_\rho \end{pmatrix}\begin{pmatrix}\phi_1\\ \phi_2\\ \phi_3\end{pmatrix} \\
&-\frac{\hbar^2}{2m}\frac{1}{\rho^2}\begin{pmatrix} \left(\frac{\partial}{\partial\phi} + i\omega_\phi\right)^2 & 0 & 0 \\ 0 & \frac{\partial^2}{\partial\phi^2} & 0 \\ 0 & 0 & \left(\frac{\partial}{\partial\phi} - i\omega_\phi\right)^2 \end{pmatrix}\begin{pmatrix}\phi_1\\ \phi_2\\ \phi_3\end{pmatrix} \\
&+\begin{pmatrix} \frac{1}{2}(u_2+u_3)-E & \frac{1}{2\sqrt{2}}(-u_2+u_3) & \frac{1}{2\sqrt{2}}(-u_2+u_3) \\ \frac{1}{2\sqrt{2}}(-u_2+u_3) & \frac{1}{4}(2u_1+u_2+u_3)-E & \frac{1}{4}(-2u_1+u_2+u_3) \\ \frac{1}{2\sqrt{2}}(-u_2+u_3) & \frac{1}{4}(-2u_1+u_2+u_3) & \frac{1}{4}(2u_1+u_2+u_3)-E \end{pmatrix}\begin{pmatrix}\phi_1\\ \phi_2\\ \phi_3\end{pmatrix} = 0,
\end{aligned} \tag{12}$$

i.e.,

$$\mathbf{V} = \mathbf{G}^{\dagger}\mathbf{U}\mathbf{G} = \begin{pmatrix} \frac{1}{2}(u_2+u_3) & \frac{1}{2\sqrt{2}}(-u_2+u_3) & \frac{1}{2\sqrt{2}}(-u_2+u_3) \\ \frac{1}{2\sqrt{2}}(-u_2+u_3) & \frac{1}{4}(2u_1+u_2+u_3) & \frac{1}{4}(-2u_1+u_2+u_3) \\ \frac{1}{2\sqrt{2}}(-u_2+u_3) & \frac{1}{4}(-2u_1+u_2+u_3) & \frac{1}{4}(2u_1+u_2+u_3) \end{pmatrix}, \tag{13}$$

with $\boldsymbol{\omega}_\rho = \dfrac{Pf\rho^2\sin(3\phi)}{2w}$ and $\boldsymbol{\omega}_\phi = \dfrac{2P^2\rho^2 - f^2\rho^4 - Pf\rho^3\cos(3\phi)}{2w}$.

If the so called BO approximation is imposed considering the dynamics only occurring at enough low energies on the ground state, the upper electronic states become classically closed ($|\psi_1| >> |\psi_i|, i = 2, 3$) and such approximation on Eq. (12) brings the approximate EBO equation Eq. (14) for the ground state. On the other hand, since the conical intersection predominantly affects the nuclear wavefunction only in and around its' origin, the approximate EBOs equation (Eq. (14)) can be obtained by incorporating the degeneracy of the adiabatic PESs, namely, $u_1 \simeq u_2 \simeq u_3$ in and around the same region (CI).

$$\begin{aligned} &-\frac{\hbar^2}{2m}\left\{\left(\frac{\partial}{\partial\rho} + i\omega_\rho\right)^2 + \frac{1}{\rho}\left(\frac{\partial}{\partial\rho} + i\omega_\rho\right) + \frac{1}{\rho^2}\left(\frac{\partial}{\partial\phi} + i\omega_\phi\right)^2\right\}\phi_1 \\ &+ (u_1 - E)\phi_1 = 0, \end{aligned} \tag{14a}$$

$$-\frac{\hbar^2}{2m}\left\{\frac{\partial^2}{\partial\rho^2} + \frac{1}{\rho}\frac{\partial}{\partial\rho} + \frac{1}{\rho^2}\frac{\partial^2}{\partial\phi^2}\right\}\phi_2 + (u_2 - E)\phi_2 = 0, \tag{14b}$$

$$\begin{aligned} &-\frac{\hbar^2}{2m}\left\{\left(\frac{\partial}{\partial\rho} - i\omega_\rho\right)^2 + \frac{1}{\rho}\left(\frac{\partial}{\partial\rho} - i\omega_\rho\right) + \frac{1}{\rho^2}\left(\frac{\partial}{\partial\phi} - i\omega_\phi\right)^2\right\}\phi_3 \\ &+ (u_3 - E)\phi_3 = 0. \end{aligned} \tag{14c}$$

Finally, we perform numerical calculations by using Eq. (14a) to obtain the vibrational frequencies and carried out dynamical calculation with the same equation (Eq. (14a)) to generate the corresponding diabatic spectrum for the ground state. All these calculations are performed on the pseudo - Jahn - Teller model situation with $P = 3.9103$ and $f = 0.10748$, where the coupling constants (P and f) are defined by the parameters, K and g as $K = \sqrt{2}P = 5.53$ and $g = \sqrt{2}f = 0.152$ (Cocchini et. al. 1988).

4 Results and Discussion

4.1 Photoabsorption Spectrum

We consider a Gaussian wavepacket (GWP) as the time - independent solution of the Hamiltonian ($\hat{\mathbf{H}}(\rho, \phi) = \hat{\mathbf{T}}_{\mathbf{N}} \cdot \mathbf{1} + \frac{1}{2}\rho^2$) and perform the adiabatic - diabatic transformation with the ADT matrix (Eq. (5)) to obtain diabatic wavefunctions with different initial position of the GWP in the column matrix. As an example, the diabatic wavefunction starting with the initial wavefunction located on the ground state is given by: $\boldsymbol{\psi}^{dia} = A\boldsymbol{\psi}^{adia}$, with $\boldsymbol{\psi}^{adia} = (\mathrm{GWP}, 0, 0)$. In the case of adiabatic calculations, namely, BO and EBO, the corresponding propagations are performed from ground state with the same GWP.

The nuclear wavefunction obtained by FFT - Lanczozs method is used to calculate the autocorrelation function ($C(t)$) and the Fourier transform of $C(t)$ gives the photoabsorption spectra,

$$I(\omega) \propto \omega \int_{-\infty}^{\infty} C(t) \exp(i\omega t) dt, \tag{15}$$

where

$$C(t) = \langle \Psi(t) | \Psi(0) \rangle, \tag{16}$$

$$= \langle \Psi^{\star}(\frac{t}{2}) | \Psi(\frac{t}{2}) \rangle. \tag{17}$$

Eq. (17) is more accurate, computationally faster and convenient to implement than the previous equation (Eq. (16)). On the other hand, Eq. (17) is valid only if the initial wavefunction is real and the Hamiltonian is symmetric.

Figures 1(a), (c) and (e) display the absolute values of the autocorrelation function, when the dynamics starts with the initial wavefunction located on the ground state, for the BO, Diabatic and EBO Hamiltonian with zero energy gap ($\Delta = 0$) between A- and E- type states. Fig. 1(a) shows that the system dynamics under BO Hamiltonian is much more correlated compared to the cases (c) and (e). It is quite interesting to note that the autocorrelation functions ($|C(t)|$) obtained from diabatic and EBO calculations (Figs. 1(c) and (e)) have closer agreement with each other. These features lead to peak by peak matching in their corresponding spectrum (Figs. 1(d) and (f)), whereas the spectrum (Fig. 1(b)) arising due to BO calculation is mismatching by many peaks with the corresponding EBO and Diabatic spectrum (Figs. 1(d) and (f)).

4.2 Vibrational Spectrum

When the energy difference (Δ) between the A- and E- type states of the pseudo - Jahn - Teller model for the Na_3 cluster is considered to be zero, the

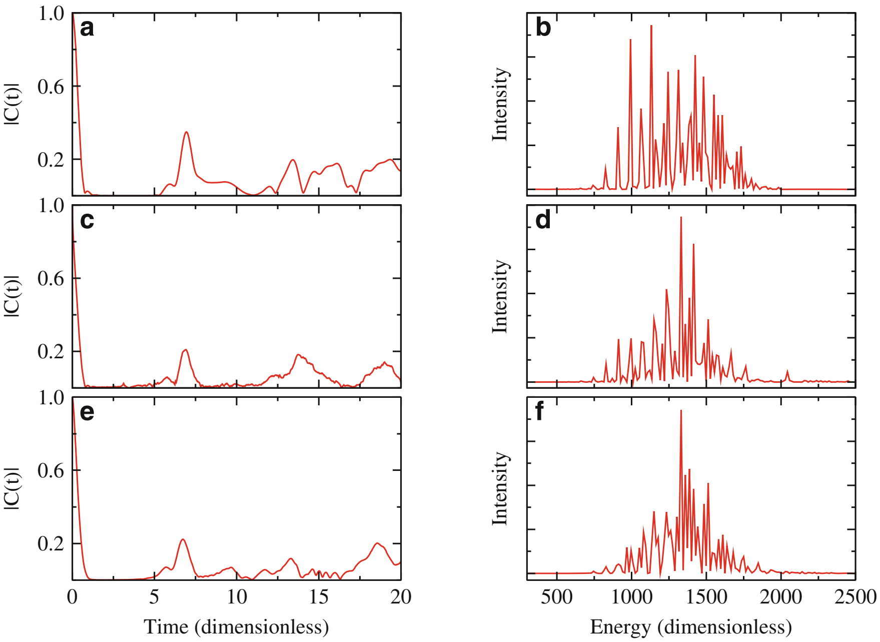

Fig. 1. The autocorrelation functions calculated by using (a) Born - Oppenheimer, (c) Diabatic and (e) Extended Born - Oppenheimer Hamiltonian with zero ($\varDelta = 0$) energy gap between A- and E- type states starting with the initial wavefunction located on the ground state, whereas figures (b), (d), (f) display the corresponding photoabsorption spectra.

Curl of the NAC terms appears identically zero and provides a theoretically valid EBO equation in and around the conical intersection point among the electronic states. We have calculated the contribution of ground state on the photoabsorption spectrum either by using diabatic Hamiltonian or by invoking EBO equation (see Fig. 1). The agreement of our EBO results with accurate diabatic ones at $\varDelta = 0$ clearly demonstrates the numerical validity of EBO equation (see Fig. 1) and thereby, the formulated EBO equation at $\varDelta = 0$ is expected to provide accurate vibrational frequencies (see Table I) for the ground state at least upto the energy sufficiently lower than the excited electronic states. Table I shows that some of the vibrational frequencies calculated (Puzari et. al. 2004) by using BO Hamiltonian differ substantially from the corresponding frequencies obtained from EBO Hamiltonian and demonstrates the effect of upper electronic state on the ground through non - adiabatic process.

Table 1. The theoretically calculated vibrational frequencies (in cm^{-1}) for the ground adiabatic surface within BO and EBO approximation ($P = 3.9103$ and $f = 0.10748$).

$\nu_i^{BO} - \nu_0$	$\nu_i^{EBO} - \nu_0$	$\nu_i^{EBO} - \nu_i^{BO}$	$\nu_i^{BO} - \nu_0$	$\nu_i^{EBO} - \nu_0$	$\nu_i^{EBO} - \nu_i^{BO}$
70.770	70.771	0.0005	429.341	434.137	4.7964
82.749	82.748	-0.0003	441.298	446.639	5.3414
141.041	141.042	0.0013	446.639	454.427	7.7881
151.240	151.239	-0.0001	454.425	456.590	2.1646
165.387	165.386	-0.0008	467.115	467.921	0.8058
210.691	210.693	0.0028	483.832	483.902	0.0701
218.798	218.795	-0.0034	487.010	490.121	3.1108
231.363	231.359	-0.0036	492.134	493.688	1.5541
247.851	247.849	-0.0010	493.691	495.426	1.7356
279.428	279.451	0.0229	509.827	502.266	-7.5611
284.978	284.975	-0.0032	514.828	513.718	-1.1094
285.022	285.061	0.0398	518.138	514.828	-3.3102
296.017	296.072	0.0553	527.237	522.556	-4.6808
310.867	310.818	-0.0487	540.542	536.537	-4.0052
330.001	330.024	0.0230	546.201	540.757	-5.4441
346.289	346.668	0.3790	547.499	546.189	-1.3108
348.616	348.024	-0.5927	557.916	557.563	-0.3538
359.230	358.686	-0.5442	572.776	566.042	-6.7336
371.578	370.949	-0.6289	572.776	571.672	-1.1036
388.426	389.708	1.2817	575.562	573.880	-1.6813
404.080	402.268	-1.8117	587.224	575.559	-11.6653
406.747	411.230	4.4835	592.166	577.528	-14.6373
411.234	411.855	0.6217	599.025	590.195	-8.8300
411.945	412.051	0.1057	602.060	599.028	-3.0318
420.148	422.613	2.4652	622.941	613.922	-9.0194
425.976	429.339	3.3630	630.620	630.639	0.0190

5 Evidence

When the energy gap between the third state ($1^2A_1'/2^2A_1'$) and the doubly degenerate states ($2^2E'/3^2E'$) of the model diabatic Hamiltonian for Na_3 cluster (Cocchini et. al. 1988) is assumed to be zero, the Curl for each NAC element turns out to be identically zero leading to a theoretically valid Extended Born - Oppenheimer equation. The numerical calculations explore the validity of the EBO equation by calculating the non - adiabatic effects on the photoabsorption spectrum for the ground state appears encouraging with respect to the diabatic results, particularly, when the gap between A - and E - type states approach to zero. At the same time, when we calculate the vibrational eigenspectrum of the ground adiabatic state by using BO and EBO equations, it appears clearly that non - adiabatic terms strongly affect the BO spectrum.

Acknowledgement. We acknowledge financial support from the **Department of Science and Technology (DST, Government of India)** through the project no: SR/S1/PC/13/2008 for the years 2008 to 2011. BS acknowledges support from **UGC, Government of India** through the DSA-SAP-III program.

References

Adhikari, S., and Billing, G. D., 1999, J. Chem. Phys., 111, 40
Adhikari, S., Billing, G. D., Alijah, A., Lin, S. H., Baer, M., 2000, Phys. Rev. A, 62, 32507:1-7
Althorpe, S. C., 2006, J. Chem. Phys., 124, 084105
Baer, M., 1975, Chem. Phys. Lett., 35, 112
Baer, M., in *Theory of Chemical Reaction Dynamics*, edited by M. Baer (CRC Press, Boca Raton, FL, 1985), Vol. II, Chap. 4
Baer, M., 1997, J. Chem. Phys., 107, 10662
Baer, M., Charutz, D., Kosloff, R., Baer, R., 1996, J. Chem. Phys. 105, 9141
Baer, M., Englman, R., 1996, Chem. Phys. Lett., 265, 105
Baer, M., Lin, S. H., Alijah, A., Adhikari, S., Billing, G. D., 2000, Phys. Rev. A, 62, 32506:1-8
Born, M., Oppenheimer, J. R., 1927, Ann. Phys. (Leipzig), 84, 457
Cocchini, F., Upton, T. H., Andreoni, W., 1988, J. Chem. Phys., 88, 6068
Herzberg, G., Longuet - Higgins, H. C., 1963, Discuss Faraday Soc., 35, 77
Juanes-Marcos, J. C., Althorpe, S. C., 2003, Chem. Phys. Lett., 381, 743
Kendrick, B., 2000, J. Chem. Phys., 112, 5679
Kendrick, B., 2003, J. Phys. Chem. A, 107, 6739
Kuppermann, A., Wu, Y. -S. M., 1993, Chem. Phys. Lett., 205, 577
Lepetit, B., Kuppermann, A., 1993, Chem. Phys. Lett., 166, 581
Longuet - Higgins, H. C., 1961, Adv. Spectrosc. (NY), 2, 429
Longuet - Higgins, H. C., 1975, Proc. R. Soc. London, Ser. A, 344, 147
Mead, C. A., 1980, J. Chem. Phys., 72, 3839
Mead, C. A., Truhlar, D. G., 1979, J. Chem. Phys., 70, 2284
Puzari, P., Sarkar, B., Adhikari, S., 2004, J. Chem. Phys. 121, 707
Sarkar, B., Adhikari, S., 2006, J. Chem. Phys. 124, 074101
Sarkar, B., Adhikari, S., 2007, Indian J. Phys., 81 (9) 925
Sarkar, B., Adhikari, S., 2008, J. Phys. Chem. A, 112, 9868
Sarkar, B., Adhikari, S., 2009, Int. J. Quan. Chem., 109, 650
Varandas, A. J. C., Xu, Z. R., 2000, J. Chem. Phys., 112, 2121

"Recent Advances in Spectroscopy:
Theoretical, Astrophysical, and Experimental Perspectives"
Eds. Chaudhuri R K, Mekkaden M V, Raveendran A V, Satya Narayanan A
Astrophysics and Space Science Proceedings, Springer-Verlag, Berlin, 2010.

Kubo Oscillator and its Application to Stochastic Resonance: A Microscopic Realization

Jyotipratim Ray Chaudhuri[1] and Sudip Chattopadhyay[2]

[1] Department of Physics, Katwa College
Katwa, Burdwan 713130, India
`jprc_8@yahoo.com`
[2] Department of Chemistry, Bengal Engineering and Science University,
Shibpur, Howrah - 711 103, India
`sudip_chattopadhyay@rediffmail.com`

Summary. Starting from a microscopic system-reservoir Hamiltonian, we realize the damped Kubo-type oscillator and observe the non-monotonic dependence of output signal of the underdamped oscillator on the parameters of multiplicative noise.

1 Introduction and Theoretical Development

The random arrival of electrons at the anode vacuum tube translates into an audible and annoying hiss at the loudspeaker. Engineers over decades have sought to minimize the effects of this noise in electronic circuits and communication systems. And so noise in a dynamical system is usually considered as a nuisance. But in certain nonlinear systems, including electronic circuits and biological sensory organs, the presence of noise can play a constructive role in the detection of weak periodic signals via a mechanism known as *stochastic resonance* (SR). The original work on stochastic resonance by Benzi et al (1981) in which the term was coined, was in the context of modelling the switching of Earth's climate between ice ages and periods of relative warmth with a period of about 10^5 years. The eccentricity of the Earth's orbit varies with the period, but according to current theories, the variation is not strong enough to cause such a dramatic climate change. Considering bistable potential as a climate potential, where two minima present the ice ages and relatively warm ages, Benzi et al (1981) in their seminal paper in 1981 suggested that a co-operative phenomena between the weak periodic variation in eccentricity and other random fluctuations due to short time climate fluctuations, such as, annual fluctuations in solar radiation might account for the strong periodicity observed. They also correctly pointed out that this is not strictly a resonance in the sense of an increased response when a driving frequency is tuned to the natural frequency of the system. Rather, the signal-to-noise ratio is maximized when some parameter is tuned near a certain value. The suggestion that SR might rule the periodicity of the primary cycle of recurrent ice ages was raised independently by Nicolis & Nicolis (1981). The first experimental verification of the stochastic resonance was given by Fauve & Heslot (1983) in an ac driven Schmitt trigger. The stochastic resonance was also realized in a key experiment in stable ring laser (McNamara et al 1988). Soon after, the studies of SR became high on the list of outstanding problems in statistical physics (Gammaitoni et al 1998, 1993). Presently, SR has found many applications in physics and biology (McNamara et al 1988). Since nonlinearity presents difficulties for theoretical analysis, linear models show quasi-nonlinear behavior including SR (Fulinsky 1995) and also allow for an exact analytical treatment. The linearity of the problems permits the inclusion of inertial effects which are usually neglected. In this way, we are led to the problem of periodically driven undamped harmonic oscillator with multiplicative noise. A model that is much studied is that of a harmonic oscillator with a random frequency: $\frac{d^2x}{dt^2} + \gamma \frac{dx}{dt} + \omega^2[1 + \eta(t)]x = a \sin(\Omega t) + f(t)$ where $\eta(t)$ and $f(t)$ represent the multiplicative and additive noise, respectively. Although this model has a long history (Bourret et al 1973), further research on both the internal dynamics (Ziller & Pikovsky 1973) and on the response to the driving force is still in progress. The importance of this model lies in its generic appearance in physics, biology, and economics (Mukamel 1973; Jung 2002; Turelli 1977; Kampen 1992; Sato 1992). Since its introduction by Kubo and Anderson (Anderson 1954; Kubo 1954) in the context of the line-shape theory, stochastic approaches of which have found wide application in condensed-phase spectroscopy (Anderson 1954; Kubo 1954) ranging from magnetic resonance spectroscopy, nonlinear spectroscopy (Mukamel 1973) to single molecule spectroscopy (Jung 2002). The stochastic line-shape theory of Kubo and Anderson (Jung 2002) is based on the equation of motion for the transition dipole (Anderson 1954; Kubo 1954): $\frac{d\mu(t)}{dt} = i\omega(t)\mu(t)$ where $\omega(t)$ is the stochastic frequency of the oscillator. The Kubo and Anderson approach is based on the Markovian assumption. However, single molecule studies (Moernet & Kaldor 1989; Orrit & Bennard 1990) have revealed that in some cases the underlying dynamics in the condensed-phase is highly non-Markovian in nature (Wang & Wolynes 1990; Gangopadhyay & Tanimura 1998).

In this article starting from a microscopic system-reservoir model we realize the damped Kubo-type oscillator, i.e. oscillator with a fluctuating frequency and study the output signal of the underdamped linear oscillator with a random frequency subject to a periodic force analytically to observe that the output signal shows non-monotonic dependence on the parameter of multiplicative color noise; the stochastic resonance.

To begin with, we consider that the system is coupled to a harmonic heat bath with characteristic frequency sets $\{\omega_j\}$. The coupling between the system and the bath is, in general, nonlinear. Initially at $t = 0$, the bath is in thermal equilibrium at a temperature T. At $t = 0_+$, an external noise agency is switched on and the bath starts getting modulated by the noise agency. The Hamiltonian for the composite system can be written as:

$$H = H_S + H_B + H_{\text{SB}} + H_{\text{int}} = \frac{p^2}{2} + V(x) + \sum_{j=1}^{N} \left\{ \frac{p_j^2}{2} + \frac{1}{2}\omega_j^2 \left(q_j - c_j f(x)\right)^2 \right\} + H_{\text{int}} \tag{1}$$

In Eq. (1), q_j and p_j are bath variables, c_j is the coupling constant and $f(x)$ is some smooth well behaved function of the system variable. H_{int} takes care of the interaction between bath and the external fluctuation $\epsilon(t)$:$H_{\text{int}} = \sum_{k=1}^{N} \kappa_j h(q_j)\epsilon(t)$, κ_j being the strength of the interaction and $h(q_j)$ is an arbitrary analytical function of bath variables and in general, nonlinear. In what follows we choose $h(q_j) = \frac{1}{2}q_j^2$. The external noise $\epsilon(t)$ is considered to be stationary, Gaussian with the statistical properties:

$$\langle \epsilon(t) \rangle = 0; \quad \langle \epsilon(t)\epsilon(t') \rangle = 2D\psi(t - t') \tag{2}$$

where D is the strength of the external noise and ψ is some arbitrary decaying memory kernel. From Eq. (1), the various equations of motion for the system and bath variables are found to be

$$\dot{x} = p; \quad \dot{p} = -V'(x) + \sum_{j=1}^{N} c_j \omega_j^2 \left(q_j - c_j f(x)\right) f'(x) \tag{3}$$

$$\dot{q}_j = p_j; \quad p_j = -\omega_j^2 \left(q_j - c_j f(x)\right) - \kappa_j \frac{dh}{dq_j}\epsilon(t) \tag{4}$$

Using the explicit form of the function $h(q_j)$, Eq. (4) becomes:

$$\ddot{q}_j + \left\{\omega_j^2 + \kappa_j \epsilon(t)\right\} q_j = c_j \omega_j^2 f(x) \tag{5}$$

To solve Eq. (5) we assume, $q_j(t) = q_j^0(t) + \kappa_j q_j^1(t)$ (where $q_j^1(t)$ is a small perturbation around $q_j^0(t)$) which is a solution of the equation:

$$\ddot{q}_j^0(t) + \omega_j^2 q_j^0(t) = c_j^2 \omega_j^2 f[x(t)] \tag{6}$$

The $q_j^1(t)$ satisfies the equation: $\ddot{q}^1(t) + \omega_j^2 q_j^1(t) = -q_j^0(t)\epsilon(t)$which has been written on the physical condition that at $t = 0$ the heat bath is in thermal equilibrium, which then is modulated by an external fluctuation $\epsilon(t)$ at time $t = 0_+$. Under this condition $q_j(0) = q_j^0(0)$ and $p_j(0) = p_j^0(0)$. This implies that $q_j^1(0) = p_j^1(0) = 0$. Making use of the formal solutions of Eq. (6), we obtain the following expression for $q_j(t)$ as

$$
\begin{aligned}
q_j(t) = {} & \left\{q_j^0(0) - c_j f[x(0)]\right\} \cos\omega_j t + \frac{p_j(0)}{\omega_j}\sin\omega_j t \\
& - c_j \int_0^t dt' \cos\omega_j(t-t') f'[x(t')]\dot{x}(t') - \frac{\kappa_j}{c_j}\int_0^t dt' \sin\omega_j(t-t')\epsilon(t')q_j^0(t')
\end{aligned} \tag{7}
$$

Now inserting Eq. (7) into Eq. (3) we obtain the dynamical equation for the system variable as

$$
\begin{aligned}
\dot{x} &= p \\
\dot{p} &= -V'(x) - f'(x)\int_0^t dt' \gamma(t-t') f'[x(t')]p(t') + f'(x(t))\xi(t) \\
& \quad -f'(x)\sum_{j=1}^{N} c_j\kappa_j\omega_j \int_0^t dt' \sin\omega_j(t-t')\epsilon(t')q_j^0(t')
\end{aligned} \tag{8}
$$

where the random force $\xi(t)$ and the memory kernel $\gamma(t)$ are given as

$$
\begin{aligned}
\xi(t) &= \sum_{j=1}^{N} c_j\omega_j^2 \left[\{q_j^0(0) - c_j f(x(0))\}\cos\omega_j t + \frac{p_j(0)}{\omega_j}\sin\omega_j t\right] \\
\gamma(t) &= \sum_{j=1}^{N} c_j^2\omega_j^2 \cos\omega_j t
\end{aligned}
$$

At this juncture we assume that the bath variables $\{q_j(0), p_j(0)\}$ are distributed according to the Gaussian form with the probability distribution function: $W\{q_j(0), p_j(0)\} = \frac{1}{Z}\exp\left(-\frac{H_B + H_{\mathrm{SB}}}{k_B T}\right)$, where Z is the partition function. The statistical properties of the fluctuating forcing terms become: $\langle\xi(t)\rangle = 0$ and $\langle\xi(t)\xi(t')\rangle = 2\gamma(t-t')k_B T$. To identify Eq. (8) as a generalized Langevin equation, we have to impose some conditions on the coupling coefficients c_j and κ_j, on the bath frequencies ω_j and number N of the bath oscillators which will ensure that $\gamma(t)$ is indeed dissipative. As $N \to \infty$, one replaces the sum by an integral over ω weighted by a density of state $\rho(\omega)$. Thus, to obtain a finite result in the continuum limit, the coupling function $c_j = c(\omega)$ and $\kappa_j = \kappa(\omega)$ are chosen as $c(\omega) = \frac{c_0}{\sqrt{\tau\omega}}$ and $\kappa(\omega) = \kappa_0$ where c_0 and κ_0 are constants and τ is the correlation time of the heat bath. The choice of $\kappa(\omega)$ is the simplest one where we assume that every bath mode is excitetd with the same intensity. This simplest choice makes the relevant term finite for $N \to \infty$. Consequently, $\gamma(t)$ becomes $\gamma(t) = \frac{c_0^2}{\tau}\int d\omega\rho(\omega)\cos\omega t$. If we assume that the density of modes $\rho(\omega)$ of the heat bath is Lorenzian,

$$
\rho(\omega) = \frac{2\tau}{\pi(1+\omega^2\tau^2)}
$$

then the expression for $\gamma(t)$ is found to be

$$\gamma(t) = \frac{c_0^2}{\tau} \exp\left(-\frac{|t|}{\tau}\right)$$

which reduces to the following form:

$$\gamma(t) = 2c_0^2 \delta(t)$$

for vanishingly small correlation time ($\tau \to 0$) and consequently one obtains the δ- correlated noise processes describing Markovian dynamics.

Taking into consideration all the above assumptions and assuming that the system variables evolve much more slowly in comparison to the external noise $\epsilon(t)$, in the limit $\tau \to 0$, eq. (8) reduces to

$$\dot{x} = p;\;\; \dot{p} = -V'(x) - \gamma[f'(x)]^2 p + f'(x)\xi(t) + \gamma\kappa_0 f(x) f'(x)\epsilon(t) \tag{9}$$

$\gamma = c_0^2$ and $\langle \xi(t)\xi(t') \rangle = 2\gamma k_B T \delta(t-t')$. From Eq. (9) we observe that the dissipation is state-dependent which is a manifestation of the nonlinear system-bath coupling, and the position dependence in the fluctuations arises from two different sources. The term $f'(x)\xi(t)$ is due to nonlinear coupling of the system to the heat-bath at time $t = 0$, whereas $G(x)\xi(t)$ $[G(x) = \gamma\kappa_0 f(x) f'(x)]$ arises due to the nonlinear driving of the heat bath by the external noise agency $\epsilon(t)$ at time $t = 0_+$.

We now consider that the system reservoir coupling is linear $[f(x) = x]$ and our system is a harmonic oscillator of unit mass with frequency ω_0, $V(x) = \frac{1}{2}\omega_0^2 x^2$. Then the Langevin equation, Eq. (9) becomes

$$\ddot{x} + \gamma\dot{x} + [\omega_0^2 + \eta(t)]x = \xi(t) \tag{10}$$

where $\eta(t) = -\gamma\kappa_0\epsilon(t)$. It is interesting to note that Eq.(10) represents the noise-driven Kubo oscillator.

To study the resonance phenomena, we now consider a forced damped Kubo oscillator:

$$\ddot{x} + \gamma\dot{x} + [\omega_0^2 + \eta(t)]x = \xi(t) + A \sin \Omega t \tag{11}$$

At this point we assign the statistical property of the external noise $\epsilon(t)$; $\epsilon(t)$ is assumed to be Gaussian with zero mean and Ornstein-Zerike correlation:

$$\langle \epsilon(t) \rangle = 0; \langle \epsilon(t)\epsilon(t') \rangle = \exp\left(-\frac{|t-t'|}{\tau_\epsilon}\right)$$

so that the noise $\eta(t)$ satisfies the following relations:

$$\langle \eta(t) \rangle = 0; \langle \eta(t)\eta(t') \rangle = \sigma \exp\left(-\frac{|t-t'|}{\tau_\epsilon}\right) \quad \text{with} \;\; \sigma = \gamma^2\kappa_0^2. \tag{12}$$

The second-order differential Eq. (11) can be rewritten as two first-order differential equations:

$$\frac{dx}{dt} = v \tag{13}$$

and

$$\frac{dv}{dt} = -\gamma v(t) - \omega_0^2 x(t) - \eta(t)x(t) + \xi(t) + A \sin \Omega t \tag{14}$$

which after averaging take the following form:

$$\frac{d}{dt}\langle x(t)\rangle = \langle v(t)\rangle; \quad \frac{d}{dt}\langle v(t)\rangle = -\gamma\langle v(t)\rangle - \omega_0^2\langle x(t)\rangle - \langle \eta(t)x(t)\rangle + A \sin \Omega t \tag{15}$$

where the averages are performed over the realization of both the internal and external noises. To obtain the average $\langle \eta(t)x(t)\rangle$, we adopt the Shapiro & Loginov (1998) theorem to get:

$$\frac{d}{dt}\langle \eta(t)x(t)\rangle = \langle \eta(t)\frac{dx}{dt}\rangle - \lambda\langle \eta(t)x(t)\rangle \tag{16}$$

where $\lambda = \frac{1}{\tau}$. Now multiplying Eq. (13) by $\eta(t)$, one gets after averaging

$$\langle \eta(t)\frac{dx(t)}{dt}\rangle = \langle \eta(t)v(t)\rangle \tag{17}$$

Inserting Eq. (17) into Eq. (16) results in

$$\frac{d}{dt}\langle \eta(t)x(t)\rangle = \langle \eta(t)v(t)\rangle - \lambda\langle \eta(t)x(t)\rangle \tag{18}$$

Using the procedure analogous to Eq. (16), for the quantity $\langle \eta(t)v(t)\rangle$, one gets

$$\frac{d}{dt}\langle \eta(t)v(t)\rangle = \langle \eta(t)\frac{dv}{dt}\rangle - \lambda\langle \eta(t)v(t)\rangle \tag{19}$$

Multiplying Eq. (14) by $\eta(t)$ and averaging, one obtains

$$\frac{d}{dt}\langle \eta(t)v(t)\rangle = -\gamma\lambda\langle \eta(t)v(t)\rangle - \omega_0^2\langle \eta(t)x(t)\rangle - \langle \eta^2(t)x(t)\rangle \tag{20}$$

Eq. (20) contains higher order term $\langle \eta^2(t)x(t)\rangle$ and one has to use a decoupling procedure:

$$\langle \eta^2(t)x(t)\rangle \approx \langle \eta^2(t)\rangle\langle x(t)\rangle = \sigma\langle x(t)\rangle$$

Thus we have

$$\frac{d}{dt}\langle \eta(t)v(t)\rangle = -\gamma\lambda\langle \eta(t)v(t)\rangle - \omega_0^2\langle \eta(t)x(t)\rangle - \sigma\langle x(t)\rangle - \lambda\langle \eta(t)v(t)\rangle \tag{21}$$

We then obtain a coupled system of four equations, Eqs. (15), (16), (18) and (21). These sets of equations are equivalent to the fourth order ordinary differential equation for $\langle x(t)\rangle$:

$$\begin{aligned}
&\frac{d^4}{dt^4}\langle x(t)\rangle + 2(\gamma+\lambda)\frac{d^3}{dt^3}\langle x(t)\rangle + (2\omega_0^2+\lambda^2+3\lambda\gamma+\gamma^2)\frac{d^2}{dt^2}\langle x(t)\rangle \\
&+\left\{2\omega_0^2(\lambda+\gamma)+\lambda\gamma(\lambda+\gamma)\right\}\frac{d}{dt}\langle x(t)\rangle + \left\{\omega_0^2(\omega_0^2+\lambda^2+\lambda\gamma)-\sigma\right\}\langle x(t)\rangle \\
&= (\omega_0^2+\lambda^2+\lambda\gamma-\Omega^2)A\sin\Omega t + (2\lambda+\gamma)A\cos\Omega t
\end{aligned} \tag{22}$$

We seek a solution of Eq. (22) of the form:

$$\langle x(t)\rangle = \langle x\rangle_0 + \langle x\rangle_\Omega \tag{23}$$

where the output signal $\langle x\rangle_\Omega$ is induced by the external field $\sin\omega t$ and $\langle x\rangle_0$ is determined by internal dynamics. Let us assume the solution $\langle x\rangle_\Omega$ of Eq. (23) in the form: $\langle x\rangle_\Omega = R\sin(\Omega t+\phi)$. Then, one can obtain easily:

$$R = \sqrt{\frac{\alpha_1^2+\alpha_2^2}{\alpha_3^2+\alpha_4^2}}; \quad \phi = \tan^{-1}\left(\frac{\alpha_1\alpha_3+\alpha_2\alpha_4}{\alpha_1\alpha_4-\alpha_2\alpha_3}\right) \tag{24}$$

where

$$\begin{aligned}
\alpha_1 &= A(2\lambda+\gamma)\Omega; \quad \alpha_2 = A(\Omega^2-\omega_0^2-\lambda^2-\lambda\gamma) \\
\alpha_3 &= (\Omega^2-\omega_0^2)(\Omega^2-\omega_0^2-\lambda^2)-\sigma-(3\lambda\gamma+\gamma^2)\Omega^2+\lambda\gamma\omega_0^2 \\
\alpha_4 &= \Omega(\gamma+\lambda)[2(\omega_0^2-\Omega^2)+\lambda\gamma]
\end{aligned} \tag{25}$$

We are now in a position to discuss the results obtained with our formalism to demonstrate the utility of the method. In Fig. 1 we present the dependence of the amplitudes, R of the output signal on correlation rate λ of the multiplicative color noise to observe a non-monotonic dependence of R on λ, which is a signature of SR.

2 Summarizing Remarks

In conclusion, starting from a microscopic Hamiltonian picture, we have constructed a forced damped oscillator with fluctuating frequency, the Kubo-type oscillator, and obtained a stochastic resonance phenomena. In this regard we envisage that the output signal of the under-damped oscillator depends non-monotonically on the parameters of multiplicative noise. The corresponding quantum approach is also worth studying and we shall return to damped forced quantum oscillation in the near future.

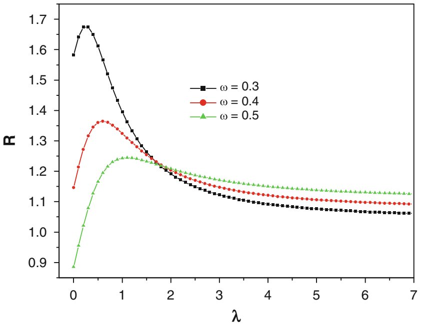

Fig. 1. Plot of R as a function of λ for various ω [all other parameters are set to be unity].

Acknowledgement. Financial support from CSIR, India [01(2257)/08/EMR-II] is thankfully acknowledged.

References

Anderson P W, J. Phys. Soc. Jpn. 9:316 (1954).
Benzi, A., Sutera, A. and Vulpiani, A., J. Phys. A, 14:L453 (1981).
Bourret, R. C., Frish, H., and Pouquet, A., Physica A 65:303 (1973).
Fauve, S. and Heslot, F., Phys. Lett. 97A:5 (1983).
Fulinsky, A., Phys. Rev. E 52:223 (1995).
Gammaitoni, L., Hanggi, P., Jung, P. and Marchesoni, F., Rev. Mod. Phys. 70:223 (1998).
Gammaitoni, L., Marchesoni, F., Menichella-Saetta, E., and Santaucci, S., Phys. Rev. E 49:4878 (1993).
Gangopadhyay, G. and Tanimura, Y., Chem. Phys. Lett. 289:97 (1998).
Jung, Y., Barkai, E. and Silbey, R. J., Adv. Chem. Phys. 123:199 (2002).
Kubo, R., J. Phys. Soc. Jpn. 9:935 (1954).
McNamara, B., Wiesendfeld, K. and Roy, R., Phys. Rev. Lett. 60:2628 (1988).
Moerner, W. E. and Kador, L., Phys. Rev. Lett. 62:2535 (1989).
Mukamel, S., Principles of Nonlinear Optical Spectroscopy (Oxford University Press, Oxford, 1995).
Nicolis, C. and Nicolis, G., Tellus, 33: 225 (1981).
Orrit, M. and Bernard, J., Phys. Rev. Lett. 65: 2716 (1990).
Sato, A. H. and Takayasu, H., Physica A 250:231 (1998).
Shapiro, V. E. and Loginov, V. M., Physica A 91:563 (1978).

Turelli, M., Theoretical Population Biology vol. 12, p-140 (Academic Press, NY, 1977).

van Kampen, Stochastic Processess in Physics and Chemistry (North-Holland, Amsterdam, 1992).

Wang, J. and Wolynes P. G., Phys. Rev. Lett. 74:4317 (1995).

Ziller, R. and Pikovsky, A., Phys. Rev. E 67:061117 (1973).

*"Recent Advances in Spectroscopy:
Theoretical, Astrophysical, and Experimental Perspectives"
Eds. Chaudhuri R K, Mekkaden M V, Raveendran A V, Satya Narayanan A
Astrophysics and Space Science Proceedings, Springer-Verlag, Berlin, 2010.*

Spectra of Conjugated Polymer Aggregates

K. Banerjee and G. Gangopadhyay

S.N. Bose National Centre for Basic Sciences, Salt Lake, Kolkata, India.
`kinshukb@bose.res.in`

Summary. We consider an interchain interaction model to understand the spectral properties of aggregates of conjugated polymers which belong to the family of polycyclic aromatic hydrocarbons, abundant in interstellar medium. As a typical model of aggregation, we have calculated the dressed eigenstates for the equivalent and inequivalent chain-dimers with classified symmetry. The various disorder-induced effects on the spectra can be explained by the dimeric chains which are generally inequivalent.

1 Introduction

It is well known that the interstellar medium as well as the meteorites and comet dust are rich in polycyclic aromatic hydrocarbons (Allamandola 1990; Salama et al 1996). Generally they are detected spectrally in the infrared region. Interstellar dust contains from elementary carbon to complex hydrogenated aggregates and carbon clusters and the most ubiquitous way of their formation is the process of aggregation (Pascoli & Polleux 2000; Klemperer & Vaida 2006; Kowk 2009). Here we specifically treat π-conjugated polymer aggregates and the impact of aggregation on the corresponding spectra.

Photoluminescence spectra of conjugated polymers vary over a wide range. The species responsible for luminescence is generally considered to be the intrachain exciton. Interchain exciton (Yan et al 1994) or polaron-pair generation can drastically alter the electronic and optical properties of individual chains. Although the interchain interaction is much more weaker than the intrachain interaction (Harrison et al 1996), some qualitatively new features appear in the luminescence spectra of interchain species. Due to the nature of the composite eigenstates of the interchain excitonic states, the interchain aggregate formation generally reduces the luminescence quantum yield as the interactions split the excitonic states with the lowest state being weakly coupled to the ground state (Kasha 1963). But detailed quantum-chemical study of poly(p-phenylenevinylene) (PPV) structures indicates that interchain interactions do not necessarily imply reduction of luminescence efficiency and positional disorder and the presence of chemical impurities can lead to substantial luminescence with slow radiative decay (Cornil et al 1998). The presence of dual luminescence due to both intra and interchain excitons are reported for photoluminescence study of PPV-Si nanocomposites (Ho et al 2001) and also for highly regioregular poly(3-hexylthiophene) (Brown et al 2003).

Recently Bittner et al (2007) have introduced an interchain exciton transfer model which explains the dual emission in terms of a strong non-Condon side band spectra from the lower dipole forbidden interchain state. Following a similar approach, we have studied the equivalent (Bittner et al 2007) and inequivalent cases of two vibrational modes which are interacting with both the chains. The Hamiltonian of the dressed eigenstates are evaluated for both the cases to study the symmetry of the eigenstates. The features of this symmetry are reflected through the absorption and emission spectra.

2 The Model System

Following Bittner et al (2007), we consider the aggregate system consisting of two independent polymer chains, where a chain is described in terms of an electronic basis with a vibrational manifold. The Hamiltonian can be defined as (Bittner et al 2007)

$$H = \sum_{n=1}^{2} |n\rangle\langle n| (\epsilon_n + \sum_{k=1}^{2} (\hbar\omega_k (a_k^\dagger a_k + \frac{1}{2}) + \hbar g_{nk} (a_k^\dagger + a_k))) \\ + \hbar V (|1\rangle\langle 2| + |2\rangle\langle 1|). \tag{1}$$

Here ϵ_n's are the vertical electronic excitation energies relative to the ground state of undimerized system. $a_k^\dagger, a_k$ are creation and annihilation operators, respectively for k-th vibrational mode having frequency ω_k with g_{nk} being the electron-phonon coupling parameter and V is the interchain interaction that transfers the excitation from one chain to the other.

The i-th eigenstate of the composite system can be expressed as

$$|\psi^i\rangle = \sum_{n_1,n_2=0}^{\infty} (C^i_{1n_1n_2}|1,n_1,n_2\rangle + C^i_{2n_1n_2}|2,n_1,n_2\rangle), \tag{2}$$

where all $C^i_{1n_1n_2}$ and $C^i_{2n_1n_2}$'s are real. We solve the stationary Schrödinger equation $H|\psi^i\rangle = \hbar\Omega_i|\psi^i\rangle$, where Ω_i is the energy of the i-th eigenstate. It is possible to obtain any high energy eigenstate and its corresponding eigenvector, depending on the dimension of the matrix equation. In the case of equivalent chain-dimer, from the sets of $C^i_{1n_1n_2}$ and $C^i_{2n_1n_2}$, we find that

$$C^i_{1n_1n_2} = \pm C^i_{2n_2n_1}, \tag{3}$$

where the plus sign corresponds to symmetric states while the minus sign to antisymmetric states.

3 Results and Discussion

3.1 Equivalent Chains

For the equivalent chains, we take the vibrational frequencies of both the modes to be equal, i.e., $\omega_1 = \omega_2$. All the parameters and also the working equations are scaled with respect to ω_1. To solve the time independent Schrödinger equation, we have taken $g_{nk} = \delta_{nk}$ and $V = 0.3$. The actual value of ω_1 is taken as $\hbar\omega_1 = 0.18$ eV, which corresponds to a standard value for C=C stretching frequency in conjugated polymers (Bittner et al 2007; Cornil et al 1997) in laboratory atmosphere.

Some energy eigenvalues (in units of $\hbar\omega_1$) for both the dimer ground states and excitonic states are listed in Table 1. The antisymmetric and symmetric states are indicated with 'asym' and 'sym' respectively, in the parentheses of the eigenvalues of the dimer excitonic states. The vibrational levels in the dimer ground state are taken as those of a two-dimensional isotropic harmonic oscillator, the lowest level containing the totally symmetric state.

ground state	excitonic state
1.00000 (nondegenerate)	0.84981(asym) 1.06236(sym)
2.00000 (doubly degenerate)	1.85018(asym) 1.89466(asym) 2.06318(sym) 2.12142(sym)

Table 1. Energies (in units of $\hbar\omega_1$) of dimer ground and excitonic states with the symmetry of the excitonic states being indicated in the parentheses.

To have more insight into the symmetry classification and to study its applicability, we have calculated the absorption and emission spectra of the chain dimer system. The initial states in optical transition are considered to be in thermal equilibrium. The spectra are calculated through the Fermi Golden rule expression. However, for the convergence of the delta function, we assume a damping factor γ which corresponds to very short probing time so that the coherence effect disappears under the time scale of consideration. We take $\gamma = 0.35\omega_1$ for the calculation of spectra.

The emission and absorption spectra for the monomer (isolated chain) and dimer system consisting of two equivalent chains are shown in Figure 1 for different transition dipole orientations, at $T = 3$ K. The absorption spectra are plotted on *per chain* basis. It is evident that both types of spectra show vibrational structure. We can easily see that absorption and emission are not symmetric for the dimer as in the case of an isolated chain (Figure 1a). The 0-0 line is absent in the emission spectra of the chain-dimer for parallel orientation of the transition dipoles; but it appears when the dipoles are antiparallel or when they are tilted. For tilted dipole orientation, we have polarized spectra in two perpendicular directions, taken as X- and Y-axes defined on a plane of the polymer sample (Figure 1d). Hence from Figure 1, we can see the effect of aggregation on the spectra by comparing the monomer and dimer spectra and also the effect of dipole geometry on the aggregate spectra.

The absence of 0-0 emission for parallel dipole orientation can be explained using symmetry of the states. At $T = 3$ K, only the lowest antisymmetric excitonic state is populated; so transition from this state to the totally symmetric ground state is symmetry forbidden.

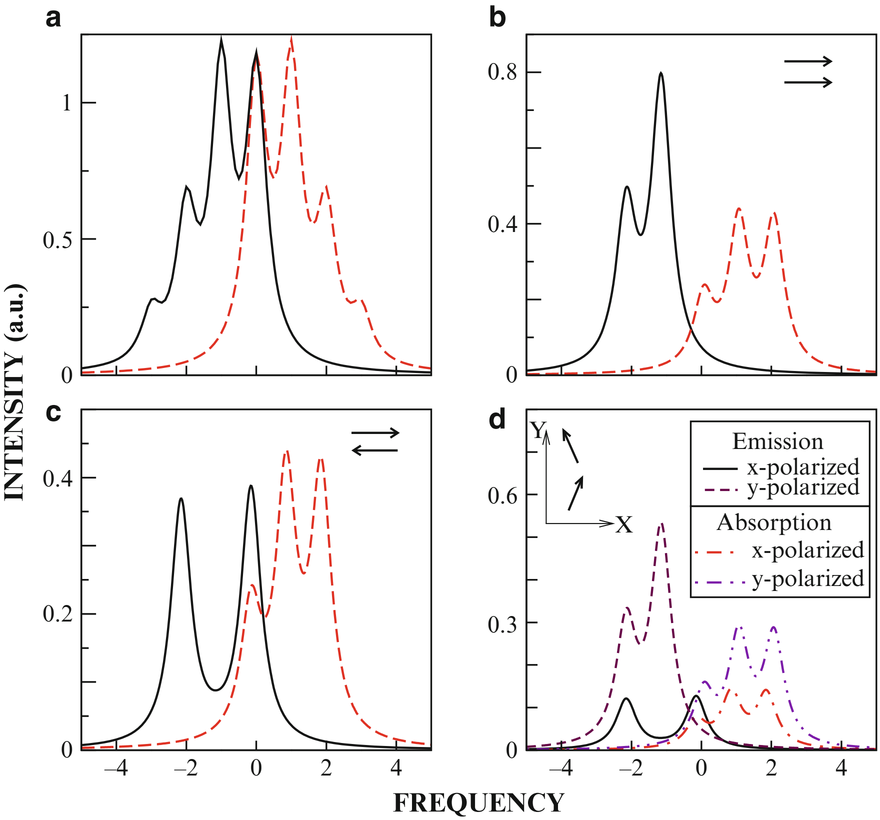

Fig. 1. (a-c) Emission(solid) and absorption(dashed) spectra of monomer and dimer with different dipole orientations at $T = 3$ K. (a) the monomer system; (b) dimer with parallel orientation of the monomer dipoles and (c) dimer with anti parallel orientation of the monomer dipoles. (d) X- and Y-polarized spectra for the dimer system with the dipoles tilted.

3.2 Inequivalent Chains

Although the equivalent chain-dimer model is a useful starting point to gain insight into the nature and effect of interchain interaction present in π-conjugated polymers, the roles played by the chemical environment and molecular disorder present in real samples are also of prime importance (Cornil et al 1998; Spano 2005). To study these effects, the values of the parameters g_{11} and ω_1 are made different from g_{22} and ω_2, respectively. One naturally expects that this should affect the symmetry and hence the spectra of the equivalent chain-dimer. The emission spectra, at $T = 3$ K, for the dimer composed of two inequivalent chains is shown in Figure 2 for different g_{22}/g_{11} and ω_2/ω_1 ratios with the transition dipoles being parallel. It is evident from the figure, that the forbidden 0-0 emission in the case of equivalent chain-dimer is allowed when the chains are inequivalent. This must be due to the relaxation of the symmetry on going from the equivalent to the inequivalent case. One can also see from Figure 2, that the 0-0 emission gains more and more intensity as the ratios g_{22}/g_{11} and ω_2/ω_1 get away from '1.0', the value taken by the equivalent chain-dimer. Also with increasing inequivalency, the emission gets red-shifted.

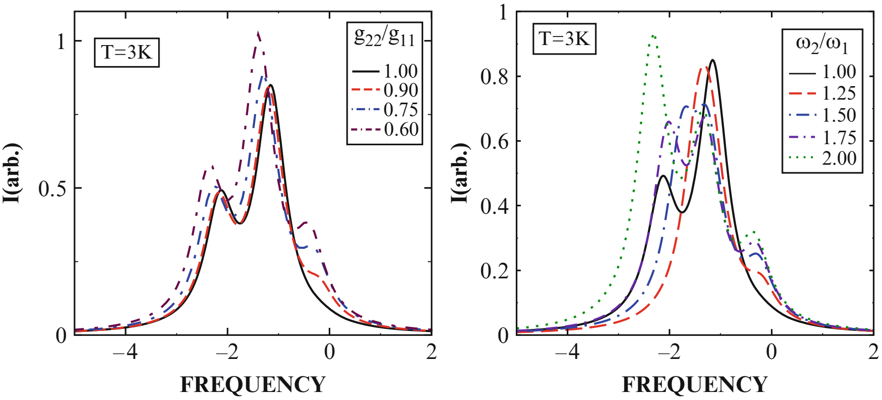

Fig. 2. Emission spectra at $T = 3$ K at different g_{22}/g_{11} and ω_2/ω_1 ratios for the inequivalent chain-dimer; $g_{22}/g_{11} = \omega_2/\omega_1 = 1.0$ indicates the equivalent chain case. The transition dipoles are taken as parallel.

4 Concluding Remarks

Dressed states are evaluated for the two interacting chains which mimics the excitetd states of polymer aggregates. It is shown that a definite symmetry classification of the aggregate states is possible in the case of two equivalent chains. The absorption and emission spectra depend strongly on the state of aggregation, the chemical atmosphere and geometry of the polymer chains. Presence of defects and impurities can drastically change the nature of emission. The model system we have studied here, can be used to simulate the effect of molecular disorder on the spectra of these conjugated polymer systems. The parameters taken for the determination of energies and spectra are relevant for π-conjugated polymers; however, the model system and the symmetry classification governing the spectra are general and can be used for various other multimeric aggregates in different media with suitable parameters.

Acknowledgement. K.Banerjee acknowledges the Council of Scientific and Industrial Research (C.S.I.R.), India for the partial financial support as a Junior Research Fellow and thanks Dr. R.K. Chaudhuri for useful discussions.

References

Allamandola, L. J., Top. Curr. Chem., 153, 1 (1990).
Bittner, E. R., Karabunarliev, S., Herz, L. M., J. Chem. Phys., 126, 191102.
Brown, P. J., Thomas, D. S., Köhler, A., Wilson, J. S., Kim, J. S., Ramsdale, C. M., Sirringhaus, H., Friend, R. H., Phys. Rev. B, 67, 064203 (2003).
Cornil, J., Beljonne, D., Heller, C. M., Campbell, I. H., Laurich, B. K., Smith, D. L., Bradley, D. D. C., Müllen, K., Brédas, J. L., Chem. Phys. Lett., 278, 139 (1997).
Cornil, J., dos Santos, D. A., Crispin, X., Silbey, R., Brédas, J. L., J. Am. Chem. Soc., 120, 1289 (1998).
Harrison, N. T., Hayes, G. R., Phillips, R. T., Friend, R. H., Phys. Rev. Lett., 77, 1881 (1996).
Ho, P. K. H., Kim, J. S., Tessler, N., Friend, R. H., J. Chem. Phys., 115, 2709 (2001).
Kasha, M., Radiat.Res., 20, 55 (1963).
Klemperer, W., Vaida, V., Proc. Natl. Acad. Sci. U.S.A., 103, 10584 (2006).
Kwok, S., Astrophys. and Space Sci., 319, 5 (2009).
Pascoli, G., Polleux, A., Astron. Astrophys., 359, 799 (2000).
Salama, F., Bakes, E. L. O., Allamandola, L. J., Tielens, A. G. G. M., Astrophys. J., 458, 621 (1996).
Spano, F. C., J. Chem. Phys., 122, 234701 (2005).
Yan, M., Rothberg, L. J., Papadimitrakopoulos, F., Galvin, M. E., Miller, T. M., Phys. Rev. Lett., 72, 1104 (1994).

"Recent Advances in Spectroscopy:
Theoretical, Astrophysical, and Experimental Perspectives"
Eds. Chaudhuri R K, Mekkaden M V, Raveendran A V, Satya Narayanan A
Astrophysics and Space Science Proceedings, Springer-Verlag, Berlin, 2010.

Studies of parity and time reversal violations in heavy polar molecules

Malaya K. Nayak

Theoretical Chemistry Section, Bhabha Atomic Research Centre, Trombay,
Mumbai-400 085, India. `mknayak@barc.gov.in`

Summary. Investigation of phenomena involving parity (P) and time reversal (T) symmetry violations is of fundamental importance in physics. A few experiments to search for the P,T-odd effects have been performed on TlF and YbF molecules and considerable progress for PbO and PbF molecules is on the way. For the interpretation of the measured experimental data, it is necessary to calculate a few molecular properties which cannot be measured experimentally. These molecular properties establish some connection between the measured data and well studied fundamental constants. Very accurate and reliable calculations of these properties usually require accurate accounting for both relativistic and correlation effects in heavy-atom systems.

In this review, we discuss the P,T-odd interaction constants W_{d} and W_{S}. The interaction constant W_{d} arises from the interaction of electron electric dipole moment (EDM) d_e with the molecular electric field, and the constant W_{S} arises due to the electron-nucleus scalar-pseudoscalar (S-PS) interaction. The knowledge of W_{d} is essential to put a reliable limit on the electron EDM d_e, where as the knowledge of W_{S} is necessary to get the information about the electron-nucleus (S-PS) coupling constant k_s, and to test the Standard Model (SM) of particle physics. Presently available theoretical results of W_{d} and W_{S} for the ground states of YbF and BaF molecules are also presented.

1 Introduction

It is well recognized that heavy atoms and heavy-polar diatomics are the prime candidates for the experimental search of permanent electric dipole moments (EDM's) arising from the violations of space inversion symmetry (P) and time reversal invariance (T). The search of non-zero P,T-odd effects in these systems with the presently accessible (expected) level of experimental sensitivity would indicate the presence of the so-called "new physics" beyond the Standard Model (SM) of electroweak and strong interaction (see Titov et al. 2006 and references therein) which is certainly of fundamental importance. Despite the well known drawbacks and unresolved problems of the SM there is very little experimental data available which would be in direct contradiction with this theory. In turn, some popular extensions of the SM, which allow one to overcome it's disadvantages, are not yet confirmed experimentally (see Commins 1999; Bernreuther et al 1991 for details).

In order to interpret the measured data in terms of fundamental constants of the above mentioned interactions, one must calculate those properties of the systems, which establish a connection between the measured data and studied fundamental constants. These properties are described by operators that are prominent in the nuclear region; they cannot be measured and their theoretical study is a non-trivial task. During the last several years the significance of (and requirement for) ab-initio calculation of electronic structure providing a high level of reliability and accuracy in accounting for both relativistic and correlation effects associated with these properties has gained importance.

In this review, we discuss the present theoretical status of the P, T-odd interaction constants W_{d} and W_{S} in YbF and BaF molecules. The P, T-odd constant W_{d} is a measure of the effective electric field $\mathbf{E}$ at the unpaired electrons, in the ground state of YbF and BaF and the knowledge of W_{d} is necessary to link the experimentally determined P, T-odd frequency shift with the electron EDM d_e. Similarly, the P, T-odd interaction constant W_{S} for the ground state of YbF and BaF molecules arises due to the electron-nucleus scalar-pseudoscalar (S-PS) interaction. The knowledge of W_{S} is necessary to link the experimentally determined P, T-odd frequency shift with the electron-nucleus (S-PS) coupling constant k_s, which can arise from the mixing of scalar and pseudoscalar particles in multi-Higgs models. It is worthwhile to mention here that an experiment to measure the EDM of YbF is currently in progress (Sauer et al 2006).

The P, T-odd interaction constants W_{d} and W_{S}, in YbF was first calculated by Titov et al (1996) using generalized relativistic effective-core potential (GRECP) method as this procedure provides reasonable accuracy with small computational cost. Titov and co-workers have also reported the results of these P, T-odd constants computed using restricted active space (RAS) self-consistent field (SCF) method (Titov et al 1996) with GRECP approach. The result of W_{d} has been further improved using an effective operator (EO) technique (Titov et al 1996). Assuming that the valence-valence electron correlation effect is negligible, Parpia (1998) has estimated W_{d} and W_{S} from the all-electron unrestricted Dirac-Fock (UDF) method in 1998. In the same year Quiney et al (1998) reported these P, T-odd interaction constants computed at the core-polarization level with all-electron DF orbitals. Though the effect of pair correlation and higher order effects to W_{d} and W_{S} are non-negligible, these terms were not included in Quiney et al's calculations. Similarly, for the BaF molecule, the first calculation of the P, T-odd interaction constants W_{d} and W_{S} was carried out by Kozlov et al (1997) using the GRECP approach at the level of SCF and RASSCF approximations.

In earlier communications, we have also reported the P, T-odd interaction constant W_{d} and W_{S} for the ground $({}^2\Sigma_{1/2})$ states of YbF and BaF molecules

Nayak & Chaudhuri (2006a,b); Nayak et al (2007) computed using all-electron DF orbitals at the level of RASCI and second order many-body perturbation theory [MBPT(2)] Nayak & Chaudhuri (2007, 2008). In this brief review, we will discuss the essential features of all these calculations.

In section 2 below, we briefly present the working equation for the P,T-odd interaction constant W_{d} and W_{S}, followed by the results and discussion in section 3.

2 Expressions for the P,T-odd interaction constants W_{d} and W_{S}

Expressions for the P,T-odd interaction constants W_{d} and W_{S} are given in many articles (Titov et al 1996; Parpia 1998; Quiney et al 1998). Some details are also given in our earlier communications Nayak & Chaudhuri (2006a); Nayak et al (2007). The P,T-odd interaction constant W_{d} is defined as

$$W_{\mathrm{d}} = \frac{2}{d_e}\langle {}^2\Sigma_{1/2}|H_{\mathrm{d}}|{}^2\Sigma_{1/2}\rangle. \tag{1}$$

where d_e is the EDM of electron. The interaction Hamiltonian H_{d} is defined as

$$H_{\mathrm{d}} = -d_e \sum_e (\gamma_e^0 - 1)\mathbf{\Sigma}_e \cdot \mathbf{E}^{mol}(r_e). \tag{2}$$

where $\gamma^0 = \beta$ and $\mathbf{\Sigma}$ are the 4-component Dirac matrices, and $\mathbf{E}^{mol}(r_e)$ is the molecular electric field at r_e.

Similarly, the P,T-odd interaction constant W_{S} is defined as

$$W_{\mathrm{S}} = \frac{2}{k_s}\langle {}^2\Sigma_{1/2}|H_{\mathrm{S}}|{}^2\Sigma_{1/2}\rangle. \tag{3}$$

where, k_s is the electron-nucleus S-PS coupling constant. The interaction Hamiltonian H_{S} is defined as

$$H_{\mathrm{S}} = i\frac{G_F}{\sqrt{2}} Z k_s \sum_e \gamma_e^0 \gamma_e^5 \rho_N(r_e) \tag{4}$$

where, γ^0 and γ^5 are the 4-component Dirac matrices and $\rho_N(r_e)$ is the nuclear charge density normalized to unity. G_F is the Fermi constant and k_s is a dimensionless S-PS interaction constant, which is defined as $Zk_s = (Zk_{s,p} + Nk_{s,n})$ where, $k_{s,p}$ and $k_{s,n}$ are electron-proton and electron-neutron coupling constants, respectively. The ground state wave functions $|{}^2\Sigma_{1/2}\rangle$ for YbF and BaF molecules are obtained using different theoretical methods.

3 Results and discussion

The P, T-odd interaction constants W_{d} and W_{S} for the ground state of YbF and BaF are calculated using the RASCI and MBPT(2) methods with all-electron fully relativistic DF orbitals. The basis set and geometry used in these calculations are identical with our previous calculations of the P, T-odd constant W_{d} Nayak & Chaudhuri (2006a,b). We refer the readers to our original papers for computational details and more exhaustive comparisons Nayak & Chaudhuri (2006a,b); Nayak et al (2007); Nayak & Chaudhuri (2007, 2008), making our discussion brief here.

Methods	W_{d}	W_{S}
Semi-empirical Kozlov (1997)	-1.26	-43.0
GRECP-RASSCF Titov et al (1996)	-0.91	-33.0
DHF Quiney et al (1998)	-0.62	-22.0
DHF+CP Quiney et al (1998)	-1.20	-42.0
UDF (unpaired electron) Parpia (1998)	-0.962	-34.6
UDF (all electrons) Parpia (1998)	-1.203	-44.0
GRECP-RASSCF-EO Mosyagin et al (1998)	-1.206	
DF Nayak & Chaudhuri (2006a); Nayak et al (2007)	-0.963	-34.2
RASCI Nayak & Chaudhuri (2006a); Nayak et al (2007)	-1.088	-41.2
MBPT(2) Nayak & Chaudhuri (2007, 2008)	-1.043	-37.1

Table 1. P, T-odd interaction constants W_{d} (in 10^{25} Hz/e-cm) and W_{S} (in kHz) for the ground $^2\Sigma_{1/2}$ state of YbF molecule.

The P, T-odd constants W_{d} and W_{S} for the ground state of YbF estimated using RASCI and MBPT(2) methods are compared with other calculations Mosyagin et al (1998); Parpia (1998); Quiney et al (1998); Titov et al (1996) and the semi-empirical result of Kozlov (1997) in Table 1. It can be seen from Table 1 that the result of W_{d} obtained using RASCI method differs by $\sim$ 13% from the latest semi-empirical result of Kozlov (1997). However, accuracy of the semi-empirical method is expected to be 80% as Kozlov pointed out in his calculations (Kozlov 1997). Similarly, the result of W_{d} estimated from the RASCI method is off by $\sim$ 9% from the estimation of Mosyagin et al (1998) based on GRECP-RASSCF-EO method and Parpia's UDF calculation. Further, it can be noticed here that the result of W_{d} estimated from the MBPT(2) method (Nayak & Chaudhuri 2007) is slightly less in magnitude, which is off by $\sim$ 4% from the result obtained using the RASCI method (Nayak & Chaudhuri 2006a). Similarly, the result of W_{S} estimated from the RASCI method Nayak et al (2007) differs by $\sim$ 6% from Parpia's UDF calculation and off by $\sim$ 4% from the latest semi-empirical calculation of Kozlov (1997). In this case also the result of W_{S} obtained from MBPT(2) method is less in magnitude from the RASCI result by $\sim$ 9%. Although, the results of W_{d} and

W_{S} obtained using MBPT(2) are less in magnitude as compared to that of the results obtained using the RASCI method, however the MBPT(2) method is quite stable with respect to choice of the orbitals in the active space, which is discussed in our earlier communication Nayak & Chaudhuri (2008)

Methods	W_{d}	W_{S}
Semi-empirical Kozlov & Labzowsky (1995)	-0.35	-11.0
SCF Kozlov et al (1997)	-0.230	-6.1
RASSCF Kozlov et al (1997)	-0.224	-5.9
SCF-EO Kozlov et al (1997)	-0.375	
RASSCF-EO Kozlov et al (1997)	-0.364	
DF Nayak & Chaudhuri (2006b); Nayak et al (2007)	-0.293	-7.7
RASCI Nayak & Chaudhuri (2006b); Nayak et al (2007)	-0.352	-9.7
MBPT(2) Nayak & Chaudhuri (2007, 2008)	-0.320	-8.4

Table 2. P, T-odd interaction constants W_{d} (in 10^{25} Hz/e-cm) and W_{S} (in kHz) for the ground ${}^2\Sigma_{1/2}$ state of BaF molecule.

The P, T-odd interaction constant W_{d} and W_{S} for the ground state of BaF calculated using RASCI and MBPT(2) methods are compared with other theoretical calculations of Kozlov et al (1997) and the semi-empirical result of Kozlov & Labzowsky (1995) in Table 2. It can be seen form Table 2 that the result of W_{d} estimated using RASCI method is $\sim$ 6(3)% off from the SCF-EO(RASSCF-EO) of Kozlov et al (1997) and is in very good agreement with the semi-empirical result of Kozlov & Labzowsky (1995). In this case also, it can be noted that the result of W_{d} estimated from MBPT(2) method (Nayak & Chaudhuri 2007) is less in magnitude and is off by $\sim$ 9% from the result of RASCI method Nayak & Chaudhuri (2006b). The result of the P, T-odd constant W_{S} in BaF, calculated using RASCI method is only off by $\sim$ 11% from the semi-empirical result of Kozlov & Labzowsky (1995), which is estimated from the experimental hyperfine structure data of Knight et al (1971). At this juncture, we emphasize that not many theoretical calculations for W_{S} are available using other correlated many-body methods. In this case, the magnitude of W_{S} obtained from MBPT(2) (Nayak & Chaudhuri 2008) is $\sim$ 13% less than the RASCI result (Nayak et al 2007). In the case of BaF molecule also the results of the P, T-odd constants obtained using MBPT(2) method are quite stable with respect to the choice of the active orbitals, however, it estimate the results of W_{d} and W_{S} which are less in magnitude from the results estimated from RASCI method.

4 Conclusion

Fully-relativistic RASCI approach and second order MBPT with sufficiently large active orbitals are employed to estimate the P, T-odd interaction constants W_{d} and W_{S} for the ground $(^2\Sigma_{1/2})$ states of YbF and BaF molecules. From our calculations using two different theoretical methods we observe that the results of the P, T-odd constants estimated using RASCI method are in close agreement with other theoretical predictions, which may be considered to be more reliable. However, estimation of these constants using MBPT(2) are always less in magnitude than the RASCI result. Further more, we find that the RASCI method is quite sensitive to the choice of active orbitals in the active space, where as MBPT(2) is quite stable with respect to this choice, which converges smoothly and quite faster.

Acknowledgement. The author wishes to thank Prof. Hans Joergen Jensen and his group for providing their DIRAC04 Jensen et al (2004) code, which is adapted with our codes. This work was partly supported by the KSKRA fellowship (Ref. No. 2007/11/1-BRNS/515) by the BRNS, DAE, India.

References

Bernreuther, W., and Suzuki, M., Rev. Mod. Phys. **63**, 313 (1991).
Commins, E. D., Adv. At. Mol. Opt. Phys. **40**, 1 (1999).
Dirac, a relativistic ab-initio electronic structure program, Release DIRAC04 (2004), written by H. J. Aa. Jensen, T. Saue and L. Visscher with contributions from V. Bakken, E. Eliav, T. Enevoldsen, T. Fleig, O. Fossgaard, T. Helgaker, J. Laerdahl, C. V. Larsen, P. Norman, J. Olsen, M. Pernpointner, J. K. Pedersen, K. Ruud, P. Salek, J. N. P. Van Stralen, J. Thyssen, O. Visser, and T. Winther (http://dirac.chem.sdu.dk).
Kozlov, M. G., J. Phys. B **30**, L607 (1997).
Kozlov M. G., and Labzowsky, L. N., J. Phys. B **28**, 1933 (1995).
Kozlov, M. G., Titov, A. V., Mosyagin, N. S., and Souchkov, P. V., Phys. Rev. A **56**, R3326 (1997).
Knight, B., Easley, W. C., and Weltner, W., J. Chem. Phys. **54**, 322 (1971).
Mosyagin, N. S., Kozlov, M. G., and Titov, A. V., J. Phys. B **31**, L763 (1998).
Nayak, M. K., and Chaudhuri, R. K., Chem. Phys. Lett. **419**, 191 (2006a).
Nayak, M. K., and Chaudhuri, R. K., J. Phys. B **39**, 1231 (2006b).
Nayak, M. K., Chaudhuri, R. K., and Das, B. P., Phys. Rev. A **75**, 022510 (2007).
Nayak, M. K., and Chaudhuri, R. K., J. Phys. Conf. Ser. **80** 012051 (2007).
Nayak, M. K., and Chaudhuri, R. K., Phys. Rev. A **78** 012506 (2008).
Parpia, F. A., J. Phys. B **31**, 1409 (1998).
Quiney, H. M., Skaane, H., and Grant, I. P., J. Phys. B **31**, L85 (1998).
Sauer, B. E., *et al.*, Atomic Physics **20**, 44 (2006), XX International Conference on Atomic Physics; ICAP 2006, edited by C. Roos, H. Haeffner and R. Blatt, (American Institute of Physics, Melrille, New York, 2006).
Titov, A. V., Mosyagin, N. S., and Ezhov, V. F., Phys. Rev. Lett. **77**, 5346 (1996).

Titov, A.V., Mosyagin, N. S., Petrov, A. N., Isaev T. A., and DeMille, D., Prog. Theor. Chem. Phys. **15**, 253 (2006).

"Recent Advances in Spectroscopy:
Theoretical, Astrophysical, and Experimental Perspectives"
Eds. Chaudhuri R K, Mekkaden M V, Raveendran A V, Satya Narayanan A
Astrophysics and Space Science Proceedings, Springer-Verlag, Berlin, 2010.

Static hyper-polarizability of open shell molecules computed at the FSMRCCSD level using constrained variational approach

A. Bag, S. Bhattacharya, and S. Pal

Physical Chemistry Division, National Chemical Laboratory,
Pune 411008, India.
`s.pal@ncl.res.in`

Summary. In recent years, there has been a significant development in the analytic derivatives of energy with respect to electric fields based on the state-of-the-art multi-reference coupled-cluster method using Lagrangian based constrained variational approach. So far, the Lagrangian based Fock space multi-reference coupled cluster (FSMRCC) method has been successfully used to calculate electrical dipole moment and polarizability of open shell molecules, particularly, doublet radicals at the ground state and the electronic excited states of closed shell molecules. In this article, Lagrangian based FSMRCC method has been implemented for the first time for calculation of hyper polarizabilites of a few doublet radicals such as OH, OF, NO and NO_2. Orbital-relaxed finite field FSMRCC values are reported for comparison.

1 Introduction

There has been excellent progress in many-body electronic structure and response properties and there are several theories, which are useful for calculation of ground state structure and response properties of closed shell molecules (Brooks *et al.* 1980; Osamura *et al.* 1982; Pople *et al.* 1979; Frisch *et al.* 1990a,b; Hasse & Ahlrichs 1993; Neilsen 1996; Head-Gordon 1999; Gdanith & Ahlrich 1988; Gdanith 1993; Hirao 1992a,b, 1993; Graham & Freed 1992; McDouall *et al* 1988). Among these, coupled-cluster based methods (*Číž*ek 1969; Mukherjee & Muherjee 1979; Nakatsuji & Hirao 1978; Koch & Jörgenson 1993) have been established as state-of-the-art methods for electronic structure and properties. Single reference coupled cluster (SRCC) method has been studied extensively for closed shell molecules (*Číž*ek 1969; Mukherjee & Muherjee 1979; Nakatsuji & Hirao 1978; Koch & Jörgenson 1993). Linear response properties of closed shell molecules in ground state using single reference coupled cluster (SRCC) method was initiated by Monkhorst (1977) and implemented by Bartlett and co-workers using Z-vector technique (Bartlett 1981; Salter *et al.* 1989; Salter & Bartlett 1989). Similar formalism was done by Jørgensen and Helgaker (Helgaker & Jörgenson 1988; Jörgenson & Helgaker 1988; Helgaker & Jörgenson 1989; Gauss & Stanton 1996; Helgaker *et al.* 1999) in the context of SRCC using Lagrange formulation.

For open-shell molecules, excited states, degenerate and near-degenerate states, single reference methods mentioned above are often not suitable and multi-determinantal description incorporating non-dynamic electron correlation is more appropriate. Multi-reference version of coupled cluster(MRCC) is a more recent development and has been used for potential energy surface and spectroscopic properties. There are two subclasses of MRCC methods, which have been studied extensively. One is the multi-root description via effective Hamiltonian approach (Durand & Malrieu 1987; Evangelisti *et al.* 1987) and the other describes a specific root, known as the state-specific MRCC approach (Chattopadhyay *et al.* 2002). In the effective Hamiltonian multi-root approach exact energies of the corresponding strongly interacting near-degenerate states are obtained as roots of effective Hamiltonian via diagonalization. This class of methods is further subdivided into the Hilbert space and Fock space approach depending on the way the dynamical part of electron correlation is described. Durand & Malrieu 1987; Evangelisti *et al.* 1987; Mukherjee 1979, 1986a,b,c; Jezioroski & Monkhorst 1982; Balkova *et al.* 1991; Sinha *et al.* 1986; Pal *et al.* 1988; Mukherjee 1989; Reitz *et al.* 1979; Kutzelnigg 1981; Haque & Kaldor 1985a,b; Lindgren 1985; Pal *et al.* 1987; Lindgren & Mukherjee 1987 Both these approaches are fully size-extensive. The Hilbert space approach uses a state universal wave operator containing different cluster operators for each of the determinants in the model space (Mukherjee 1979, 1986a,b,c; Jezioroski & Monkhorst 1982; Balkova *et al.* 1991). The method has been used for studying potential energy surface (PES), bond-dissociation, etc. However for PES, state selective MRCC method developed by Mukherjee and co-workers Chattopadhyay *et al.* 2002 has been found to be more suitable in recent years from the point of view of circumventing the important problems of intruder states. The Fock-space (FS) MRCC, (Mukherjee 1979, 1986a,b,c; Sinha *et al.* 1986; Pal *et al.* 1988; Mukherjee 1989; Reitz *et al.* 1979; Kutzelnigg 1981; Haque & Kaldor 1985a,b; Lindgren 1985; Pal *et al.* 1987; Lindgren & Mukherjee 1987) on the other hand, is found to be suitable for cases like ionization, electron-attachment and electronic excitation of molecules and is based on the concept of common-vacuum and a valence universal wave-operator. The model space is composed of near degenerate configurations obtained by combinations of electron occupancies among what are called active orbitals. The occupancies of the active orbitals are denoted in terms of number of active particles and active holes with respect to the vacuum. Parallel to this, methods like equations-of-motion coupled cluster (EOMCC) (Bartlett 1994; Geertsen *et al.* 1989; Comeau & Bertlett 1993; Stanton & Bertlett 1993, 1994; Nooijen & Bertlett 1995; Krylov 2008), symmetry adapted cluster configuration interaction (SAC-CI) (Nakatsuji *et al.* 1989; Nakatsuji & Hirao 1978; Nakatsuji 1979; Hirao *et al.* 1984; Hirao 1985) similarity transformed EOMCC (Nooijen &

Bartlett 1997a,b,c; Tobota *et al.* 2003) approaches etc. have been developed to handle cases of quasi-degeneracy.

Energy derivatives in the context of MRCC (Mukherjee 1979, 1986a,b,c; Jezioroski & Monkhorst 1982; Sinha *et al.* 1986; Pal *et al.* 1988; Mukherjee 1989) using an analytic linear response method along the line of Monkhorst's approach Monkhorst (1977) was initiated by Pal (Pal 1989, 1992) and then was implemented by Ajitha *et al.* (Ajitha & Pal 1997, 1999a, 2001; Ajitha *et al.* 1999a) for obtaining dipole moment of doublet radicals. However, this initial approach was unsatisfactory, since it requires explicit evaluation of cluster amplitude derivatives for first energy derivatives. Taking cue from the developments in SRCC context, the Lagrangian formulation using constrained variation approach (CVA) was presented by Pal and co-workers (Shamsundar *et al.* (2004)) for both Fock and Hilbert space.

The CVA method in FSMRCC framework was studied by Szalay (1995) independently. However, this method was applicable for complete model spaces (CMS) only. The CVA formulation of Shamasundar and Pal (Shamsundar *et al.* 2004; Manohar *et al.* 2006; Manohar & Pal 2007a,b; Bag *et al.* 2007, 2009) is applicable for a general incomplete model space (IMS) cases and simplifies to Szalay's formulation in the case of CMS. Both of these were based on the application of Lagrangian formulation to a specific root of the effective Hamiltonian multi-root problem. The single root method provides a cost-effective tool to obtain higher order energy derivatives with the knowledge of lower order derivatives of cluster amplitudes and a set of perturbation independent vectors, the Lagrange multipliers. The calculation of polarizabilities required computation of first derivatives of Fock space T amplitudes only, due to the existence of (2n+1) rule for T-amplitudes and (2n+2) rule for Λ amplitudes.

The computational development of the above approach was recently done by Manohar *et al.* (Manohar *et al.* 2006; Manohar & Pal 2007a,b) in Fock space frame work using singles and doubles (SD) truncation of the wave operator and the method was then implemented for analytic dipole moments and polarizabilities of doublet radicals (Manohar *et al.* 2006; Manohar & Pal 2007a; Bag *et al.* 2007) Dipole moments and polarizabilities for excited states were also implemented by Pal and co-workers (Manohar & Pal 2007b; Bag *et al.* 2009) very recently. In this article, we present the first implementation of the next important energy derivative i.e. first hyper- polarizability which requires calculation of the first derivatives of the Λ amplitudes. As a pilot application, we present the first static hyper-polarizabilities of a few doublet radicals at the ground state, which can be treated as one hole or one particle Fock space sector with respect to the RHF configuration of the corresponding anion/cation of the radical as vacuum. We have discussed the theoretical back ground in brief followed by implementation details and finally results and discussion of our pilot applications.

2 Theoretical back ground

The constraint variational approach in FSMRCC frame work for evaluation of response properties has been discussed in detail in various articles (Manohar *et al.* 2006; Manohar & Pal 2007a,b; Bag *et al.* 2007, 2009; Shamsundar *et al.* 2004). In this article, a brief description is given only for third-order response properties.

The universal wave operator for one hole problem is given as

$$\Omega = \{e^{T^{(0,0)}} e^{T^{(0,1)}}\} \tag{1}$$

and for one particle system, the wave operator is given by,

$$\Omega = \{e^{T^{(0,0)}} e^{T^{(1,0)}}\} \tag{2}$$

Under singles and doubles (SD) approximation, the cluster amplitudes (T) of every sector will contain only one-body and two-body parts. Following Mukherjee (Mukherjee 1986a,b,c; Lindgren & Mukherjee 1987), Sinha *et al.* (1986), and Pal *et al.* (1987) the above valence universal cluster operator satisfies Bloch equation.

$$H\Omega P^{k,l} = \Omega \tilde{H}^{k,l}_{\mathit{eff}} P^{k,l}; \forall k, l = 0, 1 \tag{3}$$

where, $\tilde{H}^{(1,1)}_{\mathit{eff}}$ includes contributions from all of the lower sector effective Hamiltonians in addition to the highest sector part. The diagonalization of the effective Hamiltonian yields the roots, which are the energies of the corresponding exact states. Due to normal ordering, sub-system embedding condition (SEC) holds and hence lower order cluster amplitudes decoupled from higher order cluster amplitudes. Thus, evaluation of cluster amplitudes should starts from the lowest sector i.e. (0,0) sector.

The energy of a specific state of the ionized system is given by

$$E_\mu = \sum_{ij} \tilde{C}^{(0,1)}_{\mu i} (H_{\mathit{eff}})^{(0,1)}_{ij} C^{(0,1)}_{j\mu} \tag{4}$$

We construct the Lagrangian to minimize the energy expression given above, with the constraint that the MRCC equations are satisfied for the μ^{th} state. Thus, for the μ^{th} state, the Lagrangian is given as,

$$\begin{aligned}\Im = {} & \sum_{ij} \tilde{C}^{(0,1)}_{\mu i} (H_{\mathit{eff}})^{(0,1)}_{ij} C^{(0,1)}_{j\mu} \\ & + P^{(0,1)} \Lambda^{(0,1)} P^{(0,1)} P^{(0,1)} [H\Omega - \Omega H^{(0,1)}_{\mathit{eff}}] P^{(0,1)} \\ & + P^{(0,1)} \Lambda^{(0,1)} Q^{(0,1)} Q^{(0,1)} [H\Omega - \Omega H^{(0,1)}_{\mathit{eff}}] P^{(0,1)} \\ & + P^{(0,0)} \Lambda^{(0,0)} Q^{(0,0)} Q^{(0,0)} H\Omega P^{(0,0)} \\ & - E_\mu \left(\sum_{ij} \tilde{C}^{(0,1)}_{\mu i} C^{(0,1)}_{j\mu} - 1 \right)\end{aligned} \tag{5}$$

The Λ in Eq. (5) are the Lagrange multipliers. In the complete model space case, the effective Hamiltonian has an explicit expression in terms of cluster operators, as a result of which, the closed part in the Lagrange multipliers vanishes. The Eq. (5) thus reduces to

$$\begin{aligned}\Im = &\sum_{ij} \tilde{C}^{(0,1)}_{\mu i} (H_{\mathit{eff}})^{(0,1)}_{ij} C^{(0,1)}_{j\mu} \\ &+P^{(0,1)}\Lambda^{(0,1)}Q^{(0,1)}Q^{(0,1)}[H\Omega - \Omega H^{(0,1)}_{\mathit{eff}}]P^{(0,1)} \\ &+P^{(0,0)}\Lambda^{(0,0)}Q^{(0,0)}Q^{(0,0)}H\Omega P^{(0,0)} \\ &-E_{\mu}\left(\sum_{ij}\tilde{C}^{(0,1)}_{\mu i}C^{(0,1)}_{j\mu} - 1\right) \end{aligned} \tag{6}$$

Differentiation of Eq. (6) with respect to Λ results into the equation for cluster amplitudes, i.e., the Bloch equation. Cluster amplitudes are decoupled from the Λ amplitudes. The Λ equations are also decoupled from the cluster amplitudes though they appear in the Λ) equations. Λ equations are solved by making Eq. (6) stationary with respect to the cluster amplitudes. In the presence of external field, the Lagrangian and the parameters $\Upsilon = \{H_{\mathit{eff}}, C, \tilde{C}, E, \Omega, \Lambda\}$ become perturbation dependent. These can be expanded in Taylor series.

$$\Upsilon(g) = \Upsilon^{(0)} + g\Upsilon^{(1)} + \frac{1}{2!}g^2\Upsilon^{(2)} + \frac{1}{3!}g^3\Upsilon^{(3)} + \ldots \tag{7}$$

The Lagrangian defined in Eq. (6) can be differentiated with respect to the field g to obtain the Lagrangians at every order. Energy derivative of the n^{th} order is just the Lagrangian of the corresponding order. Using the (2n+1) rule for cluster amplitudes and (2n+2) rule for Λ amplitudes, first and second order Lagrangian may be represented in terms of Λ, T and T' only. Thus, calculation of dipole moment and polarizability require the evaluation of T, T' and Λ. But, calculation of hyper-polarizability, which is the third order Lagrangian, requires the evaluation of Λ' along with T, T' and Λ. Λ' is evaluated by making the first order Lagrangian stationary with respect to the cluster amplitudes. The general expressions for the first, second and third order derivatives for one valence problem are presented in appendix of reference 44.

3 Implementational details

For one-valence problems nearest ionized or electron attached states should be chosen for SCF calculation which is the reference vacuum for FSMRCC. In general, results are irrespective of the choice of vacuum. However, it is necessary to mention that the vacuum should be chosen in a way such that required Fock space would be the lowest sector among all other possibilities and would be of same symmetry as target molecule. As it is mentioned above, using SEC, cluster amplitudes were evaluated starting from (0,0) sector to the highest sector but Λ amplitudes were calculated exactly in the reverse order. To solve (0,1) and (1,0) sector amplitudes, we first store $(He^{T^{(0,0)}})_c$, which is called $\bar{H}$. The closed part of $\bar{H}$, i.e. $\bar{H}_{cl}$ is the ground state energy. Open parts of $\bar{H}$ can further be classified into one body, two body, three body parts and so on. Under the singles and doubles (SD) approximation, only up to three body parts of $\bar{H}$ contribute to ($T^{(0,1)}$ and $T^{(1,0)}$ as well as to $\Lambda^{(0,1)}$ and $\Lambda^{(1,0)}$ equations. Following (n+1) rule for cluster amplitudes and (2n+1) rule for Λ amplitudes, derivatives of both these parameters were required for third order response properties and hence were evaluated for calculation of hyper-polarizability. The Jacobi iterative procedure has been used for the calculation of Λ and $\Lambda^{(1)}$ amplitudes as well as all Fock space cluster amplitudes. Ground state geometries of target molecules have been used for SCF calculation. We have compared the results of our analytic non-relaxed CVA-FSMRCC values with relaxed finite field FSMRCC results. For the latter, field perturbation was introduced at the SCF level itself. Relaxed finite field hyper-larizabilities were calculated as finite differences of polarizabilities using three points in steps of ± 0.001au finite field.

Table 1. Comparison of CVA-FSMRCC hyper-polarizability values of OF molecule with orbital relaxed finite field values. Z-axis is molecular axis. [All results are in atomic units.]

Basis	Property	CVA-FSMRCCSD	FF-FSMRCC
aug-cc-pVDZ	β_{zzz}	-18.75	-18.53
	$\beta_{yyy} = \beta_{xxx}$	0.02	0.00
Sadlej-pVTZ	β_{zzz}	-41.99	-43.70
	$\beta_{yyy} = \beta_{xxx}$	0.05	0.01

4 Results and discussion

In this section, we have presented some preliminary applications of non-relaxed CVA-FSMRCC method for calculation of static hyper-polarizability of a few doublet radicals; OH, OF, NO and NO_2. All of these molecules have an unpaired electron in ground state electronic configuration and hence ionized or electron attached states of these molecules have closed shell electronic configuration. With respect to the closed shell configuration mentioned above, respective molecule may be considered as one valence system. We have compared our non-relaxed CVA-FSMRCCSD results with relaxed finite field (FF) FSMRCCSD results.

Table 2. Comparison of CVA-FSMRCC hyper-polarizability values of OH molecule with orbital relaxed finite field values. Z-axis is molecular axis. [All results are in atomic units.]

Basis	Property	CVA-FSMRCCSD	FF-FSMRCC
aug-cc-pVDZ	β_{zzz}	-17.55	-22.50
	$\beta_{yyy} = \beta_{xxx}$	0.06	0.01
Sadlej-pVTZ	β_{zzz}	-12.86	-17.14
	$\beta_{yyy} = \beta_{xxx}$	0.01	0.00

Oxygen mono-fluoride radical can be viewed as ionized state of oxygen mono-fluoride anion resulting from removal of an electron from the HOMO which has π character. Thus, for FSMRCC calculations, RHF of oxygen mono-fluoride anion was chosen as vacuum. With respect to this vacuum, ground state of OF molecule may be considered as one hole problem. Two-fold degenerate HOMO was taken as active orbitals. For SCF calculation, ground state geometry of OF was used R_{eq}=2.5953 a_0 (Mckellar 1983) aug-cc-pVDZ and sadlej-pVTZ basis sets have been used for calculation. Calculated results have been presented in Table 1. The closeness of both CVA-FSMRCCSD and FF-FSMRCCSD values indicate that the orbital relaxation effect is less for this molecule. It was also found that hyper-polarizability component along molecular axis is larger than two other components reported here. It is obvious that as OF is linear $\beta_{xxx} = \beta_{yyy}$.

To calculate hyper-polarizability of OH radical, OH^- was chosen as reference vacuum with respect to which OH radical may be treated as one hole problem. aug-cc-pVDZ and sadlej-pVTZ basis sets have been used for this calculation. Two-fold degenerate HOMO of OH^- was chosen as active hole. O-H bond length used for this calculation is 1.85104 a.u. Calculated hyper-polarizabilities of OH molecule have been presented in Table 2. As expected, hyper-polarizability values of OH molecule along molecular axis are very large compare to that of perpendicular to molecular axis. For OH molecule, CVA-FSMRCCSD values widely differs from FF-FSMRCCSD values which shows significant contribution of orbital relaxation effect for finite field calculation.

NO molecule may be treated as electron attached state of NO^+ with respect to which NO molecule may be considered as one particle problem of FSMRCC. Two-fold degenerate LUMO π orbitals was chosen as active particles. Addition of one electron in one of the active orbitals results in the formation of the ground state of the corresponding radical. $^2\Pi$ state of NO molecule have been reported in two different basis sets; aug-cc-pVDZ and Sadlej-pVTZ. N-O bond distance has been used for this calculation is 2.15501 a.u. Calculated results have been presented in Table 3. For linear NO molecule, $\beta_{xxx} = \beta_{yyy}$. Again, hyper-polarizability components perpendicular to molecular axis were found to be very small compare to that of the principal axis. Here, differences of hyper-polarizability values between two methods are significant and hence orbital relaxation is large for this molecule. It was found that CVA-FSMRCCSD values were nearly same for two different basis sets, which is not true for FF-FMRCCSD method.

Table 3. Components of hyper-polarizability of NO molecule. Comparison with orbital relaxed finite field FSMRCC results. Z-axis is molecular axis. [All results are in atomic units.]

Basis	Property	CVA-FSMRCC	FF-FSMRCC
aug-cc-pVDZ	β_{zzz}	-11.99	-16.41
	$\beta_{xxx} = \beta_{yyy}$	0.01	0.00
Sadlej-pVTZ	β_{zzz}	-13.82	-21.30
	$\beta_{xxx} = \beta_{yyy}$	0.03	0.02

For NO_2 molecule, NO_2^+ was used as reference vacuum. Ground state geometry as quoted by Hayes (1999) was used for RHF calculation. LUMO of NO_2^+ is a σ orbital but there is another σ orbital in virtual space which is very close in energy to LUMO and hence these two orbitals were chosen as active particles. cc-pVDZ basis and DZP basis with sp diffuse functions were used for this calculation. Calculated results for the ground state of NO_2 have been presented in Table 4. As NO_2 is a non-linear molecule we have presented three principal components of hyper-polarizability. Hyper-polarizability component along principal axis was higher than two other components presented here. The most important fact, which was found from this calculation, is that the direction of the hyper-polarizability component of this molecule is opposite to the dipole moment. Hyper polarizability values were very small for this molecule for cc-pVDZ basis and also the relaxation effect. For DZP basis with sp diffuse function hyper-polarizability values increase significantly which due to the inclusion of diffusion function. Effect of orbital relaxation is prominent for this basis.

Table 4. Components of hyper-polarizability of NO_2 molecule. Comparison with orbital relaxed finite field FSMRCC results. Z-axis is molecular axis. [All results are in atomic units.]

Basis	Property	CVA-FSMRCC	FF-FSMRCC
cc-pVDZ	β_{zzz}	4.34	6.33
	β_{xxx}	0.27	0.05
	β_{yyy}	0.22	0.04
DZP+sp	β_{zzz}	8.38	8.69
	β_{xxx}	1.06	0.25
	β_{yyy}	0.92	0.17

5 Conclusion

In this article, analytic hyper-polarizability of OH, OF, NO and NO_2 molecules have been computed using newly developed CVA-FSMRCC method. CVA-FSMRCC values were compared with orbital relaxed finite field FSMRCC values. It was found that molecules with larger values of hyper polarizabilities show significant orbital relaxation effect. Except OF molecule, all three other molecules have shown large relaxation effect. It was also found that for all test molecules, direction of hyper-polarizability is same as that of dipole moment, except NO_2 molecule, where direction is just opposite.

Acknowledgement. A. Bag acknowledges Council of Scientific and Industrial Research (CSIR), India, for financial support. Funding from Department of Science and Technology (DST), India, is also acknowledged. Computational facilities of the Center of Excellence in Computational Chemistry at N. C. L., Pune, are also acknowledged. One of us (SP) acknowledges partial financial assistance from J. C. Bose Fellowship grand of DST and Shanti Swarup Bhatnagar (SSB) prize grant of CSIR towords this work. S. Bhattacharya acknowledges University Grant commission (UGC), India.

References

Ajitha, D.; Pal, S. Phys Rev A, **56**, 2658 (1997).
Ajitha, D.; Pal, S. Chem Phys Lett, **309**, 457 (1999a).
Ajitha, D.; Pal, S. J Chem Phys, **114**, 3380 (2001).
Ajitha, D.; Vaval, N.; Pal, S. J Chem Phys, **110**, 2316 (1999a).
Bag, A.; Manohar, P. U.; Pal, S. Comp Lett, **3**, 351 (2007).
Bag, A.; Manohar, P. U.; Vaval N.; Pal, S. J Chem Phys, **131**, 024102 (2009).
Balkova, A.; Kucharski, S. A.; Meissner, L.; Bartlett, R. J. J Chem Phys, **95**, 4311 (1991).
Bartlett, R. J. Annu Rev Phys Chem, **32**, 359 (1981).
Bartlett, R. J.; Stanton, J. F., Reviews in Computational Chemistry, edited by K.B. Lipkowitz and D.B. Boyd, (VCH, New York, 1994); Vol. 5, p65
Brooks, B. R.; Laiding, W. D.; Saxe, P.; Goddard, J. D.; Yamaguchi, Y.; Schaefer, H. F. J Chem Phys, **72**, 4652 (1980).
Chattopadhyay, S.; Sinha Mahapatra, U.; Datta, B.; Mukherjee, D. Chem Phys Lett, **357**, 426 (2002).
Čížek, J. Adv Quantum Chem, **14**, 35 (1969).
Comeau, D. C.; Bartlett, R. J. Chem Phys Lett, **207**, 414 (1993)
Durand, P.; Malrieu, J. P. Adv Chem Phys, **67**, 321 (1987).
Evangelisti, S.; Daudey, J. P.; Malrieu, J. P. Phys Rev A, **35**, 4930 (1987).
Frisch, M. J.; Head-Gordon, M.; Pople, J. A. Chem Phys Lett **166**, 275 (1990a).
Frisch, M. J.; Head-Gordon, M.; Pople, J. A. Chem Phys Lett, **166**, 281 (1990b).
Gauss, J.; Stanton, J. F. J Chem Phys 1996, **104**, 2574 (1996).
Gdanitz, R. J. Chem Phys Lett, **210**, 253 (1993).
Gdanitz, R. J.; Ahlrichs, R. Chem Phys Lett, **143**, 413 (1988).

Geertsen, J.; Rittby, M.; Bartlett, R. J. Chem Phys Lett, **164**, 57 (1989).

Graham, R. L.; Freed, K. F. J Chem Phys, **96**, 1304 (1992).

Haase, F.; Ahlrichs, R. J Comput Chem, **14**, 907 (1993).

Haque, A.; Kaldor, U. Chem Phys Lett, **117**, 347 (1985a).

Haque, A.; Kaldor, U. Chem Phys Lett, **120**, 261 (1985b).

Hayes, R. G. Magn Reson Chem 1999, **37**, 583 (1999).

Head-Gordon, M. Mol Phys, **96**, 673 (1999).

Helgaker, T.; Jaszunski, M,; Ruud, K. Chem Rev 1999, **99**, 293 (1999).

Helgaker, T.; Jørgensen, P. Theor Chim Acta 1989, **75**, 111 (1989).

Helgaker, T.; Jørgenson, P. Adv Quant Chem, **19**, 183 (1988).

Hirao, K. Chem Phys Lett, **190**, 374 (1992a).

Hirao, K. Chem Phys Lett, **196**, 397 (1992b).

Hirao, K. Chem Phys Lett, **201**, 59 (1993).

Hirao, K.; Hatano, Y. Chem Phys Lett, **111**, 533 (1984).

Jezioroski, B.; Monkhorst, H. J. Phys Rev A 1982, **24**, 1668 (1982).

Jörgensen, P.; Helgaker, T. J Chem Phys, **89**, 1560 (1988).

Hirao, K. J Chem Phys, **83**, 1433 (1985).

Koch, H.; Jörgenson, P. J Chem Phys, **98**, 325 (1993).

Krylov, A. I. Ann Rev Phys Chem, **59**, 433 (2008).

Kutzelnigg, W. J Chem Phys 1981, **77**, 3081 (1981)

Lindgren, I. Phys Scr, **32**, 291 (1985).

Lindgren, I.; Mukherjee, D. Phys Rep, **151**, 93 (1987).

Manohar, P. U.; Pal, S. Chem Phys Lett, **438**, 321 (2007a).

Manohar, P. U.; Pal, S., COMPUTATIONAL METHODS IN SCIENCE AND ENGINEERING: Theory and Computation: Old Problems and New Challenges. Lectures presented at the International Conference on Computational Methods in Science and Engineering 2007b, AIP Conf Proc 2007, 963, 337

Manohar, P. U.; Vaval, N.; Pal, S. J Mol Struct THEOCHEM, **768**, 91 (2006).

McDouall, J. J. W.; Peasley, K.; Robb, A. M. Chem Phys Lett, **148**, 183 (1988).

McKellar, A. R. W. J Mol Spectrosc, **101**, 186 (1983).

Monkhorst, H. J. Int J Quantum Chem, **S11**, 421 (1977).

Mukherjee, D. Pramana, **12**, 203 (1979).

Mukherjee, D. Proc Ind Acad Sci, **96**, 145 (1986a).

Mukherjee, D. Chem Phys Lett 1986, **125**, 207 (1986b).

Mukherjee, D. Int J Quant Chem Symp, **S20**, 409 (1986c).

Mukherjee, D.; Mukherjee, P. K. Chem Phys Lett, **39**, 325 (1979).

Mukherjee, D.; Pal, S. Adv Quantum Chem, **20**, 291 (1989).

Nakatsuji, H.; Kitao, O.; Komori, M., Aspects of Many Body Effects In Molecules and Extended Systems, Lecture Notes in Chemistry; Vol. 50, edited by Mukherjee, D.; Springer-Verlag; Heidelberg, 1989, p101.

Nakatasuji, H.; Hirao, K. J Chem Phys, **68**, 2053 (1978).

Nakatsuji, H.; Hirao, K J Chem Phys, **68**, 2053 (1978).

Nakatsuji, H. Chem Phys Lett, **67**, 324 (1979).

Neilsen, I. M. B. Chem Phys Lett, **255**, 210 (1996).

Nooijen, M.; Bartlett, R. J. J Chem Phys, **102**, 3629 (1995).

Nooijen, M.; Bartlett, R. J. J Chem Phys, **106**, 6449 (1997a)

Nooijen, M.; Bartlett, R. J. J Chem Phys, **107**, 6812 (1997b).

Nooijen, M.; Bartlett, R. J. J Chem Phys, **106**, 6441 (1997c).

Osamura, Y.; Yamaguchi, Y.; Schaefer, H. F. J Chem Phys, **77**, 383 (1982).

Pal, S. Phys Rev A, **39**, 39 (1989).

Pal, S. Int J Quantum Chem, **41**, 443 (1992).

Pal, S.; Rittby, M.; Bartlett, R. J.; Sinha, D.; Mukherjee, D. Chem Phys Lett, **137**, 273 (1987).

Pal, S.; Rittby, M.; Bartlett, R. J.; Sinha, D.; Mukherjee, D. J Chem Phys, **88**, 4357 (1988).

Pople, J. A.; Krishnan, R.; Schlegel, H. B.; Binkley, J. S. Int J Quantum Chem Symp, **S13**, 225 (1979).

Reitz, H.; Kutzelnigg, W. Chem Phys Lett, **66**, 11 (1979).

Salter, E. A.; Bartlett, R. J. J Chem Phys, **90**, 1767 (1989).

Salter, E. A.; Trucks, G.; Bartlett, R. J. J Chem Phys, **90**, 1752 (1989).

Shamasundar, K. R.; Asokan, S.; Pal, S. J Chem Phys, **120**, 6381 (2004).

Sinha, D.; Mukhopadhyay, S.; Mukherjee, D. Chem Phys Lett, **129**, 369 (1986).

Stanton, J. F.; Bartlett, R. J. J Chem Phys, **98**, 7029 (1993).

Stanton, J. F.; Gauss, J. J Chem Phys, **101**, 8938 (1994).

Szalay, P. Int J Quantum Chem, **55**, 151 (1995).

Tobota, M.;Perera, S. A.; Musial, M.; Bartlett, R. J.; Nooijen, M.; Lee, J. S. J Chem Phys, **119**, 10713 (2003).

"Recent Advances in Spectroscopy:
Theoretical, Astrophysical, and Experimental Perspectives"
Eds. Chaudhuri R K, Mekkaden M V, Raveendran A V, Satya Narayanan A
Astrophysics and Space Science Proceedings, Springer-Verlag, Berlin, 2010.

Chemical shielding of closed-shell molecules using Extended Coupled-cluster theory

Lalitha Ravichandran, Sayali Joshi, and Nayana Vaval

Physical chemistry Division, National Chemical Laboratory,
Pune 411008, India. `np.vaval@ncl.res.in`

Summary. In this paper we report calculation of the nuclear magnetic shielding constant using extended coupled cluster response approach. We present the results for the HF, BH, CO and N_2 molecules. These results show importance of correlation corrections for the shielding constant.

1 Introduction

The single-reference coupled-cluster (SRCC) theory (*Čížek* 1966; Paldus & *Čížek* 1973; Coester 1958; Cöoester & Kümmel 1960; Bartlett 1981; Sekino & Bartlett 1984a; Bartlett 1995) is one of the most accurate and widely used electronic structure method for studying ground state energy, properties and spectroscopy of closed-shell molecules at the equilibrium geometry (Monkhorst 1977; Pulay 1969; Pal, Prasad, & Mukherjee 1983; Bartlett & Noga 1988; Stanton & Bartlett 1993; Kally & Gauss 2006; Adamowicz *et al.* 1984; Fitzgerald & Harrison 1986; Salter & Bartlett 1989a). Due to its in-built size-extensivity and size-consistency property SRCC has been accepted as the state-of-the-art method for electronic structure and properties of atoms and molecules. Energy derivatives obtained through analytic response approach were first developed by Monkhorst (Monkhorst 1977). Traditional CC response approach based on non-variational method did not have a (2n+1)- rule inherent in it. As a result, the expression for the first order energy derivative involves the first derivative of the wave function with respect to the external perturbation. Which means one needs to evaluate wave function derivatives with respect to all modes of perturbation for the first order property. This problem was overcome by Bartlett and co-workers (Fitzgerald & Harrison 1986; Salter & Bartlett 1989b). They implemented the idea of algebraic z-vector method introduced by Handy and Schaefer (Handy & Schaefer 1984) based on Dalgarno's interchange theorem (Dalgarno & Stewart 1957). The method is known as the Z-vector technique. This development made the non-variational CC method viable for the computation of energy derivatives, using only one extra set of perturbation-independent variables, solved through a linear equation. This and the subsequent developments by Bartlett and coworkers (Adamowicz *et al.* 1984; Fitzgerald & Harrison 1986; Salter & Bartlett 1989b) substantially facilitated efficient implementation of molecular energy gradients for SRCC, and significantly contributed to its success in quantum chemistry. However, Z-vector type of approach turned out to be a tedious job for higher-order properties such as Hessian's, polarizabilities, etc. On the other hand, a conceptually different approach, using a constrained variation method (CVM), proposed by Jørgensen and coworkers (Helgaker & Jørgensen 1988; Koch *et al.* 1990) was more useful. This approach is based on the formation of Lagrangian functional which is easily applicable to higher order energy derivatives (Jørgensen & Helgaker 1988; Helgaker & Jørgensen 1989; Helgaker, Jaszunski & Ruud 1999). Constrained variation approach involves recasting of the standard SRCC equation in a stationary framework by introducing an extra set of de-excitation amplitudes. It was shown that this method includes the Z-vector method as a zeroth-order result and transparently extends its benefits to higher-order properties. Parallel to these developments, Pal (Pal 1984,1990,1986) proposed a fully stationary response approach. In this approach choice of the energy functional is very important. Initial implementation was based on the expectation-value (XCC) functional (Pal & Ghose 1992; Ghose, Nair & Pal 1993; Ghose *et al.* 1994). The XCC functional, however, is a non-terminating series and the stationary equations resulting from the functional were truncated to a fixed power in cluster amplitudes contain disconnected terms. Bartlett and co-workers (Bartlett & Noga 1988; Bartlett *et al.* 1989) used the truncation scheme based on the order of perturbation for the XCC and Unitary CC (UCC) functional. This scheme of truncation leads to connected series, however, it is computationally expensive to implement this approach beyond third order of perturbation.

Extended coupled cluster (ECC) functional based on a double-similarity transformation of the Hamiltonian is other energy functional implemented by Pal and co-workers (Vaval *et al.* 1994; Vaval & Pal 1996; Vaval *et al.* 2001). The ECC functional developed by Arponen and co-workers (Arponen 1993; Arponen *et al.* 1987; Bishop *et al.* 1987), uses bi-orthogonal vectors and is shown by Arponen to have a special double-linking structure. Linear form of the left amplitudes gives SRCC equations when differentiated with respect to the left amplitudes. This double linking structure of the bi-orthogonal or ECC functional not only ensures natural termination of the series, but also provides fully connected amplitude equations, even when truncated to a fixed power in number of cluster amplitudes. Being variational, method enjoys the advantage of (2n+1)-rule i.e. it satisfies Hellmann Feynman theorem. The natural termination of the functional occurs at high order and for the practical purpose needs to be truncated. CC response approach is extensively used for the electric properties (Vaval *et al.* 1994; Vaval & Pal 1996; Vaval *et al.* 2001; Bartlett & Noga 1988; Bartlett *et al.* 1989) however, there are not many reports on magnetic properties (Manohar *et al.* 2004; Helgaker, Jaszunski & Ruud 1999). Magnetic response property calculations are not straight forward like electric response properties. The Hamiltonian of the system in the presence of external magnetic field depends on the gauge of the magnetic vector potential. Proper gauge origin should hence be chosen for the evaluation of the magnetic properties (London 1937). Various attempts were made earlier at the SCF level (London 1937; Ditchfield 1972, 1974; Hameka 1958; Kussmann & Ochsenfelda 2007) as well as correlated levels (Kutzelnigg *et al.* 1993; Coriani *et al.* 1998; Gauss 1994, 1992; Gauss & Stanton 1996, 1995a,b) to eliminate the problem of gauge-variance of magnetic properties to some extent. Recently Manohar *et al.* (Manohar *et al.* 2004), reported the ECC response for magnetizability of the closed shell molecules. GIAO-based techniques have been implemented for the coupled-cluster singles and doubles (CCSD) (Gauss 1993) method as well as for the CCSD(T) approach (Gauss & Stanton 1995a) in which triple excitation effects are approximated based on perturbative guidelines. Coupled-cluster calculations of NMR shifts have been very successful in achieving experimental accuracy especially when partial triples are included. However, when system is dominated by non-dynamic correlation it is important to use multi-determinantal based theory like multi-configurational SCF (MCSCF) (Kutzelnigg *et al.* 1993; Coriani *et al.* 1998). While CCSD and CCSD(T) appear to be the best approaches for highly accurate calculations in most cases it is computationally very expensive.

In this paper we report the shielding constant for the closed shell molecules using extended coupled cluster response approach. Section 1.1 discusses theory of the shielding constant and CC response approach. Results and discussion on them are presented in Section 1.2. Section 2 gives conclusions.

1.1 Theory

The theory of nuclear magnetic resonance (NMR) and electron paramagnetic resonance (EPR) (Kaupp *et al.* 2004; Helgaker, Jaszunski & Ruud 1999) parameters is the study of an atom or a molecule in external homogeneous magnetic field of different origin. Inclusion of electron correlation effects is very important for the accurate prediction of nuclear magnetic shielding constants and the related NMR chemical shifts. At least for molecular calculations with atom-centered basis functions, center of mass represents the preferred choice of gauge origin. Nuclear magnetic shielding tensor is a mixed second-order energy derivative. Calculation of NMR chemical shifts thus requires evaluation of a second derivative of the energy with respect to the magnetic field and nuclear magnetic moment. The perturbation involved is a imaginary perturbation, transforming the real wave function of the unperturbed molecule into complex field-dependent wave-function. Thus, magnetic properties, unlike electric properties and other second-order quantities, cannot be computed easily using numerical differentiation techniques. Hence, development of analytic response approach for the calculation of magnetic properties was necessary and represented the main bottleneck in the development of correlated schemes for the calculation of chemical shifts.

The Hamiltonian in the presence of a magnetic field can be written as

$$H = H_0 + \sum_j \frac{\partial H}{\partial B_j} B_j + \sum_N \sum_i \frac{\partial H}{\partial m_i^N} m_i^N + \\ \sum_N \sum_i \sum_j \frac{\partial^2 H}{\partial B_j \partial m_i^N} B_j m_i^N + \cdots \tag{1}$$

H_0 is the usual field-free, non-relativistic Hamiltonian of a molecule and the perturbation contributions are given by

$$\frac{\partial H}{\partial B_j} = \frac{1}{2} \sum_k ((r_k - R_o) \times P_k) \tag{2}$$

$$\frac{\partial H}{\partial m_i^N} = \alpha^2 \sum_k ((r_k - R_N) \times P_k)_i / \mid r_k - R_N \mid^3 \tag{3}$$

$$\frac{\partial^2 H}{\partial B_j \partial m_i^N} = \frac{\alpha^2}{2} \sum_k (r_k - R_o)(r_k - R_N)\delta_{ij} - (r_k - R_o)_i (r_k - R_N)_j / \mid r_k - R_N \mid^3 \tag{4}$$

Where r_k and P_k are the position and momentum operators for the kth electron, R_o is the gauge origin, R_N represents the position of the Nth nucleus and α is fine structure constant.

The tensor element of NMR shielding constant can be computed as the corresponding second derivative of the electronic energy

$$\sigma_{ij}^N = \left(\frac{\partial^2 E}{\partial m_i^N \partial B_j} \right)_{B=0; m_i^N=0} \tag{5}$$

Similar to the magnetizability, shielding constant also has diamagnetic and paramagnetic component. In the case of closed shell molecule the diamagnetic nuclear spin -electron orbit operator contributes to the shielding constant. Diamagnetic contribution can be obtained through expectation value approach. For the paramagnetic shielding constant we need the response of the wave function. Thus, we need to get the derivative of the CC cluster amplitudes with respect to the nuclear magnetic moment first, then we evaluate the derivative of the cluster amplitudes with respect to the magnetic field.

Only, after having obtained both the derivative cluster amplitudes we can get the paramagnetic contribution for the shielding constant. For the calculation of NMR shielding we have used fully variational CC response approach based on extended coupled cluster functional. Variational methods satisfy Hellman -Feynman theorem which is very useful for the higher order properties. This Means with the help of first order response wave-function we can calculate the properties up to third order. The form of the energy functional in ECC is

$$E_0 = \langle \phi_0 \mid e^S (He^T)_L \mid \phi_0 \rangle_{DL} \tag{6}$$

where, L means linked and DL is double linked. This makes functional naturally terminating and we never end up with disconnected diagrams for the amplitude equations. Thus the properties obtained using this functional are size-extensive. Though the functional is naturally terminating it terminates at quite high order and needs truncation for the practical application. We have used the singles and doubles (CCSD) approximation. Thus, within CCSD approximation we have included all the terms for the one and two body $\bar{H} = ((He^T)_{conn,open})$in the energy as well as derivative energy functional. We can see that we have two set of amplitudes D and T. Thus, the price one pays to get terminating series is double the number of amplitudes as well as double the number of equations. To get the equation for the cluster amplitudes we differentiate energy expression with respect to t as well as s. For the derivative amplitude equations we differentiate derivative energy expression with respect to the unperturbed t and s amplitudes only. For the details of the ECC response see refs. (Vaval *et al.* 1994; Vaval & Pal 1996; Vaval *et al.* 2001).

The cluster amplitudes of S and T operators as well as those of the derivative $S^{(1)}$ and $T^{(1)}$ operators are obtained using a stationary condition. The double-linked nature of the functional guarantees that the terms generated by the deletion of a vertex from the energy/energy derivative diagram remains connected. Thus, the stationary equations resulting from the variation of the functional with respect to the cluster amplitudes are themselves connected. This yields the equations for the amplitudes of the cluster operators S and T, denoted as $s^{(0)}$ and $t^{(0)}$. The following set of equations are solved to obtain the above amplitudes: (7)

$$\frac{\delta E}{\delta t^{(0)}} = 0; \frac{\delta E}{\delta s^{(0)}} = 0$$

The functional, at the stationary point, E_{stat} , has a simplified structure, due to the stationary condition of cluster amplitudes. To obtain the derivative amplitude equations, one makes the derivative energy functional $E^{(1)}$ stationary with respect to the ground state $s^{(0)}$ and $t^{(0)}$ amplitudes. This explicit derivative functional depends on the amplitudes $s^{(0)}$,$t^{(0)}$, $s^{(1)}$ and $t^{(1)}$. Thus, the equations

$$\frac{\delta E^{(1)}}{\delta t^{(0)}} = 0; \frac{\delta E^{(1)}}{\delta s^{(0)}} = 0 \tag{7}$$

provide us with the equation for $s^{(1)}$ and $t^{(1)}$ amplitudes. The double-linked structure of the $E^{(1)}$ leads to the connectivity of the terms in the equations for derivative cluster amplitudes. The resulting higher order properties (up to first hyper-polarizability) are thus fully size-extensive.

Table 1. Nuclear magnetic shielding constants values of B in BH. All results are in *ppm*.

Basis	Method	σ^d_{xx}	σ^d_{zz}	σ^p_{xx}	$\bar{\sigma}$
cc-pVQZ ^{11}B	SCF	214.01	198.81	-708.31	-263.26
	ECC	214.03	199.55	-619.75	-203.97
	MCSCF	214.09	199.71	-570.47	-171.02
cc-pV5Z ^{11}B	SCF	214.01	198.82	-713.08	-266.43
	ECC	214.00	199.53	-624.58	-207.21
	MCSCF	214.09	199.71	-573.88	-173.30
	FCI (Gauss & Rudd 1995)				-170.08
	Extrapolated FCI				-183.08
cc-pVQZ ^{1}H	SCF	17.77	33.63	2.53	24.75
	ECC	18.19	33.66	2.15	24.90
	MCSCF	18.28	33.69	2.33	24.97
cc-pV5Z ^{1}H	SCF	17.72	33.64	2.83	24.90
	ECC	18.11	33.65	2.41	24.89
	MCSCF	18.22	33.69	2.60	25.12
	FCI (Gauss & Rudd 1995)				24.60
	Extrapolated FCI				24.90

1.2 Results and Discussion

In this paper we report the shielding constants for some closed shell molecules using extended coupled cluster method. The nuclear magnetic shielding constant σ can be defined as the second derivative of the energy with respect to the external magnetic field B and a nuclear magnetic moment m_N. In the perturbation formulation, the shielding constant can be written in terms of a diamagnetic and paramagnetic contribution, where the former is calculated as an expectation value of the diamagnetic shielding operator (DS) while the latter is calculated as a response property of the paramagnetic spin-orbit (PSO) and orbital Zeeman (LG) operators. It is known that electron correlation and basis set plays important role in the accurate determination of nuclear magnetic shielding constants. Here we report absolute values of shielding constants. In particular for magnetic properties it is very important to have large basis sets to counter gauge origin problem. Thus, we have chosen a basis set of at least valence triple- zeta quality. We report the shielding constants for the HF, BH, N_2 and CO molecules. For BH and N_2 we have used cc-pVXZ (X=QZ,5Z) without g and h functions, whereas for Hydrogen fluoride and carbon monoxide molecules we used cc-pVTZ and cc-pVQZ basis sets. We compare our results with the MCSCF results obtained using DALTON program (Dalton). We also compare with the experimental values wherever results are available. For boron hydride we have used cc-pVQZ and cc-pV5Z basis without g and h functions. The bond distance used was $1.2328\AA$. We perform MCSCF calculations in the same basis using 4 electrons and 15 active orbitals as our CAS space. We observe that the effect of electron correlation is large for the paramagnetic component compared to the diamagnetic shielding constant for Boron. The electron correlation reduces paramagnetic component of the shielding constant by 12% in ECC and almost by 20% in MCSCF method compared to SCF values in case of Boron in BH molecule. For BH we report the full configuration interaction (FCI) results available for triple zeta plus basis as well as extrapolated FCI value (Gauss & Rudd 1995). These results are obtained using a large basis set. Though, the FCI results are not in a basis we have used but it can be used to get the qualitative trend of the correlated shielding values compared to SCF. Coupled cluster overestimates the shielding constant compared to FCI value. With larger basis it enhances, same trend is observed for FCI as well as MCSCF. Table 1 reports the results for the shielding constant of ^{11}B and ^{1}H in BH. For ^{1}H we observe ECC values are in good agreement with the MCSCF as well as extrapolated FCI values. Hydrogen fluoride is another system studied for the shielding constant. We have used cc-pVTZ and cc-pVQZ basis without any g functions. Table 2 reports results for the diamagnetic and paramagnetic components of the shielding constants of Fluorine as well as Hydrogen in HF. Here too we compare our results with the experimental (Raynes 1978; Hindermann & Cornwell 1968) as well as MCSCF results obtained using 4 electrons and 10 orbitals. With increase in basis set paramagnetic component of the shielding reduced and total shielding constant value is in good agreement with the experimental shielding constant. CC results are in good agreement with the MCSCF results. For ^{1}H in hydrogen fluoride both the basis set gives good results compared to experimental value (Jameson *et al.* 1981). For hydrogen, change in shielding constant is very small as basis set convergence is almost reached.

It is interesting to study the shielding constants for molecules with multiple bond. Nitrogen and carbon monoxide are interesting systems for the study of magnetic shielding constants. We have studied ^{15}N in cc-pVQZ and cc-pV5Z without any g and h functions. We also report MCSCF results obtained using rather small active space of 4 electrons and 6 orbitals. It can be seen that the paramagnetic component of the shielding constant is reduced considerably by electron correlation in coupled cluster method for both the basis sets, whereas in MCSCF it is not so. In fact, as we go from cc-pVQZ to cc-pV5Z basis coupled cluster reduces the paramagnetic component of the shielding, although in MCSCF it increases. Compared to experiment, coupled cluster underestimates the shielding constant, whereas MCSCF is in good agreement with the experiment. Discrepancy of the CC could be attributed

Table 2. Nuclear magnetic shielding constants values of HF

Basis	Method	σ^d_{xx}	σ^d_{zz}	σ^p_{xx}	$\bar{\sigma}$
cc-pVTZ ^{1}H	SCF	8.77	44.13	12.04	28.59
	ECC	8.88	44.46	12.29	28.93
	MCSCF	9.82	44.44	12.14	29.45
cc-pVQZ ^{1}H	SCF	8.48	44.07	11.67	28.13
	ECC	9.49	44.34	11.80	28.98
	MCSCF	9.49	44.37	11.73	28.96
^{1}H	Expt.(Raynes 1978)				28.5±0.2
cc-pVTZ ^{19}F	SCF	481.88	481.75	-112.36	406.93
	ECC	481.90	481.52	-115.07	405.06
	MCSCF	481.98	481.74	-111.84	407.03
cc-pVQZ ^{19}F	SCF	481.81	481.69	-104.21	412.29
	ECC	481.89	481.48	-106.91	410.64
	MCSCF	481.97	481.81	-104.04	412.99
^{19}F	Expt.(Raynes 1978)				410±6

to the relaxation missing at the CCSD level. Inclusion of partial triples may improve results. MCSCF introduces relaxation which may be the reason why MCSCF, though is done over smaller space, is closer to experimental values. Table 4 reports shielding constants for ^{13}C and ^{17}O in cc-pVTZ and cc-pVQZ basis without any g functions. We compare our results with the MCSCF results obtained using 10 electrons and 12 active orbitals. It can be seen from the Table 4, that the paramagnetic component of the shielding for ^{13}C is reduced in both the basis sets by almost 9% due to electron correlation. ECC as well as MCSCF predicts positive shielding constant, whereas SCF gives negative shielding constant. Thus, effect of electron correlation is seen to be important for ^{13}C. However, neither ECC nor MCSCF is closer to the experimental results. Though, CC gives considerably less value compared to MCSCF. For the ^{17}O we observe shielding constant is reduced in ECC and MCSCF compared to SCF considerably emphasizing the effect of electron correlation. Both ECC and MCSCF are in close agreement to each other.

2 Conclusion

In this paper we report the shielding constants for the Hydirdes BH and HF along with multiple bonded systems N_2 and CO. Accuarate calculation of shielding constant is by far more challenging as values for the shielding are very sensitive to the basis set chosen and electron correlation effects. We see that for the ^{1}H in HF and BH basis set limit is almost reached and hence shielding constant is closer to the experimental or FCI value. However, for other cases we have not reached the basis set limit. In particular for multiple

Table 3. Nuclear magnetic shielding constants values of N_2 in *ppm*

Nuclear shielding constants in N_2					
Basis	Method	σ^d_{xx}	σ^d_{zz}	σ^p_{xx}	$\bar{\sigma}$
cc-pVQZ ^{15}N	SCF	362.67	338.70	-681.46	-99.62
	ECC	363.02	339.56	-597.12	-42.89
	MCSCF	362.96	339.30	-618.42	-57.21
cc-pV5Z ^{15}N	SCF	361.89	338.71	-639.82	-108.38
	ECC	362.77	339.57	-589.05	-37.66
	MCSCF	362.73	339.31	-621.60	-59.48
^{15}N Expt.(Jameson *et al.* 1981)					-61.6±0.2

Table 4. Nuclear magnetic shielding constants values of CO

C and O nuclear shielding constants in CO *ppm*					
Basis	Method	σ^d_{xx}	σ^d_{zz}	σ^p_{xx}	$\bar{\sigma}$
cc-pVTZ ^{13}C	SCF	297.77	271.10	-459.78	-17.64
	ECC	297.13	272.66	-417.48	11.32
	MCSCF	298.30	272.74	-413.48	13.52
cc-pVQZ ^{13}C	SCF	297.12	271.03	-461.58	-7.77
	ECC	297.63	272.60	-427.11	4.54
	MCSCF	299.68	272.63	-419.55	9.05
^{13}C Expt.(Jameson & Jamenson 1987)					3.0±0.9
cc-pVTZ ^{17}O	SCF	430.54	410.46	-754.65	-74.25
	ECC	430.93	410.08	-681.87	-30.60
	MCSCF	430.98	410.00	-689.43	-36.11
cc-pVQZ ^{17}O	SCF	431.95	410.48	-760.49	-83.50
	ECC	430.47	410.18	-694.37	-39.17
	MCSCF	430.45	410.24	-639.30	-39.07
^{17}O Expt.(Wasylishen 1984)					-42.3±17.2

bonded systems it might be useful to choose basis sets with more tight S functions. Partial inclusion of triples might improve results.

Acknowledgement. Authors acknowledge Department of Science and Technology (DST) India, for the financial support. One of the authors (LR) thank CSIR for financial support. Computational facilities of the Center of Excellence in Scientific Computating at N. C. L., Pune, are also acknowledged.

References

Adamowicz L., Laidig W. D., Bartlett R. J., *Int. J. Quantum Chem.* **S18**, 245 (1984).

Arponen J., *Annals. Phys.* **151**, 311-382 (1983).

Arponen J., Bishop R. F., Pajanne E., *Phys. Rev. A* **36**, 2519 (1987).

Bartlett R. J., *Annu. Rev. Phys. Chem* **32**, 359-402 (1981).

Bartlett R. J., *In Modern Electronic Structure Theory* D. R. Yarkony, Ed.; World Scientific Singapore, 1995; 1047.

Bartlett R. J., Kucharshi S. A., Noga J., *Chem. Phys. Lett.* **155**, 133-140 (1989).

Bartlett R. J., Noga J. *Chem. Phys. Lett.* **150**, 29-36 (1988).

Bishop R., Arponen J., Pajanne E., *Phys. Rev. A.* **36**, 2519-2538 (1987).

Čížek J., *J. Chem. Phys.* **45**, 4256-4266 (1966).

Cöester F., *Nucl Phys* **1**, 421 (1958).

Cöester F., Kümmel H, *Nucl Phys* **17**, 477 (1960).

Coriani S., Jaszunski M., Rizzo A., Ruud K., *Chem. Phys. Lett.* **287**, 677 (1998).

Dalgarno A., Stewart A. L., *Proc. R. Soc. London, Ser. A* **238**, 269 (1957).

Ditchfield R., *J. Chem. Phys* **56**, 5688 (1972).

Ditchfield R., *J. Chem. Phys* **27**, 789 (1974).

Dalton 2.0 C. Angeli, K. L. Bak, V. Bakken, O. Christiansen, R. Cimiraglia, S. Coriani, P. Dahle, E. K. Dalskov, T. Enevoldsen, B. Fernandez, C. Httig, K. Hald, A. Halkier, H. Heiberg, T. Helgaker, H. Hettema, a H. J. Aa. Jensen, D. Jonsson, P. Jrgensen, S. Kirpekar, W. Klopper, R. Kobayashi, H. Koch, A. Ligabue, O. B. Lutns, K. V. Mikkelsen, P. Norman, J. Olsen, M. J. Packer, T. B. Pedersen, Z. Rinkevicius, E. Rudberg, T. A. Ruden, K. Ruud, P. Salek, A. Sanchez de Meras, T. Saue, S. P. A. Sauer, B. Schimmelpfennig, K. O. Sylvester-Hvid, P. R. Taylor, O. Vahtras, D. J. Wilson, and H. Agren,

Fitzgerald G. B., Harrison R. J., Bartlett R. J., *J. Chem. Phys.* **85**, 5143 (1986).

Gauss J. *Chem. Phys. Lett* **191**, 614 (1992).

Gauss J., *J. Chem. Phys.* **99**, 3629 (1993).

Gauss J. *Chem. Phys. Lett.* **229**, 198 (1994).

Gauss J., Stanton J. F., *J. Chem. Phys.* **104**, 2574 (1996).

Gauss J., Stanton J. F., *J. Chem. Phys.* **102**, 251 (1995a).

Gauss J., Stanton J. F., *J. Chem. Phys.* **103** 3561 (1995b).

Gauss J., Ruud K., *Int. J. Quantum Chem. Symp.* **29**, 437 (1995)

Ghose K. B., Nair P. G., Pal S., *Chem. Phys. Lett.* **211**, 15 (1993).

Hameka H., *Mol. Phys* **1**, 203 (1958).

Handy N.C., Schaefer III H.F., *J. Chem. Phys.* **81**, 5031 (1984).

Helgaker T., Jaszunski M, Ruud K., *Chem. Rev.* **99**, 293 (1999).

Helgaker T., Jørgensen P., *Theor. Chim. Acta.* **75**, 111 (1989).

Helgaker T., Jørgensen P., *Adv. Quant. Chem.* **19**, 183 (1988).

Hindermann D. K., Cornwell C. D., *J. Chem. Phys.* **48**, 4148 (1968).

Jameson C. J., Jameson A. K., Oppusunggu D., Wille S., Burrell P., Mason J., *J. Chem. Phys.* **81**, 74 (1981).

Jameson A. K., Jameson C. J., *Chem. Phys. Lett.* **134**, 461 (1987).

Jørgensen P., Helgaker T., *J. Chem. Phys.* **89**, 1560 (1988).

Kally M., Gauss J., *J. Mole. Struc. THEOCHEM* **768**, 71 (2006).

Kaupp M., Bühl M., Malkin V. G., *Calculation of NMR and EPR Parameters: Theory and applications* Wiley-VCH (2004).

Koch H., Jensen H. J. A., Jørgensen P., Helgaker T., Scuseria G. E., H. F. Schaefer III H. F., *J. Chem. Phys.* **92**, 4924 (1990).

Kussmann J. and Ochsenfelda C., *J. Chem. Phys.* **127**, 054103 (2007)

Kutzelnigg W., van Wüllen W. C., Fleischer U., Franke R., Mourik T. V., *In Nuclear Magnetic Shieldings and Molecular Structure; Tossell, J. A., Ed.; NATO ASI series; Plenum: New York,* (1993).

London F. J., *Phys. Radium* **8**, 397 (1937).

Manohar P.U., Vaval N., Pal S., *Chem. Phys. Lett.* **387**, 442 (2004).

Monkhorst H., *J. Inter. J. Quantum Chem* **S11**, 421-427 (1977).

Pal S, *Theor. Chim. Acta.* **66**, 151 (1984); *Phys. Rev.A* **42**, 4385 (1990). *ibid* **34**, 2682 (1986).

Pal S., Ghose . B., *Cur. Sci.* **63**, 667 (1992).

Pal S. , Prasad M. D., Mukherjee D., *Theor. Chim. Acta.* **62**, 523 (1983).

Paldus J., *Čížek* J., *in Energy, Structure and Reactivity* D. W. Smith, Mcrae. Ed. Wiley, NY 1973.

Pulay P., *Mol. Phys* **17**, 197-204 (1969).

Raynes W. T., *Nucl. Magn. Reson.* **7**, 1 (1978).

Salter E., Trucks T. W., Bartlett R., J., *J. Chem. Phys* **90**, 1752 (1989a).

Salter E. A., Bartlett R. J., *J. Chem. Phys.* **90**, 1767 (1989b).

Sekino H., Bartlett R. J., *Int. J. Quantum Chem. Symp.* **18**, 255–263 (1984a).

Stanton J. F., Bartlett R. J., *J. Chem. Phys.* **99**, 5178 (1993).

Vaval N., Ghose K. B., Nair P. G., Pal S., *Proc. Ind. Acad. Sci.* **106**, 387 (1994).

Vaval N., Ghose K. B., Pal S., *J. Chem. Phys* **101**, 4914 (1994).

Vaval N., Kumar A. B., Pal S.: *Int. J. Mol. Sci.* **2**, 89 (2001).

Vaval N., Pal S., *Phys. Rev. A* **54**, 250 (1996).

Wasylishen R. E., Mooibroek S., Macdonald J. B., *J. Chem. Phys.* **81**, 1057 (1984)

“Recent Advances in Spectroscopy:
Theoretical, Astrophysical, and Experimental Perspectives”
Eds. Chaudhuri R K, Mekkaden M V, Raveendran A V, Satya Narayanan A
Astrophysics and Space Science Proceedings, Springer-Verlag, Berlin, 2010.

Multi-Disciplinary Role of Atomic Astrophysics: From Stellar Interiors to Cancer Research Via Nanotechnology

Anil K. Pradhan[1,2], Sultana N. Nahar[1], Maximiliano Montenegro[1], Enam A. Chowdhury[3], Kaile Li[4], Chiranjib Sur[5], and Yan Yu[6]

[1] Department of Astronomy, The Ohio State University, Columbus Ohio 43210, USA pradhan.1@osu.edu
[2] Chemical Physics Program, Department of Chemistry, The Ohio State University
[3] Department of Physics, The Ohio State University
[4] Radiation Oncology Division, The Ohio State University Medical School
[5] High Performance Computing Group, IBM India Software Lab, Bangalore 560 071, India, chiranjib.sur@in.ibm.com
[6] The Thomas Jefferson University Medical College, Philadelphia, PA 19107, USA yan.yu@jefferson.edu

Summary. We discuss the application of atomic physics to two diverse topics: Astrophysical opacities that determine the flow of radiation through the interior of stars, and biomedical research using nanotechnology for novel methodologies for cancer diagnostics and therapy (theranostics). Recent determination of solar abundances suggests that a re-examination of the absolute accuracy of these opacities might be in order. A discussion of the Opacity Project work and possible sources of missing opacity and uncertainties in atomic data is presented with a view to possible solution of the solar abundances problem. Another major application is shaping up in biomedicine and nanotechnology: A paradigm change and transition from conventional broadband X-ray imaging (such as in CT scanners or common X-ray sources) to precision monochromatic spectroscoppy for cancer theranostics. A novel methodology — Resonant Theranostics — is proposed to exploit K_α resonances due to deep inner-shell transitions that trigger Auger processes in heavy elements. The methodology can be used to build laboratory monochromatic X-ray sources for imaging using K_α emission, as well as for therapy using K_α absorption by high-Z nanoparticles or radiosenstizing agents embedded in cancerous tumors. This review of recent work demonstrates the scope and power of multi-disciplinary research in general, particularly highlighting the role of atomic physics as an enabling scientific tool from astronomy to medicine.

1 Introduction

Over two decades ago two independent projects — the Opacity Project (hereafter OP [Seaton et al. 1994; Opacity 1995]) and OPAL ([Rogers & Iglesias 1992], and references therein) — were initiated to revise the then available astrophysical opacities. The efforts were launched in response to a “plea for re-examination” [Simon 1982] of the older Los Alamos opacites, that failed to account for basic observed phenomena such as the Cepheid pulsation period ratios when incorporated in stellar interior models. As is now well known, both OP and OPAL resulted in considerably higher opacities, by factors of 2-3 or higher, and did indeed solve the Cepheid and other problems. Both projects involved an enormous effort, but employed quite different physical formulations for opacities calculations, for the atomic physics methods to compute the basic atomic data and the equations-of-state (EOS). Nevertheless, the final OP and OPAL results converged for the crucial quantity of interest, the Rosseland Mean Opacity (RMO), to within 10%.

However, in recent years several lines of investigation have revealed problems in stellar astrophysics related to opacities. The foremost is the unexpectedly large discrepancy in solar surface abundances, long regarded as the ‘standard’, and accurately determined from spectroscopy. But recently derived abundances from elaborate 3-D Non-Local-Thermodynamic-Equilibrium (NLTE) convection models imply a reduction in the most abundant light metals (CNONe) by an astounding 30-45% [Asplund et al. 2005]. This discrepancy and possible causes have been amply discussed in literature (an extensive discussion is given by Basu and Antia [Basu and Antia 2008]). The new reduced abundances are in serious conflict with those derived from accurate observations from helioseismology and stellar interior models.

Stellar opacity is the common feature in stellar models. More to the point, the *absolute* accuracy of opacities directly determines the uncertainties in the models. The inverse relationship between opacities and abundances is obvious (To wit: Any increase in opacities would lead to commensurately lower abundances). It is estimated that an increase between 11-21% around the base of the solar convection zone $R_\odot(CZ) = 0.73R_\odot$ (Log T $\approx$ 6.34) may greatly ameloriate the situation. $R_\odot(CZ)$ is the boundary between the radiative and the convection zone, and is one of the tightly constrained parameters from helioseismology. Analyzing many stellar models, Basu and Antia ([Basu and Antia 2008]) note that at least an increase of 10% is required (also J. Bahcall, private communication). Thus we face the conundrum: The required increase is more than the level of agreement between OP and OPAL, but numerically not by a large amount compared to the enhancement already achieved. The logical conclusion is that higher precision is needed.

Advances in theoretical methods in the intervening two decades since the OP now enable much more accurate and consistent atomic data to be computed. A number of these developments were carried out by the group at OSU, partially under the follow-up project to the OP called the Iron Project

(Hummer et al. 1993; www.astronomy.ohio-state.edu/~pradhan). At the same time, the availability of high-performance massively parallel computational platforms also makes it possible now to undertake more accurate recalculation of opacities.

2 The Need for Re-examination of Opacities

This critical discussion entails the atomic physics of missing opacity, accuracy, and consistency of OP data. In the OP work about two decades ago we devoted considerable effort to compute atomic data using the state-of-the-art R-matrix method [Hummer et al. 1993]. A primary feature of the R-matrix method is the inclusion of radiative excitations via autoionizing resonances in photoionization cross sections. But its application to large-scale calculations necessitated compromises in accuracy, as described in the seminal paper summarising the OP work ([Seaton et al. 1994]). Some of these were: neglect of relativistic fine structure, high-energy cross sections, and inner-shell excitations.

In addition to accuracy, a bigger problem turned out to be completeness. The R-matrix calculations (even the non-relativistic version employed in the OP) became too cumbersome for the codes and computational resources available at that time. Therefore, a considerable amount of radiative data was computed with a much simpler method, using the atomic structure code called SUPERSTRUCTURE. For example, most of the data for iron ions Fe VIII–XIII was thus obtained (referred to as the PLUS data in [Seaton et al. 1994]). Based on OPAL work, it was known that these Fe ions are of crucial importance around the so-called Z-bump, vital for Cepheid pulsation models around Log (T) $\approx$ 5.2–5.3. That is because there are a huge number of M-shell transitions $n = 3 \longrightarrow n' \geq 3$. The problem with the inner-shell data was also redressed in the past few years using another version of SUPERSTRUCTURE [Seaton & Badnell 2004].

Could there still be some atomic data that might result in missing opacity? In spite of the inclusion of inner-shell data, the outer-shell atomic data in the revised OP calculations remained the same Seaton et al. 1994. Therefore, a number of resonance complexes corresponding to several Rydberg series of levels were not included. Many calculations since the OP work, particularly under the Iron Project by the OSU group, have shown that outer-shell radiative excitations into autoionizing resonances that lie *below* the inner-shell ionization energies are excluded. Fig. 1 compares photoionization cross sections of an excited state of two ions in the Boron isolelectronic sequence, O III and Fe XXI, from OP and from more recent work. The cross sections exhibit huge *photoexcitation-of-core* (PEC) resonances (first identified by Yu and Seaton [Seaton et al. 1994]). These complexes of (PEC) resonances converge on to the inner-shell ionization threshold energy with a large jump. But the crucial fact is that the effective cross sections are much higher than the

OP data, and enhanced throughout the $n = 2 - 3$ energy range by up to two orders of magnitude.

As inferred from Fig. 1, the missing opacity may lie in an energy range from few eV to few hundreds of eV, depending on the element and ionization stage. Low-lying excited states of most ionization stages of abundant elements exhibit similar structures. This could be of direct relevance at temperatures and densities up to $R_{\odot}(CZ)$ around Log $T \sim 6$.

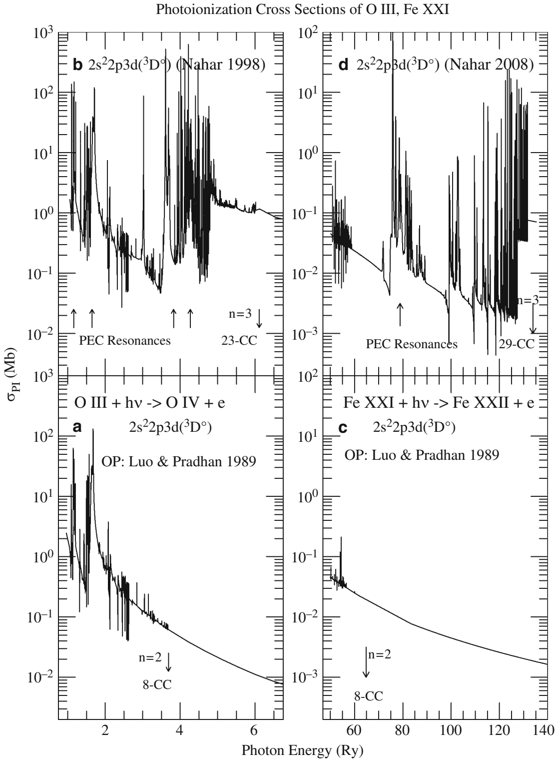

Fig. 1. Missing resonances in photoionization cross sections of C-like O and Fe: bottom panels (a,c) — OP data, top panels (b,d) — more recent calculations which show that large resonance complexes were not included in OP data, and could account for some missing opacity. Note the abscissa in Rydbergs. References: Nahar 1998 [Nahar 1998], Luo and Pradhan [Seaton et al. 1994].

Apart from limited treatment of atomic structure, affecting accuracy and resulting in missing resonances, the OP atomic calculations were non-relativistic and in LS coupling. Therefore, a siginificant omission is that of intercombination transitions that involve spin-change but are permitted by change in parity and angular momentum. Although the total line strength in intercombination lines is only a fraction of that in dipole allowed transitions (no spin-change), both are E1 transitions and the effect is of the order of 15–20%. A limited number of intercombination lines ($n \leq 6$) were included later [Seaton & Badnell 2004]. But, as mentioned above, since most of the OP data for Fe ions does *not* employ the R-matrix method, we expect the *absolute accuracy* to be no better than the OPAL data also computed using an atomic structure code (with a parametrized atomic potential). Therefore it would not be surprising if it is ascertained that there are systematic uncerainties in both the OP and OPAL data.

Although much of fine structure splitting is subsumed by line broadening, a proper treatment should incoroporate relativistic fine structure more accurately than the current OP data. In the past few years, members of the OSU group, especially former graduate student G.X. Chen in collaboration with W. Eissner, have developed an extended version of the relativistic R-matrix method in the Breit-Pauli approximation used in the Iron Project work [Hummer et al. 1993]. The OP data were computed or obtained in a variety of approximations and sources. In particular, the iron data was from six different sources, which raises some concern about consistency if not accuracy. And it was known that the loss of accuracy owing to restricted approximations for the low-ionization stages of iron Fe I–V, and other Fe-group elements, was especially severe [Seaton et al. 1994; Seaton & Badnell 2004]. It therefore became necessary to include the corresponding transition probabilities from other sources. Although low ionization stages do not affect the RMOs in a signficant manner, they are crucial in computing radiative accelerations, and may well account for some of the large differences between OP and OPAL [Delahaye & Pinsonneault 2006].

3 Opacity and Radiation Force

Once the opacity is known, the radiative force exerted by photons on a given atom may be readily computed, and photon absorption and scattering processes are responsible for radiation pressure. Opacities and radiative accelerations computed by OP have been made available from an electronic dataserver called OPSERVER (Mendoza et al. [Mendoza et al. 2007]), located at the Ohio Supercomputer Center at OSU and accessible from: *http://opacities.osc.edu.* Fig. 2 is a schematic diagram for the computation of OP opaciites.

It is a non-trivial task to process all of the archived atomic data for proper input into the opacities code. It involves interface and mapping of data at computing energies onto a photon-frequency mesh. The standard variable for mapping is $u = h\nu/kT$. We define a "Rosseland window" in the range $-2.5 \leq Log\ u \leq 1.5$, which samples the monochromatic opacity with a given number of mesh points. Given the frequency-temperature correlation from the EOS, and the Planck function, the u-range is chosen so as to ensure that there is negligible contribution to opacity for any ion from outside the Rosseland window. This task is performed by the code INTERFACE (Pradhan,

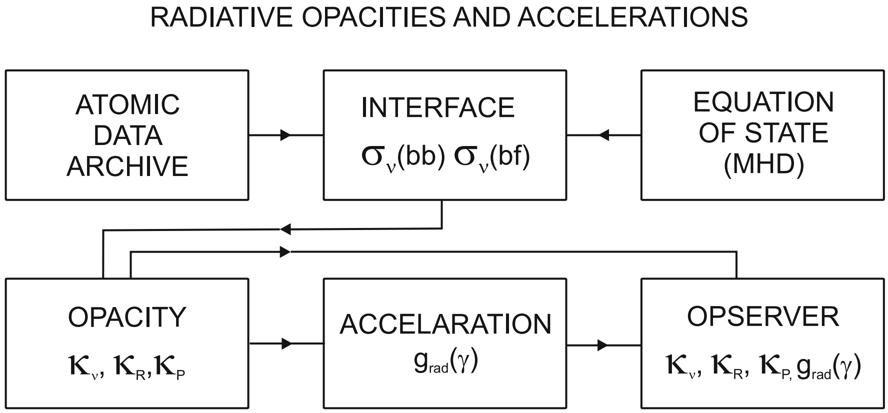

Fig. 2. Schematic diagram of OP opacities computations.

unpublished), which also computes radiative line damping parameters using the bound-bound radiative transition probabilities, labeled as 'bb-data' which contains f-values for all allowed and intercombination E1 transitions. INTERFACE maps and produces the bb files as wells the files for bound-free photoionization cross sections, labeled as bf files, for each ion.

The MHD EOS code [Seaton et al. 1994] independently produces tables of ionization fractions, scattering contributions, Stark broadening, and other parameters. The first calculation would be to use the standard EOS data as in the current OP. Later steps would follow as mentioned above.

The opacities code OPACITY requires the bb and bf atomic data files from INTERFACE and the EOS tables. Calculations for the monochromatic opacity κ_ν are carried out for each ion along isotherms in *Log T* for a range of Log electron densities N_e. It is also useful to tabulate results along the variable $\mathrm{R} = \rho/T_6^3$ ($T_6 = T \times 10^{-6}$) defined by OPAL. The Rosseland Mean Opacity κ_R is defined in terms of κ_ν as

$$\frac{1}{\kappa_R} = \frac{\int_0^\infty g(u)\frac{1}{\kappa_\nu}du}{\int_0^\infty g(u)du}, \quad g(u) = u^4 e^{-u}(1 - e^{-u})^{-2}, \tag{1}$$

where $g(u)$ is the Planck weighting function corrected for stimulated emission. The κ_ν is primarily a function of the oscillator strengths f, photoionization cross sections σ_ν, level populations N_i, and the line profile factor ϕ_ν,

$$\kappa_\nu^{bb}(i \rightarrow j) = \left(\frac{\pi e^2}{m_e c}\right) N_i f_{ij} \phi_\nu, \qquad \kappa_\nu^{bf} = N_i \sigma_\nu. \tag{2}$$

Fig. 3 illustrates κ_ν(Fe IV) recently computed using the more accurate and extensive radiative R-matrix calculations by Nahar and Pradhan [Nahar & Pradhan 2005] including fine structure, compared to the original OP data. The difference in the Rosseland means is up to 50% at the (T, N_e) shown (close to maximum abundance of Fe IV). Although the Nahar and Pradhan calculations were also in LS coupling, they used a much larger wavefunction expansion than in the OP work. As noted, for such reasons the final OP calculations used the more complete bb data for lines of Fe I–V from the Kurucz database (R.L .Kurucz: www.harvard.edu/amp, which also includes fine structure). Fig. 3 shows the importance of completeness, but the accuracy issue is unresolved.

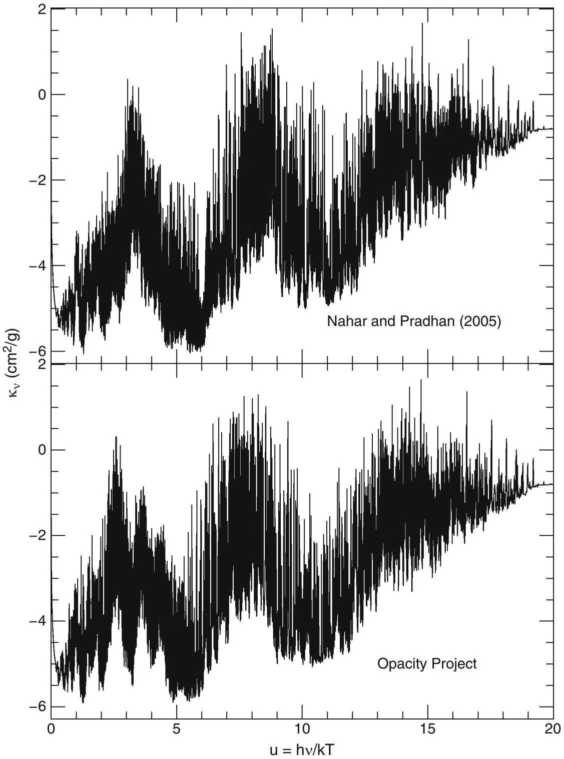

Fig. 3. Monochromatic opacity of Fe IV at Log T(K) = 4.5 and Log $N_e(cm^{-3}) = 17$ — Recent calculations using new R-matrix calculations with fine structure (Nahar and Pradhan [Nahar & Pradhan 2005]), and the original OP data [Seaton et al. 1994]. Although the overall features look similar, there are considerable differences in detail and in Rosseland Mean Opacities of 10-50%.

4 SUMMARY: The Opacity Project and the Solar Abundance Problem

The possible solution to fundamental problems with solar models that have emerged in recent years appears to lie in stellar opacity. Helioseismology, equations-of-state, solar abundances, and stellar interiors models, are discordant in surprising and unexpected manner. The practical necessity of solving this problem can hardly be overstated, owing to the Sun as the standard that is the key to understanding much of astrophysics. As noted by stellar researchers, a 10-20% revision of opacities would go a long way to resolving many discrepancies. At the same time, the minimum uncertainties in atomic physics are at least in that range if not much higher. In addition, computed theoretical data reveal several sources of missing opacity or *systematic* inaccuracy in the approximations employed.

5 From Stellar Opacities to Resonant Theranostics

In summary, there is some uncertainty in existing opacities calculations owing to the fact that resonances due to inner-shell excitations have not yet been fully included. Related effects such as autoionization widths, and plasma broadening, are not accounted for. However, the *resonance phenomena* so extensively studied under the OP have found a novel, and surprising, application in biomedical physics aimed at cancer diagnostics and therapy (theranostics) using nanotechnology.

6 Resonant Theranostics

Recently, we have proposed an integrated scheme for X-ray Resonant Theranostics (therapy and diagnostics) along these lines [Silver et al. 2008; Pradhan et al. 2009; Montenegro et al. 2009] based on resonant monochromatic X-ray sources. X-rays interact efficiently with high-Z elements and many radiosensitized reactive agents are molecular compounds or moieties containing heavy elements, such as bromodeoxyuridine (BUdR), iododeoxyuridine (IUdR) and cisplatin (cis-Pt) with bromine, iodine, and platinum ($Z = 35, 53$, and 78) respectively. BUdR and IUdR are widely used in medical imaging, cisPt or Cyclo-Pt are utilized in cancer therapy. The high-Z elements undergo Auger fluorescence when irradiated by X-rays at energies, for example, above the ionization energy of the innermost (K) shell. Radiation induced ionization of atoms can cause DNA strand breakups in malignant cells. Low-energy electrons resulting from Auger breakups can cause single and double strand DNA breakups via electron attachment resonances (references in [Pradhan et al. 2009]).

However, while X-ray interaction with heavy elements is well known, the detailed physical properties of high-Z elements are relatively unknown, either experimentally or theoretically. The problem becomes progressively more difficult with Z, especially for elements at the high-end of the periodic table such as gold, which is finding increasing usage in nanobiotechnology. Gold is generally non-reactive and therefore ideal for constructing nanoparticles for medical use for *in vivo* treatment. Laboratory experiments using gold nanoparticles injected into mice tumors, and then irradiated with high energy 140-250 keVp X-rays, have shown considerable reduction in tumor sizes [Hainfield et al. 2004; Cho 2005]. Gold is particularly appropriate for such experiments owing to its non-toxicity and high Z (= 79). Nanoparticle form entails sizes from a few to a few tens of nm, and in principle sufficient to penetrate cell vascula provided the size is < 30 nm or so. X-ray irradiation then enhances the radiation dose uptake, with consequent damage to the malignant cells with embedded nanoparticles.

6.1 Broadband vs. Monochromatic X-rays Sources

The broadband radiation sources employed in these experiments are the generally available X-ray generators in medical facilities. They are X-ray sources with energy output in the form of a bremsstrahlung spectrum, and deliver radiation up to the stated peak voltage. The shape of the output bremsstrahlung spectrum extends up to the peak voltage (kVp) between the cathode and the anode of the generating X-ray tube. Most of the flux from traditional X-ray sources covers an extremely broad range, well over half the total energy range, and a maximum around 1/3 the peak value [Sundaraman et al. 1973]. For example, for a 250 kVp source the X-ray output ranges between 40-250 keV photon energies, with a broad maximum around ~80keV. Since the Au K-edge $E_I(K) = 80.729$ keV, a 250 kVp source is capable of ionizing all inner n-shells and subshells of the gold atom with L,M,N,O,P edges at approximately 12-14, 3.4-2.2, 0.11-0.9, 0.01-0.11, 0.0.009 keV respectively. Of course, much higher energy accelerators are also in common medical usage, say those with up to 6 MVp peak voltage and a broad maximum around 2 MeV.

The main problem with using broadband bremsstrahlung X-ray sources (ordinary devices, accelerators, or CT scanners) is as follows. The low-energy $\sim$ 10-30 keV) flux is absorbed by body tissue close to the skin before reaching the desired target (e.g. tumor); at the same time high-energy X-rays (> 1 MeV) barely interact with the light elements and compounds (e.g. H_2O). Therefore, both the low-energy and the high-energy X-rays are inefficient in terms of proper medical use in imaging or therapy. For optimal usage and to obviate unnecessary exposure to healthy tissue the incident X-rays should be in precisely the right energy range, which can be pre-determined, commensurate with dosimetric parameters such as depth and shape as well as the particular physical chemistry of the radiosensitizing agents. But relatively high energy X-rays still are needed to ensure sufficient penetration and to minimize photoabsorption which scales roughly as E^{-3} [NIST]. With the exception of the K-edges, the photoionization cross section decreases rapidly with energy and the efficiency of radiation absorption diminishes. Therefore, the incident X-rays need to be not only monochromatic but also pre-selected for maximum interaction cross sections. While it is promising that irradiation and subsequent breakup of high-Z atoms may be a useful tool in cancer theranostics, the precise interaction of X-rays as a function of incident energy and the target atomic structure needs to be studied in order to understand and improve the techniques and the concepts involved. The primary aim of this review is to outline, in principle, the theranostical efficacy of monochromatic X-rays with high-Z elements.

But while broadband X-ray sources are generally used in medical practice, narrow-band or monochromatic X-ray sources such as synchrotron based devices and laser produced plasmas are available [Zhavoronkov et al. 2005; Andiel et al. 2001; Moribayashi et al. 2001; Berger & Motz 2004]. The most useful characteristic of these sources is their capability to generate monochromatic beams of high intensity photon fluxes. Indeed it is well known that the output spectra of ordinary X-ray tubes prominently display $K\alpha, K\beta$ emission lines superimposed on a bremsstrahlung background [Sundaraman et al. 1973], and can be easily isolated, albeit with lower X-ray fluxes which may still be used for diagnostic imaging. Devices widely employed in X-ray atomic physics such as the Electron-Beam-Ion-Traps may be used as possible monochromatic sources [Silver et al. 2008]. In addition, advances are being made in generating ultrashort K-shell radiation using femtosecond laser pulses impinging on thin solid material [Reich et al. 2000]. These sources can be utilized not only for basic studies of matter at atomic and molecular scales, but also to probe materials at nanoscales for applications to nanotechnology and biomedical imaging and spectroscopy. Large energy deposition in a small target would produce a transient plasma on short time scales. It is of interest to investigate the material properties of such ‘plasmoids’, and to ascertain the related physical constants as a function of the incident X-ray energy and nuclear charge Z all along the Periodic Table, and other extrinsic parameters such as density and size of the targeted material.

6.2 Auger Processes: Monochromatic X-ray Diagnostics and Therapeutics

The relevant atomic and molecular computations are extremely difficult owing to the fact that both the relativistic effects and many-electron correlation effects need to be considered explicitly. Moreover, careful attention needs to be paid to the energy dependence on the incident photon energy, particularly in energy ranges where resonant phenomena occur with large transition probabilities and cross sections. Available cross sections for attenuation of X-rays by the atoms of different elements have been computed using atomic physics methods that yield only the background cross sections, as from the on-line databases at the *National Institute for Standards and Technology* (NIST: www.nist.gov [NIST]). For molecular systems containing a given high-Z element, we assume that the dominant X-ray interaction is with that element.

Fig. 4 shows these photoelectric attenuation coefficients for high-Z neutral Fe and Au, compared with a low-Z element O.

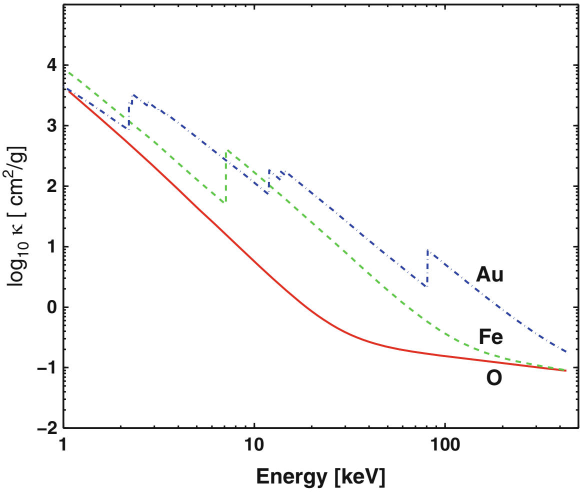

Fig. 4. Background photoabsorption attenuation coefficients κ NIST for neutral O, Fe, and Au. The rise in κ at various energies correspond to ionization edges of the K, L, M (sub)-shells of Au, and the K-shell of Fe. The oxygen K-edge lies at 0.53 keV and is not seen (from [Pradhan et al. 2009]).

K-shell ionization may be initiated by any photon with energy above the K-edge. As shown in Fig. 5, that would trigger Auger decays leading to a cascade of secondary photon emission and electron ejection. The most probably decay is K_α emission, that occurs with fluorescence yield of over 95% in the L → K transition in high-Z atoms [Pradhan et al. 2009].

6.3 Monochromatic X-ray Emission for Imaging

Using a broadband X-ray source, such as readily available in medical facilities and which produce a bremsstrahlung output spectrum from an ordinary X-ray tube, we can generate pure monochromatic K_α radiation. Perhaps the earliest example to scatter broadband radiation and isolate a monochromatic wavelength was in 1923 when Arthur Compton demostrated the Compton effect in [Compton 1923a,b]. He used a Molybdenum anode X-ray tube to reflect X-rays from a graphite plate at different angles: 45, 90, and 135 degrees. That produced monochromatic Mo K_α X-rays which were then scattered from a crystal to measure the wavelength shift precisely using the Bragg formula. However, Compton noted that while eliminating the bremsstrahlung background, the intensity of Mo K_α radiation was reduced by a factor of 1/25000.

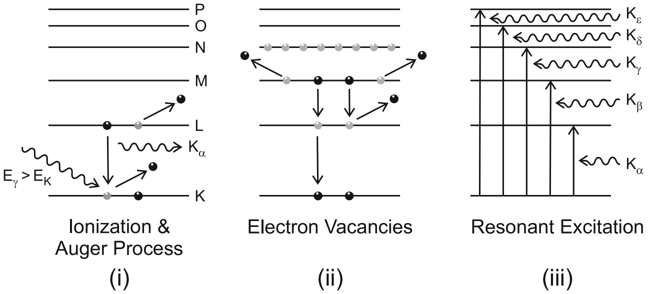

Fig. 5. The Auger process and resonant excitation (from [Pradhan et al. 2009]: (i) K-shell ionization, $K\alpha$ emission and/or L-shell Auger electron emission, (ii) multiple electron vacancies created by K-shell ionization due to Auger electron ejections from higher shells and radiative decays, (iii) resonant excitation from the K-shell to higher shells by $K\alpha$, $K\beta$, etc. by incident photons. The gold atom has electronic shells up to $n = 6$, or the P-shell.

A gas cell or solid target of high-Z material may be irradiated by an X-ray tube that produces broadband bremsstrahlung radiation. The K_α radiation would be emitted isotropically and may be detected perpendicular to the primary X-ray beam at 90 degrees, as in the classic Compton configuration or adaptation thereof. X-ray imaging can then be carried out using monochromatic K_α emission, with little background (as noted by Compton in 1923!) and vastly reduced radiation exposure compared to the broadband X-ray source itself. Since the K_α emission is isotropic, it is reduced by a geometric factor of $1/4\pi$ in any given direction. A cylindrical configuration to ameliorate this problem is proposed by Huang et al. [Huang et al.], who also carry out Monte Carlo simulations using the code GEANT4 (see also Montenegro et al. [Montenegro et al. 2009]).

6.4 Monochromatic X-ray Absorption for Therapeutics

For resonance driven therapeutics we can utilize any K_α source of sufficient intensity for resonant absorption following K-shell ionization. Since each K-shell ionization produces one or two L-shell vacancies [Pradhan et al. 2009], resonant K_α absorption can be achieved. For example, we may use an ordinary X-ray tube that produces bremsstrahlung radiation up to 100 keV. If the target is gold (Z = 79) with K-edge at ∼81 keV, then it can produce K_α radiation at ∼68 keV for imaging of a target made of another element, or a combination of elements such as in body tissue. The therapeutics mechanism is complemetary to imaging. We can resonantly excite gold atoms from the K-shell thereby reversing or enhancing the efficacy of Auger cascades. Resonant threrapeutics can be utilized for optimally localized energy deposition at energies corresponding to Au K_α emission/absorption at 68 keV, as well as higher resonances due to excitation from the K-shell, as shown in Fig. 5 (iii) and via resonances in Fig. 6.

Using the transition probabilities for excitation from the K-shell into L,M,N,O and P shells of gold ions, calculated by Nahar et al. [Nahar et al. 2008], we compute resonant attenuation coefficients shown in Fig. 6 from Pradhan et al. [Pradhan et al. 2009]. The resonant excitation cross sections in Fig. 6 can be orders of magnitude higher than the background cross sections for Au in Fig. 4.

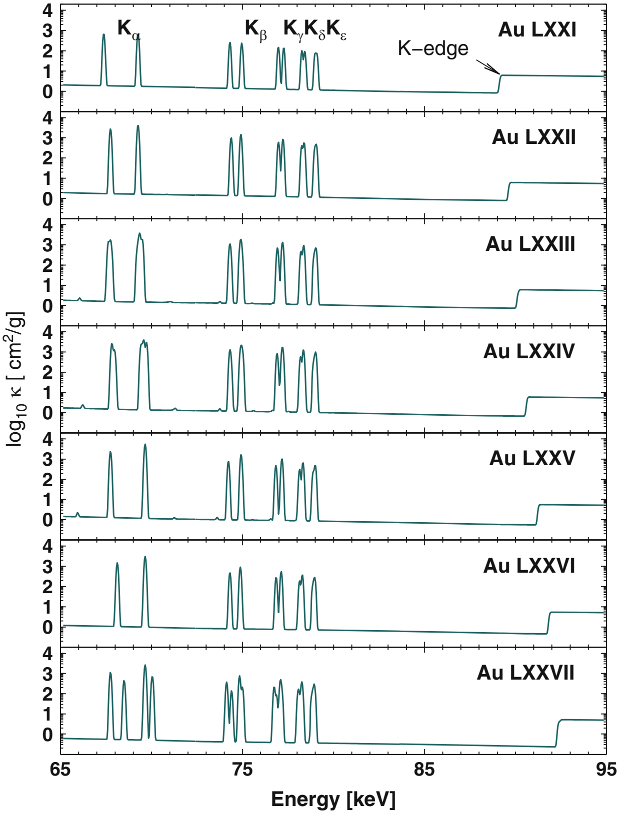

Fig. 6. Total resonant K-shell and non-resonant X-ray mass attenuation coefficients $\kappa(cm^2/g)$ for gold ions (note the log scale on the Y-axis). The resonances correspond to excitation probabilities for K_α , K_β , etc. transitions in gold ions with F-like (top panel) to Li-like (bottom panel) ion cores. Resonant cross sections can be orders of magnitude higher than the K-edge jump on the extreme right.

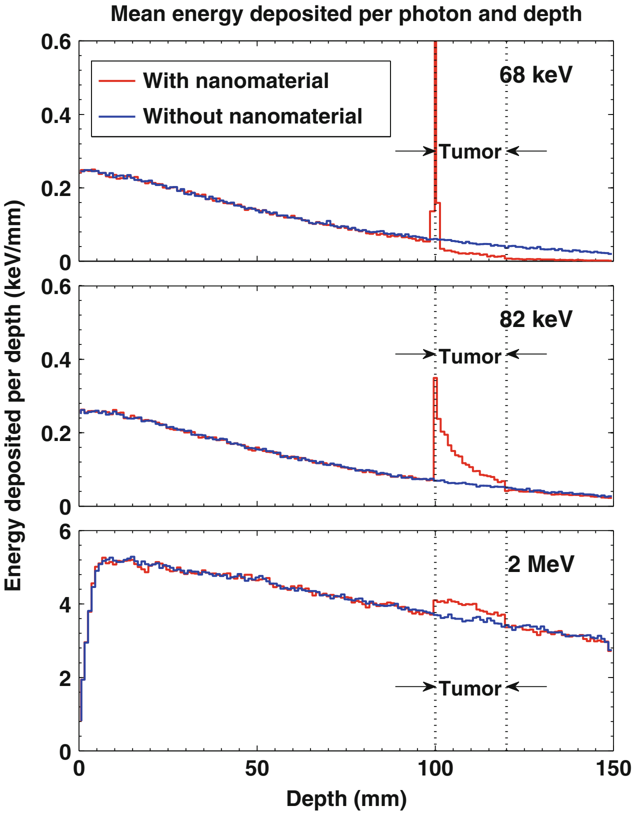

Fig. 7. Energy deposited by depth across a water phantom with a 2 cm tumor, injected with gold nanoparticles, at a depth of 10 cm in the body. Resonant energy absorption is shown for three monochromatic X-ray beams: top panel — 68 keV (averaged Kα resonant energy); middle panel — 82 keV (K-edge energy), and bottom panel — 2 MeV (high energy). The region between 100 and 120 mm represents the tumor embedded with gold nanoparticles at concentration of 5 mg/ml. The presence of gold nanoparticles increases the energy deposited at the tumor site; this effect is strongest at the resonant K_α energy (top panel) and least at the highest energy 2 MeV. The K-edge energy at $\sim$ 82 keV has significant absorption, but much less than at 68 keV by several factors.

6.5 Monte Carlo Simulations of Resonant Absorption by Gold Nanoparticles

Montenegro et al. [Montenegro et al. 2009] have carried out numerical simulations using the Monte Carlo code GEANT4. They model a phantom that simulates a tumor located 10 cms inside the body and embedded with gold nanoparticles. Three irradiating monochromatic X-ray sources are considered: (i) the resonant K_α energy 68 keV, (ii) just above the K-shell ionization energy, 82 keV, where the K-shell photoionization cross section is at its maximum

(Fig. 4), and (iii) a very high energy of 2 MeV characterstic of the energy where the bremsstrahlung X-ray spectrum from linear accelerators has a broad peak. High energy linear accelerators are used as broadband X-ray sources for deeper penetration in the body for imaging and therapy. The three sets of results from GEANT4 simulations are illustrated in Fig. 7. It is seen that resonant K_α absorption at 68 keV can lead to a sharp peak indicating that complete absorption takes place at that energy, in contrast to less efficient absorption following the K-edge at 82 keV.

7 Conclusion

We have attempted to highlight the diversity and the range of multi-disciplinary applications of atomic physics by focusing on two major scientific problems, one in astronomy and the other in biomedicine.

We would like to acknowledge support from the Large Interdisciplinary Grants award from OSU for Computational Nanoscience on Fundamental Atomic and Molecular Scales. The computational work was carried out at the Ohio Supercomputer Center in Columbus Ohio.

Disclaimer: The material presented is that of the author (CS) and IBM is not responsible or liable for any information presented in this paper.

References

Andiel U., Eidmann K., and Witte K., Phys. Rev. E 63, 026407 (2001).

Asplund M., Grevesse N., Sauval A. J., Cosmic Abundances as Records of Stellar Evolution and Nucleosynthesis: In ASP Conf. Ser., Vol. 336, 25, (2005).

Basu S. and Antia H. N., Physics Reports, 457, 217 (2008).

Berger M. and Motz J. W., Nucl. Inst. and Meth. in Phys. Res. B 226, 327 (2004).

Cho S. H., *Phys. Med. Biol.* **50**, N163 (2005).

Compton A. H., Physical Review, 21, 494 (1923a).

Compton A. H., Physical Review, 22, 409 (1923b).

Delahaye F. and Pinsonneault M., *Astrophys. J.*, 649, 529 (2006).

Hainfield J. F., Slatkin D. N., and Smilowitz H. M., *Phys. Med.Biol.* **49**, N309 (2004).

Huang K., Pradhan A. K., Nahar S. N, Montenegro M., Yu Y., 31st Annual International IEEE EMBS Conference (in press).

Hummer D. G., Berrington K. A., Eissner W., Pradhan A. K., Saraph H. E., and Tully J. A., *Astron. Astrophys.* **279**, 298 (1993).

Mendoza C., Seaton M. J., Buerger P., Bellorin A., Melendez M., Gonzalez J., Rodriguez L. S., Palacios E., Pradhan, C.J. Zeippen, *Mon. Not. R. astr. Soc.*, 378, 1031 (2007).

Montenegro M., Nahar S. N., Pradhan A. K., Huang K., Yu Y., J. Phys. Chem. A 113, 12364 (2009).

Moribayashi K., Sasaki A., and Zhidkov A., Phys. Scr. T92, 185 (2001).

Nahar S. N., *Physical Review A* 58, 3766 (1998).

Nahar S. N. and Pradhan A. K., *Astron. Astrophys.*, 437, 345 (2005). **2008**, *21*, 30.

Nahar S. N., Sur C., and Pradhan, A. K., JQSRT, 109, 1951 (2008).

National Institute for Standards and Tchnology, Physical Reference Data (www.nist.gov/Phys.Ref.Data).

The Opacity Project Team, *The Opacity Project* Vols. 1 & 2, Institute of Physics Publishing (1995).

Pradhan A. K., Nahar S. N., Montenegro M., Yu Y., Zhang H. L., Sur C., Mrozik M., Pitzer R. M., J. Phys. Chem. A 113, 12356 (2009).

Reich C., Gibbon P., Uschmann I., and Förster E., *Physical Review Letters* 84, 4846 (2000).

Rogers F. J. and Iglesias C. A., *Astrophys. J. Supp. Ser.*, 79, 507 (1992).

Seaton M. J. and Badnell N. R., *Mon. Not. R. astr. Soc.*, 354, 457 (2004).

Seaton M. J., Yu Y., Mihalas D., and Pradhan A. K., *Mon. Not. R. astr. Soc.* 266, 805 (1994).

Silver E., Pradhan A. K., and Yu Y., *RT Image*, 21, 30 (2008).

Simon N. R., *Astrophys. J.*, 260, L87 (1982).

Sundararaman V., Prasad M. A., and Vora R. B., Phys. Med. Biol. 18, 208 (1973).

Zhavoronkov N., Gritsai Y., Bargheer M., Woerner M., and Elsaesser T., Appl. Phys. Letts. 86, 244107 (2005).

"Recent Advances in Spectroscopy:
Theoretical, Astrophysical, and Experimental Perspectives"
Eds. Chaudhuri R K, Mekkaden M V, Raveendran A V, Satya Narayanan A
Astrophysics and Space Science Proceedings, Springer-Verlag, Berlin, 2010.

Recent Developments in Polarized Line Formation in Magnetic Fields

K. N. Nagendra, M. Sampoorna, and L. S. Anusha

Indian Institute of Astrophysics, Bangalore 560 034, India. `knn@iiap.res.in`

Summary. The nature of solar surface magnetism has been an open problem in solar physics. In this paper we address three frontline problems of spectropolarimetry of the Sun. We first review the theoretical formulation and numerical solutions of Zeeman absorption and then the Hanle scattering phenomena in 'turbulent magnetic fields'. We show that the mean emergent Stokes profiles cannot be obtained by simply averaging the scattering and absorption opacities, respectively, over a given distribution of the random field (except when the micro-turbulence prevails). A new formulation of the transfer equation is necessary to study the astrophysically interesting meso-turbulence case. Such formulations of the stochastic polarized radiative transfer problems for absorbing and scattering media are developed only in recent years. We review them and show some results computed by our new formulations.

Until recent years the solution of the polarized line radiative transfer equation in LTE (Zeeman absorption in strong fields), and its NLTE counterpart (Hanle scattering in weak fields), were treated as two disparate problems. The reason for this artificial division was more due to the theoretical and numerical difficulties encountered in the solution of the combined Hanle-Zeeman radiative transfer equation. A very general form of the transfer equation was formulated only a decade ago, for the case of complete frequency redistribution. A more difficult case of partial frequency redistribution is explored by us recently. We review these developments through a study of the Hanle-Zeeman effect in arbitrary strength magnetic fields.

1 Introduction

The radiative transfer equation represents one of the most fundamental equations in astrophysics. It is an energy balance equation that describes the transmission and reflection (scattering) of radiation in a stellar atmosphere. In a general form it describes the non-equilibrium thermodynamic processes responsible for the net outflow of radiant energy from the stellar atmosphere.

In this review we focus on the processes responsible for the 'generation and transfer' of polarized radiation in an astrophysical plasma. Polarization is produced by (a) scattering of anisotropic radiation by atoms and/or (b) emission/absorption of radiation by atoms in an external magnetic field. Scattering can give rise to polarization even in the absence of magnetic fields (‘resonance scattering’). A modification to this scattering brought about by the weak magnetic fields is called ‘Hanle-effect’ (Hanle 1924). Scattering in arbitrary fields is termed Hanle-Zeeman effect (Stenflo 1998; Sampoorna et al. 2007a).

The paper is organized into three parts. In the first part (cf. Sect. 2.2) we review our recent work on polarized Zeeman line formation in turbulent magnetic media. In the second part we discuss the effects of magnetic turbulence (stochasticity) on the Hanle scattering polarization (see Sect. 2.3). The relevant radiative transfer equations are formulated and solved. Stochastic polarized line formation theory has a diagnostic potential in stellar spectroscopy. The third part of the review (cf. Sect. 3) concerns our recent formulation of the theory of Hanle-Zeeman effect, and solution of the relevant transfer equation.

2 Line formation in magnetically turbulent media

2.1 Historical context

It is now well established that 99% of the solar photospheric volume is filled with magnetic fields that are hidden from direct measurements. What actually has been measured so far through Zeeman effect (that diagnoses only strong kG fields), constitutes just 1% accounting for the deterministic part of the total field. The enigmatic nature of the hidden field (which is proposed to be turbulent) is still an unsolved problem in solar physics.

Turbulence causes formation of eddies of different length scales. The average eddy size $l_{\rm eddy}$ is called the ‘correlation length’. Magnetic fields in the stellar atmosphere become turbulent as the field lines get tangled up by the turbulent fluid motion (under the frozen-in condition : gas pressure larger than the magnetic pressure). The photon mean free path $l_{\rm photon}$ ($= 1/\kappa_\nu$, where κ_ν is absorption coefficient) defines the radiative transfer length scale. When $l_{\rm photon} >> l_{\rm eddy}$ the effects of turbulence in non-scattering problems can be included by averaging the Zeeman line absorption matrix over a probability density function (PDF) of the random magnetic field. This is called the micro-turbulent limit, which is widely used in line formation theory. The form of Zeeman line transfer equation in the micro-turbulent limit was first written by Stenflo (1971). The effect of micro-turbulent magnetic field on Zeeman line absorption matrix was first studied by Dolginov & Pavlov (1972), and Domke & Pavlov (1979), which was revisited in greater detail by Frisch et al. (2005).

The extension of micro-turbulence to absorbing-scattering media involves averaging over both the absorption matrix and the scattering phase matrix. Here we confine our attention to the averaging over the weak field Hanle phase matrix. Such a calculation was first presented by Stenflo (1982) who proposed turbulent Hanle effect as a diagnostic tool to determine the solar hidden fields. His simplified approach (based on single scattering) gave a lower limit of 10 G for this general turbulent field. Through a realistic 1D radiative transfer modeling of the scattering polarization in Sr I 4607 Å line, Faurobert et al. (2001) estimated this photospheric general field to be less than 20 G. The recent work of Trujillo Bueno et al. (2006) based on 3D radiative transfer modeling of the solar atmosphere shows that the photospheric turbulent fields could be in the range of 60-130 G. All these authors use a micro-turbulent magnetic field distributed according to an angularly isotropic PDF, with constant given mean field B_0, or an exponential field strength distribution.

The macro-turbulent limit ($l_{\mathrm{photon}} << l_{\mathrm{eddy}}$) consists of performing an averaging of the emergent specific intensity $\boldsymbol{I}_\nu$ over a PDF. A deterministic field radiative transfer problem is first solved for each realization of the magnetic field in a macro-structure. The emergent solution is then averaged to obtain the mean solution. Multi-component models to represent unresolved macro-structures were introduced by Stenflo (1971, 1994).

The general regime of meso-turbulence ($l_{\mathrm{photon}} \approx l_{\mathrm{eddy}}$) requires the solution of ‘stochastic polarized transfer equation with random coefficients’. For the Zeeman effect, an exact solution method was first given by Landi Degl’Innocenti (1994). A more sophisticated version of this theory was proposed by Frisch et al. (2006). A qualitatively similar approach was taken by Carroll & Staude (2006). The general theory of line transfer for a meso-turbulent Hanle scattering problem was developed recently by Frisch (2006). A numerical method to solve this newly formulated transfer equation is given in Frisch et al. (2009, see also Anusha et al. 2009).

2.2 Stochastic line radiative transfer in an absorbing medium

Theoretical formulation :

In this section we restrict ourselves to the simpler case of Stokes vector ($\boldsymbol{I} = (I, Q, U, V)^{\mathrm{T}}$) transfer equation in a truly absorbing medium (LTE). We consider the specific case of Zeeman line formation in a 1D semi-infinite constant property media with a linear variation of the source vector (the Milne-Eddington model). We model random magnetic field $\boldsymbol{B}(s)$ by a KAP (Kubo-Anderson Process). A KAP is a step-wise stationary Markov process. The idea of using KAP is to describe the atmosphere in terms of several eddies (see left panel of Fig. 1) having lengths distributed according to Poisson’s law with a given density ν (number of jumps/unit optical depth). We assume that in each eddy ($s_{i-1} < s < s_i$) the magnetic field remains constant ($\boldsymbol{B}(s) = \boldsymbol{B}_i$), and it takes values according to a chosen PDF, denoted $P(\boldsymbol{B})$.

The mean Stokes vector $\boldsymbol{I}$ is calculated by averaging over the length distribution of the eddies, and $P(\boldsymbol{B})$. A KAP is thus characterized by a correlation length ($1/\nu$) and a PDF, the selection of which is guided by the structure that is being modeled. The transfer equation for the particular case of the rays propagating outwards along the surface normal is written as

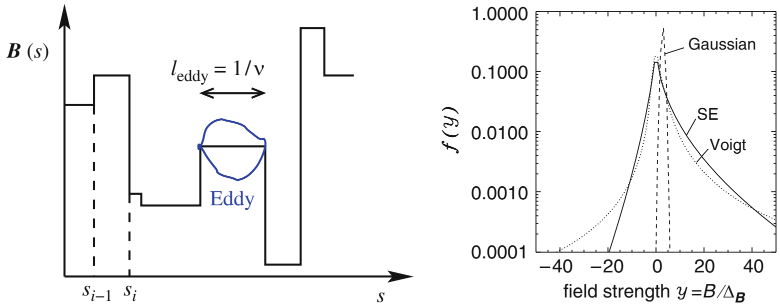

Fig. 1. Left panel: A typical Kubo-Anderson process $\boldsymbol{B}(s)$ with density ν (mean correlation length is $1/\nu$). Right panel: Three different field strength PDFs are used. The rms fluctuation (full width) $\varDelta_B = 6\,\mathrm{G}$ and mean field $y_0 = B_0/\varDelta_B = 2.9$.

$$\frac{\mathrm{d}\boldsymbol{I}}{\mathrm{d}\tau_c} = \left(\hat{E} + \beta\hat{\varPhi}\right)(\boldsymbol{I} - \boldsymbol{S}), \tag{1}$$

where $\hat{\varPhi}$ is the Zeeman line absorption matrix, $\boldsymbol{S}$ is the source vector given by $\boldsymbol{S}(\tau_c) = (C_0 + C_1\tau_c)\boldsymbol{U}$ with $\boldsymbol{U} = (1\,0\,0\,0)^{\mathrm{T}}$, τ_c being the continuum optical depth, and $\beta = \kappa_0/\kappa_c$ with κ_0 and κ_c being frequency integrated line and continuum opacities. Following Landi Degl'Innocenti & Landolfi (2004), the formal solution of Eq. (1) at $\tau_c = 0$ is

$$\boldsymbol{I}(0) = \left[C_0\hat{E} + C_1\int_0^\infty \hat{O}(0,\tau_c)\,\mathrm{d}\tau_c\right]\boldsymbol{U}, \tag{2}$$

where $\hat{O}(0,\tau_c)$ is the evolution operator. We are actually interested in the calculation of the mean emergent Stokes vector $\langle\boldsymbol{I}(0)\rangle_{\mathrm{KAP}}$ defined as

$$\langle\boldsymbol{I}(0)\rangle_{\mathrm{KAP}} = \left[C_0\hat{E} + C_1\int_0^\infty \left\langle\hat{O}(0,\tau_c)\right\rangle_{\mathrm{KAP}}\mathrm{d}\tau_c\right]\boldsymbol{U}. \tag{3}$$

We recall that the notation $\langle ... \rangle_{\mathrm{KAP}}$ means that we need to perform two averages, one over the length distribution of the eddies and the other over a PDF. The first averaging can be analytically performed, as we consider a simple Milne-Eddington atmospheric model. The averaging over the PDF is performed, in general, numerically (analytical averaging is possible in the micro-turbulent regime - see Frisch et al. 2005).

Following Brissaud & Frisch (1974), we establish a convolution type integral equation for $\langle\hat{O}(0,\tau_c)\rangle_{\mathrm{KAP}}$ that is solved by a Laplace transform method to obtain $\langle\boldsymbol{I}(0)\rangle_{\mathrm{KAP}}$. We prefer to calculate the residual Stokes vector $\boldsymbol{r}(0) = [\boldsymbol{I}_{\mathrm{c}}(0) - \boldsymbol{I}(0)]/C_1$, where the continuum intensity $\boldsymbol{I}_{\mathrm{c}}(0) = (C_0 + C_1)\boldsymbol{U}$. After averaging over all the realizations of the random fields we obtain

$$\left\langle\boldsymbol{r}(0)\right\rangle_{\mathrm{KAP}} = (1+\nu)\hat{R}_{\mathrm{macro}}\left(\frac{\beta}{1+\nu}\hat{\varPhi}\right)\left[\hat{E} + \nu\hat{R}_{\mathrm{macro}}\left(\frac{\beta}{1+\nu}\hat{\varPhi}\right)\right]^{-1}\boldsymbol{U}, \tag{4}$$

for an arbitrary value of ν. Here $\hat{R}_{\text{macro}}(\lambda\hat{\Phi}) \equiv \langle \lambda\hat{\Phi}[\hat{E} + \lambda\hat{\Phi}]^{-1}\rangle$, with λ, a scalar. The macro and micro turbulent limits can be recovered by setting $\nu = 0$ and ∞, respectively in Eq. (4).

Numerical results on turbulent Zeeman effect:

We illustrate the sensitivity of $\langle \boldsymbol{r}(0)\rangle_{\text{KAP}} = (\langle r_I\rangle, \langle r_Q\rangle, \langle r_U\rangle, \langle r_V\rangle)^{\text{T}}$ to the choice of the PDFs. The model used has a damping parameter $a = 0$, line strength $\beta = 10$, and correlation length $1/\nu = 1/5$. Further the line has a wavelength around 5000 Å, a Landé factor of 3 and a Doppler width of $1.5\,\text{km s}^{-1}$.

In the solar atmosphere, both the field strength and its orientation fluctuate. Hence we need a PDF that can represent the combined fluctuations. We propose such 'composite PDFs', generally guided by the nature of field distribution in solar atmospheric structures. Examples of such PDFs are:

$$P(y, \mu_B, \chi_B)\,\text{d}\mu_B\,\text{d}\chi_B\,\text{d}y = \frac{(p+1)}{2\pi}\begin{cases} P_{\text{V}}(y, a_B)\mu_B^p \text{d}\mu_B\,\text{d}\chi_B\,\text{d}y, \\ C\text{e}^{-|y|^k}\mu_B^p\text{d}\mu_B\,\text{d}\chi_B\,\text{d}y. \end{cases} \quad (5)$$

Here $\theta_B = \cos^{-1}\mu_B$ and χ_B are the random field orientation with respect to the atmospheric normal, and C is the normalization constant. $P_{\text{V}}(y, a_B)$ is the Voigt function (that now depends on the non-dimensional field strength y and magnetic damping parameter a_B), and $\text{e}^{-|y|^k}$ is the stretched exponential (SE) distribution with k being the stretching parameter. The angular fluctuations are taken care by a cosine power law term μ_B^p where $p = |y|/y_t$ with $y_t = B_t/\Delta_B$, and B_t is the transition field strength between isotropic (in the weak field regime), and peaked (in the strong field regime) distribution. Such composite PDFs are expected to describe the general behavior of observed solar magnetic field to some degree of realism - a large volume filled by weak isotropic fields, and a very small volume filled by strong well directed fields.

For illustrations we choose $B_t = 500\,\text{G}$ and $50\,\text{G}$. The $\langle r_{Q,U,V}\rangle$ computed using these composite PDFs are shown in Fig. 2 for $\mu = 0.1$. We use asymmetric Voigt and SE functions (Sampoorna et al. 2008) with a mean field $y_0 = 2.9$, to represent the fluctuations only in the field strength. The width Δ_B (rms fluctuation) of the PDF is found to be 6 G by an analysis of the solar magnetogram data (see Stenflo & Holzreuter 2003). γ_B, which represents Δ_B converted to Zeeman shift in Doppler width units, is 0.0084 for this choice of Δ_B. As $\gamma_B \ll 1$, the $\langle r_I\rangle$ profiles remain insensitive to the turbulent field related parameters (not shown here). For $y_t = 8$ the PDF becomes more and more anisotropic (larger contribution from wings), resulting in larger degree of linear polarization. For $y_t = 80$, a situation opposite to the above prevails, causing $\langle r_{Q,U}\rangle$ to decrease considerably (solid and dashed lines). $\langle r_U\rangle$ is very small in magnitude as it is generated purely by magneto-optic effects. The sensitivity of $\langle r_V\rangle$ to y_t is similar to that of $\langle r_Q\rangle$ but weaker.

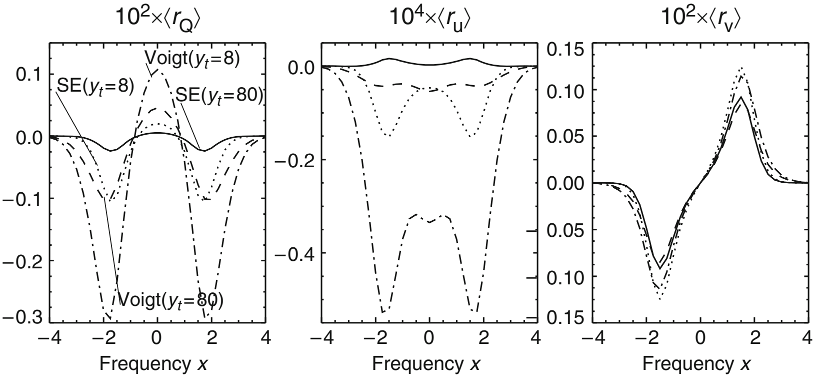

Fig. 2. Effect of choice of the composite PDFs. Larger the transition field strength y_t smaller is the polarization, as the composite PDFs become more and more isotropic.

2.3 Stochastic radiative transfer equation in a scattering medium

Theoretical formulation:

In this section we address a more involved case of polarized line scattering in a stochastic medium. We restrict our attention to the so called complete frequency redistribution (CRD : meaning complete non-coherence during scattering process within a line profile), and ignore the continuum contribution.

The polarized radiative transfer equation for the Hanle effect:

The relevant transfer equation in standard form is (see Nagendra et al. 1998):

$$\mu \frac{\partial \boldsymbol{I}(\tau, x, \boldsymbol{n})}{\partial \tau} = \varphi(x)\big[\boldsymbol{I}(\tau, x, \boldsymbol{n}) - \boldsymbol{S}(\tau, \boldsymbol{n})\big], \tag{6}$$

where $\boldsymbol{I} = (I, Q, U)^{\mathrm{T}}$ and the Stokes source vector $\boldsymbol{S}$ is defined as

$$\boldsymbol{S}(\tau, \boldsymbol{n}) = \boldsymbol{G}(\tau) + (1-\epsilon)\int_{-\infty}^{+\infty} \mathrm{d}x' \oint \frac{\mathrm{d}\Omega'}{4\pi}\varphi(x')\hat{P}_{\mathrm{H}}(\boldsymbol{n}, \boldsymbol{n'}; \boldsymbol{B})\boldsymbol{I}(\tau, x', \boldsymbol{n'}). \tag{7}$$

Here ϵ is the thermalization parameter, $\boldsymbol{G}(\tau) = \epsilon B_{\nu_0}\boldsymbol{U}$ with $\boldsymbol{U} = (1, 0, 0)^{\mathrm{T}}$ and B_{ν_0} the Planck function, and $\hat{P}_{\mathrm{H}}(\boldsymbol{n}, \boldsymbol{n'}; \boldsymbol{B})$ is the Hanle phase matrix. The non-axisymmetry of the radiation is built into the Stokes vector form of the transfer equation. It is advantageous to work with the 'reduced form' of Eq. (6) that is obtained through the expansion of $\boldsymbol{I}$ and $\boldsymbol{S}$ in the form:

$$I_i(\tau, x, \boldsymbol{n}) = \sum_{KQ} \mathcal{T}_Q^K(i, \boldsymbol{n})\mathcal{I}_Q^K(\tau, x, \mu); \quad S_i(\tau, \boldsymbol{n}) = \sum_{KQ} \mathcal{T}_Q^K(i, \boldsymbol{n})\mathcal{S}_Q^K(\tau), \tag{8}$$

where $i = 0, 1, 2$. The 'reduced intensity' $\mathcal{I}_Q^K$ is now independent of the azimuthal angle of the radiation field (axi-symmetric). Notice that the reduced source vector $\mathcal{S}_Q^K$ is even angle independent! By substituting Eq. (8) in to Eq. (6), we can derive a standard form of the transfer equation for the 6-component reduced intensity vector $\boldsymbol{\mathcal{I}}$:

$$\mu \frac{\partial \boldsymbol{\mathcal{I}}(\tau, x, \mu)}{\partial \tau} = \varphi(x) \left[\boldsymbol{\mathcal{I}}(\tau, x, \mu) - \boldsymbol{\mathcal{S}}(\tau) \right], \tag{9}$$

where the 6-component reduced source vector is now written as

$$\boldsymbol{\mathcal{S}}(\tau) = \boldsymbol{\mathcal{G}}(\tau) + \hat{N}(\boldsymbol{B}) \int_{-\infty}^{+\infty} \mathrm{d}x \, \frac{1}{2} \int_{-1}^{+1} \mathrm{d}\mu' \, \varphi(x) \hat{\Psi}(\mu') \boldsymbol{\mathcal{I}}(\tau, x, \mu'). \tag{10}$$

The matrix $\hat{N}(\boldsymbol{B})$ contains $\boldsymbol{B}$ dependence coming from the Hanle effect, and $\hat{\Psi}(\mu)$ describes angular dependence coming from the Hanle phase matrix. For details on this expansion procedure and the definition of $\mathcal{T}_Q^K$ etc., we refer to Frisch (2007). In the presence of a random magnetic field of finite correlation length, Eq. (9) becomes a stochastic Hanle transfer equation. To solve such an equation we need to first specify the model for the random field.

Representation of random (stochastic) magnetic field :

In the case of line transfer with pure absorption, the photons do not change the direction. Therefore it is easy to represent the randomness of the field by a Markov process. However in scattering problems, the photons change the direction randomly (multiple scattering). Hence defining the field randomness (both in the strength and orientation), together with the random walk of the photons in a consistent manner is a difficult task. The difficulty is the following: Suppose the magnetic field is a Markov process (meaning, future depends only on the present and is independent of the past), taken to be along the atmospheric normal. In this case the radiation field $\boldsymbol{\mathcal{I}}$ at a point $\boldsymbol{r}$ on a line-of-sight (LOS) in the direction $\boldsymbol{n}$ depends on magnetic field values below and above the point $\boldsymbol{r}$ along $\boldsymbol{n}$. As a result the joint process $\{\boldsymbol{B}(\boldsymbol{r}); \boldsymbol{\mathcal{I}}(\boldsymbol{r})\}$ is not a Markov process, and hence, the stochastic transfer problem cannot be solved by the standard Fokker-Planck techniques (Brissaud & Frisch 1974). A way out of this situation is to assume that $\boldsymbol{B}$ is random in time domain. Such an approach was used by Frisch & Frisch (1976) for random velocities with a finite correlation length. Again we use KAP to model the magnetic field randomness, but defined with respect to time. Thus, $\boldsymbol{\mathcal{I}}$ should also be time-dependent (i.e., solution of a time-dependent transfer equation). Now the joint process $\{\boldsymbol{B}(t); \boldsymbol{\mathcal{I}}(t)\}$ becomes a Markov process, and hence, one can apply the standard techniques of solving the stochastic differential equation.

Transfer equation for the conditional mean Stokes parameters :

We are interested in calculating the 6-component mean Stokes parameters

$$\langle \mathcal{I}_Q^K \rangle = \int\int \mathcal{P}(\boldsymbol{B},\boldsymbol{\mathcal{I}};t)\,\mathcal{I}_Q^K\,\mathrm{d}\mathcal{I}_0^0\,\mathrm{d}\mathcal{I}_0^2\,\ldots\,\mathrm{d}\mathcal{I}_2^2\,\mathrm{d}^3\boldsymbol{B}, \tag{11}$$

where $\mathcal{P}(\boldsymbol{B},\boldsymbol{\mathcal{I}};t)$ is the probability density of the joint process $\{\boldsymbol{B}(t);\boldsymbol{\mathcal{I}}(t)\}$. It is a priori not known because $\boldsymbol{\mathcal{I}}$ itself depends on random field $\boldsymbol{B}$ and $\boldsymbol{\mathcal{I}}$ has to be obtained from a solution of the stochastic transfer equation. To overcome this implicit nature of the problem we can work with an intermediate quantity called "conditional mean Stokes vector" with components

$$\mathcal{I}_Q^K(t,\tau,x,\mu|\boldsymbol{B}) = \frac{1}{P(\boldsymbol{B})}\int \mathcal{P}(\boldsymbol{B},\boldsymbol{\mathcal{I}};t)\,\mathcal{I}_Q^K\,\mathrm{d}\mathcal{I}_0^0\,\mathrm{d}\mathcal{I}_0^2\,\ldots\,\mathrm{d}\mathcal{I}_2^2. \tag{12}$$

The conditional mean Stokes vector satisfies a time-dependent transfer equation (Frisch 2006). Here $\boldsymbol{B}$ plays the role of an additional independent variable of the problem. In particular we look for stationary solution $\boldsymbol{\mathcal{I}}(\tau,x,\mu|\boldsymbol{B})$ only, which can be obtained by setting $t \to \infty$ in the time-dependent transfer equation. The stationary solution satisfies the following transfer equation :

$$\begin{aligned}\mu\frac{\partial\boldsymbol{\mathcal{I}}(\tau,x,\mu|\boldsymbol{B})}{\partial\tau} &= \varphi(x)\,[\boldsymbol{\mathcal{I}}(\tau,x,\mu|\boldsymbol{B}) - \boldsymbol{\mathcal{S}}(\tau|\boldsymbol{B})]\\ &+ \nu\Big[\boldsymbol{\mathcal{I}}(\tau,x,\mu|\boldsymbol{B}) - \int\boldsymbol{\mathcal{I}}(\tau,x,\mu|\boldsymbol{B}')P(\boldsymbol{B}')\,\mathrm{d}^3\boldsymbol{B}'\Big].\end{aligned} \tag{13}$$

The conditional source and mean intensity vectors respectively are :

$$\boldsymbol{\mathcal{S}}(\tau|\boldsymbol{B}) = \boldsymbol{\mathcal{G}}(\tau) + \hat{N}(\boldsymbol{B})\boldsymbol{\mathcal{J}}(\tau|\boldsymbol{B}), \tag{14}$$

$$\boldsymbol{\mathcal{J}}(\tau|\boldsymbol{B}) = \int_{-\infty}^{+\infty}\frac{1}{2}\int_{-1}^{+1}\varphi(x)\hat{\Psi}(\mu)\boldsymbol{\mathcal{I}}(\tau,x,\mu|\boldsymbol{B})\,\mathrm{d}\mu\,\mathrm{d}x. \tag{15}$$

The mean Stokes vector is now given by

$$\langle\boldsymbol{\mathcal{I}}\rangle(\tau,x,\mu) = \int P(\boldsymbol{B})\boldsymbol{\mathcal{I}}(\tau,x,\mu|\boldsymbol{B})\,\mathrm{d}^3\boldsymbol{B}. \tag{16}$$

Clearly, the use of conditional mean Stokes vector cleverly avoids an explicit knowledge of $\mathcal{P}(\boldsymbol{B},\boldsymbol{\mathcal{I}};t)$. Applying the above averaging to Eq. (13), we obtain the transfer equation for $\langle\boldsymbol{\mathcal{I}}\rangle(\tau,x,\mu)$ as

$$\mu\frac{\partial}{\partial\tau}\langle\boldsymbol{\mathcal{I}}\rangle(\tau,x,\mu) = \varphi(x)\big[\langle\boldsymbol{\mathcal{I}}\rangle(\tau,x,\mu) - \langle\boldsymbol{\mathcal{S}}\rangle(\tau)\big]. \tag{17}$$

It is not possible to write an integral equation for $\langle\boldsymbol{\mathcal{S}}\rangle(\tau)$ (except in the microturbulent limit). We first calculate $\boldsymbol{\mathcal{S}}(\tau|\boldsymbol{B})$ and then average it over $P(\boldsymbol{B})$.

By substituting the formal solution of Eq. (13) into Eq. (15) (see Frisch et al. 2009, for details) we obtain an integral equation for $\boldsymbol{\mathcal{S}}(\tau|\boldsymbol{B})$ as

$$\boldsymbol{\mathcal{S}}(\tau|\boldsymbol{B}) = \boldsymbol{\mathcal{G}}(\tau) + \hat{N}(\boldsymbol{B})\Lambda[\boldsymbol{\mathcal{S}}], \tag{18}$$

where $\Lambda[\boldsymbol{\mathcal{S}}]$ and $\hat{\mathcal{L}}$ operator are defined as

$$\Lambda[\boldsymbol{\mathcal{S}}] = \int_0^T d\tau' \Big\{ \hat{\mathcal{L}}(\tau - \tau'; \nu) \boldsymbol{\mathcal{S}}(\tau' | \boldsymbol{B}) +$$

$$[\hat{\mathcal{L}}(\tau - \tau'; 0) - \hat{\mathcal{L}}(\tau - \tau'; \nu)] \int P(\boldsymbol{B}') \boldsymbol{\mathcal{S}}(\tau' | \boldsymbol{B}') \, \mathrm{d}^3 \boldsymbol{B}' \Big\}, \tag{19}$$

$$\hat{\mathcal{L}}(\tau; \nu) = \int_{-\infty}^{+\infty} \int_0^1 \frac{1}{2\mu} \hat{\Psi}(\mu) \mathrm{e}^{-\frac{|\tau|}{\mu}(\varphi(x) + \nu)} \varphi^2(x) \, \mathrm{d}\mu \, \mathrm{d}x. \tag{20}$$

A polarized approximate lambda iteration method can be devised to solve Eq. (18) (see Frisch et al. 2009, for details).

Numerical results on turbulent Hanle effect :

Here we present some results on the turbulence effects in a Hanle scattering media. The atomic and atmospheric models are defined by a set of parameters $(T, a, \epsilon, B_{\nu_0})$ where T is the optical thickness of the slab. In all the calculations we assume a normal Zeeman triplet, an electric-dipole transition and no depolarizing collisions. For the magnetic field, the free parameters are the Hanle efficiency factor $\Gamma_B = e g_{\mathrm{u}} B / (2 m c A_{\mathrm{ul}})$ in standard notation; the polar angles $(\theta_{\mathrm{B}}, \chi_{\mathrm{B}})$; the density ν of jumping points; and the PDF $P(\boldsymbol{B})$.

Fig. 3a shows the dependence of linear polarization on the correlation length. An isotropic angular distribution with an exponential field strength distribution is used. Since the PDF is azimuthally symmetric, $\langle U \rangle = 0$. Further, as we consider scattering in weak fields Stokes $\langle I \rangle$ remains insensitive to the changes in the free parameters of $\boldsymbol{B}$, and hence not shown.

For optically thin ($T \ll 1$) and thick ($T \gg 1$) lines the $\langle Q \rangle / \langle I \rangle$ profiles can be explained well in terms of micro-turbulence. For intermediate values of T, the $\langle Q \rangle / \langle I \rangle$ profiles sensitively depend on ν. The micro limit is reached for $\nu = 10$ itself, because ν occurs in an exponential term (see Eq. (20)). In Frisch et al. (2009) it is shown that single scattering is a good approximation for both optically thin, and very thick slabs. In the former the number of scatterings are too small (1-2). In the latter the photons may suffer a large number of scatterings inside the slab, but it is the last few ones near the free boundary that contribute to the emergent polarization. In other words polarization is a surface phenomenon. It can be shown that just 4-5 scatterings suffice to reach the final value of $\langle Q \rangle / \langle I \rangle$ in very thick slabs. For slabs of intermediate thickness a full-scale solution of the transfer equation is essential, as the single scattering approximation breaks down. The accuracy of the single scattering approximation progressively improves as one goes from Rayleigh scattering to deterministic field Hanle scattering, and finally to micro-turbulent Hanle scattering. As the single scattering approximation does not depend on ν, the emergent $\langle Q \rangle / \langle I \rangle$ for optically thin and very thick slabs also do not depend on ν. The same thing cannot be said of the lines with intermediate thickness (say $T = 10$), where correlation length effects become important.

In Fig. 3b we compare the micro-turbulent $\langle Q \rangle / \langle I \rangle$ computed using two different field strength distributions with an isotropic angular distribution. A large difference is seen in the line core region, because the exponential PDF is strongly peaked in the weak field region, compared to the Voigt PDF.

In Fig. 3c we present $\langle Q\rangle/\langle I\rangle$ computed with composite PDFs given in Eq. (5) with the asymmetric Voigt function. As the transition field strength y_t (between the isotropic and peaked angular distribution) increases, larger domains of the field strength PDF become isotropic. This results in a decrease in $\langle Q\rangle/\langle I\rangle$, finally reaching isotropic distribution for large values of y_t $(= 80)$.

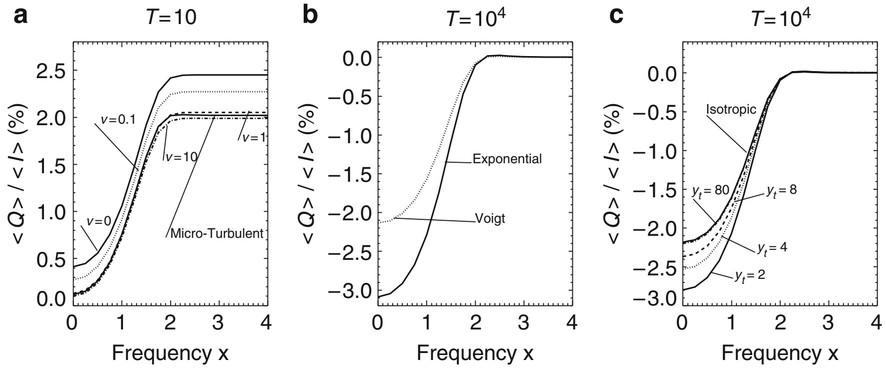

Fig. 3. Effect of turbulence in a Hanle scattering media. Model parameters: $(a, \epsilon, B_{\nu 0}) = (10^{-3}, 10^{-4}, 1)$. (a) shows the influence of correlation length. (b) and (c) show the effects of different PDFs. The field parameter $\Gamma_\sigma = ge\Delta_B/(2mcA_{\rm ul}) = 1.588$ when $g = 3$, $\Delta_B = 6\,$G and $A_{\rm ul} = 10^8$ s^{-1}. In (b) the angular distribution is isotropic, whereas field strength PDF are different. For (c) we use a composite PDF with a coupling between angular and field strength distributions.

3 Scattering polarization in arbitrary strength magnetic fields - the Hanle-Zeeman effect

3.1 Historical context

The solar atmosphere with its magnetically active regions harbor a whole range of field strengths (milligauss to kilogauss fields). Hence we need a general form of the radiative transfer equation that is valid in this entire range. Such a transfer equation was formulated by Stenflo (1994).

Until recent years, polarized line transfer equation in the presence of deterministic magnetic fields has been solved in two extreme limits, namely, true absorption in strong fields (Zeeman line transfer in LTE) neglecting the scattering effects, and resonance scattering in weak fields (Hanle line transfer in NLTE) neglecting Zeeman absorption. In a correct treatment of NLTE line formation in arbitrary strength magnetic fields, one has to take into account the 'Zeeman absorption matrix' and 'scattering redistribution matrix (RM)' together. The latter describes the correlations in frequency, angle and polarization between the incoming and outgoing photons in a scattering event. In the early years Hanle RM for weak fields was used in the line transfer computations (Faurobert-Scholl 1991; Nagendra et al. 1998; Manso Sainz & Trujillo-Bueno 1999). In these papers a hybrid approximation for RM was used, where the frequency correlation part was assumed to be CRD, and the angular correlation to be the Hanle phase matrix (Stenflo 1978; Landi Degl'Innocenti & Landi Degl'Innocenti 1988). However partial frequency redistribution (PRD) is a better description of the frequency correlation. Such PRD computations retaining the hybrid approximation were performed by Faurobert-Scholl (1991) and Nagendra et al. (1999).

A derivation of RM with a proper treatment of PRD dates back to Omont et al. (1973). A correct form of the RM suitable for radiative transfer computation had to wait until the work of Bommier (1997a,b). The laboratory frame RMs for weak fields were written in a factorized form taking frequency and polarization correlations properly into account through appropriate branching ratios. Such factorization takes place in the two dimensional (x, x') frequency space. This domain based RMs were used in transfer computation by Nagendra et al. (2002), who used a time consuming perturbation method.

To diagnose the solar magnetic fields of arbitrary strength we need RMs that are valid in the entire field strength regime (milligauss to kilogauss). We call such a scattering matrix as Hanle-Zeeman RM. A QED theory of scattering in arbitrary fields was given by Bommier (1997b). The classical analogue of the same is presented in Bommier & Stenflo (1999). In these papers the RM was derived in the rest frame of the atom. The corresponding laboratory frame expressions which are essential for line transfer computations were derived in Sampoorna et al. (2007a). It was shown in Sampoorna et al. (2007b) that for the specific case of $J = 0 \to 1 \to 0$ transition the classical and quantum theories give exactly identical RMs. These RMs were later included by Sampoorna et al. (2008b) in line transfer computations using a simple perturbative approach. No high speed iterative methods (like the one based on approximate lambda operator) has so far been developed to solve this problem, which remains a challenge to numerical radiative transfer.

3.2 Theoretical formulation

The transfer equation for the Stokes vector $(I, Q, U, V)^{\mathrm{T}}$ in a magnetically absorbing and scattering medium is given by

$$\mu\, \partial \boldsymbol{I}(\tau, x, \boldsymbol{n})/\partial\tau = (\hat{\Phi} + r\hat{E})\boldsymbol{I}(\tau, x, \boldsymbol{n}) - [(r\hat{E} + \epsilon\,\hat{\Phi})B_{\nu_0}\boldsymbol{U} + \boldsymbol{S}_{\mathrm{scat}}(\tau, x, \boldsymbol{n})], \quad (21)$$

where the scattering integral is defined as

$$\boldsymbol{S}_{\mathrm{scat}}(\tau, x, \boldsymbol{n}) = \int_{-\infty}^{+\infty} \oint \hat{R}(x, \boldsymbol{n}; x', \boldsymbol{n}'; \boldsymbol{B})\boldsymbol{I}(\tau, x', \boldsymbol{n}')\frac{\mathrm{d}\Omega'}{4\pi}\mathrm{d}x', \quad (22)$$

in standard notation. Here $r = 1/\beta$ is the ratio of continuum to the line center opacity. The Hanle-Zeeman redistribution matrix $\hat{R}$ is the heart of the problem. It represents PRD in line scattering, namely an appropriately weighted combination of frequency coherent and frequency non-coherent (respectively Hummer's type II and III) scattering. The weighting factors are the branching ratios which contain the physics of various types of collisions (Domke & Hubeny 1988; Nagendra 1994; Bommier 1997b) in polarized line formation theory. It is worthwhile to note that elastic collisions (denoted by Γ_{E}) are responsible for destroying the frequency correlation between the incoming and outgoing photons, while the depolarizing collisions $D^{(K)}$ cause destruction of the atomic alignment and orientation. As in Nagendra et al. (2002) we solve Eqs. (21) and (22) using a perturbation method (see Sampoorna et al. 2008b).

To illustrate the nature of the RM we perform a single scattering experiment in which an unpolarized monochromatic ray is incident on the atom, and undergoes a 90° scattering. The magnetic field is chosen to be parallel to the scattered ray, so that there is maximum impact of the Hanle effect on line scattering. Fig. 4 shows the scattered Stokes profiles in (x, x') space for a stronger field of $v_B = g\nu_{\mathrm{L}}/\Delta\nu_{\mathrm{D}} = 3$. The contour plot below exhibits the 2D domain structure in the (x, x') space. This figure illustrates the interesting case of Rayleigh scattering in strong fields. In a 90° scattering event only two σ-components are scattered. In the $\log I$ profile they are displaced on both sides of the line center and are well separated because the Zeeman shift is 3 Doppler width. Far from the line center and Zeeman components, scattering is Rayleigh like and hence the linear polarization of scattered ray is 100% (see along the first diagonal of the Q/I panel in Fig. 4). Also at line center (far from the Zeeman component), Rayleigh scattering applies and hence the scattered radiation is again 100% but with opposite sign (see Bommier 1997b, Sect. 6). $U/I = 0$ for two reasons: (i) the field is strong enough to cause Hanle saturation (no rotation of the polarization plane); (ii) the choice of geometry, namely magnetic field along the LOS. Further for the same reasons, V/I is large, and reaches a maximum of unity at the position of Zeeman components.

3.3 Numerical results for the Hanle-Zeeman effect

Here we discuss line formation with the angle-averaged Hanle-Zeeman RM, for the case of a medium that is self emitting and effectively thin ($\epsilon T \ll 1$).

Figure 5 shows the emergent profiles for $\mu = 0.11$ and $\varphi = 0°$. The Hanle strength parameter Γ_B is used as a free parameter. In panels (a) and (b) we compare the solutions obtained by solving Eq. (6) (using scalar absorption coefficient) and Eq. (21) (using the Zeeman absorption matrix) respectively. For weak fields $\Gamma_B \leq 10$ (which corresponds to $v_B \leq 0.01$), the solutions with and without Zeeman absorption do not differ. This shows that in weak fields one may neglect the contributions from the off-diagonal elements of the polarized Zeeman absorption matrix (as done in the past: see e.g. Faurobert-Scholl 1991;

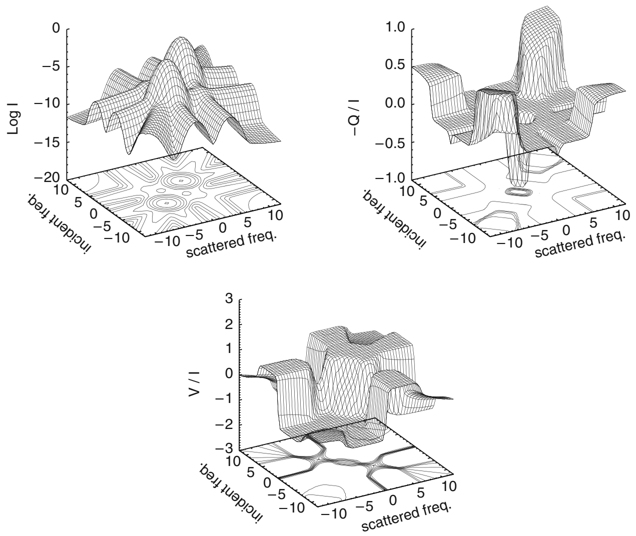

Fig. 4. Stokes parameters vs. incident frequency x' and scattered frequency x, in a 90° single scattering event involving a pencil of unpolarized incident radiation. The model parameters are $[a,\, v_B,\, \Theta;\, \epsilon,\, \Gamma_{\rm E}/\Gamma_{\rm R},\, D^{(K)}/\Gamma_{\rm R}] = [10^{-3},\, 3,\, 90°;\, 0,\, 1,\, 0]$. Such a model corresponds to an equal mix of both type II and III redistribution. $\Gamma_{\rm R}$ denotes the radiative rate. V/I stays within the range $(-1,+1)$, although we use a z-scale $(-3,+3)$ in order to avoid overlapping of surface and contour plots.

Nagendra et al. 1998). For $(\Gamma_B > 10, v_B > 0.01)$ there are considerable differences in the Q/I and U/I profiles between the two cases. The regime of field strengths covered in this figure (2.5 - 250 G) is the domain which was studied traditionally ignoring the anisotropic elements of the absorption matrix. From the figure it is clear that one should not neglect the anisotropic absorption in the transition regime of weak → hectogauss fields in the solar atmosphere, where both Zeeman anisotropic absorption and Hanle anisotropic scattering contribute significantly and simultaneously. The general form of transfer equation given in this paper takes care of this transition regime between weak to hectogauss magnetic fields in the solar photosphere.

4 Conclusions

In this review we highlight three important developments in the polarized line formation theory applied to the solar atmosphere. The first problem concerns a revisit to the Zeeman line formation in turbulent fields. We show that finite correlation length effects (meso-turbulence) are important for Zeeman lines. In the second part we discuss Hanle transfer equation in turbulent fields, and show that Hanle scattering is insensitive to the correlation length - and therefore micro-turbulence is a good approximation. Both Zeeman absorption

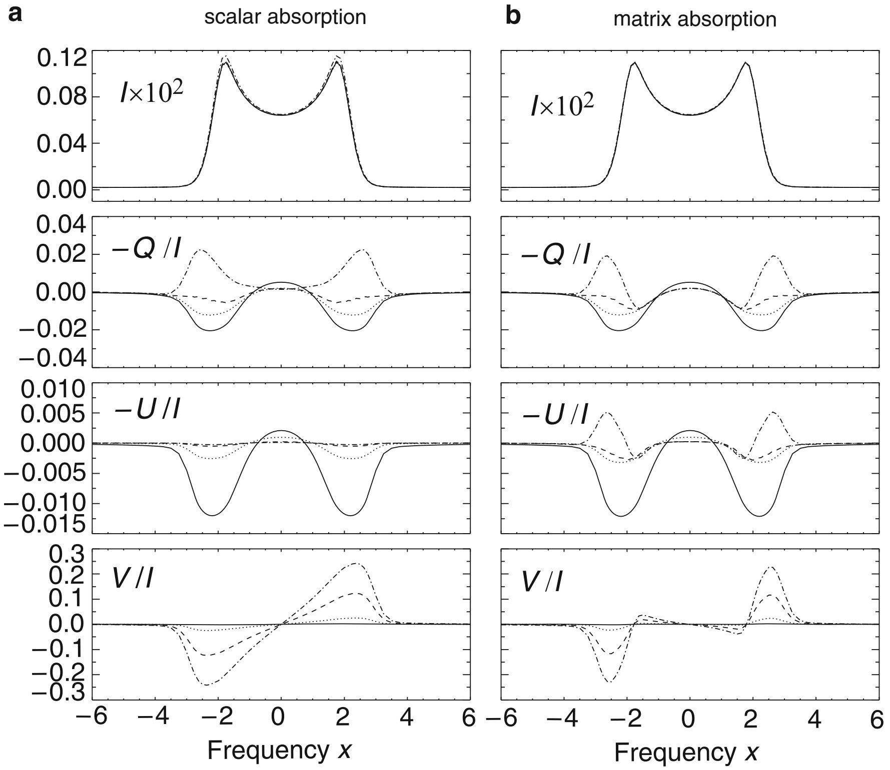

Fig. 5. Comparison of the solutions computed using a scalar absorption coefficient (panel a) and the full Zeeman absorption matrix (panel b), for $\mu = 0.11$ and $\varphi = 0°$. Model parameters: $(T, a, \epsilon, r, \Gamma_{\rm E}/\Gamma_{\rm R}, D^{(K)}/\Gamma_{\rm R}) = (20, 10^{-3}, 10^{-4}, 10^{-7}, 1, 0.5)$. Magnetic field orientation: $(\theta_B, \chi_B) = (30°, 0°)$. Line types: solid $(\Gamma_B = 1, v_B = 0.001)$; dotted $(10, 0.01)$; short-dashed $(50, 0.05)$; dash-dotted (100, 0.1).

and Hanle scattering sensitively depend on the choice of vector PDF - which describes how magnetic field fluctuates in both strength and direction. The third problem we address is the polarized line transfer with PRD, for arbitrary strength deterministic magnetic fields. This problem could not be attempted in the past as the relevant PRD redistribution matrices were not available. Using our new derivation of this Hanle-Zeeman redistribution matrix, we now solve the concerned transfer equation. We present a few interesting results.

References

Anusha, L. S., Sampoorna, M., Frisch, H., Nagendra, K. N. 2009, in Magnetic coupling between the Interior and Atmospheres of the Sun, eds. S. S. Hasan & R. J. Rutten, Astrophys. & Space Sci. Procs., Springer, Heidelberg, in press

Bommier, V. 1997a, A&A, 328, 706

Bommier, V. 1997b, A&A, 328, 726
Bommier, V., Stenflo, J. O. 1999, A&A, 350, 327
Brissaud, A., Frisch, U. 1974, Journal of Mathematical Physics, 15, 524
Carroll, T. A., Staude, J. 2006, in Solar Polarization 4, eds. R. Casini & B. W. Lites, ASP Conf. Ser., 358, 137
Dolginov, A. Z., Pavlov, G. G. 1972, Soviet Astronomy, 16, 450
Domke, H., Pavlov, G. G. 1979, Ap&SS, 66, 47
Faurobert, M., Arnaud, J., Vigneau, J., Frisch, H. 2001, A&A, 378, 627
Faurobert-Scholl, M. 1991, A&A, 246, 469
Frisch, H. 2006, A&A, 446, 403
Frisch, H. 2007, A&A, 476, 665
Frisch, H., Anusha, L. S., Sampoorna, M., Nagendra, K. N. 2009, A&A, 501, 335
Frisch, H., Frisch, U. 1976, MNRAS, 175, 157
Frisch, H., Sampoorna, M., Nagendra, K. N. 2005, A&A, 442, 11
Frisch, H., Sampoorna, M., Nagendra, K. N. 2006, A&A, 453, 1095
Hanle, W. 1924, Z. Phys., 30, 93
Domke, H., Hubeny, I. 1988, ApJ, 334, 527
Landi Degl'Innocenti, E. 1994, in Solar Surface Magnetism, eds. R. J. Rutten & C. J. Schrijver, 29
Landi Degl'Innocenti, E., Landolfi, M. 2004, ASSL, 307, Polarization in Spectral Lines
Landi Degl'Innocenti, M., Landi Degl'Innocenti, E. 1988, A&A, 192, 374
Manso Sainz, R., Trujillo-Bueno, J. 1999, in Solar Polarization, eds. K. N. Nagendra & J. O. Stenflo, ASSL, 243, 143
Nagendra, K. N. 1994, ApJ, 432, 274
Nagendra, K. N., Frisch, H., Faurobert-Scholl, M. 1998, A&A, 332, 610
Nagendra, K. N., Frisch, H., Faurobert, M. 2002, A&A, 395, 305
Nagendra, K. N., Paletou, F., Frisch, H., Faurobert-Scholl, M. 1999, in Polarization, eds. K. N. Nagendra & J. O. Stenflo, ASSL, 243, 127
Omont, A., Smith, E. W., Cooper, J. 1973, ApJ, 182, 283
Sampoorna, M., Nagendra, K. N., Frisch, H., Stenflo, J. O. 2008, A&A, 485, 275
Sampoorna, M., Nagendra, K. N., Stenflo, J. O. 2007a, ApJ, 663, 625
Sampoorna, M., Nagendra, K. N., Stenflo, J. O. 2007b, ApJ, 670, 1485
Sampoorna, M., Nagendra, K. N., Stenflo, J. O. 2008b, ApJ, 679, 889
Stenflo, J. O. 1971, in Solar Magnetic Fields, ed. R. Howard, IAU Symp., 43, 101
Stenflo, J. O. 1978, A&A, 66, 241
Stenflo, J. O. 1982, Solar Phys., 80, 209
Stenflo, J. O. 1994, Solar Magnetic Fields (Dordrecht: Kluwer)
Stenflo, J. O. 1998, A&A, 338, 301
Stenflo, J. O., Holzreuter, R. 2003, Astronomische Nachrichten, 324, 397
Trujillo Bueno, J., Asensio Ramos, A., Shchukina, N. 2006, in Solar Polarization 4, eds. R. Casini & B. W. Lites, ASP Conf. Ser., 358, 269

"Recent Advances in Spectroscopy:
Theoretical, Astrophysical, and Experimental Perspectives"
Eds. Chaudhuri R K, Mekkaden M V, Raveendran A V, Satya Narayanan A
Astrophysics and Space Science Proceedings, Springer-Verlag, Berlin, 2010.

Discrete Space Theory of Radiative Transfer: Application

M. Srinivasa Rao

Indian Institute of Astrophysics, Koramangala, Bangalore 560034, India.
msrao@iiap.res.in

Summary. The method of obtaining the solution of radiative transfer equation using discrete space theory (DST) is described with (1) interaction principle for different geometries (2) star product (3) calculation of radiation field at internal points. Some of the important steps to obtain the solution of radiative transfer equation in spherical symmetry are also mentioned. Applications of DST are discussed with their results in two cases (a) study of reflection effect in close binary systems and (b) to compute KI 769.9 nm emission line profiles from N-type stars.

1 Introduction

The study of transfer of radiation is pursued in several areas of scientific research such as astrophysics, reactor physics and meteorology. Astrophysics is one of the earliest areas of activity in whch serious studies took place. It was George Stokes (Stokes 1856, 1860) who first developed the concept of invariance in his glass plate problem. He showed how the reflectance remains invariant when an additional glass plate is added to a system of parallel plates of glass plates. Lord Rayleigh (Rayleigh 1920) obtained transmission and reflection factors in more complicated situations such as dispersive medium.

The idea of addition of layer of arbitrary thickness to semi-infinite layer was proposed by Ambarzumian (Ambarzumian 1942) and noticed that the reflection characteristics remain invariant in such situations. The idea was used by Chandrasekhar (Chandrasekhar 1960) to solve several problems through H-functions in a semi-infinite medium and X & Y functions in a finite medium. So layers with general properties can be added and their transmission and reflection properties can be calculated directly by utilizing the "Interaction Principle" (Redheffer 1962, Preisendorfer 1965; Grant & Hunt 1969). Interaction principle is a manifestation of the conservation of radiant flux. It balances the emergent radiation with that of reflected and transmitted input radiation together with the internally generated radiation.

2 Interaction principle

Let I represent the specific intensity and i and o represent the incident and output intensities at the boundaries of A and B in one-dimensional geometry, A B C D in two-dimensional geometry and at surfaces A B C D E F in three-dimensional geometry. Let t and r represent the transmission and reflection operators and $S(A), S(B)$ represent the internal source term.

2.1 Interaction principle for (A) one (B) two and (C) three dimensional geometry

(A) The output intensities in terms of the input intensities for Fig. 1(A) is as follows:

$$I(\mathrm{A}, o) = t(\mathrm{B}, \mathrm{A}) I(\mathrm{B}, i) + r(\mathrm{A}, \mathrm{A}) I(\mathrm{A}, i) + S(\mathrm{A}) \tag{1}$$

$$I(\mathrm{B}, o) = t(\mathrm{A}, \mathrm{B}) I(\mathrm{A}, i) + r(\mathrm{B}, \mathrm{B}) I(\mathrm{B}, i) + S(\mathrm{B}) \tag{2}$$

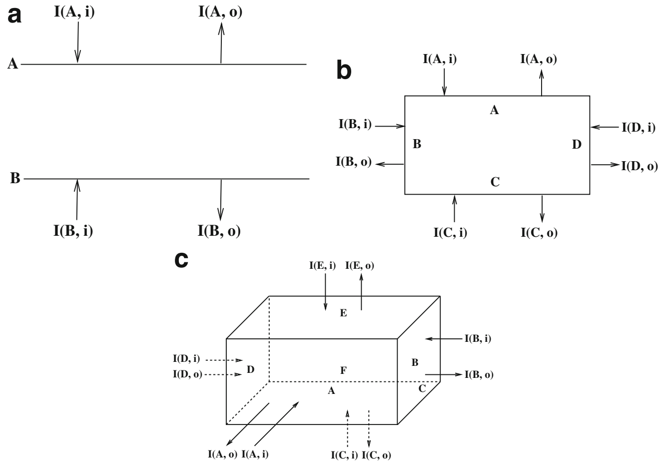

Fig. 1. Interaction principle (A) One dimensional slab (B) Two dimensional plane (C) Three dimensional cuboid.

The above can be written in a matrix form

$$\begin{pmatrix} I(\mathrm{A}, o) \\ I(\mathrm{B}, o) \end{pmatrix} = \begin{pmatrix} r(\mathrm{A}, \mathrm{A}) & t(\mathrm{B}, \mathrm{A}) \\ t(\mathrm{A}, \mathrm{B}) & r(\mathrm{B}, \mathrm{B}) \end{pmatrix} \begin{pmatrix} I(\mathrm{A}, i) \\ I(\mathrm{B}, i) \end{pmatrix} + \begin{pmatrix} S(\mathrm{A}) \\ S(\mathrm{B}) \end{pmatrix}. \tag{3}$$

(B) The output intensities in terms of the input intensities for Fig. 1(B) is as follows:

$$I(\mathrm{A},o) = r(\mathrm{A},\mathrm{A})I(\mathrm{A},i)+t(\mathrm{B},\mathrm{A})I(\mathrm{B},i)+t(\mathrm{C},\mathrm{A})I(\mathrm{C},i)+t(\mathrm{D},\mathrm{A})I(\mathrm{D},i)+S(\mathrm{A}) \tag{4}$$

Similarly, for the other sides I(B, o), I(C, o), I(D, o) can also be written in matrix form Peraiah (1984).

(C) For three dimensional geometry the output intensities in terms of the input intensities for Fig. 1(C) are as follows:

$$\begin{aligned} I(\mathrm{A},o) = {} & t(\mathrm{A},\mathrm{B})I(\mathrm{B},i) + t(\mathrm{A},\mathrm{C})I(\mathrm{C},i) + t(\mathrm{A},\mathrm{D})I(\mathrm{D},i) + t(\mathrm{A},\mathrm{E})I(\mathrm{E},i) \\ & + t(\mathrm{A},\mathrm{F})I(\mathrm{F},i) + r(\mathrm{A},\mathrm{A})I(\mathrm{A},i) + S(\mathrm{A}) \end{aligned} \tag{5}$$

Similarly, for other sides I(B, o),I(C, o),I(D, o), E(E, o), F(F, o). This can also be written in the matrix form Peraiah (1984).

For a spherically symmetric atmospheres output intensities can be written in terms of input intensities. Let us consider a shell with boundaries (n, n+1) as shown in Fig. 2(A), the interaction principle can be written as follows:

$$\begin{pmatrix} \mathbf{I}^{+}_{n+1} \\ \mathbf{I}^{-}_{n} \end{pmatrix} = \mathbf{S}(n, n+1) \begin{pmatrix} \mathbf{I}^{+}_{n} \\ \mathbf{I}^{-}_{n+1} \end{pmatrix} + \sum(n, n+1) \tag{6}$$

[Ref. Peraiah (2002)(Chapter 6, Page 155) for matrix $\mathbf{S}$(n, n+1) and $\sum$(n, n+1)].

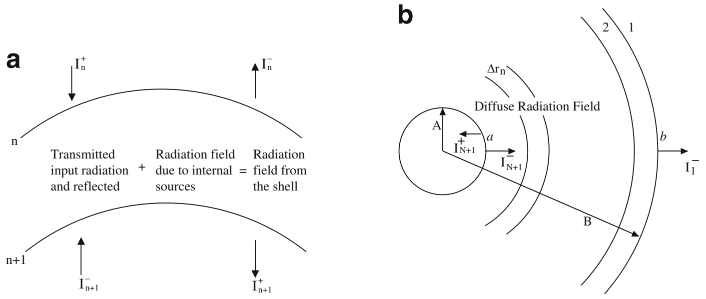

Fig. 2. Schematic diagram shows the (A) interaction principle for spherical case (B) diffuse radiation field.

2.2 Star Product

If there is another shell with boundaries (n+1, n+2) adjacent to (n, n+1), interaction principle for this shell can be written as

$$\begin{pmatrix} \mathbf{I}^{+}_{n+2} \\ \mathbf{I}^{-}_{n+1} \end{pmatrix} = \mathbf{S}(n+1, n+2) \begin{pmatrix} \mathbf{I}^{+}_{n+1} \\ \mathbf{I}^{-}_{n+2} \end{pmatrix} + \sum(n+1, n+2) \tag{7}$$

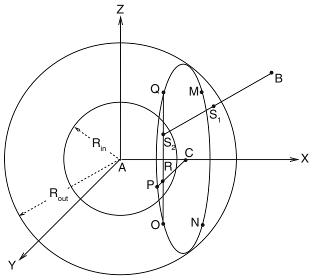

Fig. 3. Schematic diagram of the Cartesian co-ordinate system in X-Y-Z geometry; Rao & Varghese (2008).

where **S**(n+1, n+2) is also similarly defined. If we combine the two shells (n, n+1) and (n+1, n+2), then the interaction principle for the combined shell is written as

$$\begin{pmatrix} \mathbf{I}^{+}_{n+2} \\ \mathbf{I}^{-}_{n} \end{pmatrix} = \mathbf{S}(n, n+2) \begin{pmatrix} \mathbf{I}^{+}_{n} \\ \mathbf{I}^{-}_{n+2} \end{pmatrix} + \sum(n, n+2). \qquad (8)$$

Redheffer (1962) calls **S**(n, n+2) the star product of the two S-matrices **S**(n, n+1) and **S**(n+1, n+2). The star product can be written as

$$\mathbf{S}(n, n+2) = \mathbf{S}(n, n+1) \star \mathbf{S}(n+1, n+2). \qquad (9)$$

See ref. (Redheffer (1962)) for other details.

3 Method of obtaining the solution of transfer equation

We shall consider equation of transfer with monochromatic radiation field scattering isotropically and follow the steps to obtain the solution of transfer equation

(i) We divide the medium as shown in Fig. 2(B) into number of "cells" whose thickness is less than or equal to the critical (τ_{crit}). The critical thickness is determined on the basis of physical characteristics of the medium. τ_{crit} ensures the stability and uniqueness of the solution.

(ii) Now the integration of the transfer equation is performed on the "cell" which is two-dimensional radius - angle grid bounded by $[r_n, r_{n+1}] \times [\mu_{j-\frac{1}{2}}, \mu_{j+\frac{1}{2}}]$ where $\mu_{j+\frac{1}{2}} = \sum_{k=1}^{j} C_k, j = 1, 2 \ldots . J$, where C_k are the weights of Gauss Legendre formula.

(iii) By using the interaction principle described in eraiah and Grant (1973), we obtain the reflection and transmission operators over the "cell".

(iv) Finally we combine all the cells by the star algorithm described in Peraiah & Grant (1973) and obtain the radiation field.

(v) Using discrete space theory the solution is developed for a non-LTE two level atom case. We represent the integration by summation, derivatives by the differences for frequency (x), angle (μ) and radius (r).
The above mentioned steps (i)-(iv) have to be followed to obtain the solution of transfer equation in spherical symmetry and for details refer Peraiah (2002, Chapter 6, Page 179).

4 Applications of radiative transfer equation in spherical symmetry:

The DST method is a finite difference, discrete ordinate method which is very accurate and easy to generalize to different physical problems. It is applied for
1) reflection effect in close binaries, for calculating the self radiation of the primary component in a binary system,
2) K1 emission lines from circumstellar shells of N-Type star R Scl and
3) Stellar winds in O and B type stars: Hydrogen atmosphere
4) To study the effects of aberration and advection in a plane parallel medium in motion and
5) Non-magnetic resonance scattering polarization in spherically symmetric media, polarized line formation in moving media, Complete Redistribution (CRD), Partial Redistribution (PRD) and many other applications. The first two cases are presented in the next section.

5 Results and discussion

5.1 Calculation of irradiation in 3D geometry, Fig. 3:

Peraiah (Peraiah 1983), Peraiah & Rao (Peraiah & Rao 1983, 1998, 2002), Rao & Peraiah (Rao & Peraiah 2000) studied effect of reflection in a close binary system in two dimensional geometry when secondary component is assumed to be a point source (2) an extended source and (3) effect on spectral lines. They concluded that the reflection effect phenomenon has to be considered while modeling the close binary system. Since three dimensional approach is more realistic than the two dimensional, recently, Srinivasa Rao & Varghese (2008) calculated the reflected radiation from an extended surface of the primary component of a close binary system in a 3-dimensional Cartesian coordinate geometry. They assumed that the secondary component is a point source and moves in circular orbits with respect to the primary component. The specific intensity of the radiation field on the primary component is estimated along the line of sight observer at infinity (Fig. 3).

The coordinates of the secondary component was set as (x_2, y_2, z_2) where the radiation is incident on the primary component. The following cases were considered to calculate the direction cosines of the lines which were parallel to the Z-axis and also parallel to the line of sight. In their calculations secondary component positioned at different places like; Case 1: $x_2 = \mathrm{R}$, $y_2 = 0$, $z_2 = 0$; Case 2: $x_2 = \mathrm{R}\sin\frac{\pi}{4}$, $y_2 = 0$, $z_2 = \mathrm{R}\cos\frac{\pi}{4}$; and Case 3: $x_2 = 0$, $y_2 = 0$, $z_2 = \mathrm{R}$. It is noticed that the radiation field changes depending upon the position of the secondary component and shown in the surface contours (Srinivasa Rao & Varghese (2008)).

5.2 Calculation of KI emission line profiles from circumstellar envelope:

It is commonly observed that many super giants of O and B type stars and red giants have circumstellar shells and formed due to various reasons. We rarely obtain high resolution observations of the emission lines formed in these shells. Gustafsson et al (1997) (hereafter GEKOO) observed KI 769.9 nm line from three N-type stars R Scl, VAql and X TrA. The emission line profiles of K I presented in the Fig. 2 of GEKOO are observed at two different position angles and these show significantly different characteristics.

DST radiative transfer is applied to calculate the KI emission line profiles formed in the circumstellar envelope of the N-type star R Scl. The input data was taken from GEKOO regarding expansion velocity, mass loss rate, radii etc. The equation of line transfer in spherically symmetric approximation in a comoving frame is applied to obtain the radial distribution of the source functions. Using these source functions, the emergent intensities along the line of sight are calculated by using the formal solution of radiative transfer. The theoretical line profiles are generated at different radii. The velocity of expansion with $V_B = 5$ mean thermal units (mtu) resembles the observed profiles. It is also important to calculate the equivalent width of the line and compare with the observations which is under progress and the detailed calculations will be given in a forth coming paper.

6 Merits and Demerits of the method:

The DST method can be generalized for more complicated physical situations like, 2D and 3D-geometry. Accuracy and stability of the numerical solution can be checked to the machine accuracy. Self consistency checks like reflection and transmission matrices, flux conservation are used to ensure the correct coding and accuracy of the discrete representation of the method. The algorithm of DST is written in such a way that the code can be written for parametric study. While changing the required parameters one can compare the results with different geometries of the problem like plane parallel to spherical and comoving frame to rest frame etc.

Application to the realistic atmospheric modeling work, leads to increased dimensionality of the matrices in the algorithm heading to large memory and CPU time requirement.

7 Conclusion:

DST is a very accurate method and can be generalized to different physical problems. In this paper, only two applications of the method are discussed: 1) reflection effect in close binaries and 2) KI emission lines from circumstellar shells of N type stars.

Acknowledgement. The author would like to thank the conference organizers for inviting him to the meeting and also wish to thank Dr Elenora Antokhina for providing some of the references.

References

Ambarzumian, V. A., "On the scattering of light by the planetary atmospheres, Azh (Astronomicheskii Zhurnal), 19, 1, (1942)

Chandrasekhar, S., Radiative Transfer, Dover, New York, (1960)

Grant, I. P., Hunt, G. E., Proc. Roy. Soc. Lond. A 21, 313, 183-197, (1969a); *ibid.* 21, 313, 199-216, (1969b)

Gustafsson, B., Eriksson, K., Kiselman, D., Olander, N., and Olofsson, H., A & A, 318, 535, (1997)

Peraiah, A., AP&SS, 108, 209, (1984)

Peraiah, A., An Introduction to Radiative Transfer: Methods and applications in astrophysics, Cambridge, (2002)

Peraiah, A., Grant, I. P, J. inst. Math. Applic. 12, 75, (1973)

Peraiah, A., J. Astrophys. Astron, 3, 485,(1982); *ibid* 4, 151, (1983)

Peraiah, A., Rao, M. S., J. Astrophys. Astron, 4, 175, (1983)

Peraiah, A., Rao, M. S., A & A. Suppl., 132, 45,(1998)

Peraiah, A., Rao, M. S., A & A. Suppl., 389, 945,(2002)

Preisendorfer, R. W., Radiative transfer in Discrete Spaces, Pergamon Press, Oxford,(1965)

Rao, M. S., Peraiah, A., A & A. Suppl., 145, 525,(2000)

Rao, M. S., Varghese, B. A., SAJ, (in press), (2008)

Rayleigh, L., On a Theorem Analogous To The Virial Theorem, "Scientific papers of Lord rayleigh IV, p 492, Cambridge, (1920)"

Redheffer, R. M., J. Math, and Phys., 41, 141, (1962)

Stokes, G., Proceedings of the Royal Society, XI:545-557, 1860.

Stokes, G., On the composition and resolution of streams of polarized light from diferent sources. Cambridge, Philosophical Society Transactions, IX:399-416, 1856.

"Recent Advances in Spectroscopy:
Theoretical, Astrophysical, and Experimental Perspectives"
Eds. Chaudhuri R K, Mekkaden M V, Raveendran A V, Satya Narayanan A
Astrophysics and Space Science Proceedings, Springer-Verlag, Berlin, 2010.

Solar Spectroscopy and (Pseudo-)Diagnostics of the Solar Chromosphere

Robert J. Rutten

Sterrekundig Instituut, Utrecht University, Utrecht, The Netherlands
Institutt for Teoretisk Astrofysikk, Oslo University, Oslo, Norway.
`R.J.Rutten@uu.nl`

Summary. I first review trends in current solar spectrometry and then concentrate on comparing various spectroscopic diagnostics of the solar chromosphere. Some are actually not at all chromospheric but just photospheric or clapotispheric and do not convey information on chromospheric heating, even though this is often assumed. Balmer Hα is the principal displayer of the closed-field chromosphere, but it is unclear how chromospheric fibrils gain their large Hα opacity. The open-field chromosphere seems to harbor most if not all coronal heating and solar wind driving, but is hardly seen in optical diagnostics.

1 Solar spectroscopy

During this wide-ranging conference I gave a wide-ranging review covering spectroscopy of the solar photosphere, chromosphere, and corona including condensed tutorials[1] of line formation theory for these disparate domains. Being page-limited, I only summarize some major review points here and then concentrate on optical diagnostics of the solar chromosphere – arguably the hardest solar nut to crack (Judge & Peter 1998).

Solar atmosphere physics. A major quest of solar physics is to understand the intricate interplay between solar magnetism, gas dynamics, and radiation that makes the solar atmosphere such an outstanding research laboratory and also governs our space environment. The photosphere, chromosphere, and corona represent optically thick, effectively thin, and optically thin interaction domains with much variation in plasma-β. They differ much in research techniques and in researcher specialisms, but do require holistic synthesis.

Spectroscopy is a key research tool in this endeavor. It differs from other astronomy in that the solar atmosphere displays its interactions in resolvable fine structure that varies on short time scales. Solar spectroscopy therefore

---

[1] http://www.astro.uu.nl/~rutten/Lectures_on.html; for a non-condensed syllabus see http://www.astro.uu.nl/~rutten/Lecture_notes.html.

requires high time resolution, both observationally and interpretationally, in addition to high angular resolution and large diagnostic diversity.

Solar physics now. Solar physics is experiencing a tremendous boost from three developments: wavefront correction enabling $0.1''$ resolution from meter-class optical telescopes, continuous multi-wavelength high-cadence monitoring from space, and increasing realism of numerical MHD simulations of solar-atmosphere fine structure. Photosphere–chromosphere–corona coupling is a key research topic and becomes addressable at the level of detailed understanding rather than wishful cartoon/mechanism thinking.

Classical spectroscopy. Traditionally, solar spectroscopy concentrated on abundance determination using solar spectrum atlases and assuming LTE with a best-fit plane-parallel hydrostatic-equilibrium model photosphere (review: Rutten 2002). This practice and the resulting standards in helioseismology and stellar evolution theory have been upset by Asplund's turning to 3D time-dependent Nordlund-Stein granulation simulations and obtaining significantly smaller abundance values for key elements such as oxygen, carbon and nitrogen (e.g., Asplund et al. 2004; review: Nordlund et al. 2009).

Trends in observation. The emphasis of current solar spectrometry is on imaging spectroscopy with high image quality, improving spatial and temporal coverage and resolution by limiting the spectral sampling to only moderate spectral resolution in only specific diagnostic lines. Optically this is done best with Fabry-Pérot interferometers (IBIS, Cavallini 2006, Reardon & Cavallini 2008; CRISP, Scharmer 2006, Scharmer et al. 2008; the new Göttingen one, Bello González & Kneer 2008). They sample selected line profiles sequentially in time. Instantaneous integral-field spectrometry using fiber and/or lenslet arrays for field reformatting is highly desirable but remains on the horizon (Rutten 1999b; Lin et al. 2004; Sankarasubramanian et al. 2009). Slit spectrometers are still in use, but only for precision spectropolarimetry and for ultraviolet emission-line measurement from space, in both cases for want of suited integral-field technology. Slits are no good because they always sample the wrong place at the wrong time. In ground-based observation, they also inhibit wavefront restoration by algorithms such as the very effective MOMFBD of van Noort et al. (2005), a must in addition to adaptive optics. In space-based observation, multi-layer mirror technology has enabled the fruitful narrow-passband EUV imaging of SOHO, TRACE, STEREO and the comprehensive monitoring promised by SDO, but, unfortunately, ultraviolet integral-field spectrometry remains a too distant hope.

Trends in interpretation. Solar-atmosphere radiative transfer modeling is presently split between data inversions and simulatory forward modeling. Inversion codes initiated by Ruiz-Cobo et al. (1990, 1992) replace the classical "semi-empirical" (= best-fit) "one-dimensional" (= plane-parallel hydrostatic-equilibrium) modeling that either assumed LTE and CRD (Holweger 1967; revised into HOLMUL by Holweger & Müller 1974) or relaxed these assumptions to NLTE and PRD (VALC, Vernazza et al. 1981, revised into FALC by

Fontenla et al. 1993). The data inversions obtain such best-fit stratifications per pixel on the solar surface and are applied particularly in photospheric spectropolarimetry. Just as for the standard models, they loose credibility higher up where clapotispheric (see below) and chromospheric fluctuations are too wild for smooth spline-function fitting or temporal averaging and vertical columns too poor a sample of 3D structure. Chromospheric line formation requires forward modeling in the form of NLTE line synthesis within numerical simulations including non-equilibrium ionization evaluation (see below). A major task is to implement 3D time-dependent radiative transfer in 3D time-dependent MHD codes. A major challenge is to make such codes fast.

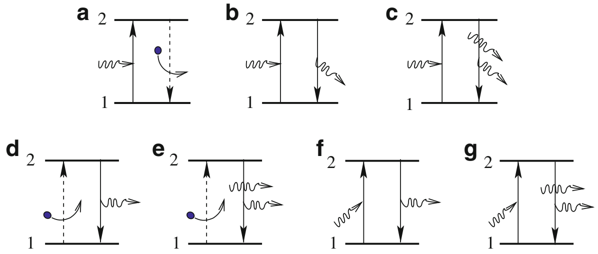

Fig. 1. Bound-bound process pairs contributing line extinction and emissivity. *Pair a*: photon destruction. *Pairs b and c*: spontaneous and induced scattering out of the beam. *Pairs d and e*: photon creation. *Pairs f and g*: scattering into the beam. From Rutten (2003).

2 Solar line formation

Fig. 1 displays all radiative excitation–deexcitation process combinations for idealized two-level atoms. Their competition defines different radiation-physics domains of spectral line formation:

- *LTE = large collision frequency*
  - up: mostly collisional = thermal creation (d + e);
  - down: mostly collisional = large destruction probability (a);
  - photon travel: “honorary gas particles” or negligible leak.
- *NLTE = statistical equilibrium or time-dependent*
  - up and down: mostly radiative = non-local sources;
  - two-level scattering: coherent/complete/partial redistribution;
  - multi-level travel: pumping, suction, sensitivity transcription.
- *coronal equilibrium = hot tenuous*
  - up: only collisional = thermal creation (only d);
  - down: only spontaneous (only d);
  - photon travel: escape / drown / scatter bf H I, He I, He II.

that also characterizes line formation in solar-atmosphere domains:

- *Photosphere.* Optical continuum and weak-line photon escape. High density makes LTE (= Saha–Boltzmann population ratios producing $S_\nu = B_\nu$) valid for optical continua and reasonable for most subordinate lines. "Height of formation" is a valid concept. The major trick is the Eddington-Barbier approximation $I_\nu(\tau_\nu = 0, \mu) \approx S_\nu(\tau_\nu = \mu) \approx B_\nu[T(\tau_\nu = \mu)]$ for quick insight and inversion constraining. Upper-photosphere resonance lines such as the Na I D lines, K I 7699 Å, and Ba II 4554 Å darken from simple resonance scattering (Uitenbroek & Bruls 1992).
- *Chromosphere.* Strong-line photon escape. LTE is invalid, statistical equilibrium is invalid, complete redistribution is invalid, instantaneous ionization equilibrium is invalid, single-fluid description is likely to be invalid. Height of formation: fibrils somewhere between the photosphere and the telescope (Rutten 2007). The major trick is the four-parameter (S_ν, τ_ν, $\lambda - \lambda_0$, $\Delta\lambda_\mathrm{D}$) cloud model of Beckers (1964), but all applications deriving temperature and density using Hα have erred in assuming instantaneous ionization/recombination balancing (see below).
- *Corona.* Immediate photon escape. Optical thinness plus the (d)-only equilibrium (but adding dielectronic recombination into the bound-free analogon) give the major trick: $\sum h\nu \propto \int n_\mathrm{ion} N_\mathrm{e}\ \mathrm{d}z = \int N_\mathrm{e}^2\,(\mathrm{d}T/\mathrm{d}z)^{-1}\ \mathrm{d}T \equiv$ "emission measure". Resonance scattering may affect the strongest lines. Bound-free scattering out of EUV-line filtergraph passbands makes neutral-hydrogen clouds appear thickly black against bright EUV-line backgrounds in EUV filtergrams (see the cartoon in Fig. 10 of Rutten 1999a).

3 Clapotisphere versus chromosphere

The LTE line-fitting HOLMUL model favored by pre-Asplund abundance determiners has no chromosphere whatsoever but a temperature stratification close to radiative equilibrium to avoid non-observed reversals (emission cores) in strong Fe I lines. Admitting realistic NLTE departures delivers the same apparent line-core excitation temperatures when there is a chromospheric temperature rise above $h \approx 500$ km (Rutten & Kostik 1982), and therefore the NLTE VALC/FALC models fudged the ultraviolet line haze (Zwaan 1975) to resemble HOLMUL LTE lines by imposing a gradual transition from pure absorption to pure scattering over the upper photosphere (Rutten 1988), so that they don't feel the VALC/FALC temperature rise which became known as "the chromosphere". However, Carlsson & Stein (1997) showed that such a global temperature rise is unlikely to occur below $h \approx 1000$ km in quiet-Sun internetwork, where intermittent shocks momentarily raise the temperature in brief spikes that dominate the time-averaged ultraviolet emissivity. I called this shock-ridden regime the "clapotisphere" (Rutten 1995) using a nautical term for fierce wave interaction. It is cartoonized in Fig. 2.

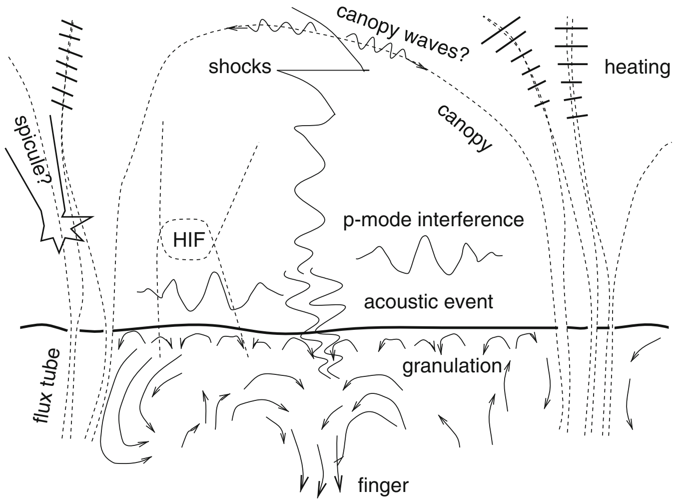

Fig. 2. Cartoon of the sub-canopy clapotisphere, pervaded by three-minute shocks. HIF stands for horizontal internetwork field (Lites et al. 1996). From Rutten (1999a).

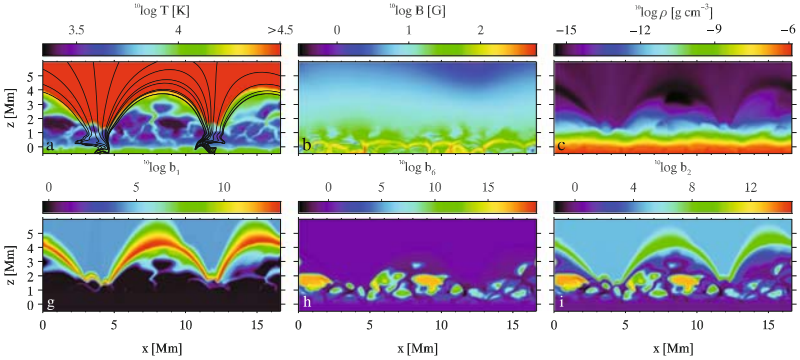

Fig. 3. Snapshot from a 2D MHD Oslo STAGGER simulation with non-equilibrium hydrogen ionization. A movie version is available at http://www.astro.uu.nl/~rutten/rrweb/talk-material/hion2_fig1_movie.mov. Each panel is a vertical plane reaching from the top of the convection zone to the corona. *Upper row*: temperature with selected magnetic field lines, field strength, gas density. *Lower row*: NLTE population departure coefficients for the ground state, ion state, and first excited state of hydrogen. All color coding is logarithmic. Two fluxtube-like magnetic concentrations are connected by high-arching field that is outlined by very large hydrogen ground-state and excited-state overpopulations (red and green arches in the lower row). The internetwork-like domain under the arches is mostly cool but pervaded by interacting shocks (clouds in the last two panels). The movie shows dynamic fibrils (De Pontieu et al. 2007a) that jut out from the magnetic concentrations and expand and contract in rapid succession. From Leenaarts et al. (2007).

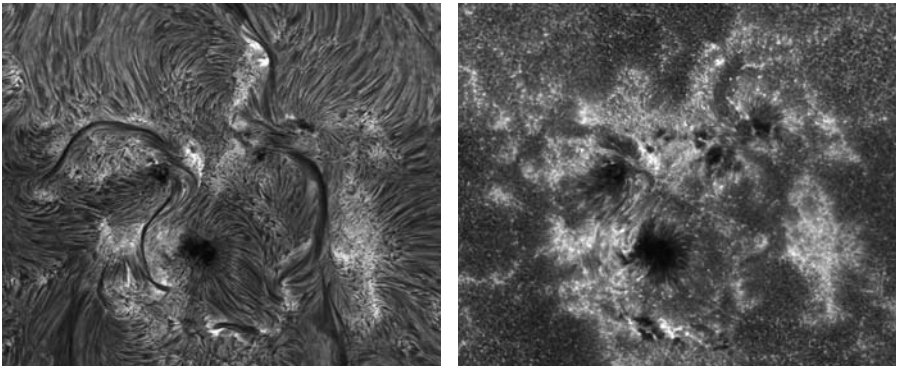

Fig. 4. Active region AR10786 imaged synchronously in Hα and Ca II H by P. Sütterlin with the Dutch Open Telescope (DOT) on La Palma on July 8, 2005. Field size 182 × 133 arcsec. The Hα imaging used a tunable Lyot filter with passband 0.25 Å FWHM, the Ca II H imaging an interference filter with passband 1.35 Å FWHM. The DOT also takes images synchronously in the G band, blue and red continua, and since recently in the Ba II 455 Å line. Many more DOT images, many DOT movies, and all reduced DOT data are available at http://dot.astro.uu.nl.

Such cartoons are now being vindicated by the numerical STAGGER simulations performed in Oslo (Hansteen et al. 2007). The STAGGER snapshot in Fig. 3 shows smooth field at heights above the canopies outlined by high arches of exceedingly large internetwork hydrogen $n = 1$ and $n = 2$ NLTE overpopulations. Clapotispheric shocks interact and dominate beneath these arches. The intershock phases are cool (first panel) and have large ion and $n = 2$ overpopulations (last two panels). These arise from sluggish recombination. Hydrogen ionizes fast in the hot shocks, but does not recombine quickly enough in the cool aftermath to settle its ion/atom balancing before the next shock comes along. The overpopulation of the $n = 2$ level, which sets the opacity of Hα, follows the ground-state overpopulations in the arches and the ion overpopulations in the clapotisphere.

So what is the chromosphere? Classically, the name denotes the thin Hα-dominated pink crescents around the eclipsed Sun glimpsed just after second and just before third contact[2]. The Hα image in Fig. 4 shows that this pink emission is dominated by long fibrils that connect various parts of active regions. In quieter areas, such Hα fibrils typically connect network across cell interiors. These fibrils constitute the chromosphere. The parallel Ca II H image maps them only in the active region and only partially even there. Elsewhere it displays clapotispheric sub-canopy shocks and H_{2V} grains. Thus, the Hα image shows the chromosphere whereas the Ca II H image is partly clapotispheric and partly chromospheric (but mostly pseudo, see below).

---

[2] As on July 22 this year in India if the weather suits.

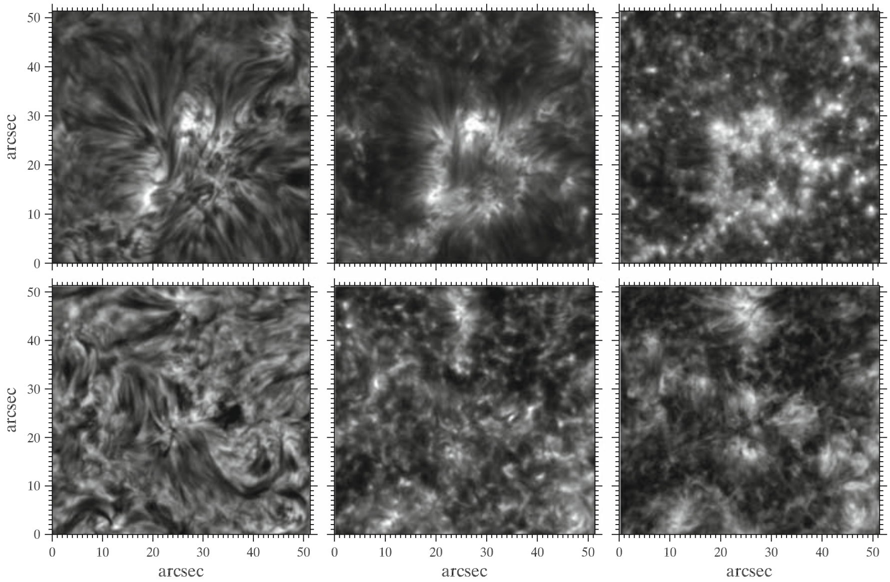

Fig. 5. Two sets of IBIS images. *Upper row*: active network in Hα, Ca II 8542 Å, Na I D$_1$. *Lower row*: quiet network in Hα, Ca II 8542 Å, Hα core width. The first five panels display the intensity of the line-profile minimum per pixel, the last panel the FWHM of the chromospheric Hα core per pixel. IBIS is the Italian double Fabry-Pérot imaging spectrometer at the Dunn Solar Telescope of the US National Solar Observatory. More detail in Cauzzi et al. (2009). Courtesy Kevin Reardon.

Fig. 5 shows similar comparisons. The active network again shows long network-spanning fibrils in Hα, but the quiet region has the clapotisphere poking through away from network even in Hα (cf. Rouppe van der Voort et al. 2007; Rutten et al. 2008). The upper Ca II 8542 Å image shows the fibrils partially, the lower one is mostly clapotispheric away from the network. The Na I D$_1$ image (third panel) also, or not even clapotispheric but just upper-photospheric since the IBIS spectroscopy shows virtually no shock signatures (Kevin Reardon, private communication). The final panel is discussed below.

4 Pseudo diagnostics of the chromosphere

Many spectral features that are commonly supposed to be chromospheric actually are "below-the-surface viewers" for which enhanced brightness has nothing to do with chromospheric emissivity or heating but with deep photon escape. The viewing pipes are Spruit fluxtubes, slender kilogauss magnetic concentrations that occur only sparsely and intermittently in quiet-Sun supergranulation cell interiors (De Wijn et al. 2005) but assemble more stably in supergranular cell boundaries to form the magnetic network. At yet larger density they constitute plage. Fig. 6 explains how they appear as “bright points” near disk center and as “faculae” towards the limb.

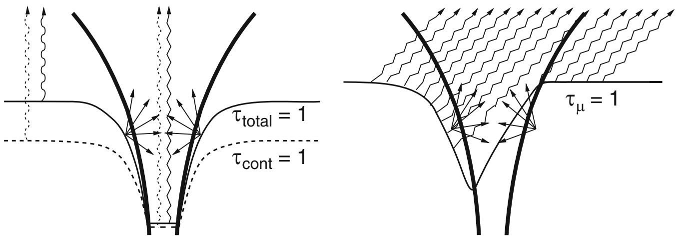

Fig. 6. Hole-in-surface fluxtube brightening. *Left*: radial viewing. The magnetic-pressure evacuation deepens the photon escape layer to well below the outside surface and causes additional deepening for neutral-atom lines through ionization, for molecular lines through dissociation, and for strong-line wings through reduced damping. The escape layers have similar temperatures inside and outside, but the tube has a flatter temperature gradient due to hot-wall irradiation. *Right*: slanted near-limb viewing. The tube evacuation causes facular sampling of the hot granule behind the tube, appearing as a bright stalk. From Rutten (1999a), after Spruit (1976).

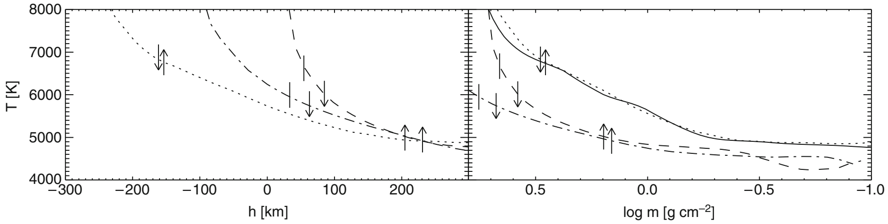

Fig. 7. Temperature stratifications in a fluxtube-like magnetic concentration (dotted), a granule (dashed) and an intergranular lane (dot-dashed) in a 3D MHD simulation. *Left*: against geometrical height. *Right*: against column mass. *Markers*: $\tau = 1$ locations for Mn I 5394.7 Å (up arrows), Fe I 5395.2 Å (down arrows), continuum in between (arrowless). The solid curve is the PLA model of Solanki & Brigljevic (1992) derived from multi-line spectropolarimetry without angular resolution. The fabulous agreement between this empirical best-fit model and the ab-initio simulation mutually vindicates these very different approaches. Both spectral lines nearly vanish in the magnetic concentration from ionization. The Mn I line is formed at much larger height in the granule and lane than the Fe I line which suffers weakening from convective Dopplershifts. From Vitas et al. (2009).

Also this old cartoon has been vindicated by recent simulations, for continuum faculae by Keller et al. (2004), for G-band faculae by Carlsson et al. (2004), for bright points in the wings of strong lines by Leenaarts et al. (2006), and for bright points in the unusually wide lines of Mn I by Vitas et al. (2009).

The latter analysis, summarized in Fig. 7, explains why the brightening seems less in all other, less wide, photospheric lines: it is not, but they show the outside granulation brighter from convective Dopplershift wash-out and so loose fluxtube contrast.

These fluxtubes have near-radiative-equilibrium stratifications across the upper photosphere, at least up to $h \approx 400$ km as sampled by the wings of Ca II H & K (Sheminova et al. 2005), just as the mean outside photosphere above the granulation. No significant mechanical heating therefore: photospheric fluxtubes brighten through deeper viewing. All solar irradiance modeling efforts that regard faculae as hot stick-up stalks and mimic such with raised-temperature upper photospheres are inherently wrong (e.g., Unruh et al. 1999; Fontenla et al. 2006; Danilović et al. 2007).

The Na I D_1 image in Fig. 5 also suggests that the network brightening in this line is mostly hole-in-the-surface viewing. The outside $\tau = 1$ surface is formed in the upper photosphere and very dark from scattering (Uitenbroek & Bruls 1992), the tube inside is likely to be as bright as the continuum from ionization. This is now verifiable with Oslo STAGGER simulations.

The 5th panel of Fig. 5 also suggests that Ca II 8542 $\AA$ gains network brightening from surface-hole viewing when not obscured by fibrils. The STAGGER simulation of Leenaarts et al. (2009) supports this notion. The fluxtube at left in their Fig. 4 obtains large brightness from deep line-center formation and Doppler brightening in a post-shock downdraft, a likely occurrence in deep-shocking fluxtubes (Steiner et al. 1998).

The Ca II H & K lines have larger opacity than Ca II 8542 $\AA$ in any imaginable structure and reach larger opacity than Hα in classical LTE modeling[3] and in one-dimensional NLTE modeling (Vernazza et al. 1981). One would therefore expect to observe a denser fibril forest at right in Fig. 4 than at left. However, the DOT Ca II H filter and all other H & K filtergraphs have far too wide passbands to isolate the line core, even the narrowest ones at 0.3 $\AA$ (Brandt et al. 1992; Hoekzema et al. 1998; Wöger et al. 2006). In addition, fibrils are very dark in H & K (Rutten et al. 2008), so that the addition of bright structures in the inner wings dominates the scene. Magnetic concentrations are likely to again function as hole-in-the-surface viewers, with the outside surface clapotispherically cool and dark except in shocks, and the tube inside and close surroundings bright by scattering photons from below (cf. Fig. 8 of Rutten 1999a, another old cartoon).

Thus, I contend that the apparent network brightness in Na I D_1 and Ca II 8542 $\AA$ imaging spectroscopy and much of the apparent network brightness in Ca II H & K filtergrams has less to do with chromospheric heating than with hole-in-the-surface viewing. Corollaries are that the Mount-Wilson Ca II H & K stellar activity monitoring (e.g., Rutten 1986; Duncan et al. 1991) delivers counts of such holes on the stellar surface, not the amount of chromospheric heating, and that the good correspondence between the various diagnostics

---

[3] http://www.astro.uu.nl/~rutten/rrweb/rjr-material/bachelor/ssa.

of Loukitcheva et al. (2009) follows naturally because they are all hole counters. And I repeat that the basal flux (review: Schrijver 1995) is most likely clapotispheric (Rutten 1999a).

5 Heating in the chromosphere

So how to diagnose chromospheric heating, or rather, the onset of coronal heating taking place in the chromosphere? My contention that most network emissivity in Na I D_1, Ca II 8542 Å and Ca II H in Figs. 4 and 5 stems from photospheric or clapotispheric view-pipe photon escape leads to the suggestion that not much chromospheric heating is seen in these images. The Hα fibrils do display chromospheric fine-structure morphology, but whether these appear dark or bright is a matter of fortuitous combination of the four cloud parameters S_ν, τ_ν, $\lambda - \lambda_0$, $\Delta\lambda_\mathrm{D}$. Only $\Delta\lambda_\mathrm{D}$ senses the temperature directly because the small atomic mass of hydrogen favors thermal over nonthermal broadening. The final panel of Fig. 5 therefore displays a measure of chromospheric temperature. It evidences heating in and near network (Cauzzi et al. 2009).

It seems likely that this network heating occurs through open-field chromospheric structures, i.e., more vertical than Hα fibrils and connecting less closely than across network cells. They are barely visible in Hα but were discovered as fast-waving "straws" in DOT Ca II H near-limb movies, appearing bright against the very dark internetwork clapotisphere (Rutten 2006), and subsequently as fast-waving "spicules-II" in Hinode Ca II H off-limb movies by De Pontieu et al. (2007b). De Pontieu et al. (2007c) identified Alfvén waves as their modulation agent and estimated that these accelerate the solar wind. Being very slender and very fast-moving, straws/spicules-II are very hard to observe on-disk (Langangen et al. 2008), but ongoing work (De Pontieu et al. 2008) suggests that they occur ubiquitously above unipolar network and plage and may supply heating through component reconnection, reminiscent of the separatrix shear proposed by Van Ballegooijen et al. (1998, 1999) and marked as cross-dashes in my old cartoon in Fig. 2. I suggest that unresolved straw heating causes the network patches of large Hα core width in the last panel of Fig. 5, some of the Ca II 8542 Å near-network fibril brightness in the second panel of Fig. 5, and the diffuse bright aureoles seen in DOT Ca II H movies around network that seem to resolve into straws in the very sharpest one[4].

Another speculation is that straw dynamics also contributes to the solar-wind FIP fractionation.

6 Discussion

There are striking and disconcerting similarities between the visibility of the corona in the form of EUV-line loops and of the chromosphere in the form of

---

[4] http://dot.astro.uu.nl/albums/movies/2006-04-24-NW-ca.avi or .mov

Hα fibrils. Both types of structure seem to map the large-scale magnetic field topology, although there is no direct proof of direct correspondence. In both cases it is a misconception to regard them as magnetic fluxtubes embedded in field-free plasma (or vacuum). Loops and fibrils chart bundles of field that for some reason contain more gas containing atoms and ions in the right state for emissivity and/or extinction in the pertinent lines than the surrounding, otherwise very similar field bundles. The actual field topology is probably more uniform than the fine-scaled emissivity/extinction structuring suggests (Judge 2006). The mass loading and dynamics of these narrow bundles are likely structured on the scales of intergranular fluxtubes by thermodynamical processes affecting these magnetic footpoints, but the actual connection topology may be as complicated as in Fig. 18 of De Pontieu et al. (2003).

A disconcerting similarity of coronal loops and chromospheric fibrils is that neither structure has yet been produced naturally in MHD simulations. Acoustic oscillations have been shown to drive and probably mass-load short dynamic fibrils jutting out from network and plage (Hansteen et al. 2006; De Pontieu et al. 2007a), but the mass loading of the long network-spanning fibrils and yet longer coronal loops remains unexplained. The overpopulation arches in Fig. 3 are promisingly similar to actual Hα fibrils, but they contain insufficient Hα opacity, notwithstanding their enormous $n=2$ overpopulation, to produce the $\tau \approx 1$ thickness in Hα that is characteristic of fibrils. This simulation was 2D only, but also the newer 3D Oslo STAGGER simulations have not produced fibrils or loops so far. Perhaps the simulation volumes are still too small, or perhaps they are too unipolar, or perhaps longer history is needed, perhaps to let trickling siphon flows build up appreciable mass loads.

Another disconcerting similarity is that both coronal loops and chromospheric fibrils delineate closed fields whereas the action lies in the open-field components, respectively driving the fast wind and heating the corona. Their visibility is meager: coronal holes are indeed holes in emissivity and chromospheric straws/spicules-II were discovered only recently. The natural emphasis on higher-visibility loops and fibrils seems to target red herrings qua importance and role.

Finally, it seems likely that the so-called transition region exists mostly as hot evaporation sheaths around these ephemeral structures (McIntosh et al. 2008; Judge & Centeno 2008; Koza et al. 2009), a far cry from the stable spherical shell invoked in one-dimensional modeling or the radial stratification wishfully assumed in many transition-region oscillation propagation studies.

References

Asplund, M., Grevesse, N., Sauval, A. J., Allende Prieto, C., Kiselman, D. 2004, A&A, 417, 751

Beckers, J. M. 1964, A Study of the Fine Structures in the Solar Chromosphere, AFCRL Environmental Research Paper No. 49, PhD thesis Utrecht University

Bello González, N., Kneer, F. 2008, A&A, 480, 265
Brandt, P. N., Rutten, R. J., Shine, R. A., & Trujillo Bueno, J. 1992, Cool Stars, Stellar Systems, and the Sun, ASP Conf. Ser., 26, 161
Carlsson, M., Stein, R. F. 1997, ApJ, 481, 500
Carlsson, M., Stein, R. F., Nordlund, Å., Scharmer, G. B. 2004, ApJ, 610, L137
Cauzzi, G., Reardon, K., Rutten, R., Tritschler, A., Uitenbroek, H. 2009, A&A, in press, arXiv:0906.2083
Cavallini, F. 2006, Solar Phys., 236, 415
Danilović, S., Solanki, S. K., Livingston, W., Krivova, N., Vince, I. 2007, in Modern solar facilities - advanced solar science, eds. F. Kneer, K. G. Puschmann, & A. D. Wittmann, 189
De Pontieu, B., Carlsson, M., McIntosh, S., Hansteen, V., Tarbell, T. 2008, 12th European Solar Physics Meeting, http://espm.kis.uni-freiburg.de, 2.15
De Pontieu, B., Hansteen, V. H., Rouppe van der Voort, L., van Noort, M., Carlsson, M. 2007a, ApJ, 655, 624
De Pontieu, B., McIntosh, S., Hansteen, V. H., et al. 2007b, PASJ, 59, 655
De Pontieu, B., McIntosh, S. W., Carlsson, M., et al. 2007c, Science, 318, 1574
De Pontieu, B., Tarbell, T., Erdélyi, R. 2003, ApJ, 590, 502
De Wijn, A. G., Rutten, R. J., Haverkamp, E. M. W. P., Sütterlin, P. 2005, A&A, 441, 1183
Duncan, D. K., Vaughan, A. H., Wilson, O. C., et al. 1991, ApJS, 76, 383
Fontenla, J. M., Avrett, E., Thuillier, G., Harder, J. 2006, ApJ, 639, 441
Fontenla, J. M., Avrett, E. H., Loeser, R. 1993, ApJ, 406, 319
Hansteen, V. H., Carlsson, M., Gudiksen, B. 2007, in The Physics of Chromospheric Plasmas, eds. P. Heinzel, I. Dorotovič, & R. J. Rutten, ASP Conf. Ser., 368, 107
Hansteen, V. H., De Pontieu, B., Rouppe van der Voort, L., van Noort, M., Carlsson, M. 2006, ApJ, 647, L73
Hoekzema, N. M., Rutten, R. J., Brandt, P. N., & Shine, R. A. 1998, A&A, 329, 276
Holweger, H. 1967, Zeitschrift fur Astrophysik, 65, 365
Holweger, H., Müller, E. A. 1974, Solar Phys., 39, 19
Judge, P. 2006, in Solar MHD Theory and Observations: A High Spatial Resolution Perspective, eds. J. Leibacher, R. F. Stein, & H. Uitenbroek, ASP Conf. Ser., 354, 259
Judge, P., Centeno, R. 2008, ApJ, 687, 1388
Judge, P. G., Peter, H. 1998, Space Science Reviews, 85, 187
Keller, C. U., Schüssler, M., Vögler, A., Zakharov, V. 2004, ApJ, 607, L59
Koza, J., Rutten, R. J., Vourlidas, A. 2009, A&A, 499, 917
Langangen, Ø., De Pontieu, B., Carlsson, M., et al. 2008, ApJ, 679, L167
Leenaarts, J., Carlsson, M., Hansteen, V., Rouppe van der Voort, L. 2009, ApJ, 694, L128
Leenaarts, J., Carlsson, M., Hansteen, V., Rutten, R. J. 2007, A&A, 473, 625
Leenaarts, J., Rutten, R. J., Carlsson, M., Uitenbroek, H. 2006, A&A, 452, L15
Lin, H., Kuhn, J. R., Coulter, R. 2004, ApJ, 613, L177
Lites, B. W., Leka, K. D., Skumanich, A., Martínez Pillet, V., Shimizu, T. 1996, ApJ, 460, 1019
Loukitcheva, M., Solanki, S. K., White, S. M. 2009, A&A, 497, 273
McIntosh, S. W., De Pontieu, B., Tarbell, T. D. 2008, ApJ, 673, L219
Nordlund, Å., Stein, R. F., Asplund, M. 2009, Living Reviews in Solar Physics, 6, 2
Reardon, K. P., Cavallini, F. 2008, A&A, 481, 897

Rouppe van der Voort, L. H. M., De Pontieu, B., Hansteen, V. H., Carlsson, M., van Noort, M. 2007, ApJ, 660, L169

Ruiz Cobo, B., del Toro Iniesta, J. C. 1992, ApJ, 398, 375

Ruiz Cobo, B., del Toro Iniesta, J. C., Collados, M., Sánchez Almeida, J. 1990, Ap&SS, 170, 113

Rutten, R. G. M. 1986, A&A, 159, 291

Rutten, R. J. 1988, in Physics of Formation of FeII Lines Outside LTE, eds. R. Viotti, A. Vittone, & M. Friedjung, IAU Coll. 94, Reidel, Dordrecht, 185

Rutten, R. J. 1995, in Helioseismology, eds. J. T. Hoeksema, V. Domingo, B. Fleck, & B. Battrick, ESA SP–376 Vol. 1, 151

Rutten, R. J. 1999a, in Magnetic Fields and Oscillations, eds. B. Schmieder, A. Hofmann, & J. Staude, ASP Conf. Ser., 184, 181

Rutten, R. J. 1999b, in High Resolution Solar Physics: Theory, Observations, and Techniques, eds. T. R. Rimmele, K. S. Balasubramaniam, R. R. Radick, ASP Conf. Ser., 183, 296

Rutten, R. J. 2002, J. Astron. Data, 8, 8

Rutten, R. J. 2003, Radiative Transfer in Stellar Atmospheres, http://www.astro.uu.nl/~rutten, Lecture notes Utrecht University

Rutten, R. J. 2006, in Solar MHD Theory and Observations: A High Spatial Resolution Perspective, eds. J. Leibacher, R. F. Stein, H. Uitenbroek, ASP Conf. Ser., 354, 276

Rutten, R. J. 2007, in The Physics of Chromospheric Plasmas, eds. P. Heinzel, I. Dorotovič, R. J. Rutten, ASP Conf. Ser., 368, 27

Rutten, R. J., Kostik, R. I. 1982, A&A, 115, 104

Rutten, R. J., van Veelen, B., Sütterlin, P. 2008, Solar Phys., 251, 533

Sankarasubramanian, K., Hasan, S. S., Rangarajan, K. E. 2009, in Magnetic Coupling between the Interior and the Atmosphere of the Sun, eds. S. S. Hasan, R. J. Rutten, Springer, Heidelberg, in press

Scharmer, G. B. 2006, A&A, 447, 1111

Scharmer, G. B., Narayan, G., Hillberg, T., et al. 2008, ApJ, 689, L69

Schrijver, C. 1995, A&A Rev., 6, 181

Sheminova, V. A., Rutten, R. J., Rouppe van der Voort, L. H. M. 2005, A&A, 437, 1069

Solanki, S. K., Brigljevic, V. 1992, A&A, 262, L29

Spruit, H. C. 1976, Solar Phys., 50, 269

Steiner, O., Grossmann-Doerth, U., Knölker, M., Schüssler, M. 1998, ApJ, 495, 468

Uitenbroek, H., Bruls, J. H. M. J. 1992, A&A, 265, 268

Unruh, Y. C., Solanki, S. K., Fligge, M. 1999, A&A, 345, 635

van Ballegooijen, A. A., Nisenson, P. 1999, in High Resolution Solar Physics: Theory, Observations, and Techniques, eds. T. R. Rimmele, K. S. Balasubramaniam, R. R. Radick, ASP Conf. Ser., 183, 30

van Ballegooijen, A. A., Nisenson, P., Noyes, R. W., et al. 1998, ApJ, 509, 435

van Noort, M., Rouppe van der Voort, L., Löfdahl, M. G. 2005, Solar Phys., 228, 191

Vernazza, J. E., Avrett, E. H., Loeser, R. 1981, ApJS, 45, 635

Vitas, N., Viticchiè, B., Rutten, R. J., Vögler, A. 2008, A&A, 499, 301

Wöger, F., Wedemeyer-Böhm, S., Schmidt, W., von der Lühe, O. 2006, A&A, 459, L9

Zwaan, C. 1975, Solar Phys., 45, 115

"Recent Advances in Spectroscopy:
Theoretical, Astrophysical, and Experimental Perspectives"
Eds. Chaudhuri R K, Mekkaden M V, Raveendran A V, Satya Narayanan A
Astrophysics and Space Science Proceedings, Springer-Verlag, Berlin, 2010.

High-resolution spectroscopy of the R Coronae Borealis and Other Hydrogen Deficient Stars

N. Kameswara Rao[1] and David L. Lambert[2]

[1] Indian Institute of Astrophysics, Bangalore 560034, India
`nkrao@iiap.res.in`
[2] The W.J. McDonald Observatory, The University of Texas, Austin, TX 78712-1083, USA
`dll@astro.as.utexas.edu`

Summary. High-resolution spectroscopy is a very important tool for studying stellar physics, perhaps, particularly so for such enigmatic objects like the R Coronae Borealis and related Hydrogen deficient stars that produce carbon dust in addition to their peculiar abundances. Examples of how high-resolution spectroscopy is used in the study of these stars to address the two major puzzles are presented: (i) How are such rare H-deficient stars created? and (ii) How and where are the obscuring soot clouds produced around the R Coronae Borealis stars?

1 Introduction

We congratulate the organizers for arranging and conducting this conference, celebrating the 150 years of the discovery by (Gustav Robert) Kirchoff and (Robert Wilhelm Eberhard) Bunsen that various gases can be easily and positively identified by a detailed study of the light they emit and absorb. As Paul Merrill (Merrill 1963) noted, a new era in astronomy began when Bunsen saw the Na D lines 'in yellow flame of an ordinary alcohol lamp whose wick was sprinkled with salt, and recognized possibilities of the chemical analysis of the most distant stars'. Thus began the era of astronomical spectroscopy. Merrill's own contributions to our discipline are legendary with his discovery of Tc I lines in the spectra of S stars signaling that element synthesis in stars was a continuing phenomena (Merrill 1952).

A few historical remarks might be appropriate. Astronomical spectroscopy in India started during the famous total solar eclipse that occurred on 1868 August 18 in which a spectroscope was first used to study the nature of solar prominences leading to the discovery of helium. Madras observatory, from which the present host Institution evolved, also played a role. Norman Robert

Pogson, then director of the observatory, used a visual spectroscope to look at the prominences and noted a bright line in the yellow close to but not coincident with sodium D lines. This was the D3 line - the same line as found by Janssen during the 1868 eclipse but by Lockyer without the aid of eclipse. The first stellar spectrum recorded in India was obtained at Madras (now Chennai); this was a spectrum of the Wolf-Rayet star γ^2 Velorum observed in 1871.

Spectroscopic analysis of some of the most enigmatic stars yet discovered is the theme of our contribution. The chosen stars are the R Coronae Borealis stars and their putative cooler relatives, the hydrogen-deficient cool carbon stars (HdCs). The enigma presented by these stars has two principal parts: (i) How did these stars become so H-deficient? and (ii) how do the RCBs but not the HdCs develop thick clouds of soot that obscure the stellar photosphere from view? Answers to these questions are emerging. Here, we highlight particular contributions to their solution from analysis of high-resolution optical and infrared spectra. Disney (2000) has lamented (tongue in cheek, we suppose) that 'the tragedy of Astronomy is that most information lies in spectra'. We would counter by substituting 'allure' for 'tragedy' and add that one should expect to apply all available observational tools in seeking answers to our questions.

R Coronae Borealis stars are a rare class of peculiar variable stars. The two defining characteristics of RCBs are (i) a propensity to fade at unpredictable times by up to about 8 magnitudes as a result of obscuration by clouds of soot, and (ii) a supergiant-like atmosphere that is very H-deficient and He-rich. The $T_{\rm eff}$ of the class ranges from 8000 to 4000 K and $\log g$ from 0.5 to 1.5 (cgs units) except for the two hotter stars DY Cen (19000 K) and MV Sgr (14000 K). The $\rm M_V$ ranges from -5 to -2.5 and $\log L$ from 4.0 to 3.2 $\rm L_\odot$. Presently, there are 52 known RCBs in the Galaxy (Tisserand *et al.* 2008; Clayton *et al.* 2009), 21 known members in the Large Magellanic Cloud and 6 in the Small Magellanic Cloud. The total number of RCBs in the Galaxy may be about 3200 (Alcock *et al.* 2001) There are only 5 known HdC stars in the Galaxy. Their detection may be hampered because they do not show RCB-like light variations, an infrared excess or a stellar wind (Geballe *et al.* 2009). They overlap the RCBs in $\rm T_{eff}$ with a spread from about 6500 to 5000 K. At the high $T_{\rm eff}$ end of the RCBs sit the Extreme helium stars (EHes) of which 21 are known in the Galaxy with $T_{\rm eff}$ from 32000 to 9000 K and $\log g$ from 0.75 to 4.0. Their $\log L$ ranges from 4.4 to 3.0 $\rm L_\odot$. Here, we give no more than passing attention to the EHes and other, even hotter H-deficient stars that may form an evolutionary sequence with the HdCs and RCBs.

A fascinating aspect of RCBs is that they present several faces to observers, like the Hindu mythological god Karthikeya (son of Kritthikas -Pleiades) with his six faces. The faces presented to our view are (i) a chemically peculiar supergiant, (ii) a variable star obscured without warning from our view by clouds of soot, (iii) a small amplitude pulsation both in light and radial velocity with a period around 40 days, (iv) an infrared source producing dust and blowing it away after several days, weeks, months or even years as clouds, (v) a hot stellar wind, and (vi) and may even be a central star of a low density nebula as evidenced by the presence of nebular lines of [O II], [N II] (Fig. 1) and [S II]. They also have putative relatives of higher and lower temperatures, as intriguing as Karthikeya's relatives.

Our emphasis is on insights obtainable from high-resolution spectra with the assumption that relevant atomic and molecular data of adequate precision and completeness are to be provided from laboratory and theoretical spectroscopic studies. This assumption is patently false, as is no surprise to practicing astronomical spectroscopists. On the chance that a reader of this paper may wish to take up a challenge, we mention two aspects of the incompleteness of knowledge of the spectrum of neutral carbon that compromise some analyses of the spectra of RCBs.

Spectra of RCBs are crossed by many lines of C I, as noted by Keenan & Greenstein (1963). One might refer to the spectrum of a RCB as arising from a column of somewhat contaminated high-temperature carbon vapour. A great step forward in identifying the C I lines was made when Johansson (1965) extended the laboratory spectrum and knowledge of the C I term system. With modern spectra of RCBs, many suspected C I lines remain unidentified and cry out for a new laboratory investigation of the C I spectrum. Today, astronomical spectroscopists often require more than a set of wavelengths and a table of energy levels. This is certainly true for the pursuit of an abundance analysis leading to the chemical composition of a RCB. Abundance analysis at a minimum requires knowledge of the gf-values for identified lines including the C I lines. Asplund *et al.* (2000) report on an extensive abundance analysis of RCBs and their uncovering of a 'carbon problem' which may arise because the adopted theoretical gf-values or the photoionization cross-sections for neutral carbon were too large by a factor of about four. (Asplund et al. also suggested possible ways to reduce the carbon problem without appealing to deficiencies in atomic physics.) Where are the physicists who will attack the spectrum of the carbon atom with the precision and thoroughness that we seek?

2 Major Puzzles

As stated in the Introduction, the two principal puzzles presented by the RCBs concern their origins and their ability to produce soot clouds. The HdCs share the puzzle about their origins but not that of soot production. Of course, the 'dust' puzzle might incorporate the HdCs with the RCBs by asking 'Why is it that RCBs but not the HdCs, which are on average cooler than the RCBs, are prone to soot production?'

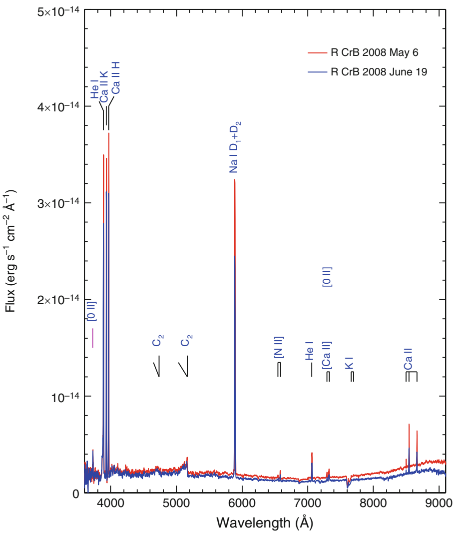

Fig. 1. Low resolution spectra obtained on 2008 May 6 and 2008 June 19 with the Himalayan Chandra Telescope (HCT) during the current minimum of R CrB which began in 2007. Emission lines are identified. A variety of emission lines both broad and sharp are present during deep minimum. Several forbidden lines of [O II], [N II] representing low density nebular gas are also present (see text).

2.1 Origins

The basic problem is to understand how a H-deficient star evolves from a H-rich single or binary star; H-poor He-rich gas clouds capable of sustaining stellar nurseries have not been found. Complete resolution of the problem would show how the classes of H-deficient stars – HdCs - RCB - EHe - beyond – are or are not related.

Presently, there are two principal hypotheses for the origins:(i) the double-degenerate (DD) scenario and (ii) a late thermal pulse or final flash (the FF scenario) in a luminous star on the white-dwarf cooling track.

In the DD scenario, a He white dwarf is accreted by a C-O white dwarf as loss of orbital energy drives the white dwarfs to merge. There are rather specific ranges of initial masses and separations for normal (H-rich) stars in a binary to merge and produce a H-deficient He-rich star. (Other combinations produce other odd stars such as a single white dwarf with a mass exceeding Chandrasekhar's limit that must go bang in the night or day.) The post-merger product has the greatly extended envelope required for a supergiant RCB and HdC star. Subsequent evolution follows the canonical post-AGB contraction to the white dwarf track (Webbink 1984; Iben & Tutukov 1984; Saio & Jeffery 2002).

In the FF scenario, H-rich post-AGB single stars reach the white dwarf cooling track with the potential to experience a final thermal pulse in their

He-shell. Under particular conditions, the thin surviving H-envelope may experience H-burning. Onset of the pulse leads to a return of the star to a supergiant-like form but, if conditions are ripe, this supergiant will be H-poor and He-rich. Subsequent evolution takes the supergiant across the HR-diagram to the white dwarf cooling track. Schonberner (1979), Iben *et al.* (1983), Renzini *et al.* (1990), and Herwig (2001) among others discuss aspects of the FF scenario. Enigmatic stars such as FG Sge and Sakurai's object (V4334 Sgr) are commonly identified as FF scenario products.

Quantitative comparison of predictions of the FF and DD scenario and the observations of the RCB and HdC stars involves several dimensions. Our focus here is on the chemical composition obtainable only from examination of the spectrum of RCB and HdC stars. The (preferably) high-resolution spectra from the ultraviolet, optical and near-infrared are analyzed with model atmospheres computed for the appropriate composition (Asplund *et al.* 2000; Pandey *et al.* 2006; García-Hernández *et al.* 2009). Recent elemental abundance studies of C, N, O in particular seem to favour the DD scenario for the RCBs and HdCs (Asplund et al. 2000; Saio & Jeffery 2002; Pandey et al. 2006).

Two remarkable pieces of observational evidence tilt the balance in favour of the DD scenario. First, Clayton *et al.* (2005, 2007) made the dramatic discovery that ^{18}O is more abundant than ^{16}O from moderate resolution spectra of HdC and RCB stars showing the first-overtone CO vibration-rotation bands at about 2.3 microns. Second, Pandey (2006) for EHes and Pandey, Lambert & Rao (2008) for RCBs showed that ^{19}F was drastically overabundant. The ^{18}O and F results show that the DD scenario was not a quiescent mixing process but either involved nucleosynthesis during the merger and/or subsequently during the evolution of the merged product to and from its supergiant phase.

It is amusing to see how this discovery of ^{18}O was made in HD137613, as told us by Tom Geballe. He got an email from Geoffrey Clayton at 5:30 p.m on 2004 November 10: 'Hi Tom. I have this spectrum of the first overtone CO bands in the HdC star, HD 137613. I took a look at it and the bands were split, so I said to myself, oh well there's ^{13}CO, but the extra components aren't at the right wavelengths. So I'm a bit mystified. Take a look at the attached plot and see if you have an idea of what this is'. To which Tom replied: ' That is amazing!! I happen to have a book of CO wavelengths that I calculated when I was a grad student in the 70s. All dv = 1 and dv = 2 lines of all isotopic species. These bandheads match 12C18O!! The first three bandheads (2-0, 3-1, 4-2) of ^{12}C^{18}O are at 2.349, 2.378, and 2.408. I also looked 12C17O and it doesn't match. How could a star have as much ^{18}O as ^{16}O? What kind of star is this? Cheers and congrats, Tom (Geballe 2008).

High resolution spectroscopy is essential for properly estimating the isotope ratios ^{16}O to ^{18}O, ^{16}O to ^{17}O (as well as detection of the weak lines of ^{19}F). García-Hernández et al. (2009) used a spectral resolution of 50000 in their analysis of the 2.3 micron CO bands. They confirmed Clayton et al.'s result of a high ^{18}O overabundance for HdCs and the RCB S Aps obtaining a ratio of ^{16}O to ^{18}O of 0.5 in HdCs and the ratio 16 for S Aps (Fig.2). The high resolution optical spectra obtained with the Harlan J. Smith telescope at the McDonald Observatory and with the Vainu Bappu Telescope at Kavalur led to the discovery that ^{19}F is enhanced by a factor of several hundreds to a 1000 times solar in these stars. In passing we note that Harlan J. Smith and M.K. Vainu Bappu were great friends.

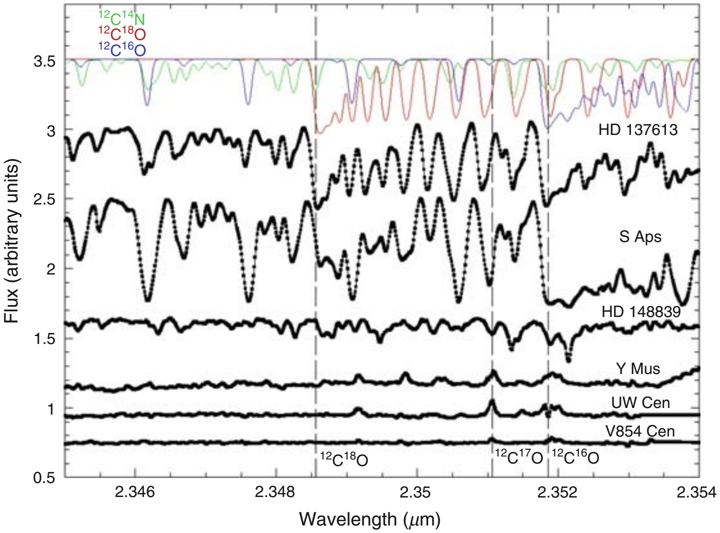

Fig. 2. High resolution spectra of two HdC stars and four RCBs in the region of 2-0 band of ^{12}C^{18}O at 2.3485 microns. The top plots show synthetic spectra computed for the HdC star HD137613 for two CO isotopologues and CN. This figure is from García-Hernández et al. (2009).

There can be no doubt that ^{18}O and ^{19}F were synthesized in or subsequent to the creation of the RCBs and HdCs. Before full acceptance of the DD scenario is made, the scenario has to account for the nucleosynthesis of these and other observable elemental and isotopic abundances. In principle, as first noted by Warner (1967), ^{18}O may be synthesized by α-capture from abundant ^{14}N. This may occur during the merger in the DD scenario but not with ease in the FF scenario. The reservoir of ^{14}N is finite and probably not easily restored, thus, one wonders what cuts off the high temperatures at the point that there remains an observable amount of nitrogen. Other complexities remain. In particular, some RCBs and one HdC show an appreciable amount of lithium, presumably ^{7}Li. Discussions of the nucleosynthesis in and following the merger are provided by Clayton *et al.* (2007), Pandey, Lambert & Rao (2008), and García-Hernández et al. (2009). Additional high-resolution spectroscopy, especially in the infrared, is desirable to determine the O isotopic abundances across the RCB sample.

The FF scenario does plausibly account for other stars. Most notable among the FF candidates are FG Sge, V4334 Sgr and V605 Aql (Clayton et al. 2005). It is not impossible that RCBs from the FF scenario lurk among the known Galactic, LMC and SMC examples.

2.2 Dust Production by RCBs

Historically, RCB stars were the first stars in which circumstellar dust production was invoked to explain brightness variations, i.e., the dramatic declines of several magnitudes (Loreta 1934; O'Keefe 1939). It is now well established that soot (carbon) clouds form close to the star and obstruct the star light reaching us. Such clouds have now been imaged in the infrared around RY Sgr at distances of about 1000 stellar radii (de Laverny & Mekarnia 2004). These clouds were formed presumably closer to the star; observational constraints prohibited their detection close to the star.

Questions abound concerning the dust. What provides the trigger for dust production in or around the star? How may dust condense in or around such hot stars as RCBs? The trigger appears to be related to the atmospheric pulsations which are revealed by light and radial velocity variations. Pugach (1977) noted a correlation between the beginning of a light decline and pulsation phase in RY Sgr. It has now been shown by Crause, Lawson & Henden (2007) for four stars, by longterm monitoring of the brightness, that when a decline happens it does so at a particular phase although not every pulsation results in a decline. Woitke *et al.* (1996) developed a model for dust formation following a pulsation-induced shock in the upper atmosphere. When the pulsation amplitudes are large, the temperatures and densities in the post-shock gas are predicted to be conducive for nucleation to occur. The question intriguing spectroscopists is – how may we observe a strong shock develop from a pulsation? What evidence may we offer that dust condensation actually takes place in the atmosphere of the star? Can we detect the presence of cool gas from which dust could condense? High-resolution spectroscopic observations prior to the onset of the minimum are crucial to studying such questions.

Recently, R CrB has entered a prolonged light decline that commenced on July 2007 and has not yet ended (July 2009). This is one of the deepest minima the star has had in several decades, reaching more than 9 magnitudes. At minimum the star shows a variety of emission lines including broad (fwhm of 250 km s^{-1}) emission lines of He I, H & K lines of Ca II, Na I D lines (Fig.1) and sharp (fwhm $\leq$ 15 km s^{-1}) emission lines due to Fe II, Ti II etc. (Rao *et al.* 1999). We postpone the discussion of this intriguing emission spectrum for a later occasion. We were fortunate to catch the star just on the verge of the decline. Our optical spectra obtained at the McDonald Observatory and at Vainu Bappu Observatory have a spectral resolution over 60000. Fig. 3 shows the light curve with the dates of our spectroscopic observations marked. The spectral changes that R CrB underwent even prior to light minimum may provide important clues to the phenomenon of dust production.

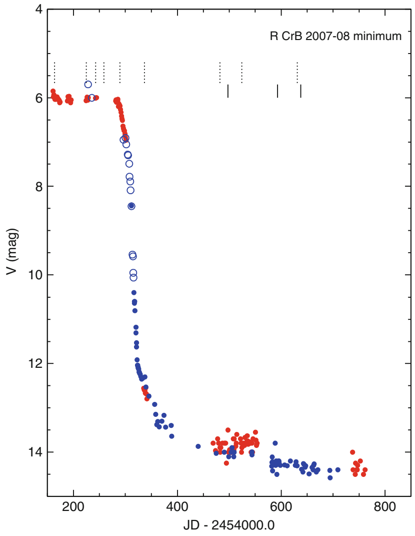

Fig. 3. The visual (red dots) light curve of R CrB from 2007 March to 2008 October. Blue dots refer to V magnitudes, blue circles are either no-filter or unknown filter measurements, red dots are daily averages of the visual estimates. All the data are obtained from AAVSO data base. The minimum started around 2007 July 10. Dates on which high-resolution spectra were obtained are indicated by the dashed lines at the top. The dates on which low-resolution spectra from the HCT are shown as short lines.

3 Prelude to Minimum: The Spectrum at Maximum Light

The present series of spectra that precede the light minimum starts on 2007 March 4. Spectra at maximum light are dominated by lines of C I, O I, N I, Si I and S I in addition to the many lines of neutral and ionized metals seen in spectra of normal F-G supergiants.

The star remained at maximum until 2007 July 10 when the decline in light started. In the following account, we discuss briefly the spectral changes that took place during maximum light. Even four months prior to the onset of the minimum, the star appears to be disturbed with emission in some line cores suggesting a component with an inverse P-cygni profile. Line doubling of the absorption lines is seen two months prior to the onset. The blue and red components of the doubled lines showed a different level of excitation for the rising gas ($T_{\rm exc}$ of 4300 K) from the infalling gas ($T_{\rm exc}$ of 5600 K).

Some lines, like Ti II 5154 Å, are not doubled but show emission in the line core. Even the cores of the Na I D lines show emission compared to the reference spectrum at 'normal' maximum light. Moreover, the radial velocity of the emissions is same as that of the star.

The absorption lines also broadened without altering their equivalent widths a month and half before the onset of minimum as though the starlight was passing through a scattering medium (see Fig. 4). Study of such line broadening requires high spectral resolution.

Some aspects of the spectroscopic changes months ahead of the decline beginning in 2007 July are not unusual. For example, line doubling appears to be a regular feature of stars such as R CrB and RY Sgr where the atmospheric pulsation is seen clearly. It will be of interest to see if these changes occur at the same or similar phases in the pulsation. Perhaps, there is a quasi-steady amplification of the changes at the particular phase lasting a sequence of several pulsations and culminating in the physical conditions amounting to the trigger for a decline. Examination of this idea will call for routine observations of a RCB such as R CrB, RY Sgr or V854 Cen, a star prone to frequent declines. Considerable observing time may be wasted in that the declines are unpredictable and irritation of Telescope Allocation Committees seems assured. But these datasets are most likely to reveal new phenomena that may tighten the link between pulsation and the trigger for dust production. For example, the spectroscopic variations – line asymmetry, doubling, radial velocity and strength – may be more extreme at particular phases.

More significantly, major disturbances were present in the spectrum of R CrB three days prior to the descent. Comparison of pre-maximum and 2007 July 7 spectra shows that most lines in 2007 July 7 spectrum have shifted-absorption components (Fig. 5) in addition to the usual photospheric lines. Fig. 5 shows a comparison of the spectrum on 2007 July 7 with respect to an undisturbed spectrum obtained on 1995 August 17 illustrating the additional absorption components to several lines that appear in the 2007 July 7 spectrum. However, the C I lines do not show such additional absorption components. Note that, while the neutral metal lines (e.g., Fe I, and Cr I) show strong blue-shifted components, the ionized metal lines (e.g., Fe II, and Cr II) show red-shifted components on 2007 July 7. Such differences suggests that rising and falling gases have different levels of ionization. As further shown in Fig. 6 during the descent to minimum the blue (ionized) and redshifted (neutral) components are separated by 53 km s^{-1} probably as a result of passage of a strong shock. Of seemingly particular relevance to dust production, the 2007 July 7 spectrum also displays lines of the C_2 Phillips system showing the presence of gas at temperatures (1000 to 800 K, Figs. 7 and 8) suggestive of a site for dust nucleation. One supposes these unusual line profiles and the appearance of cool gas are manifestations of the shock induced by the pulsation that triggered the decline.

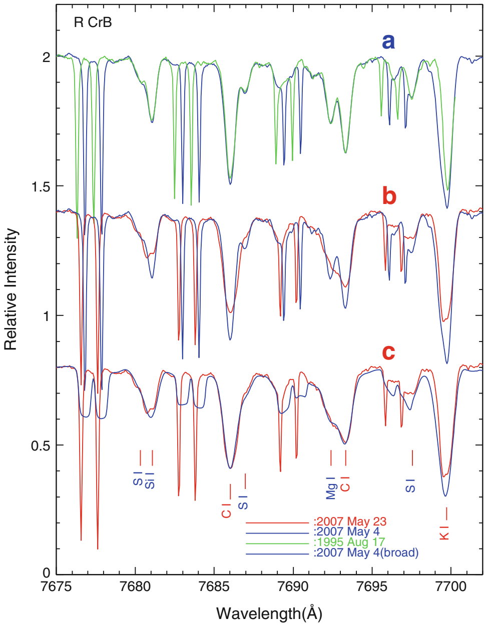

Fig. 4. Figure illustrates the broadening of stellar spectrum prior to the onset of the light minimum. (a) The spectrum on 2007 May 4 (blue) is similar to a typical maximum one (green - 1995 August 17). (b) shows the spectral lines on 2007 May 23 (red) are broader than in the spectrum obtained 19 days earlier (blue). In (c) the 2007 May 4 spectrum is artificially brodened without changing the equivalent widths to match the 2007 May 23 spectrum. Only the line shapes got altered.

3.1 2007 July 7-10 –At the edge of the descent

Absorption lines of C_2 Phillips system

The $^{12}C_2$ Swan bands are fairly strong in the spectrum of R CrB. Bandheads of the 0-0 band at 5165 Å, the 1-0 band at 4737 Å, and the 0-1 band at 6174 Å are readily identified. More interestingly, the spectrum of 2007 July 7 shows weak bands of the Phillips system of C_2 in absorption – see Fig. 7 for examples of lines from the 2-0 band. These C_2 lines not present in the regular stellar spectrum are shifted in velocity from the stellar lines and present with a red and a blue component. Our spectra show that the Phillips lines were not present on 2007 June 6 spectrum, a month before the onset of the decline.

Rotational temperatures of 1048±30 K and 784±30 K were obtained (Fig. 14) for the blue component at -14.5 km s^{-1} and the red component at $+5$ km s^{-1}, respectively, using the molecular data given by Bakker *et al.* (1997). The corresponding molecular column densities are 7.7×10^{14} cm^{-2} and 4.5×10^{14} cm^{-2}. The radial velocities of C_2 molecules of -14.5 km s^{-1} and $+5$ km s^{-1} suggest cool gas rising relative to the star with stellar lines giving

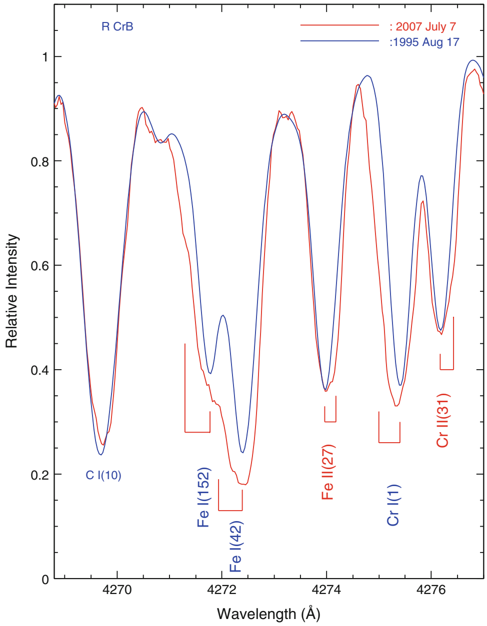

Fig. 5. Comparison of the spectral lines of C I, Fe I, Fe II, Cr I, and Cr II in the disturbed spectrum on 2007 July 7(red), prior to the descent in light, with a normal undisturbed spectrum on 1995 August 17 (blue). Note various additional absorption components to both ionized and neutral lines in 2007 July 7.

the radial velocity of 21 km s^{-1}. The cooler gas is less rapidly rising than the warmer molecular gas.

These rotational temperatures show that there was gas at the condensation temperatures conducive to formation of carbon soot. Similar detections of cool C_2 molecules have been reported by us for V854 Cen (Rao & Lambert 2000), R CrB (Rao, Lambert & Shetrone 2006) , and V CrA (Rao & Lambert 2008). But these detections were during minimum light. In contrast, the present detection of cool C_2 molecules at maximum light but on the verge of a minimum is significant and leads to the conclusion that the light minima are indeed caused by formation of dust grains. Woitke et al's (1996) model seems to be consistent with observations! Intense spectroscopic coverage of the days leading up to a descent to a minimum is an important unfulfilled challenge made more by difficult by the unpredictable onset of the descent.

4 The stellar wind

A mark that distinguishes RCBs from HdCs is the absence from the latter's defining characteristics, the declines – deep or even shallow – that are such a strong feature of the RCBs. Absence of declines accounts for the lack of an

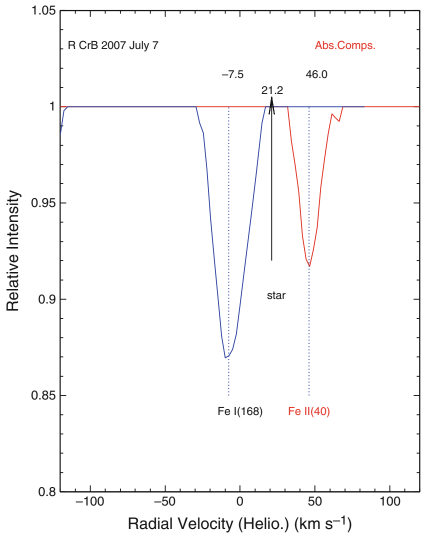

Fig. 6. Typical velocities of the extra absorption components to neutral (Fe I-blue-shifted) and ionized (Fe II- red-shifted) lines on 2007 July 7. The arrow denotes the radial velocity of the star measured from high excitation lines without components on 2007 July 7. Note the infalling and expanding layers have a velocity difference over 50 km s^{-1} that represents the atmospheric shock velocity.

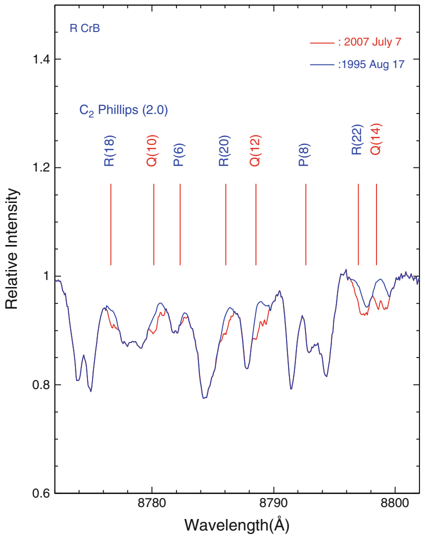

Fig. 7. The spectrum of R CrB on 2007 July 7 (red) in the region 8780 Å superposed on the reference spectrum obtained on 1995 August 17 (blue). Absorption lines of the $^{12}C_2$ Phillips 2-0 band are seen as extra absorptions in the 2007 July 7 spectrum but are absent from the 1995 August 17 spectrum. Line doubling in the C_2 lines can also be seen.

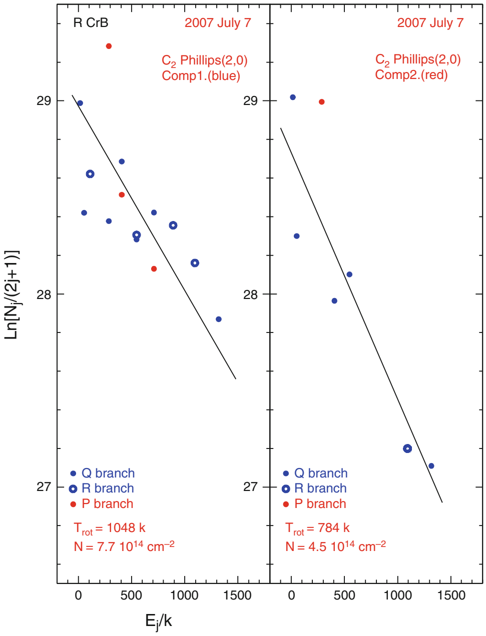

Fig. 8. Boltzmann plots of the red and blue absorption components of C_2 2-0 lines of the Phillips system from the spectrum of R CrB obtained on 2007 July 7. Blue filled circle, open circle and red filled circle symbols refer to Q, R and P branch lines, respectively.

infrared excess from the HdCs. Another distinguishing mark between RCBs and HdCs is the presence of a stellar wind from RCBs but not from HdCs. Are these two marks different sides of one difference between the two groups of H-deficient stars? Clayton, Geballe & Bianchi (2003) reported the presence of a P-Cygni profile for the He I 10830 Å line at maximum light for several RCBs. These observations show that the RCBs possess a stellar wind with an outflow velocity of 200 to 300 km s^{-1}. Then, Rao, Lambert & Shetrone (2006) showed that in R CrB the strong photospheric lines, particularly the O I 7771 Å line, had a pronounced blue wing suggesting a component with an expansion velocity of 120 km s^{-1}. Examination of profiles of other lines showed a component associated with the stellar wind with the velocity proportional to the excitation energy of the lines, i.e., the range of lines sample the region in the upper atmosphere where the wind is accelerating to the (possibly terminal) velocity measured from the He I 10830 Å line. Our high-resolution spectra now show that a stellar wind may be common, perhaps ubiquitous, among RCBs.

The temporal dependence of the RCB stellar wind is not yet fully known. There is no indication that it depends greatly or at all on the phase of the pulsation cycle. Long-term behaviour is also not known. Observations at the 1995–1996 minimum of R CrB suggest that the wind-affected wings of the O I lines are undisturbed even though the core is affected by transient emission in the early decline (Rao et al. 1999). What drives this wind? Is there any connection with magnetic fields? In the R CrB wind, low excitation lines (e.g., the Al I resonance lines) show variability on a short time scale but there is no change in the high excitation lines. Examination of magnetically-sensitive and magnetically-insensitive Fe I lines of comparable strength and excitation potential from a series of high-resolution spectra of R CrB taken at maximum light suggests the variability in the former, but not in the latter (Rao 2008). This result suggests a connection between surface magnetic field and the wind. The relation between the (apparently) permanent and (seemingly) pulsation phase-independent wind and trigger for a decline is as yet unknown.

In contrast, Geballe, Rao, and Clayton (2009) examined the five known HdCs at the He I 10830 Å line on high-resolution spectra and found no evidence of a stellar wind. The absence of a wind and the lack of deep declines among the HdCs and the presence of a wind among the RCBs with their deep declines is suggestive that the wind or the presence of an extended atmosphere as a result of the wind is a necessary condition for occurrence of deep declines.

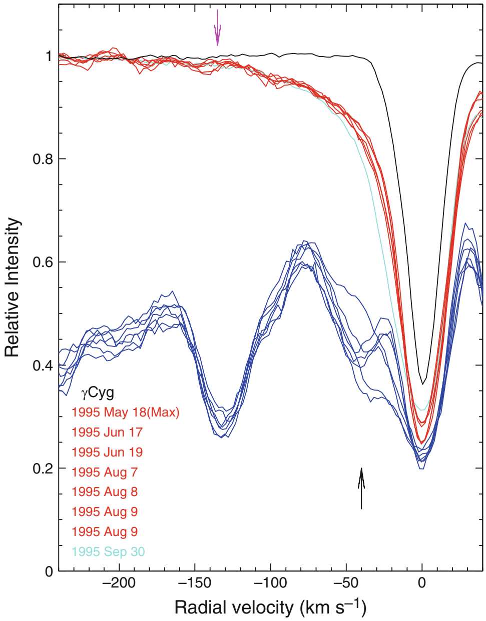

Fig. 9. Profiles of O I 7771 Å (red) and Al I 3944 Å (blue) in R CrB obtained at different times and adjusted to the stellar velocity. Note the variability in the low excitation Al I profiles and the unchanged high excitation O I line profile. The wind velocity suggested by these lines is 50 km s^{-1} for Al and 120 km s^{-1} for O. O I profile of a normal supergiant gamma Cyg (black) is shown for comparison.

5 Concluding remarks

Answers are slowly emerging for the important questions posed by RCB and HdC stars concerning the origin of these H-deficient stars, and the mechanisms by which a cloud of soot forms and obscures the star. Evidence suggests that the DD rather than the FF scenario provides a superior accounting for the elemental abundances of C, N and O for RCB stars and their likely relatives, the extreme Helium (EHe) stars and cool hydrogen deficient (HdC) stars. The FF scenario does plausibly account for other stars. Most notable among the FF candidates are FG Sge and V4334 Sgr, also known as Sakurai's object and V605 Aql (Clayton *et al.* 2006). It is not impossible that RCBs from the FF scenario lurk among the analysed sample attributed in the main to the DD scenario.

The process of soot formation is most likely associated with the atmospheric pulsation which, on occasions at a certain phase of the pulsation, leads to a stronger than usual shock in the atmosphere such that the physical conditions are conducive to molecule formation and dust nucleation, as envisaged by Woitke et al.(1996). How the dust grains grow and soot clouds form represent questions for future study.

As our essay has hopefully shown, high-resolution optical and infrared spectra have and will prove crucial to addressing the leading questions about the H-deficient RCB and HdC stars. In preparing the paper, we came across a collection of articles on modern high-resolution spectroscopic techniques. There, the leading chapter by Sir Harry Kroto carried the title 'Old spectroscopists forget a lot but they do remember their lines' (Kroto 2009). This pair of old spectroscopists remember at least the important lines.

Acknowledgement. We acknowledge with thanks the variable star observations from the AAVSO database. This research has made use of the SIMBAD database, operated at CDS, Strasbourg, France. Our sincere thanks to the editors of this volume for accepting with admirable patience our delay in submitting this article. This research has been supported in part by a grant (F-634) to DLL from the Robert A. Welch Foundation of Houston, Texas.

References

Alcock,C., et al . 2001, Ap.J, 554, 298

Asplund, M., Gustafsson, B., Lambert, D. L., Rao, N. K., 2000, A&A, 353, 287

Bakker, E.J., van Dishoeck, E.F., Waters, L.B.F., Schoenmaker, T., 1997, A&A, 323, 469

Clayton, G.C., Geballe, T.R., Bianchi, L. 2003, ApJ, 595, 412

Clayton, G.C., Kerber, F., Pirzkal, N., De Marco, O., Crowther, P.A., Fedrow, J.M. 2006, ApJ, 646, L69

Clayton, G.C., Geballe, T.R., Herwig, F., Fryer, C., Asplund, M. 2007, ApJ, 662, 1220

Clayton, G.C., Herwig, F., Geballe, T.R., Asplund, M., Tenenbaum, E.D., Engelbracht, C.W., Gordon, K.D., 2005, ApJ, 623, L141, ApJ, 662, 1220
Clayton, G.C., Kilkenny, D.,Wils, P., Welch, D.L., 2009, astro-ph 0904.0631
Crause, L.A., Lawson, W.A., Henden, A.A. 2007, MNRAS,375, 301
de Laverny, P., Mekarnia, D. 2004, A&A,428, L13
Disney, M.J. 2000, astro-ph 0009020, General Relativity and Gravitation, 32, 1125
García-Hernández D.A., Hinkle, K.H., Lambert,D.L., Eriksson, K. 2009, ApJ, 696, 1733
Geballe, T.R., Rao, N.K., Clayton, G.C., 2009, Ap.J., 698, 735
Geballe, T.R., 2008, (personal communication)
Herwig, F. 2001, Ap& SS, 275, 15
Iben, I.Jr., Tutukov, A. 1984, Ap.JS, 54, 355
Iben, I.Jr., Kaler, J.B., Truran,J.W., Renzini,A. 1983, Ap.J, 264, 605
Johansson, L.1965, Arkiv f. Fysik, 31, 201
Keenan, P.C., Greenstein, J.L., 1963, Perkins Obs. Contr. Ser. II, no. 13
Kroto, H. 2009, in ed Jaan Laane., Frontiers of Molecular Spectroscopy, Elsevier(publisher), 1
Loreta, E. 1934, A.N, 254, 151
Merrill, P. W., 1952, ApJ, 116, 21
Merrill, P. W., 1963, in ‘Space Chemistry’, Univ. of Michigan press, Ann Arbor
O’Keefe, J.A. 1939, Ap.J, 90, 294
Pandey, G., 2006, Ap.J, 648, L143
Pandey, G., Lambert, D.L., Rao, N.K. 2008, Ap.J, 674,1068
Pandey, G., Lambert, D.L., Jeffery, C.S., Rao, N.K. 2006, ApJ, 638, 454
Pugach, A.F., 1977, IBVS, 1277
Rao N.K. 2008, in Werner,K., Rauch,T., eds., Hydrogen Deficient Stars, ASPC,391, 25
Rao N.K., Lambert D.L., 2000, MNRAS, 313, L3
Rao N.K., Lambert D.L., 2008, MNRAS, 384, 477
Rao N.K., Lambert D.L., Adams, M.T., Doss, D.R., Gonzalez, G., Hatzes, A.P., James, R., Johns-Krull, C.M., Luck, R.E., Pandey, G., Reinsch, K., Tomkin, J., Woolf, V.M. 1999, MNRAS, 310, 717
Rao, N.K., Lambert, D.L., Shetrone, M.D. 2006, MNRAS, 370, 941
Renzini, A. 1990, in Cacciari,C., Clementini,G., eds., Confrontation Between Stellar Pulsation and Evolution, ASPC, 11, 549
Saio, H., Jeffery, C.S. 2002, MNRAS, 333, 1210
Schönberner, D., 1979, A&A, 103, 119
Tisserand, P. et al., 2008, A&A, 673
Warner, B., 1967, MNRAS, 137, 119
Webbink, R.F. 1984, Ap.J, 277, 355
Woitke, P., Goeres, A., Sedlmayr, E., 1996, A&A, 313, 217

“Recent Advances in Spectroscopy:
Theoretical, Astrophysical, and Experimental Perspectives”
Eds. Chaudhuri R K, Mekkaden M V, Raveendran A V, Satya Narayanan A
Astrophysics and Space Science Proceedings, Springer-Verlag, Berlin, 2010.

Simultaneous X-ray and Optical Observations of the T Tauri star TW Hya

Sushma V. Mallik[1], N.S. Brickhouse[2], and A.K. Dupree[2]

[1] Indian Institute of Astrophysics, Bangalore 560034, India. `sgvmlk@iiap.res.in`
[2] Harvard-Smithsonian Center for Astrophysics, Cambridge, MA 02138 USA `dupree@cfa.harvard.edu`

Summary. We report preliminary results obtained from a spectroscopy and photometry campaign of the T Tauri star TW Hya in February- March, 2007. A long HETG observation with CHANDRA and simultaneous optical observations around the world have been carried out to investigate the relationship between the X-ray emission and optical variability and to connect these to the accretion and wind characteristics of the star.

1 Introduction

TW Hya is unique in many ways. It is ∼10 Myr old, one of the oldest T Tauri stars still accreting material from its circumstellar disk onto the star via accretion streams that are believed to be magnetically funnelled. It is nearby at a distance ∼ 50pc and isolated from the sites of star formation, and therefore has minimal obscuration effects. The $H\alpha$ emission line is unusually broad with FWHM often as large as 200-400 km^{-1} and has a distinct weakening of the short wavelength side of the profile (a ‘blue asymmetry’) implying the presence of a stellar wind/mass outflow. TW Hya is also one of the brightest T Tauri stars in X-rays. An HST image has confirmed that it is oriented pole-on (Krist *et al.* 2000), with the circumstellar (CS) disk almost face-on in the sky having a small inclination angle of ∼ 6° (Qi *et al.* 2006), and as a result reddening effects are negligible. The accretion and wind characteristics of the star therefore can be studied without confusion from its CS disk. Because of these attributes, the star continues to intrigue astronomers as it offers a unique opportunity to study the important process of stellar accretion.

TW Hya shows a rich but confusing pattern of photometric variability. The rotation period has been reported at different epochs in the past to range from 1.28 (Herbst & Koret 2004) to 2.8 days (Lawson & Crause 2005) and even periods determined from recent observations. A detailed analysis based on observations over several years by Mekkaden (1998) yielded a period of 2.196 days for the light variation. With spot modelling, this variation was ascribed to a hot spot with T = 8450K, almost situated at the pole and covering a small fractional surface area. In addition to this periodic light variation, sudden brightenings lasting for a day or two were also noticed which could be due to short-lived hot spots produced by a varying accretion rate. These seem to be a regular feature of TW Hya. Since the brightenings could occur at any photometric phase, they could completely mask the periodic variation and thus hide the true period of the star.

The other controversy relates to the relative roles that accretion and coronal emission play in contributing to the source of its X-ray emission. It is possible that X-ray emission from accretion on to T Tauri stars may be diminished because the hot shock from the accreting material might form too deep in the photosphere for the X-rays to escape. Also, accretion-dominated X-ray production challenges the long-standing view that X-rays from T Tauri stars originate in coronal magnetic loops which is supported by many CHANDRA observations of star forming regions (Gagné *et al.* 2004; Preibisch *et al.* 2005). However, Kastner *et al.* (2002) argue for an accretion origin of X-rays based on the O VII and Ne IX forbidden (f) to intercombination (i) line ratios from the X-ray spectrum of TW Hya obtained from a single 48s HETG/CHANDRA observation. These yield densities $N_e \sim 10^{13} cm^{-3}$, much higher than found in coronal sources where they lie between $2 \times 10^{10} - 10^{12} cm^{-3}$.

2 World wide campaign of observations

In order to resolve this controversy, CHANDRA devoted a major Guest Observer program (N.S. Brickhouse, PI) to a long (500 ks) HETG observation of TW Hya to obtain a high quality spectrum during 15 February - 3 March, 2007 with short gaps in between (15-17 Feb : 160ks; 26 Feb-3 Mar : 160+160+20ks). Simultaneous optical observations were carried out at several observatories around the world to provide almost continuous coverage to relate the accretion properties and variability of TW Hya to its X-ray emission. These are listed below :

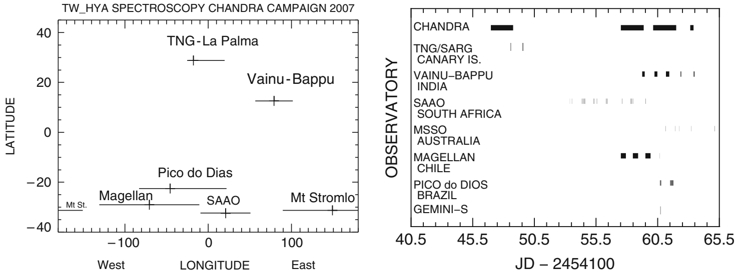

Fig. 1. The world wide campaign. *Left panel:* Location of the observatories in longitude. *Right panel:* Observations acquired during the campaign.

1. MIKE echelle spectra from the 6.5m Magellan/Clay telescope, Chile (A.K. Dupree)
2. Echelle spectra from the 2.3m telescope at Mt. Stromlo, Australia (M.S. Bessell & W.A. Lawson)
3. SARG echelle spectra from the TNG at La Palma (DDT time & R. Pallavicini)
4. Coude spectra from the 1.6m telescope at Pico do Dias, Brazil (J. Luna)
5. Echelle spectra from the 2.3m telescope at VBO, India (S.V. Mallik)
6. Photometry & spectroscopy at SAAO, South Africa (W.A. Lawson & L.A. Crause)
7. IR spectra with Phoenix on Gemini-S (S. Schuster)

It is evident from Fig. 1 (*left panel*) that the Vainu Bappu Observatory (VBO) at Kavalur, India fits in the gap, being at just the right longitude to complete the coverage. At RA = $11^h01^m52^s$, TW Hya is observable practically all night during Feb./Mar. Several spectra were obtained each night from Feb.27 to Mar.3 with the echelle spectrograph on the 2.3m telescope at VBO at a resolution of 28000. Fig. 1 (*right panel*) shows that the coverage by various observatories around the world occurs in conjunction with the CHANDRA measurements.

3 X-ray emission observations

Fig. 2 (*top panel*) displays the X-ray light curve measured with CHANDRA. Excluding the flare that occurred over 20ks of the 500ks observation, the total X-ray flux from TW Hya varied by a factor of 2; it did not show any periodic variations during the CHANDRA sequence that spanned 16.5 days. This is in contrast to the periodic variability observed in the optical spectra obtained at the same time. Line-based light curves from the low temperature (2.4 MK) gas associated with the shock show less variability than light curves from the hot (10 MK) coronal gas. The flare appears to be coronal in nature. It may be difficult to separate the variability of the accretion emission from that of the corona in order to compare with optical photometry.

4 The behaviour of $H\alpha$ line profiles

The optical observations were strikingly different. Here we will highlight the $H\alpha$ spectra from VBO and Magellan. A detailed report of all optical observations is given elsewhere (Dupree *et al.* 2007). Fig. 3a shows the spectra from VBO superposed over one another for the nights Feb27-Mar3. For each night, it is averaged over all the profiles for that night except for Mar.2. Profiles of the first 2 nights (27, 28 Feb. 2007) are highly anomalous and the variation in the profile shape and strength in subsequent nights is remarkable. There is unusual enhanced emission on the negative velocity (‘blue’ side) of the profile

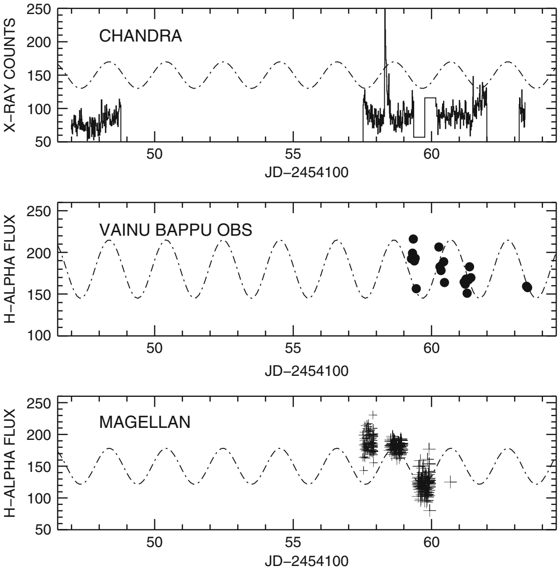

Fig. 2. Total X-ray CHANDRA counts binned in 1000s intervals vs. time (*top panel*); $H\alpha$ fluxes from the Vainu Bappu Observatory measures (*centre panel*), and the MIKE echelle spectrograph on the Magellan/Clay telescope at Las Campanas, Chile (*lower panel*). A sine curve (period 2.06d) is overlaid on each data set.

allowing the broad accretion profile to assume a natural symmetric shape; later the blue emission became weaker and the asymmetry was re-established on subsequent nights, the profile then assuming its typical shape. The Magellan/MIKE spectra with much better S/N ratio obtained by Dupree et al. (2009) during Feb.26-Mar 1 showed a similar pattern in line profile shapes. A 20ks X-ray flare occurred between night 1 and 2 of the MIKE observations as seen in Fig. 2. The spectrum of night 1 already looked anomalous and therefore may not be related to the occurrence of the flare. Flares occur quite frequently in stars like TW Hya but the $H\alpha$ profiles observed in 2007 are very different from the numerous profiles of TW Hya in the literature. For comparison, those observed in 2004 by Dupree *et al.* (2007) are reproduced here in Fig. 3b. These revealed periodic systematic variations in the flux, velocity and the shape of the profile. Absorption features occurred at high outflow velocities between -100 km s^{-1} and -300 km s^{-1}. They were stable in velocity and recurred similarly in 2006. The fact that there are variations suggests accretion is not uniformly distributed over the stellar hemisphere in view and is consistent with the photometric variations found by Lawson & Crause (2005) and Mekkaden (1998). But the repetition of absorption notches at the same velocities implies stable atmospheric structures, possibly controlled by the stellar magnetic field configuration that channels the accreting material from the disk to the star.

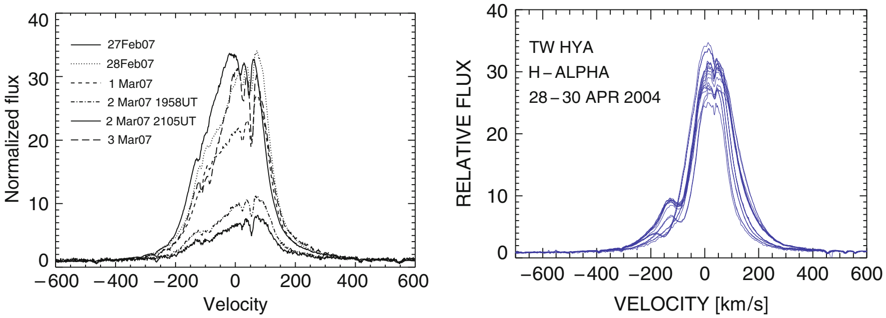

Fig. 3. a) 2007 spectra of $H\alpha$ from VBO. b) 2004 $H\alpha$ spectra at Magellan.

However, the $H\alpha$ profiles of 2007 are not like any seen in the past, to our knowledge. The largest difference appears as an enhancement of emission on the short wavelength side. This anomalous phenomenon is unlikely to arise from enhanced accretion because the long wavelength side of the profile should show a similar large enhancement. We note that the observed X-ray emission does not change during this period. It may be that this apparent excess blue emission reflects a changing wind opacity. Although optical profiles from T Tauri stars are usually modelled as arising from accretion (Muzerolle *et al.* 2000), our observations imply that wind opacity has a substantial role in modifying the profiles. The stellar wind appears to be suppressed. The observed profile changes may result from a changing viewing orientation of the accreting column and/or wind as the star rotates, causing more or less opacity or from a fundamental change in the magnetic field configuration or both. It is clear that TW Hya is in an active phase of accretion and/or wind and that the accretion/wind pattern did indeed change between 2004 and 2007. Much more is to be extracted from the spectra observed and the analysis is in progress. A summary of the optical observations will be given elsewhere (Dupree et al. 2009). Work is also in progress to derive temperatures and densities from a variety of diagnostics contained in the CHANDRA data (Brickhouse *et al.* 2009).

5 Mystery of the rotation period

Fig. 2 shows a sine curve placed through the X-ray light curve and the $H\alpha$ fluxes obtained at the VBO and Magellan. The period of 2.057d was derived from the SAAO $H\alpha$ coverage over the 7 day interval during the gap in CHANDRA measures. This is close to what Mekkaden (1998) obtained but differs from other periods that have been measured. Does the period change? Or does it appear to change? The picture of TW Hya variability is a complex one, particularly in view of recent radial velocity variation measurements of TW Hya by Setiawan *et al.* (2008) revealing a clear spectroscopic sinusoidal signal with a period of 3.56d which they interpreted as an indication of a 10 M_{Jup} planet orbiting around it. However, this claim has not held up. Huelamo *et al.* (2008) question the possibility and propose that Setiawan et al.'s observations could be reproduced by photospheric spot-induced spectral line shifts. Their own spectroscopic and photometric data are suggestive of the presence of short-lived hot spots that appear and disappear, hiding the true period of the star. Through sheer coincidence, the MOST satellite observed TW Hya (Rucinski *et al.* 2008) exactly during the time when RV observations of Setiawan et al. were collected. The MOST run lasted 11 days and indeed led to a detection of a well-defined photometric period of 3.7d. Because of the significance of this result and because the 2007 run was too short, it observed TW Hya in 2008 again for 47 days continuously. The picture of the 2008 run was very different. The strong 3.7d periodicity was entirely absent. According to Rucinski et al. (2008), it does not seem related to a possible planet because it disappeared within one year. Instead, a number of periodic components appear to be present at 7.7, 5.1, 3.3, 2.5, 1.7, 1.25d. This so called flicker noise variability spectrum may be a manifestation of hot spots, short-lived structures anchored in different parts of the accretion disk and thus masking the true rotation period. So the big question of the rotation period of TW Hya remains!

References

Brickhouse, N.S. et al., 2009, in preparation
Dupree, A.K., et al., 2009, in preparation
Dupree, A.K., et al., 2007, Cool Stars 14, ASP Conf Series 384, CD-ROM (astro-ph 0702395)
Gagné, M., et al., 2004, ApJ, 613, 393
Herbst,W., & Koret, D.L., 1988, AJ, 96, 1949
Huelamo, N., et al., 2008, A&A, 489, L9
Kastner, J.H., et al., 2002, ApJ, 567, 434
Krist, J.E., et al., 2000, ApJ, 538, 793
Lawson, W.A., & Crause, L.A., 2005, MNRAS, 357, 1399
Mekkaden, M.V., 1998, A&A, 340, 135
Muzerolle, J., et al., 2000, ApJ, 535, L47
Preibisch, T., et al., 2005, ApJS, 160, 401
Qi, C., et al., 2006, ApJ, 636, L157
Rucinski, S.M., et al., 2008, MNRAS, 391, 1913
Setiawan, J., et al., 2008, Nature, 451, 38

"Recent Advances in Spectroscopy:
Theoretical, Astrophysical, and Experimental Perspectives"
Eds. Chaudhuri R K, Mekkaden M V, Raveendran A V, Satya Narayanan A
Astrophysics and Space Science Proceedings, Springer-Verlag, Berlin, 2010.

Element Abundance Determination in Hot Evolved Stars

Klaus Werner

Institute for Astronomy and Astrophysics, Kepler Center for Astro and Particle Physics, University of Tübingen, Sand 1, 72076 Tübingen, Germany.
`werner@astro.uni-tuebingen.de`

Summary. The hydrogen-deficiency in extremely hot post-AGB stars of spectral class PG1159 is probably caused by a (very) late helium-shell flash or a AGB final thermal pulse that consumes the hydrogen envelope, exposing the usually-hidden intershell region. Thus, the photospheric element abundances of these stars allow us to draw conclusions about details of nuclear burning and mixing processes in the precursor AGB stars. We compare predicted element abundances to those determined by quantitative spectral analyses performed with advanced non-LTE model atmospheres. A good qualitative and quantitative agreement is found for many species (He, C, N, O, Ne, F, Si, Ar) but discrepancies for others (P, S, Fe) point at shortcomings in stellar evolution models for AGB stars. Almost all of the chemical trace elements in these hot stars can only be identified in the UV spectral range. The *Far Ultraviolet Spectroscopic Explorer* and the *Hubble Space Telescope* played a crucial role for this research.

1 Introduction

The chemical evolution of the Universe is driven by the nucleosynthesis of elements in stars. Evolved stars return a significant fraction of their mass to the interstellar medium. This matter is enriched with heavy elements which were produced in the stellar interior and dredged-up to the surface by convective motions. For quantitative modeling of galactic chemical evolution it is crucial to know the stellar yields of chemical elements, i.e., how much metals are produced by which stars. Yields are computed from stellar evolution models, however, several uncertainties in modeling can strongly affect the yields. Among the most serious problems are mixing processes (convection) and some particular nuclear reaction rates. One solution to these problems is a comparison of predicted surface abundances with observations. Quantitative spectroscopy is therefore a powerful tool to calibrate free modeling parameters, e.g., those associated with convective overshoot.

This paper is restricted to evolved low-mass stars, or to be more precise, to hot post-AGB stars. About 95% of all stars in our Galaxy end their life as a white dwarf. These low- and intermediate-mass stars ($\approx$1–8 $\mathrm{M}_\odot$) roughly produce 50% of the metal yields, mainly during the phase of AGB evolution in combination with strong radiatively-driven mass loss. We demonstrate here that quantitative abundance analyses of particular elements in post-AGB stars provide valuable insight into AGB-star nucleosynthesis processes.

We further confine our paper to very hot *hydrogen-deficient* post-AGB stars. The reason is that these particular objects offer the unique possibility to directly access the nucleosynthesis products. Why do we concentrate on hot stars, i.e., those having $T_{\rm eff}\approx$100 000 K? This is because the spectra of cooler objects are wind-contaminated. These are the Wolf-Rayet type central stars of planetary nebulae and their atmospheres are much more difficult to model. In addition, very weak spectral features from rare elements can be smeared out by atmospheric motion and become undetectable. We also exclude from our studies hot white dwarfs and subdwarf O/B stars, because their nucleosynthesis history was wiped out by diffusion effects in their atmospheres.

2 Quantitative spectral analysis of PG1159 stars

We report on our work on PG1159 stars, a group of 40 extremely hot hydrogen-deficient post-AGB stars (Werner & Herwig 2006). Their effective temperatures ($T_{\rm eff}$) range between 75 000–200 000 K. Many of them are still heating up along the constant-luminosity part of their post-AGB evolutionary path in the HRD ($L \approx 10^4\,\mathrm{L}_\odot$) but most of them are already fading along the hot end of the white dwarf cooling sequence (with $L \gtrsim 10\ \mathrm{L}_\odot$). Luminosities and masses are inferred from spectroscopically determined $T_{\rm eff}$ and surface gravity ($\log g$) by comparison with theoretical evolutionary tracks. The position of analysed PG1159 stars in the "observational HR diagram", i.e. the $T_{\rm eff}$–$\log g$ diagram, are displayed in Fig. 1. The high-luminosity stars have low $\log g$ (≈ 5.5) while the low-luminosity stars have a high surface gravity (≈ 7.5) that is typical for white dwarf (WD) stars. The derived masses of PG1159 stars have a mean of 0.62 $\mathrm{M}_\odot$, a value that is practically identical to the mean mass of WDs. The PG1159 stars co-exist with hot central stars of planetary nebulae and the hottest hydrogen-rich (DA) white dwarfs in the same region of the HR diagram. About every other PG1159 star is surrounded by an old, extended planetary nebula.

What is the characteristic feature that discerns PG1159 stars from "usual" hot central stars and hot WDs? Spectroscopically, it is the lack of hydrogen Balmer lines, pointing at a H-deficient surface chemistry. The proof of H-deficiency, however, is not easy: The stars are very hot, H is strongly ionized and the lack of Balmer lines could simply be an ionisation effect. In addition, every Balmer line is blended by a Pickering line of ionized helium. Hence, only detailed modeling of the spectra can give reliable results on the photospheric composition. The high effective temperatures require non-LTE modeling of the atmospheres. Such models for H-deficient compositions have only become

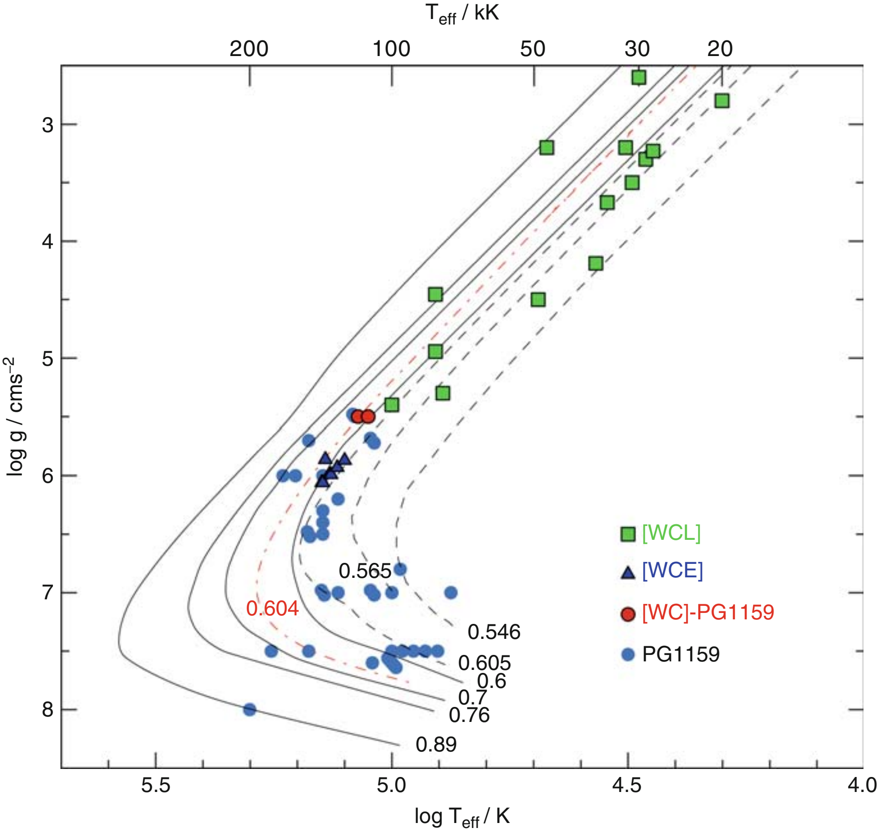

Fig. 1. Hot hydrogen-deficient post-AGB stars in the g–T_{eff}–plane. We identify Wolf-Rayet central stars of early and late type ([WCE], [WCL], from Hamann (1997)), PG1159 stars (from Werner & Herwig (2006)) as well as two [WC]–PG1159 transition objects (Abell 30 and 78). Evolutionary tracks are from Schönberner (1983) and Blöcker (1995) (dashed lines), Wood & Faulkner (1986) and Herwig (2003) (dot-dashed line) (labels: mass in $M_\odot$). The latter $0.604\,M_\odot$ track is the final CSPN track following a VLTP evolution and therefore has a H-deficient composition.

available in the early 1990s after new numerical techniques have been developed and computers became capable enough.

The first quantitative spectral analyses of optical spectra from PG1159 stars indeed confirmed their H-deficient nature (Werner *et al.* 1991). It could be shown that the main atmospheric constituents are C, He, and O. The typical abundance pattern is C=0.50, He=0.35, O=0.15 (mass fractions). It was speculated that these stars exhibit intershell matter on their surface, however, the C and O abundances were much higher than predicted from stellar evolution models. It was further speculated that the H-deficiency is caused by a late He-shell flash, suffered by the star during post-AGB evolution,

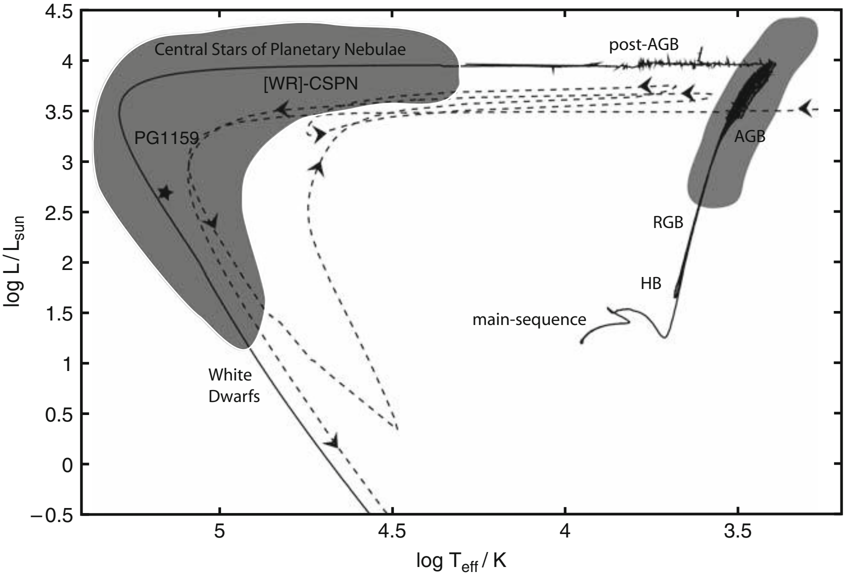

Fig. 2. Complete stellar evolution track with an initial mass of $2\,M_\odot$ from the main sequence through the RGB phase, the HB to the AGB phase, and finally through the post-AGB phase that includes the central stars of planetary nebulae to the final WD stage. The solid line represents the evolution of a H-normal post-AGB star. The dashed line shows a born-again evolution of the same mass, triggered by a very late thermal pulse, however, shifted by approximately $\Delta \log T_{\rm eff} = -0.2$ and $\Delta \log L/\,L_\odot = -0.5$ for clarity. The "$\star$" shows the position of PG1159-035 (Werner & Herwig 2006).

laying bare the intershell layers. The re-ignition of He-shell burning brings the star back onto the AGB, giving rise to the designation "born-again" AGB star (Iben *et al.* 1983). If this scenario is true, then the intershell abundances in the models have to be brought into agreement with observations. By introducing a more effective overshoot prescription for the He-shell flash convection during thermal pulses on the AGB, dredge-up of carbon and oxygen into the intershell can achieve this agreement (Herwig *et al.* 1999). Another strong support for the born-again scenario was the detection of neon lines in optical spectra of some PG1159 stars (Werner 1994). The abundance analysis revealed Ne=0.02, which is in good agreement with the Ne intershell abundance in the improved stellar models.

If we accept the hypothesis that PG1159 stars display former intershell matter on their surface, then we can in turn use these stars as a tool to investigate intershell abundances of other elements. Therefore, these stars offer the unique possibility to directly see the outcome of nuclear reactions and mixing processes in the intershell of AGB stars. Usually the intershell is kept hidden below a thick H-rich stellar mantle and the only chance to obtain information about intershell processes is the occurrence of the 3rd dredge-up. This indirect view of intershell abundances makes the interpretation of the nuclear and mixing processes difficult, because the abundances of the dredged-up elements may have been changed by additional burning and mixing processes in the H-envelope (e.g., hot-bottom burning). In addition, stars with an initial mass below 1.5 $M_\odot$ do not experience a 3rd dredge-up at all.

We note that the central stars of planetary nebulae of spectral type [WC] are believed to be immediate progenitors of PG1159 stars, representing the evolutionary phase between the early post-AGB and PG1159 stages. This is based on spectral analyses of [WC] stars which yield very similar abundance results (Hamann 1997). We do not discuss the [WC] stars here because the analyses of trace elements are much more difficult or even impossible due to strong line broadening in their rapidly expanding atmospheres.

3 Three different late He-shell flash scenarios

The course of events after the final He-shell flash is qualitatively different depending on the moment when the flash starts. We speak about a very late thermal pulse (VLTP) when it occurs in a WD, i.e. the star has turned around the "knee" in the HR diagram and H-shell burning has already stopped (Fig. 2). The star expands and develops a H-envelope convection zone that eventually reaches deep enough that H-burning sets in (a so-called hydrogen-ingestion flash). Hence H is destroyed and whatever H abundance remains, it will probably be shed from the star during the "born-again" AGB phase. A late thermal pulse (LTP) denotes the occurrence of the final flash in a post-AGB star that is still burning hydrogen, i.e., it is on the horizontal part of the post-AGB track, before the "knee". In contrast to the VLTP case, the bottom of the developing H-envelope convection zone does not reach deep enough layers to burn H. The H-envelope (having a mass of about 10^{-4} $M_\odot$) is mixed with a few times 10^{-3} $M_\odot$ intershell material, leading to a dilution of H down to about H=0.02, which is below the spectroscopic detection limit. If the final flash occurs immediately before the star departs from the AGB, then we talk about an AFTP (AGB final thermal pulse). In contrast to an ordinary AGB thermal pulse the H-envelope mass is particularly small. Like in the LTP case, H is just diluted with intershell material and not burned. The remaining H abundance is relatively high, well above the detection limit ($H \gtrsim 0.1$).

There are three objects, from which we believe to have witnessed a (very) late thermal pulse during the last ≈100 years. FG Sge suffered a late flash in 1894 (Gonzalez *et al.* 1998). The star became rich in C and rare earth elements. It most probably was hit by an LTP, not a VLTP, because it turned H-deficient only recently (if at all, this is still under debate). As of today, FG Sge is located on or close to the AGB.

V605 Aql experienced a VLTP in 1917 (Clayton & Marco 1997). Since then, it has quickly evolved back towards the AGB, began to reheat and is now in its second post-AGB phase. It has now an effective temperature of the order 100 000 K and is H-deficient.

Sakurai's object (V4334 Sgr) also experienced a VLTP, starting around 1993 (Duerbeck & Benetti 1996). It quickly evolved back to the AGB and became H-deficient. Recent observations indicate that the reheating of the star already began, i.e., its second departure from the AGB might just have begun.

The spectroscopic study of FG Sge and Sakurai's object is particularly interesting, because we can observe how the surface abundances change with time. The stars are still cool, so that isotopic ratios can be studied from molecule lines (Pavlenko *et al.* 2004) and abundances of many metals can be determined. The situation is less favorable with the hot PG1159 stars: All elements are highly ionised and for many of them no atomic data are available for quantitative analyses. On the other hand, in the cool born-again stars the He-intershell material is once again partially concealed.

4 Comparison of observed and predicted abundances

Abundance analyses of PG1159 stars are performed by detailed fits to spectral line profiles. Because of the high $T_{\rm eff}$ all species are highly ionized and, hence, most metals are only accessible by UV spectroscopy. Optical spectra always exhibit lines from He II and C IV. Only the hottest PG1159 stars display additional lines of N, O, and Ne (N V, O VI, Ne VII). For all other species we have utilized high-resolution UV spectra that were taken with the *Hubble Space Telescope* (HST) and the *Far Ultraviolet Spectroscopic Explorer* (FUSE). FUSE allowed observations in the Lyman-UV range ($\approx$ 900–1200 Å) that is not accessible with HST, and this turned out to be essential for most results reported here.

A number of chemical elements could be identified (F, P, S, Ar). In addition, very high ionisation stages of several elements, which were never seen before in stellar photospheric spectra, could be identified in the UV spectra for the very first time (e.g. Si V, Si VI, Ne VIII). To illustrate this, we display in Figs. 3–6 details of FUSE and HST spectra of PG1159 stars of particularly interesting wavelength regions, together with synthetic line profile fits.

Hydrogen – Four PG1159 stars show residual H with an abundance of 0.17. These objects are the outcome of an AFTP. All other PG1159 stars have H $\lesssim$ 0.1 and, hence, should be LTP or VLTP objects.

Helium, carbon, oxygen – These are the main constituents of PG1159 atmospheres. A large variety of relative He/C/O abundances is observed. The approximate abundance ranges are: He=0.30–0.85, C=0.15–0.60, O=0.02–0.20. The spread of abundances might be explained by different numbers of thermal pulses during the AGB phase.

Nitrogen – N is a key element that allows us to decide if the star is the product of a VLTP or a LTP. Models predict that N is diluted during an LTP so that

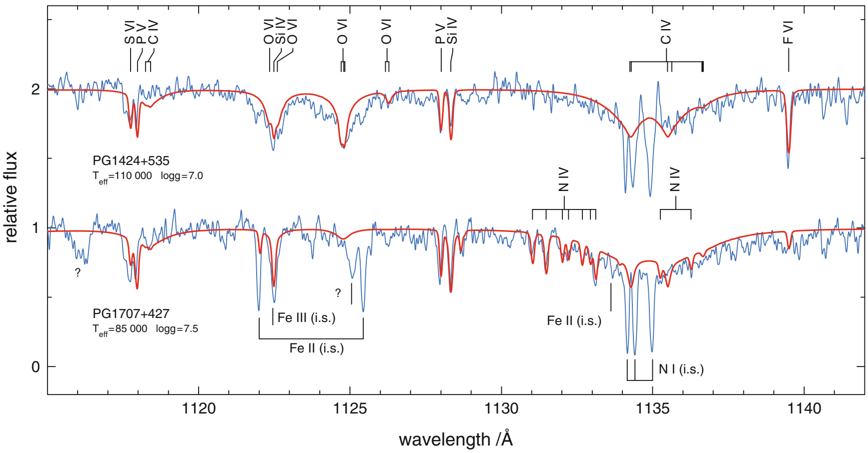

Fig. 3. Detail from FUSE spectra of two relatively cool PG1159 stars. Note the following features. The F VI 1139.5 Å line which is the first detection of F at all in a hot post-AGB star; the P V resonance doublet at 1118.0 and 1128.0 Å, the first discovery of P in PG1159 stars; the N IV multiplet at 1132 Å. Also detected are lines from Si IV and S VI. The broader features stem from C IV and O VI (Reiff *et al.* 2007).

in the end N=0.1%. This low N abundance is undetectable in the optical and only detectable in extremely good UV spectra. In contrast, a VLTP produces nitrogen (because of H-ingestion and burning) to an amount of 1% to maybe a few percent. N abundances of the order 1% are found in some PG1159 stars, while in others it is definitely much lower.

Neon – Ne is produced from ^{14}N that was produced by CNO burning. In the He-burning region, two α-captures transform ^{14}N to ^{22}Ne. Stellar evolution models predict Ne=0.02 in the intershell. A small spread is expected as a consequence of different initial stellar masses. Ne=0.02 was found in early optical analyses of a few stars and, later, in a much larger sample observed with FUSE (Werner *et al.* 2004).

Fluorine – F was discovered by Werner *et al.* (2005) in hot post-AGB stars; in PG1159 stars as well as H-normal central stars. A strong absorption line located at 1139.5 Å remained unidentified until we found that it stems from F VI. The abundances derived for PG1159 stars show a large spread, ranging from solar to up to 250 times solar. This was surprising at the outset because ^{19}F, the only stable F isotope, is very fragile and easily destroyed by H and He. A comparison with AGB star models of (Lugaro *et al.* 2004), however, shows that such high F abundances in the intershell can indeed be accumulated by the reaction $^{14}\mathrm{N}(\alpha,\gamma)^{18}\mathrm{F}(\beta^{+})^{18}\mathrm{O}(\mathrm{p},\alpha)^{15}\mathrm{N}(\alpha,\gamma)^{19}\mathrm{F}$, the amount depending on the stellar mass. We find a good agreement between observation and theory. Our results also suggest, however, that the F overabundances found in AGB

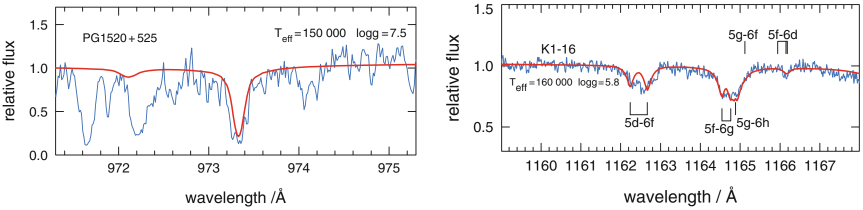

Fig. 4. *Left:* First identification of the Ne VII 973.3 Å line, shown here in the FUSE spectrum of the PG1159 star PG1520+525. This strong absorption feature is seen in the spectra many hot post-AGB stars, but remained unidentified for some years Werner *et al.* (2004). *Right:* Discovery of Ne VIII lines in the FUSE spectrum of the PG1159-type central star of K 1-16. This is the first detection of Ne VIII in any photospheric spectrum (Werner *et al.* 2007b). Lines from this ion are only exhibited by the very hottest post-AGB stars ($T_{\rm eff}\geq$140 000 K).

stars (Jorissen *et al.* 1992) can only be understood if the dredge-up of F in the AGB stars is much more efficient than hitherto thought.

Silicon – The Si abundance in evolution models remains almost unchanged. This is in agreement with the PG1159 stars for which we could determine the Si abundance.

Phosphorus – Systematic predictions from evolutionary model grids are not available; however, the few computed models show P overabundances in the range 4–25 times solar (Lugaro priv. comm.). This is at odds with our spectroscopic measurements for two PG1159 stars, that reveal a solar P abundance.

Sulfur – Again, model predictions are uncertain at the moment. Current models show a slight (0.6 solar) underabundance. In strong contrast, we find a large spread of S abundances in PG1159 stars, ranging from solar down to 0.01 solar.

Argon – This element has been identified very recently for the first time in hot post-AGB stars and white dwarfs (Werner *et al.* 2007a). Among them is one PG1159 star for which a solar Ar abundance has been determined (Fig. 5). This is in agreement with AGB star models which predict that the Ar abundance remains almost unchanged.

Lithium – Unfortunately, PG1159 stars are too hot to exhibit Li lines because Li is completely ionised. If Li were detected then it must have been produced during a VLTP. The discovery of Li in Sakurai's star is a strong additional hint that it underwent a VLTP and not an LTP.

Iron and Nickel – Fe VII lines are expected to be the strongest iron features in PG1159 stars. They are located in the UV range. One of the most surprising results is the non-detection of these lines in three PG1159 stars examined (K1-16, NGC 7094, PG1159-035; see, e.g., Fig. 6). The derived upper abundance limits (e.g., Werner *et al.* (2003); Jahn *et al.* (2007)) indicate that iron is depleted by about 0.7–2 dex, depending on the particular object. Iron depletions were also found for the PG1159-[WC] transition object Abell 78 as well

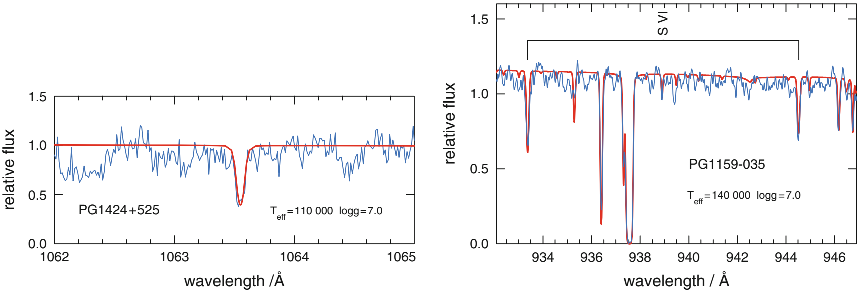

Fig. 5. *Left:* Discovery of the Ar VII 1063.55 Å line in the FUSE spectrum of the PG1159 star PG1425+535. This is the first detection of Ar VII in the photospheric spectrum of hot a post-AGB star Werner *et al.* (2007a). *Right:* FUSE enabled the first abundance determination of sulfur in PG1159 stars. Shown here is the S VI resonance doublet in the prototype of the PG1159 spectral class, PG1159−035 (Jahn *et al.* 2007).

as for several PG1159 progenitors, the [WC] stars. Such high Fe depletions are not in agreement with current AGB models. Destruction of ^{56}Fe by neutron captures is taking place in the AGB star intershell as a starting point of the s-process; however, the resulting depletion of Fe in the intershell is predicted to be small (about 0.2 dex). It could be that additional Fe depletion can occur during the late thermal pulse. In any case, we would expect a simultaneous enrichment of nickel, but up to now we were unable to detect Ni in PG1159 stars at all. While the solar Fe/Ni ratio is about 20, we would expect a ratio close to the s-process quasi steady-state ratio of about 3. Fittingly, this low ratio has been found in Sakurai's (cool) LTP object.

Trans-iron elements – The discovery of s-process elements in PG1159 stars would be highly desirable. However, this is at present impossible due to the lack of atomic data. From the ionization potentials we expect that these elements are highly ionised like iron, i.e., the dominant ionization stages are VI – IX. To our best knowledge, there are no laboratory measurements of so highly ionised s-process elements that would allow us to search for atomic lines in the observed spectra. Such measurements would be crucial to continue the element abundance determination beyond the current state.

5 Conclusions

It has been realized that PG1159 stars exhibit intershell matter on their surface, which has probably been laid bare by a late final thermal pulse. This provides the unique opportunity to study directly the result of nucleosynthesis and mixing processes in AGB stars. Spectroscopic abundance determinations of PG1159 photospheres are in agreement with intershell abundances predicted by AGB star models for many elements (He, C, N, O, Ne, F, Si, Ar).

For other elements, however, disagreement is found (Fe, P, S) that points at possible weaknesses in the evolutionary models.

Acknowledgement. I thank the conference organizers for travel support and particularly for their kind hospitality and assistance.

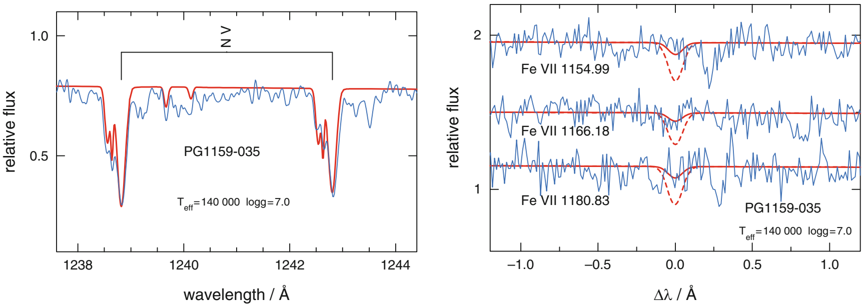

Fig. 6. *Left:* The high spectral resolution of HST/STIS allows us to distinguish the photospheric N V resonance doublet from the weak blueshifted ISM components. This enabled the first reliable N abundance determination in the prototype PG1159-035 (Jahn *et al.* 2007). *Right:* From the absence of Fe VII lines in the FUSE spectrum a Fe deficiency is concluded. Model spectra were computed with solar and 0.1 solar Fe (Jahn *et al.* 2007).

References

Blöcker, T. 1995, A&A, 299, 755

Clayton, G. C. & De Marco, O. 1997, AJ, 114, 2679

Duerbeck, H. W. & Benetti, S. 1996, ApJ Lett., 468, L111

Gonzalez, G., Lambert, D. L., Wallerstein, et al.1998, ApJS, 114, 133

Hamann, W.-R. 1997, IAU Symp. 180, ed. H. J. Habing & H. J. G. L. M. Lamers (Kluwer), 91

Herwig, F. 2003, IAU Symp. 209, ed. S. Kwok, M. Dopita, & R. Sutherland, ASP, 111

Herwig, F., Blöcker, T., Langer, N., & Driebe, T. 1999, A&A, 349, L5

Iben, Jr., I., Kaler, J. B., Truran, J. W., & Renzini, A. 1983, ApJ, 264, 605

Jahn, D., Rauch, T., Reiff, E., Werner, K., Kruk, J. W., & Herwig, F. 2007, A&A, 462, 281

Jorissen, A., Smith, V. V., & Lambert, D. L. 1992, A&A, 261, 164

Lugaro, M., Ugalde, C., Karakas, A. I., et al.2004, ApJ, 615, 934

Pavlenko, Ya. V., Geballe, T. R., Evans, A., et al.2004, A&A, 417, L39

Reiff, E., Rauch, T., Werner, K., Kruk, J. W., & Herwig, F. 2007, in 15th European Workshop on White Dwarfs, eds. R. Napiwotzki, M.R. Burleigh, ASP Conference Series, 372, 237

Schönberner, D. 1983, ApJ, 272, 708
Werner, K. & Rauch, T. 1994, A&A, 284, L5
Werner, K. & Herwig, F. 2006, PASP, 118, 183
Werner, K., Heber, U., & Hunger, K. 1991, A&A, 244, 437
Werner, K., Deetjen, J. L., Dreizler, S., et al.2003, IAU Symp. 209, ed. S. Kwok, M. Dopita, & R. Sutherland, ASP, 169
Werner, K., Rauch, T., Reiff, E., Kruk, J. W., & Napiwotzki, R. 2004, A&A, 427, 685
Werner, K., Rauch, T., & Kruk, J. W. 2005, A&A, 433, 641
Werner, K., Rauch, T., & Kruk, J. W. 2007a, A&A, 466, 317
Werner, K., Rauch, T., & Kruk, J. W. 2007b, A&A, 474, 591
Wood, P. R. & Faulkner, D. J. 1986, ApJ, 307, 659

"Recent Advances in Spectroscopy:
Theoretical, Astrophysical, and Experimental Perspectives"
Eds. Chaudhuri R K, Mekkaden M V, Raveendran A V, Satya Narayanan A
Astrophysics and Space Science Proceedings, Springer-Verlag, Berlin, 2010.

Elemental abundances in CEMP stars: $r-$ and $s-$process elements

Aruna Goswami, Subramania P Athiray, and Drisya Karinkuzhi

Indian Institute of Astrophysics, Bangalore 560034, India. `aruna@iiap.res.in`

Summary. A number of Carbon-Enhanced Metal-poor (CEMP) stars are known to exhibit enhancement of both $r-$ and $s-$process elements. An understanding of the relative contributions from r− and s−process would provide insight into the production mechanisms, nucleosynthetic sites and origins of the heavy elements observed in the stars. We have investigated ways to delineate the observed abundances into their respective $r-$ and $s-$process contributions. Preliminary results obtained using appropriate model functions in the framework of a parametric model are discussed.

1 Introduction

CEMP stars are classified as CEMP-*s* or CEMP-*r* based on the observed enhancement of abundances of heavy elements of $s-$ and $r-$process, respectively. These elements are formed primarily by captures of neutrons by iron-peak seeds; however, recent studies by several authors(Gallino et al. 1998; Goriely & Mowlavi 2000; Busso et al. 2001) have predicted efficient production of the third peak s-process element lead (Pb) in very metal-poor environments characterized by lack of iron-seed nuclei.

Production mechanisms of $s-$ and $r-$process require not only two widely different astrophysical sites but also very different time scales. They also require different neutron fluxes; the time scale for neutron capture by iron-seed elements for s-process is much longer than that required for their beta decay and in $r-$process much shorter than the beta decay time scale. Identification of an explicit stellar site for $s-$process nucleosynthesis started with the works of Weigert (1966) and Schwarzschild & Harm (1967) on the thermal pulse calculations. Slow neutron-capture elements are now believed to be produced due to partial mixing of protons into the radiative C-rich layers during thermal pulses that initiate the chain of reactions ^{12}C(p,γ)^{13}N(β) ^{13}C(α,n) ^{16}O in a narrow mass region of the He intershell during the inter-pulse phases of a low-mass AGB star. Rapid neutron-capture process elements are thought to be produced during SN explosions or neutron star mergers.

Classification and analysis of a number of CEMP stars in the recent past provided evidence of enhancement of both $s-$ and $r-$elements (Goswami 2005; Hill et al. 2000; Goswami et al. 2006, 2007, 2010; Jonsell et al. 2006). The upper limit in the metallicity of stars showing double enhancement is [Fe/H] ≤ -2 (HE 1305+0007 with [Fe/H] $= -2.0$ (Goswami et al. 2006)). In spite of several efforts, a physical explanation for the observed double enhancement is still lacking (Qian & Wasserburg 2003; Wanajo et al. 2006).

Heavy element abundances in the solar system have contributions from both $r-$ and $s-$process in different proportions. The first step to understand the nucleosynthetic origin of the heavy elements is to determine the relative contributions from the $s-$ and $r-$process to the observed abundances. We have investigated ways to delineate the observed abundances into their respective $r-$ and $s-$process contributions. Identification of the dominant processes contributing to the heavy element abundances in CEMP stars is likely to provide clues to the physical mechanism(s) responsible for the observed double enhancements in these objects.

2 A parametric model based analysis

There have been several efforts to explain the solar system abundances of elements associated with slow neutron capture process. One of the early models that could reproduce the observed solar system σN curve with a good agreement is the parametric model of Howard et al. (1996). The model used an exponential distribution of neutron exposures via sequential irradiation. A fit for solar system σN curve was obtained by optimizing the neutron density and temperature which in turn optimized the mean neutron exposure. This model was used by Aoki et al. (2001) to study $s-$process elemental abundances in metal-poor stars. Zhang et al. (2006) also utilized a parametric model to explain the observed abundances of metal-poor double enhanced stars. We have explored the origin of neutron-capture elements by comparing the observed abundances with the predicted $s-$ and $r-$process contribution using appropriate model function in the framework of a parametric model.

2.1 Methodology

We have utilized the solar system $r-$ and $s-$process isotopic abundances of stellar model of Arlandini et al. (1999). The observed elemental abundances are scaled to the metallicity of the corresponding CEMP stars and normalized to their respective barium abundances. Elemental abundances are then fitted with the parametric model functions

$$log\epsilon_i = A_s N_{s,i} + A_r N_{r,i} \tag{1}$$

$$log\epsilon_i = A_s N_{s,i} + (1 - A_s) N_{r,i} \tag{2}$$

for the stars listed in Table 1. A_s and A_r are the component coefficients that correspond to contributions from the $s-$ and $r-$process respectively. $N_{s,i}$ and $N_{r,i}$ are the i^{th} element abundance produced by $s-$ and $r-$process respectively. The best fit curve obtained for HE 1305+0007 and HD 5223 are shown in Figs 3 and 4, respectively. The observed abundances for HE 1305+0007 and HD 5223 are taken from Goswami et al. (2006); for all other stars listed in Table 1, the observed abundances are taken from a compilation of Jonsell et al. 2006 (Table 1).

Table 1. Best fit co-efficients and reduced χ^2 values for a sample of CEMP stars

Star name	Best fit values for $\log\epsilon = A_sN_s + A_rN_r$			Best fit values for $\log\epsilon = A_sN_s + (1-A_s)N_r$	
	A_s	A_r	χ^2	A_s	χ^2
HE 1305+0007(r+s)	0.47±0.11	0.53±0.09	1.07	0.75±0.08	0.94
HD 5223(CH)	0.60±0.20	0.37±0.16	1.12	0.66±0.15	1.46
HD 209621(r+s)	0.57±0.10	0.42±0.08	1.08	0.47±0.08	1.94
LP 625-44(r+s)	0.78±0.01	0.05±0.07	1.43	1.01±0.06	2.11
CS 31062-012(r +s)	0.60±0.08	0.39±0.08	1.11	0.60±0.07	0.84
CS 22898-027(r +s)	0.56±0.07	0.41±0.05	1.19	0.60±0.05	1.14
HE 2148-1247(r +s)	0.56±0.05	0.43±0.04	1.08	0.57±0.04	0.97
HE 0338-3945(r +s)	0.60±0.05	0.38±0.05	0.96	0.63±0.05	0.94
CS 22880-074(r +s)	0.73±0.08	0.22±0.07	1.29	0.76±0.07	1.74
HD 196944(s)	0.861±0.08	0.08±0.12	1.30	1.01±0.06	0.29

2.2 Error analysis

Errors in the derived abundances arise mainly from two sources, random errors as well as systematic errors arising from uncertainties in the adopted atmospheric parameters. Both errors play important roles in deciding the goodness of fit of the parametric model function and hence the model. In most cases for the stars listed in Table 1, the metallicities are determined using Fe I and Fe II lines with an error in the range of ±0.2 to ±0.3 dex as indicated by the derived standard deviation σ. The abundances of the heavy elements are derived usually by spectrum synthesis calculations. Estimated fitting errors range between 0.1 and 0.3 dex. For the parametric model function fits we have adopted ±0.2 dex as the error in the observed abundance data for the stars HE 1305+0007, HD 5223 and HD 209621 as given by Goswami et al. (2006). For all other stars the errors are taken from the respective references given in Jonsell et al. (2006); for the star HD 196944, out of five references mentioned in the paper by Jonsell et al. (2006), the value given by Aoki et al. (2001) is adopted. The reported abundance of lead (Pb) in HD 5223 is quoted as an upper limit in Goswami et al. (2006); we have therefore used the lead abundance in this star as 1.95 instead of 2.15 given by the authors.

3 Results and Conclusions

The derived coefficients A_s and A_r from the model fits using parametric model function (1) are indicative of fractional contributions coming from the $s-$ and $r-$process respectively.

HE 1305+0007 This star was first classified as a CEMP-r/s stars by Goswami et al. (2006). Model calculation indicates that $r-$process contribution is slightly higher than that of the $s-$process with $A_r = 0.53 \pm 0.09$ and $A_s = 0.47 \pm 0.11$.

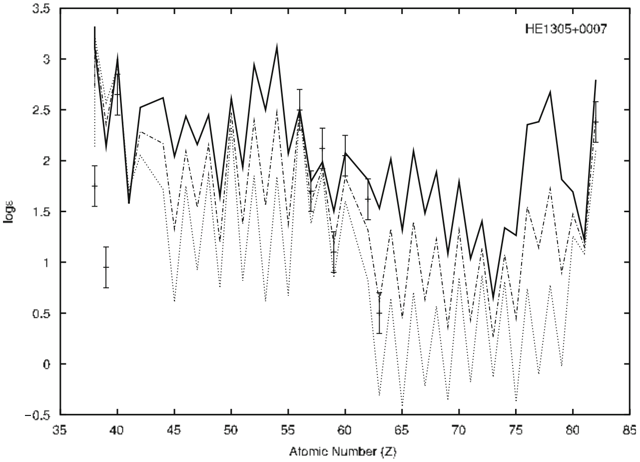

Fig. 1. Abundance patterns of heavy elements from Arlandini *et al.* (Stellar model). Solid line shows abundances due to only r–process; dotted line is of s−process only and dashed line indicates abundance pattern derived from a simple average of r− and s−processes. The patterns are normalized to Ba. The points with error bars are observed abundances in HE 1305+0007 and are taken from Goswami et al. (2006).

HD 5223, HD 196944, LP 625-44, CS 22880-074 These stars belong to the CEMP-s group; they exhibit enhanced $s-$process elemental abundances. With a good agreement with observations, the dominancy of the $s-$process in these objects is also noticed from the model analysis. The component coefficients of $s-$process are A_s = 0.60 ± 0.20, 0.86 ± 0.08, 0.78 ± 0.01 and 0.73 ± 0.08 respectively and the component coefficients of $r-$process A_r are respectively 0.37 ± 0.16, 0.08 ± 0.12, 0.05 ± 0.07 and 0.22 ± 0.07.

HD 209621, CS 31062-012, CS 22898-027, HE 2148-1247, HE 0338-3945 In a recent high resolution spectroscopic analysis of the star HD 209621, it is shown that the neutron-capture elements in HD 209621 primarily originate in s−process; however, estimated [Ba/Eu] = +0.35 places the star in the

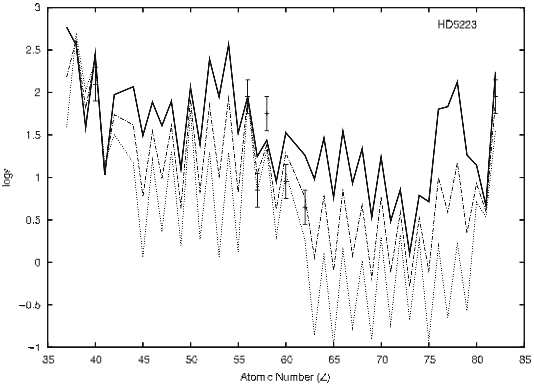

Fig. 2. Same as Fig 1, shown for HD 5223.

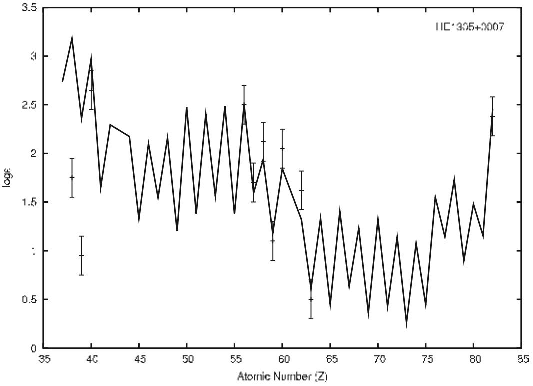

Fig. 3. The best fit curve obtained with the parametric model function $\log\epsilon_i = (A_s N_{s,i} + A_r N_{r,i})$. Observed abundances (points with error bars) in HE 1305+0007 are from Goswami et al. (2006).

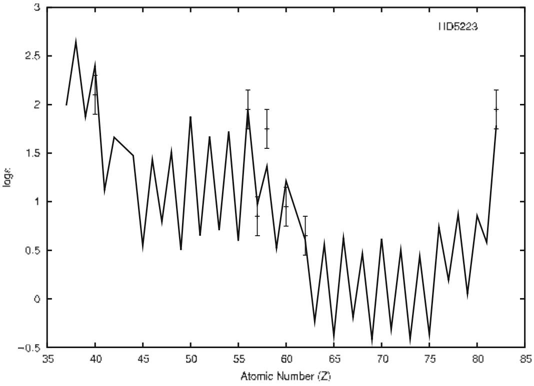

Fig. 4. Same as Fig 3, for HD 5223

group of CEMP-(r+s) stars (Goswami & Aoki 2010). The other four stars are listed as r+s stars in Jonsell et al. (2006). Our model fits coefficients A_s for these objects are respectively 0.568 ± 0.10, 0.59 ± 0.08, 0.56 ± 0.07, 0.56 ± 0.05 and 0.60 ± 0.05; the corresponding A_r values are 0.42 ± 0.08, 0.39 ± 0.08, 0.40 ± 0.05, 0.43 ± 0.04 and 0.37 ± 0.05 respectively. As is noticed A_s values are slightly higher than the values of A_r in these stars except in HE 1305+0007 where the component coefficient A_r indicates dominance of $r-$process over $s-$. Following CEMP stars classification scheme of Beers & Christlieb (2005) these stars however fall into CEMP-$r+s$ stars with [Ba/Eu] estimates as 0.35, 0.36, 0.35, 0.38 and 0.47 respectively. In this classification scheme C-enhanced stars with [Ba/Eu] ≥ 0.5 are classified as CEMP-s stars.

A precise knowledge of the dominant mode of production (either $s-$ or $r-$) of the heavy elements would help to identify and construct a consistent and a realistic physical scenario involving explicit production sites, environment and precise physical mechanism(s) that could explain the origin of this rare class of objects.

As evident from the results presented in Table 1, calculations carried out using model function (2) also show similar fractional contributions from $s-$ and $r-$process in these objects. However, the constraint of making the sum of the coefficients A_s and A_r equal to unity strikes out the possibility of finding additional mechanisms which would have contributed to the observed abundances.

Acknowledgement. Funding from the DST Project No. SR/S2/HEP-09/2007 is gratefully acknowledged.

References

Aoki, W., Ryan, S. G., Norris, J. E., et al., ApJ, **561**, 346 (2001)
Arlandini, C., Kappeler, F., Wisshak, K., et al., ApJ, **525**, 886 (1999)
Beers, T. C. and Christlieb, N., ARAA, **43**, 531 (2005)
Busso, M. et al., ApJ, **557**, 802 (2001)
Gallino, R., Arlandini, C., Busso, M. et al. ApJ, **497**, 388 (1998)
Goriely, S., Mowlavi, N. S., A&A, **362**, 599 (2000)
Goswami, A., MNRAS, **359**, 531 (2005)
Goswami, A., Aoki, W., Beers, T. C., et al., MNRAS, **372**, 343 (2006)
Goswami, A., Bama, P., Shantikumar, N. S., et al., BASI, **35**, 339 (2007)
Goswami, A., Aoki, W., MNRAS (in press) (2010)
Goswami, A., Karinkuzhi, D., Shantikumar, N. S., MNRAS, **402**, 1111 (2010)
Hill, V., Barbuy, B., Spite, M., Spite, F., et al., A&A, **353**, 557 (2000)
Howard, W. A., Mathews, G. J., Takahashi, K., et al., ApJ, **309**, 633 (1996)
Jonsell, K., Barklem, P. S., Gustafsson, B., et al., A&A, **451**, 651, (2006)
Qian, Y. Z. and Wasserburg, G. J., ApJ, **588**, 1099 (2003)
Schwarzschild, M. and Harm, R., ApJ, **150**, 961 (1967)
Wanajo, S., Nomoto, K., et. al. ApJ, **636**, 842 (2006)
Weigert, A., ZA, **64**, 395 (1966)
Zhang, B., Ma, K., Zhou, G., ApJ, **642**, 1075 (2006)

"Recent Advances in Spectroscopy:
Theoretical, Astrophysical, and Experimental Perspectives"
Eds. Chaudhuri R K, Mekkaden M V, Raveendran A V, Satya Narayanan A
Astrophysics and Space Science Proceedings, Springer-Verlag, Berlin, 2010.

Spectroscopic survey of emission line stars in open clusters

Subramaniam, A. and Mathew, B.

Indian Institute of Astrophysics, Bangalore - 560 034, India. `purni@iiap.res.in`, `blesson@iiap.res.in`

Summary. We summarize a study of emission-line stars in young open clusters. The study was done in two phases. The first phase was the survey, where the emission stars in young open clusters were identified using the slitless spectral images. The identified emission stars were then studied in detail using their slit spectra in the 3700–9000 *Å* range. The results of the study suggest that there could be two mechanisms responsible for the Be phenomenon. The early type B stars are likely to become Be stars in the second half of their MS lifetime, whereas the late type B stars are likely to be born as Be stars.

1 Introduction

Open clusters are dynamically associated system of stars, which are presumed to be formed from giant molecular clouds through bursts of star formation. Apart from the coeval nature of the stars, they are assumed to be at the same distance and have the same chemical composition. Hence it is a perfect place to study emission stars since we do not have a hold on these parameters in the field. Young open clusters are found to contain emission stars since the emission stars undergo evolution over a time scale of less than 100 Myr. Early type emission stars are broadly classified as Classical Be (CBe) stars and Herbig Be (HBe) stars. A Be star is defined as a non-super giant B-type star whose spectrum has, or had at some time, one or more Balmer lines in emission (Collins 1987). CBe stars are fast rotators (70−80% of the critical velocity) whose circumstellar disk is formed through decretion mechanism (wind/outflow) (Porter & Rivinius 2003). Jaschek & Jaschek (1983) has identified 12% of the stars in the Bright Star Catalogue as Be stars. Herbig Ae/Be (HAeBe) stars are intermediate mass pre-main sequence (PMS) stars, found to possess a natal accretion disk which is a remnant of star formation (Hillenbrand et al. 1992). Maeder et al. (1999) suggested the influence of metallicity in Be star formation by indicating a higher fraction of Be stars in low-metallicity clusters. Mermilliod (1982) studied 94 Be stars in 34 open clusters. He found that the distribution of Be stars peaked at spectral type B1−B2 and B7−B8, confirming earlier results. He also found that the Be stars occupy the whole main sequence (MS) band and are not confined to the region of termination of the MS. Recently, Mcswain & Gies (2005) conducted a photometric survey of 55 southern open clusters and identified 52 definite Be stars and 129 probable candidates. They also reported that the spin-up effect at the end of the MS phase cannot explain the observed distribution of Be stars.

The Be mechanism still is not well understood and also its dependence on the stellar mass and age. Be stars found in open clusters are ideal targets to understand the above. These are probably the only targets to understand the evolution of the decretion disk, its properties including the angular momentum, radius and density with age. In order to address the above, a slitless spectroscopic survey of 207 clusters were performed. This is a major survey considering the number of surveyed clusters and the emission stars detected. Some of the results obtained in this survey are presented here.

2 Slit-less spectroscopic survey

Emission-line stars in young open clusters are identified to study their properties, as a function of age, spectral type and evolutionary state. 207 open star clusters were observed using slitless spectroscopy method using the 2-m Himalayan Chandra Telescope (HCT), located in Hanle and operated by IIA. In this survey, 157 emission stars were identified in 42 clusters. The result of this survey was published by Mathew et al. (2008). They found 54 new emission-line stars in 24 open clusters, of which 19 clusters were found to house emission stars for the first time. Rich clusters like NGC 7419, NGC 663, NGC 2345, NGC 6649, *h* Persei, χ Persei are also rich in emission-line stars (25, 22, 12, 7, 6 and 6 emission stars respectively). We classify rich clusters as those with 6 or more emission stars. The detailed table is given in Mathew et al. (2008). About 20% clusters harbour emission stars. The optical colour magnitude diagram (CMD) along with Near-IR Colour-Colour diagram (NIR CCDm) and nebulosity was used to classify the emission stars into CBe and HAeBe category. Most of the emission stars in the survey belong to CBe class ($\sim$ 92%) while $\sim$ 6.3% is HBe and remaining $\sim$1.7% is HAe. The youngest clusters to have CBe stars are IC 1590, NGC 637 and NGC 1624 (all 4 Myr old) while NGC 6756 (125-150 Myr) is the oldest cluster to have CBe stars. The CBe stars are located all along the MS in the optical CMDs of clusters of all ages, which indicates that the Be phenomenon is unlikely due to core contraction near the turn-off.

2.1 Frequency distribution of emission star clusters with age

Since the ages of most of the clusters which house the emission star are known, the appearance of emission stars as a function of age can be studied. Among the surveyed 207 open clusters, 140 were younger than 100 Myr, 39 clusters were older than 100 Myr while the ages of 28 clusters are unknown. Out of the total number of clusters surveyed 20.28 % has been found to have emission stars. The fraction of clusters which have emission stars with respect to the total surveyed clusters as a function of age is shown as histogram in Fig. 1. We found 48 clusters fall in the age bin 0−10 Myr, of which 18 have emission stars. Similarly 8 out of 29 clusters have e-stars in 10−20 Myr age bin while 4 out of 10 clusters have e-stars in 20−30 Myr age bin. The maximum fraction of clusters which house CBe stars were found to fall in the age bin 0−10 Myr and 20−30 Myr (∼ 40%). There seems to be a dip in the fraction of CBe clusters in the 10−20 Myr age bin. For older clusters, the estimated fraction ranges between 10−25%. The reduction in the fraction from 0−10 Myr age bin to 10−20 Myr age bin could be due to evolutionary effects and also due to the MS evolution of the probable HBe stars. There seems to be an enhancement in the cluster fraction with Be stars in the 20−30 Myr age bin bin. This is suggestive of an enhancement in the Be fraction in this age bin indicating a possible evolutionary effect on the angular momentum of mostly early type stars.

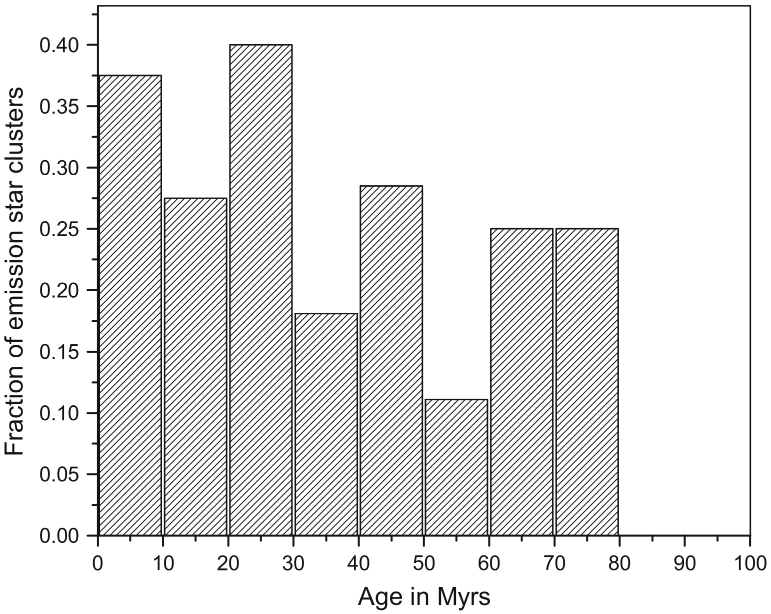

Fig. 1. Fraction of clusters which have emission line stars with respect to the total number of clusters surveyed in each bin.

We find that CBe phenomenon is pretty much prevalent in clusters younger than 10 Myr, $\sim$ 40% of clusters house CBe stars and about 20% CBe stars are about 10 Myr. Mcswain & Gies (2005) also find a good fraction of clusters to have CBe stars in this age bin. Thus, these CBe stars are born as CBe stars, rather than being evolved to become CBe stars. Since we do not find any CBe stars earlier than B1 in clusters of this age range, our results mildly suggest that this happens mainly for spectral types later than B1.

We also find that the fraction of clusters with CBe stars significantly increases in the age range 20−30 Myr, similar to that found by Wisniewski & Bjorkman (2006) (10−25 Myr) and Mcswain & Gies (2005) (10−20 Myr). All these results put together indicate that there is an enhancement in the 10−30 Myr age range. These suggest that stars in these clusters evolve to become CBe stars. Thus, there could be two mechanisms responsible for the Be phenomenon. Rapid rotation is generally considered as the reason for the CBe phenomenon. The first mechanism, being rapid rotation, is where the stars start off as CBe stars early in their lifetime, as indicated by CBe stars in very young clusters. These probably are born fast-rotators. These type of stars are found in all age groups of clusters. These types of stars are likely to be later than B1, as indicated by the paucity of very early type CBe stars in young clusters. The second mechanism is responsible for the enhanced appearance of Be stars in the 10−30 Myr age group clusters. This is likely to be an evolutionary effect. The 10−30 Myr age range has a large number of CBe stars with spectral types earlier than B1. This component is probably due to the structural or rotational changes in the early B-type stars, in their second half of the MS life time.

3 Spectroscopic properties of emission stars

The spectroscopic observations of the identified individual emission stars in clusters were obtained using HFOSC instrument mounted on HCT. A comparative analysis of the spectral lines of 157 surveyed emission-line stars is presented in Mathew & Subramaniam (2010).

As an example, the results for the young open cluster, IC 1590 is presented below. From the analysis of optical, Near-IR photometry and nebulosity we found that star 1 belongs to HBe category while 2 and 3 are HAe and CBe respectively (Mathew et al. (2008)). From UBV CCD photometry star IC 1590-1 was estimated to belong to B8.5 spectral type while stars 2 and 3 were found to be A0 and B2 respectively. The spectral features of these emission stars are given below. All the Balmer lines except H_α and H_β are found in absorption (Fig. 2). The emission profile of H_α shows P-Cygni nature for star 2 and double-peak for star 3 while it is normal single peak profile for star 1. The P-Cygni profile indicates that the H_α line might be formed in wind/outflow, which is a characteristic of HAeBe star. The double-peak H_α

profile is usually indicative of the CBe stars. H_β is found to have an asymmetric emission in absorption profile for stars 1 and 2 while it is in absorption for star 3. As seen in Fig. 1, quite a number of FeII lines (4549 *Å*, 4584 *Å*, 4924 *Å*, 5018 *Å*, 5169 *Å*, 5235 *Å*, 5276 *Å*, 5316 *Å*, 5363 *Å*) are found in emission for the stars 1 and 2 while no such nature is seen for star 3. The 5018 *Å* Fe II profile is found to show P-Cygni feature for stars 1 and 2, which is a signature of wind/outflow associated with the star. In the red region of the spectrum, calcium II (CaII) triplet (8498 *Å*, 8542 *Å*, 8662 *Å*) is found in emission along with the Paschen lines (8467(P17), 8598(P14), 8750(P12), 8862(P11)) for stars 1 and 2 while they are found to be in absorption for star 3. The helium lines (4026 *Å*, 4471 *Å*, 5876 *Å*, 6678 *Å*, 7065 *Å*) are found to be visibly present in star 3 which matches with the spectral type estimated earlier from photometry. OI 8446 *Å* spectral line shows intense emission for stars 1 and 2 while it is absent in 3. Hence the spectral line features confirms our prediction from optical and Near-IR photometry that stars 1 and 2 are pre-main sequence HAeBe stars.

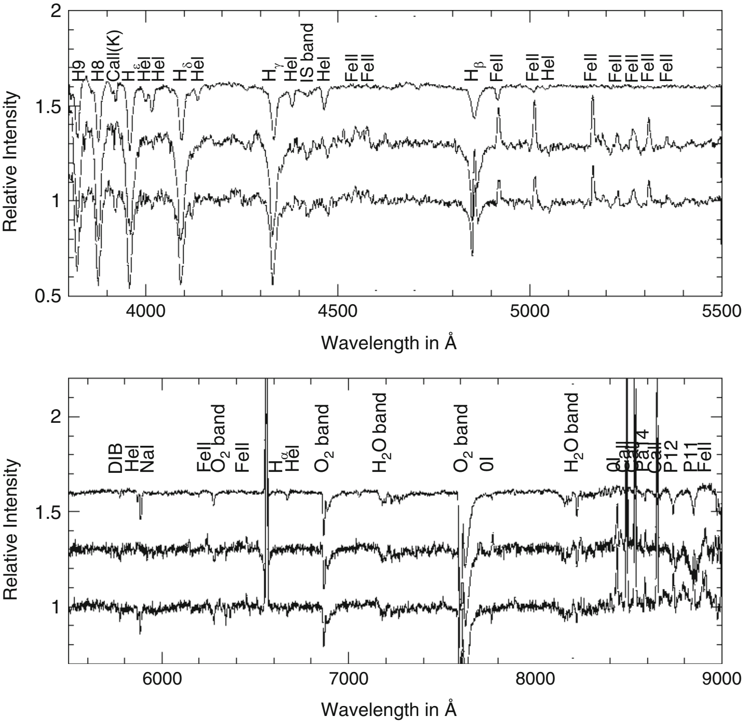

Fig. 2. The spectra of the emission stars in the cluster IC 1590 in the wavelength range 3800 – 9000*Å*. The emission stars are numbered 1, 2, 3 from bottom to top.

3.1 Main results from the survey

The main results of the survey can be summarized as:

1. From photometric analysis we deduced that early B-type stars may be evolved to CBe phase while those belonging to late B are born as CBe stars.

2. The Balmer decrement (D_{34}) of Be stars is found to range from 1.5 and 6.5 with a mean value of 3.5, unlike the typical nebular value of 2.7. The distribution of D_{34} with age, spectral type and Near-IR excess seems to confirm the bimodal origin of Be stars predicted from photometric analysis.

3. About 83% of the surveyed emission stars show FeII lines in their spectra. We found Lyman *beta* fluorescence as the mechanism for the production of $8446\mathring{A}$ line in 25% of the surveyed stars.

4. The emission region for H_α profile is found to be around 15 stellar radius, with a range of 7–30, assuming the circumstellar disk to be Keplerian.

5. The rotational velocity of candidate stars is found to be in the range 100–300 km/s, which matches with the values of field CBe stars. From the spectral line width analysis it is found that the circumstellar disk lags behind the star.

References

Collins, G. W. II., 1987, pbes.coll, 3
Hillenbrand, L. A., Strom, S. E., Vrba, F. J., Keene, J., 1992, ApJ, 397, 613
Jaschek, C., Jaschek, M. 1983, A&A, 117, 357
Maeder, A., Grebel, E. K., Mermilliod, J. C. 1999, A&A, 346, 459
Mathew, B., Subramaniam, A., Bhatt, B. C. 2008, MNRAS, 388, 1879
Mathew, B., Subramaniam, A. 2010, in preparation
Mcswain, M. V., Gies. D. R. 2005, ApJS, 161, 118
Mermilliod, J. C., 1982, A&A, 109, 48
Porter, J. M., Rivinius, T. 2003, PASP, 115, 1153
Wisniewski, J. P., Bjorkman, K. S., 2006, ApJ, 652, 458

"Recent Advances in Spectroscopy:
Theoretical, Astrophysical, and Experimental Perspectives"
Eds. Chaudhuri R K, Mekkaden M V, Raveendran A V, Satya Narayanan A
Astrophysics and Space Science Proceedings, Springer-Verlag, Berlin, 2010.

An improved Technique to Explore Disk Accretion Process in PMS Stars

Padmakar Parihar

Indian Institute of Astrophysics Koramangala, Bangalore -560034, India.
`psp@iiap.res.in`

Summary. The low mass PMS stars are found to be surrounded by thick, flared accretion disk and the disk material is supposed to be funneled onto the stellar surface by strong and predominately dipolar magnetic field. We have developed a simple technique which uses medium resolution optical spectrum and gives reliable disk accretion rate. In this paper, we briefly describe the technique and also present the preliminary results obtained.

1 Introduction

The formation of circumstellar disks is considered to be a natural process when a molecular core collapses to form a star. There are ample evidences to the presence of circumstellar disks around intermediate and low mass pre-main sequence stars, such as HAeBe and CTTS. The low mass PMS stars are found to be surrounded by thick flared accretion disks and the disk material is supposed to be funneled onto the stellar surface by strong and predominately dipolar magnetic field. A knowledge of disk accretion rates in stars of different age, mass, rotation and environment is very crucial to understand not only the formation of planets but also to shed light on stars formations as well. The disk accretion rates are primarily determined by modeling, (1) the excess blue continuum emission, (2) the optical and NIR line emission and (3) Spectral Energy Distribution (SED) over a larger wavelength regime. However, the actual procedure in the above modeling techniques are quite complicated (Herczeg & Hillenbrand 2008 and references therein). Furthermore, the accretion rates determined by different techniques do not agree well. Finally, the accretion rates are most likely variable on various time scale and to determine this intrinsi variability one needs an easy method. Keeping all these in mind, we attempted to develop a simple but reliable technique which can be used on a large sample of stars. We have applied our technique to measure the accretion rates in well known Classical T Tauri Stars (CTTS) and the results are presented here.

2 Observations and data reduction

The medium resolution spectroscopic observations of CTTS and template stars were carried out using 2-m HCT (Himalayan Chandra Telescope) of the Indian Astronomical Observatory equipped with the HFOSC spectrograph. Observations were made during a few nights in November 2006. Two different blue and red grisms, Gr14 and Gr8, were used to cover almost the whole optical spectral window (3600–9200 $\AA$). The spectroscopic observations were carried out using narrow 67 micron ($\sim 0.75''$) as well as wide 1340 micron ($\sim 15.0''$) slits. The highest resolution set by the narrow slit for these two grisms are R$\sim$1000 and R$\sim$2100, respectively. The spectral shape of the stellar spectrum obtained using narrow slit at low telescope elevation is usually highly distorted by atmospheric dispersion. To avoid the atmospheric dispersion effect in our observed spectrum, we rotated the instrument field de-rotator by the parallactic angle, which aligns the slit-length along the telescope elevation axis. On each night, observations of 2-3 spectrophotometric standards close to the CTTS and template stars were also carried out for flux calibration. The spectroscopic observations were reduced using tasks available in IRAF. After the bias subtraction and the flat field correction, stellar spectra were optimally extracted. Fe-Ne and Fe-Ar arc lamps were used for the wavelength calibration. Finally, the flux calibration was done using spectro-photometric standard stars. While doing the flux calibration, usually the average spectroscopic extinction of the site is used. If the extinction of the night differs from the average extinction of the site and the spectroscopic standard stars are observed at different airmasses, then there is a possibility of improper flux calibration. To avoid this problem, the spectroscopic extinction was determined during the same observing run.

3 The modeling technique

3.1 Computation of the excess continuum emission

It is believed that any spectra of CTTS is a composite of the central star spectrum and the excess emission coming from the disk accretion. In order to compute the excess emission in the optical spectrum due to disk accretion, we adopted the magnetospheric accretion shock model proposed by Calvet & Gullbring (1998). According to this model, a strong dipole magnetic field truncates the circumstellar disk at several stellar radii and the matter falls through magnetic fields with nearly free fall velocity. Near the stellar surface, the in-falling matter forms a shock and deposits its kinetic energy into a very localized region. This accretion energy quickly gets thermalized and is radiated away. Close to the stellar surface, the structure of the accretion column can be divided into three regions according to their source of heating: the shock and post-shock regions, the photosphere below the shock, and the preshock region above it. The shocked gas is heated to extremely high temperatures and therefore initially emits mostly soft X-rays (Calvet & Gulbring 1998). Half of this radiation is sent to the photosphere below and half to the preshock region above. In turn, a fraction of the radiation from the preshock gas is emitted back towards the star, adding further nearly one fourth of accretion energy to the heated photosphere. The flux of radiation incident on to the photosphere deposits energy over a range of optical depths, heating the gas to temperatures higher than the undisturbed surrounding stellar photosphere.

In our observable optical wavelength range, the excess emission is dominated by the heated photosphere which can be approximated by a black-body of effective temperature:

$$T_{eff} = \frac{1}{\sigma}(\sigma T_{\star}^{4} + \left(\frac{3}{4}\frac{\mathcal{F}}{}\right))^{\frac{1}{4}} \tag{1}$$

where $\mathcal{F}$ is energy flux density of the accreting matter, $T_{\star}$ is the effective temperature of the unheated photosphere and σ is the Stefan-Boltzmann constant.

Following Calvet & Gulbring (1998), we can determine $\mathcal{F}$ as a function of $\dot{M}$ and hot-spot filling factor f as:

$$\mathcal{F} = 9.8 \times 10^{10} \left(\frac{\dot{M}}{10^{-8} M_{\odot} yr^{-1}}\right) \times \left(\frac{M}{0.5 M_{\odot}}\right) \times \left(\frac{R}{0.5 R_{\odot}}\right)^{-3} \times \left(\frac{f}{0.01}\right)^{-1} \tag{2}$$

where M and R are stellar mass and radius in solar units and $\dot{M}$ is the mass accretion rate. Once the effective temperature of the heated photosphere is known, then the excess flux at each wavelength coming from stellar surface per unit area can be computed as

$$E(\lambda) = B_{\lambda}(Teff). \tag{3}$$

3.2 Determination of the accretion and extinction parameters

Once we have computed the excess emission coming from the heated photosphere, we can use the method proposed by Chelli (1999) which is a slightly modified method used by Gullbring *et al.* (1998). According to this method, the CTTS spectrum can be considered as a composite spectrum of the central PMS object and the excess emission predominately coming from the heated photosphere. Therefore, once we have a suitable template spectrum representing the central PMS object, then the CTTS spectrum can be synthesized as:

$$O_c(\lambda) = p_o 10^{-0.4 f(\lambda) A_v} \left[(1-f) S(\lambda) + f E(\lambda)\right] w(\lambda)), \tag{4}$$

where $S(\lambda)$ is the observed template spectrum, p_o is the scale factor which primarily depends on distances of CTTS and template stars, A_v is the CTTS

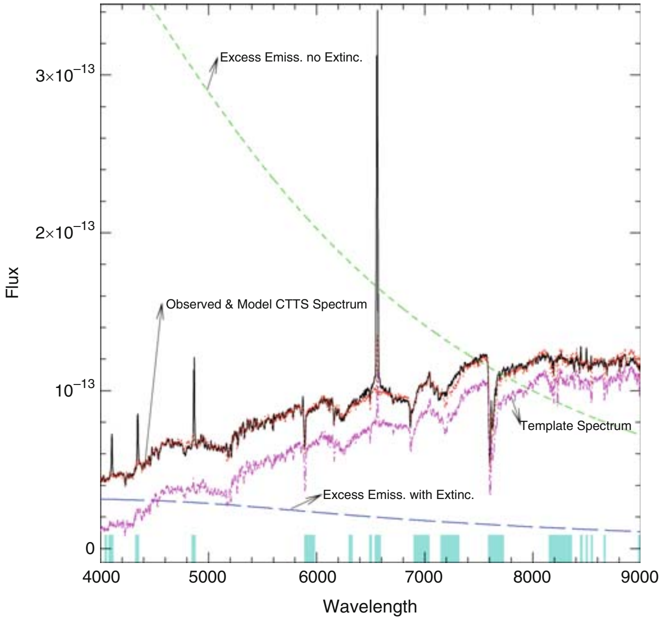

Fig. 1. Modeling the observed spectrum of BP Tau, a CTTS star with the template having a similar MK type.

extinction due to circumstellar and interstellar matter, f is the filling factor of hot spots and $w(\lambda)$ is the window function used to mask the emission line such as Balmer lines and also telluric lines (Fig.1). Here, we assume that the template spectrum has already been corrected for interstellar extinction. If $O(\lambda)$ is the flux calibrated observed spectrum of the CTTS star, the χ^2 merit function can be written as

$$\chi^2(p_o, A_v, f, \dot{M}) = \sum_{i=1}^{N} \left(\frac{(O_{c,i}(p_o, A_v, f, \dot{M}) - O_i)^2}{(\sigma_{o,i}^2 + \dot{\sigma}_{s,i}^2)} \right) \qquad (5)$$

where the scaled variance of the template spectrum is given by

$$\dot{\sigma}_{s,i}^2 = \left(p_o 10^{-0.4 f(\lambda) A_v} \sigma_{s,i} \right)^2 . \qquad (6)$$

Since χ^2 is a non-linear function of four parameters p_o, a_v, f and $\dot{M}$, therefore, the Levenberg-Marquardt technique was used to obtain the optimized value of the parameters from observation. An example of such a fitting to the observed spectrum of the BP Tau is shown in Fig 1, where we have shown the observed and fitted spectra of BP Tau, template spectrum and excess emission with and without extinction corrections.

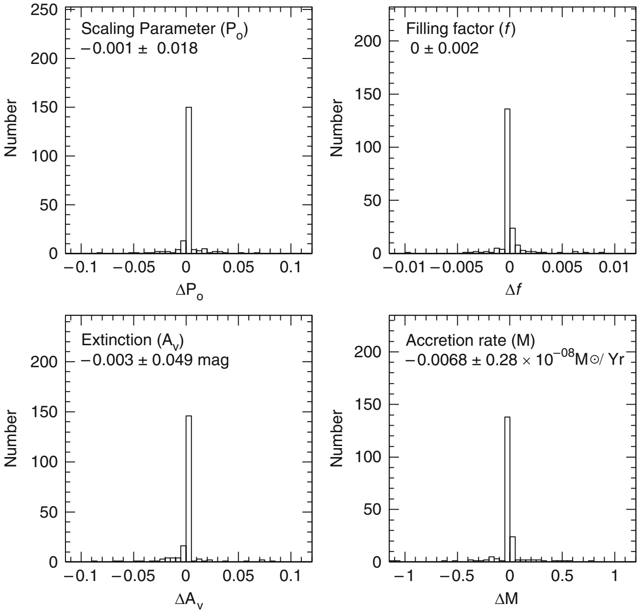

Fig. 2. Testing the reliability of the modeling technique using the synthetic spectra of accreting CTTS stars.

4 Testing the modeling technique

In order to test the reliability of the optimized parameters obtained from modeling of the observed data as described in the previous section, we assess the efficiency our technique with synthesized CTTS spectrum. For this purpose, we generated the synthetic CTTS spectrum by adding an excess emission expected from certain f and $\dot{M}$ parameters to the observed template spectrum. The error associated with the excess emission is due to photon shot noise and so the Poisson noise was added to the excess emission. Then, the spectrum was modulated with the CTTS extinction (see Eq. 1). Finally, the synthesized CTTS data was treated as the observed CTTS and modeled using the technique described in the previous sections. The recovered parameters are compared with the actual values of the parameters. This test was repeated with two hundred randomly selected parameters, having all possible values, and the results are shown in Fig. 2. It is clear from Fig. 2 that when the same template is used to synthesize the CTTS spectrum and later on to model it, the recovered parameters are almost close to the true values. Whereas, different values of the parameters are obtained when different templates are used to synthesize the CTTS spectrum and to model the spectrum. From the above test, it appears that the model parameters can be uniquely determined provided the template has a well determined extinction, and its MK spectral type matches closely with the CTTS.

Table 1. CTTS modeling results

	Present Work				Previous Work			
CTTS	Temp	A_v	f	$\dot{M}$	A_v	f	$\dot{M}^a$	$\dot{M}^b$
BP Tau	V819Tau	0.43	0.011	8.3	0.51	0.007	2.3	2.9
DN Tau	V819Tau	0.68	0.016	8.4	0.25	0.005	0.2	0.3
DF Tau	LkCa7	1.42	0.003	14.5	0.45	0.023	2.3	17.7
GM Aur	V819Tau	0.47	0.037	5.6	0.31	0.001	1.0	1.0
UY Aur	V819Tau	0.77	0.008	1.6	1.26	0.010	3.2	6.5

a: disk accretion rate from Calvet & Gullbirng (1998)
b: disk accretion rate from Gullbirng et al. (1998)

5 Modeling the well known CTTS spectra

After going through a rigorous testing of our modeling technique, we used it on a few well studied CTTS. We tried to use the same template star as used by previous researchers. The optimum values of the three parameters A_v, f and $\dot{M}$ of four stars are given in Table 1. In the same table, we also provide the values of these parameters obtained by Calvet & Gullbring (1998) and Gullbring et al. (1998). From a comparison of the accretion rate and other parameters, it appears that our values more or less closely resemble with the previous findings. A few cases where we find substantial differences in some of the parameters, we may interpret them as due to time variations or incorrectness of our/their estimates.

References

Calvet, N. and Gullbring, E, 1998, ApJ, 509, 802
Chelli, A. 1999, A&A, 342, 763
Gullbring, E., Hartmann, L., Briceno, C., & Calvet, N. 1998, ApJ, 492, 323
Herczeg, G. J., Hillenbrand, L. A., 2008, ApJ, 681, 594